2022

Charge Dynamics of InAs Quantum Dots Under Resonant and Above-Band Excitation

Gary R. Lander Jr
West Virginia University, glander@mix.wvu.edu

Recommended Citation

Lander, Gary R. Jr, "Charge Dynamics of InAs Quantum Dots Under Resonant and Above-Band Excitation" (2022). *Graduate Theses, Dissertations, and Problem Reports*. 11390.
https://researchrepository.wvu.edu/etd/11390

Charge Dynamics of InAs Quantum Dots Under Resonant and Above-Band Excitation

Gary Richard Lander

Dissertation submitted
to the Eberly College of Arts and Sciences
at West Virginia University
in partial fulfillment of the requirements for the degree of
Doctor of Philosophy in
Physics

Edward Flagg, Ph.D., Chair
Mikel Holcomb, Ph.D.
Tudor Stanescu, Ph.D.
Jeremy Dawson, Ph.D.

Department of Physics and Astronomy
Morgantown, West Virginia

Keywords:
Quantum Optics, Quantum Dots, Spectroscopy, Interferometry, Second-Order Correlation Function, Time-Resolved Fluorescence

Abstract

Charge Dynamics of InAs Quantum Dots Under Resonant and Above-Band Excitation

Gary Richard Lander

Research involving light-matter interactions in semiconductor nanostructures has been an interesting topic of investigation for decades. Many systems have been studied for not only probing fundamental physics of the solid state, but also for direct development of technological advancements. Research regarding self-assembled, epitaxially grown quantum dots (QDs) has proven to be prominent in both regards. The development of a reliable, robust source for the production of quantum bits to be utilized in quantum information protocols is a leading venture in the world of condensed matter and solid-state physics. Fluorescence from resonantly driven QDs is a promising candidate for the production of single, indistinguishable photons to be utilized in quantum information protocols, and the material/sample currently leading the research in regards to this are indium-arsenide (InAs) QDs. However, a few obstacles exist inhibiting InAs QDs' ability to be an efficient and reliable source of single, indistinguishable photons. The root sources of these problems are mostly associated with the dynamic electrical environment in the vicinity of the QDs. The electrical environment is complex due to inevitable emergence of defects and impurities in the bulk host material during epitaxial growth. The presence of these defects results in a complicated network through which charges can migrate around, into, and out of the QDs, resulting in time-dependent perturbations to the electric potential by which QDs confine charge carriers. Inevitably, this results in time-dependent fluctuations in the optical frequency of the emitted fluorescence, and ultimately a broadening of the time-averaged absorption and emission spectra, dubbed spectral diffusion. Additionally, blinking can occur, which is fluctuations of the fluorescence intensity on time scales that are large relative to the lifetime of confined excited states. Both contribute to a loss of applicability to use these samples as an efficient source of single, indistinguishable photons. The broadening of the time-averaged emission spectrum via spectral diffusion results in a loss of indistinguishability amongst photons emitted at different times, whereas blinking results in an abatement of a consistent

single photon source. Understanding the exact electrical environment in which the QDs reside, as well as the complex environment through which carriers migrate can help future implementation of both growth and excitation techniques to minimize these undesirable effects. In this dissertation we explore the electric environment of our sample, the complex pathways through which carriers migrate, and how the resulting charge dynamics affect the intensity and indistinguishability of the emitted fluorescence from resonantly driven InAs QDs.

Acknowledgements

I'd like to thank my advisor, Professor Edward Flagg, and Professors Mickey Holcomb, Tudor Stanescu, and Jeremy Dawson for sitting on my committee; I hope the subject matter described below was intriguing. I'd also like to thank the late Professor Leo Golubovic who was on my original committee. Professor Golubovic was a magnificent teacher; he received students from a multitude of different backgrounds from different colleges and universities, all of whom had different arrays of holes in their understanding of the fundamental disciplines, and he was able to fill them all. Aside from his prowess in regards to physics, Professor Golubovic was a very kind and good man, and it is very unfortunate that he is no longer with us.

I'd like to thank Professor Flagg in several regards. Under his guidance, my skills associated with presenting scientific material have progressed immensely. My writings skills, whether in regards to taking lab notes, writing detailed analysis reports, writing manuscripts to be published, communication with other scientists, etc, have also developed significantly under his guidance. Working with him one-on-one helped initialize my understanding of and ability to set up an extensive amount of different fundamental optics/optomechanics that would eventually evolve into a well-developed, sophisticated set of skills in regards to being a very capable optical engineer. Whether concerning fundamental physics or direct experimental applications, he is a talented teacher. He also entrusted me to mentor over a half dozen undergraduate students in the lab, which helped to further develop my skills as a mentor and teacher. Most importantly, I'd like to thank Professor Flagg for trusting me to figure so much out on my own. When I switched to work in his group, he was a newly hired faculty member. He had just inherited a new empty lab. Nothing was set up: no stored lab equipment, no lasers, no cryostat, no spectrometer, no interferometers, no optomechanics of any kind... nothing besides an empty optical table and empty cabinets. Being heavily involved with setting up almost every component of his lab, from installation of fundamental equipment such as lasers, the cryostat, the spectrometer, etc, to construction and optimization of a multitude of different optical systems, including a custom Fabry-Perot interferometer, Mach Zehnder interferometer, and pulse-shaper, to writing code for instrument control, data acquisition, and data analysis, I was trusted to tinker, experiment, and use every involved aspect of his lab. Struggling through instances in which I was unsure how to get something to work, and being trusted to troubleshoot, has made me a very competent experimentalist. Due to having the privilege of being exposed to such a diverse set of experiences, I'm confident that I can be put into almost any experimental laboratory, and if there are any aspects of appropriate theory, engineering, or operation and optimization of lab equipment that I do not understand, I *will* figure them out.

I'd like to thank my parents, Gary and Judie, for always supporting me both emotionally, and when they could, financially. If it weren't for them convincing me to take loans out to go to college, I would have likely never journeyed down this road to a obtain a PhD in physics. I'd also like to thank my sister, Jehna, for always being very supportive of my endeavor to become a scientist. Additionally, all three of them have always been there for me when anything serious in life arose, of which I am incredibly grateful.

I'd like to thank my girlfriend, Catherine, for being exceedingly helpful during my time writing this dissertation. Through the entire process, I was working at least part-time as a postdoctoral optical materials research scientist for a national lab, and the final couple of months was working full-time. Without her help with so much, from helping me pack and move to a new apartment, to making us countless meals, to helping clean and organize, etc, I likely would not have been able to write a good dissertation.

I'd like to thank my good friends, Logan and Robbyn. Simultaneously finishing up data acquisition for a final experiment at WVU, writing my dissertation, and working at a national lab has been extremely exhausting at times. Logan was always there to help me keep my head straight when things felt overwhelming. Robbyn and I have had countless meaningful conversations regarding both physics and philosophy, which undoubtedly has shaped the way I approach problems as a scientist.

I'd like to thank my lab mates, Disheng and Raju. Disheng was an experienced experimentalist when we both started working in Professor Flagg's lab, and he contributed to fine-tuning every skill mentioned above, and especially helped with the development of my ability to write custom code. Mentoring Raju in the lab, from teaching construction of custom optical systems, to proper use of all of the different lab equipment, to understanding appropriate theory, has not only developed my understanding of each of those disciplines, but has made me a better teacher. He has also always been a good friend.

Last, but absolutely not least, I'd like to thank my high school teachers, the late Patricia Zober, who taught physics, and the late Edward Vercoe, who taught geometry and trigonometry. If it were not for them and their recognition of my potential to become a good scientist, I may have not chosen physics to be my major in the first place.

"Our passion for learning ... is our tool for survival."

Carl Sagan

For my parents, Gary and Judie, and high school teachers, Patricia and Edward.

Contents

List of Figures

List of Abbreviations

QD	**Q**uantum **D**ot
PL	**P**hoto-**L**uminescence
RF	**R**esonance **F**luorescence
TRRF	**T**ime-**R**esolved **R**esonance **F**luorescence
RPLE	**R**esonance **P**hoto-**L**uminescence **E**xcitation spectrum
MBE	**M**olecular **B**eam **E**pitaxy
DBR	**D**istributed **B**ragg **R**eflector
FPI	**F**abry-**P**erot **I**nterferometer
MZI	**M**ach **Z**ehnder **I**nterferometer
HBT	**H**anbury **B**rown-**T**wiss
HOM	**H**ong-**O**u-**M**andel
CTW	**C**oalescence **T**ime **W**indow
BS	**B**eam **S**plitter
QWP	**Q**uarter-**W**ave **P**late
HWP	**H**alf-**W**ave **P**late
AOM	**A**cousto-**O**ptic **M**odulator
APD	**A**valanche **P**hoto-**D**iode
LCVR	**L**iquid **C**rystal **V**ariable **R**etarder
TCSPCM	**T**ime-**C**orrelated **S**ingle **P**hoton **C**ounting **M**odule

Chapter 1

Sample Structure and Background Information

1.1 Introduction

For the past few decades semiconductor quantum dots (QDs) have been a topic of interest for not only the study of novel physics, but also have been implemented in technological advancements. Fundamental physics has been probed via experiments including their interaction with photonic cavities [1, 2], quantum coupling in a quantum dot molecule [3–5], and observations of the exchange interaction of the nuclear spin reservoir with the QD spin [6, 7]. Research regarding implementation of QDs into semiconductor heterostructures for illumination purposes [8], such as in quantum dot light-emitting diodes (QLEDs) in televisions [9], automobile lighting systems [10], and skin-mounted displays to be utilized in the engineering of wearable electronics [11], have been thoroughly investigated. These heterostructures have potential to produce tighter spectra for the core red, blue, and green primary combinations, resulting in crisper images, as well as increased electrical efficiency when compared to standard LED arrays. A leading area of research regards QDs' potential to be utilized as a source of single, indistinguishable photons to create quantum bits and be implemented into quantum information protocols. Significant progress has been achieved in the past several years within the aforementioned field, including the photonic quantum logic gate controlled via the coupling of a QD and a nanocavity [12], QD spin entanglement through a spin-photon interface [13], the coherent optical control of a single electron's spin [14], as well as ultra-fast single photon switching [15].

There exist many different types of quantum dots that are manufactured for different reasons. Colloidal QDs, which are synthesized from solutions, have been being synthesized the longest. Typically, colloidal quantum dots are composed of binary compounds such as cadmium selenide, cadmium sulfide, lead selenide, indium arsenide, and indium phosphide [16, 17]. Nonthermal plasma synthesis is one of the most popular gas-phase approaches for QD fabrication. The size, shape, and composition are readily controlled in nonthermal plasma [18]. Examples are germanium and silicon QDs [19]. Additionally, epitaxially grown self-assembled QDs, such as the InAs QDs discussed in this dissertation, are commonly synthesized. In regards to being a source for single, indistinguishable photons to be utilized in quantum information protocols, epitaxially grown self-assembled QDs lie at the forefront. Due to their tight 3-dimensional confinement, epitaxially grown self-assembled QDs allow for probing of specific exciton bound states which emit single photons with very narrow line widths. These kinds of quantum dots also are most easily incorporated into complex photonic crystal nanostructures, enhancing the Purcell effect[1] [21–25]. Such qualities are attractive to the industrial community and thus have led to the development of novel technologies, such as infrared single-photon detectors, and quantum dot lasers [26].

All work discussed in this dissertation regards optical characterization of self-assembled epitaxially grown InAs QDs. Due to the tight spatial confinement of bound charges, resonant excitation of bound electronic transitions is a prominent candidate to produce single, indistinguishable photons to be utilized for quantum information protocols. However, challenges remain that inhibit these QDs from being adequate photon sources for said protocols. Due to the nature of epitaxial self-assembly, the QDs' physical positioning, sizes, and inevitable alloying throughout the sample have a degree of randomness [27]. The size and alloying affects the precise resonant energy of the bound electronic transitions, and thus the wavelength of the emitted fluorescence. The resulting ensemble of QDs with different resonant energies allows addressing of specific QDs. However, dephasing of electron spin in the QD results in a relatively short spin coherence time, which restrains the time in which one may implement quantum operations involving the electronic spin state [28]. The atoms throughout the sample all have non-zero nuclear spin and those in the region around the QD

---

[1] The Purcell effect is enhancement of a quantum emitter's spontaneous emission rate via incorporation into a resonant cavity [20].

produce a net nuclear spin in that region, the nuclear spin reservoir. Interactions of the bound charges' spins in the QD with the nuclear spin reservoir, as well as charge fluctuations in the local environment cause the QD to emit photons of slightly different frequencies at different times.

The interactions of the spin of the bound charges in the QD with the nuclear spin reservoir is an ensemble effect described by a net magnetic field created by all the magnetic moments within the nuclear spin reservoir, the Overhauser field. The random fluctuations of the nuclear spins induce a time-dependency of the Overhauser field, resulting in a dephasing of the bound charges' spins. One solution to this problem involves application of a strong magnetic field that polarizes the nuclear spin reservoir, thus reducing the fluctuations of the Overhauser field in time. There are also optical techniques to implement that can extend the coherence time on the order of microseconds, such as with a dragging effect in which dynamical nuclear polarization aligns the nuclear spins [29, 30], and coherent population trapping which locks the nuclear spins [31].

The effect induced by the fluctuating local electric environment happens on a slower timescale, roughly on the order of kilohertz [32]. The bound state energies in the QD fluctuate as charges migrate through the local environment, resulting in a time-averaged broadening of the emission spectrum. This phenomenon is called spectral diffusion [33–35]. Spectral diffusion destroys the indistinguishability of subsequently emitted photons, which is crucial for the photons to be implemented as quantum bits in quantum information protocols [36–38]. Mechanisms that induce fluctuations of the local electrical environment are Auger processes [39] and phonon-assisted migration of charge through local defects states. Research has shown that these effects persist even under resonant excitation, which is the most promising method by which single, indistinguishable photons may be produced [35, 39, 40]. Additionally, resonant excitation often changes the charge state of the QD, resulting in a situation in which the excitation laser is no longer resonant with the available charge transition, and the QD fluorescence is quenched [41]. It has been known that application of a low-power above-band laser creates charges in the local electrical environment that can migrate to the QD, returning the initial charge state of which the resonant laser is exciting [42]. However, the exact charging pathways and mechanisms through which charge carriers migrate into and out of InAs QDs, including the roles played by the bulk GaAs continuum states and the InAs wetting layer, are not well understood. Understanding the charge dynamics in InAs quantum dots is crucial to help suppress these undesired effects. My more recent work discussed in this dissertation involves studying the charge dynamics of InAs QDs embedded in a planar micro-cavity under both resonant and above-band excitation.

1.2 Growth of InAs Quantum Dots

The samples studied in this dissertation are composed of InAs QDs embedded in a planar micro-cavity defined by two distributed Bragg reflectors (DBRs). The QDs are made via molecular beam epitaxy (MBE) and Stranski-Krastanov growth [43, 44] by Glenn Solomon of NIST, Gaithersburg. Molecular beam epitaxy is the physical vapor deposition technique that produces the highest purity thin film heterostructures. Stranski-Krastanov growth involves a two-step process. Initially, thin films of adsorbates, from one to several monolayers thick, are grown layer-by-layer on a crystal substrate. The adsorbate material has a slight lattice mismatch to that of the substrate, which induces locales of high and low strain. After a certain thickness that depends on the given strain and chemical potential of the deposited film[2], further vapor deposition of the adsorbate tends to nucleate above locales of minimum strain, because these locales correspond to the lowest energy states. As further deposition of the adsorbate ensues, pyramid-like islands of the adsorbate material tend to form. Figure 1.1 illustrates the growth process of InAs QDs, as well as images depicting Stranski-Krastanov island growth and a schematic of the ultimate sample heterostructure.

Figure 1.2 depicts an archetypal schematic regarding heterostructure growth via MBE. In order to allow for vapor deposition of high-purity InAs QDs, MBE is performed in an ultra-high vacuum chamber held at approximately 10^{-11} to 10^{-10} torr. Four coil-heated effusion cells contain each adsorbate used to grow the complete heterostructure. The effusion cells are heated such that the contained elements sublime and the gaseous atoms can be shot and deposited onto the sample wafer where they can interact, forming molecular bonds and crystalline structure. For instance, simultaneous deposition of gaseous Ga and As

---

[2] For InAs QDs, this thickness is approximately 1.6 monolayers of InAs deposited on top of a GaAs substrate.

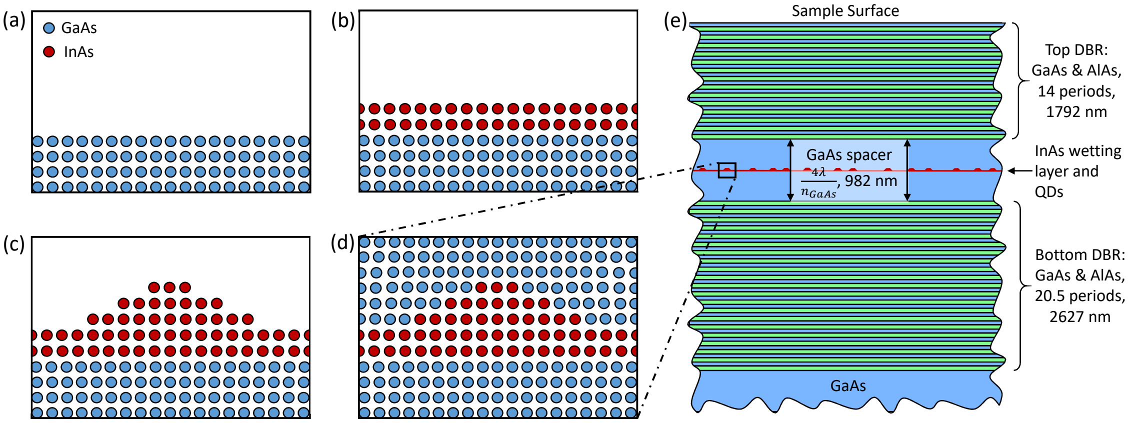

FIGURE 1.1: (a-d) Illustrations showing Stranski-Krastanov growth induced by the lattice mismatch between GaAs and InAs. (a) First, a GaAs substrate is deposited. (b) An InAs wetting layer is deposited on the GaAs substrate. InAs has a larger lattice constant than GaAs. (c) The lattice mismatch between InAs and GaAs induces locales of higher and lower strain. As InAs is further deposited, it tends to coalesce in locations above low strain between the GaAs substrate and InAs wetting layer, forming pyramid-like islands in those locations. (d) Finally, a GaAs capping layer is deposited, forming the QDs. (e) Depiction of the full sample heterostructure. The InAs wetting layer and QDs are embedded in the middle of a planar GaAs waveguide that is defined by two DBR superlattices. The thicknesses of all layers, besides the InAs wetting layer and QDs[3], are drawn to scale. λ_0 = 930 nm corresponds to the center wavelength of the fluorescence of the QD ensemble in the sample. $n_1 = n_{GaAs} = 3.45$ and $n_2 = n_{AlAs} = 2.98$ are the refractive indices of GaAs and AlAs at λ_0, respectively.

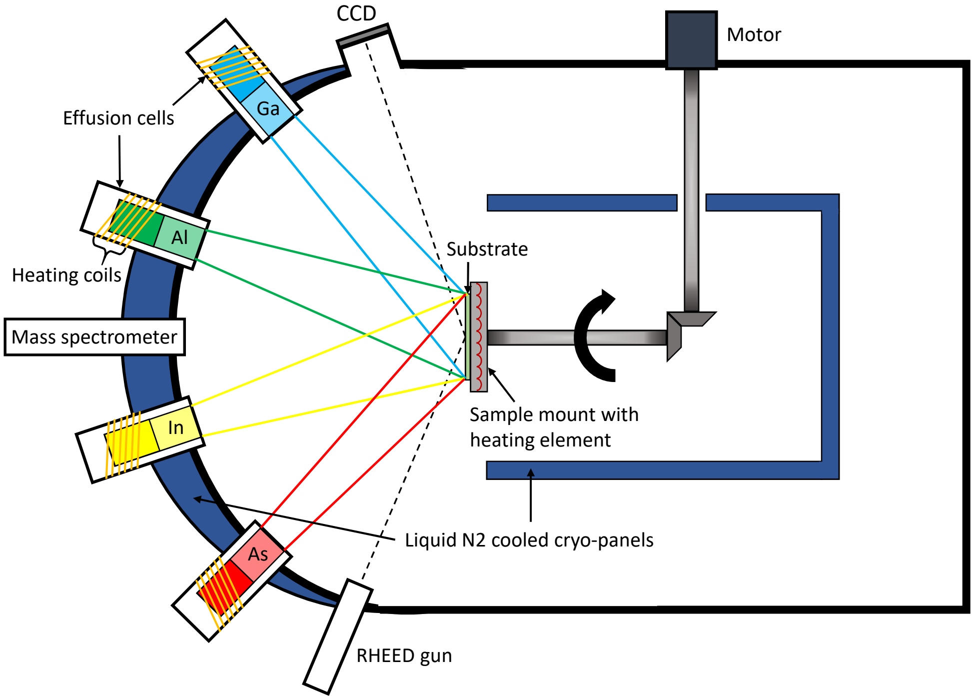

FIGURE 1.2: MBE chamber for growing InAs QDs. The high-purity group-III and group-V materials are contained and heated in the effusion cells (K-cell) which supply regulated atomic flows to allow epitaxial growth. The is rotated during growth to allow for even deposition across the sample. The liquid-nitrogen cooled shrouds condense the unwanted evaporants and improve the vacuum status around the sample. The sample is monitored by the mass spectrometer. RHEED provides real-time monitoring of the topography of the sample surface during the deposition process.

form crystalline GaAs, which has a zincblende crystal structure. The deposition rate can be controlled by the temperature of the effusion cells, as well as opening and closing of a shutter aperture at the effusion cells' outputs. The growth process is monitored via reflection high-energy electron diffraction (RHEED), where the sample surface topography is measured via diffraction of a beam of high-energy electrons reflected from the sample surface and detected by a CCD camera. A mass spectrometer is also mounted to conduct spectroscopic measurements of the sample as it's grown. Additionally, the sample is allowed to spin during vapor deposition to allow for more even distributions of the deposited adsorbates than if it wasn't spun, since the effusion cells are not mounted perpendicular to the sample surface. Lastly, the growth chamber is surrounded by a liquid-N_2-cooled shroud that acts as a sink in the vacuum for undesired impurities.

During the growth of our sample, a wafer is spun that initially has a 001-oriented GaAs substrate held at 550 K. Then, the first distributed Bragg reflector (DBR) that, in conjunction with the GaAs substrate, ultimately acts as a back-mirror is deposited. The DBR consists of a 20.5 layer superlattice composed of alternating layers of AlAs and GaAs, which have differing indices of refraction, and thus allow for reflections at the interfaces. Each layer of AlAs and GaAs is deposited to a thickness corresponding to an optical path length that is a quarter of the center Fabry-Perot mode[4] wavelength of the to-be-deposited planar microcavity. The alternating indices of refraction and correct thickness of each layer allow for reflections from different interfaces to interfere constructively, ultimately allowing for a high effective reflectivity from the DBR for a given wavelength range. The bottom DBR in our sample is engineered to have an effective reflectivity of 99.7%. After the first DBR is deposited, the first half of the GaAs spacer in which the QDs are embedded is deposited. Ultimately, the GaAs spacer's thickness is set to correspond to an optical path length in the growth direction that is four times the center wavelength of the microcavity's Fabry-Perot

---

[4] The Fabry-Perot interferometer is discussed in detail later in this chapter. Ultimately, the QDs are embedded in a planar microcavity that acts as a Fabry-Perot interferometer. This not only amplifies QD resonance fluorescence intensity due to coupling with the Fabry-Perot mode of the cavity, but is designed to preferentially emit the QD fluorescence perpendicular to the sample surface.

mode. The same wavelength is set to match the center of the resonant wavelengths of the QD ensemble to be grown in the GaAs spacer, which is approximately 930 nm. After the first half of the GaAs spacer is deposited, approximately 1.6 monolayers of InAs, called the wetting layer, is deposited. Further deposition of InAs induces Stranski-Krastanov growth, resulting in pyramid-like islands that become the QDs [27, 45]. After the growth of the InAs islands are complete, the second half of the GaAs spacer is deposited and the QDs are established. Finally, a 14 period DBR of alternating AlAs and GaAs is deposited, resulting in an effective reflectivity of 97.4%. The lower reflectivity of the top DBR encourages the fluorescence from the QDs to preferentially exit the sample from the sample surface on the side with the smaller DBR, parallel to the growth direction.

Transmission out of the Fabry-Perot cavity, through the top DBR, corresponds to the resonant Fabry-Perot modes of the planar microcavity. The thickness of the GaAs spacer d is grown to be $4\lambda_0/n_{GaAs}$, where n_{GaAs} is the refractive index of GaAs and λ_0 is the wavelength of the Fabry-Perot mode in the growth direction[5]. However, there is some finite bandwidth of wavelengths that are transmitted through the top DBR that is governed by the finesse of the Fabry-Perot cavity. Constructive interference in the planar microcavity corresponds to when the following condition is matched:

$$m\lambda = 2d\cos\theta, \tag{1.1}$$

where m is an integer, λ is the wavelength of the reflected light, d is the optical path length of the resonant cavity, and θ is the angle of the reflected light with respect to the normal of the reflective surface. Thus, different wavelengths within the transmission bandwidth of the Fabry-Perot cavity exit the sample in a conical shape, with the angle of the cone being dependent on the wavelength.

Ultimately, a piece of the sample wafer a few millimeters square is cleaved, exposing the wave-guide from the side, into which the resonant excitation laser is focused. Figure 1.3 depicts the resonant excitation and fluorescence collection scheme. Once focused into the planar waveguide, the resonant excitation light

---

[5] The Fabry-Perot mode corresponds to constructive interference of reflected light waves, resulting in a gain of the signal. Resonance of the Fabry-Perot mode is achieved when the optical path length of the cavity is an integer number of half wavelengths of the reflected light. The Fabry-Perot Interferometer is discussed in further detail later in this chapter.

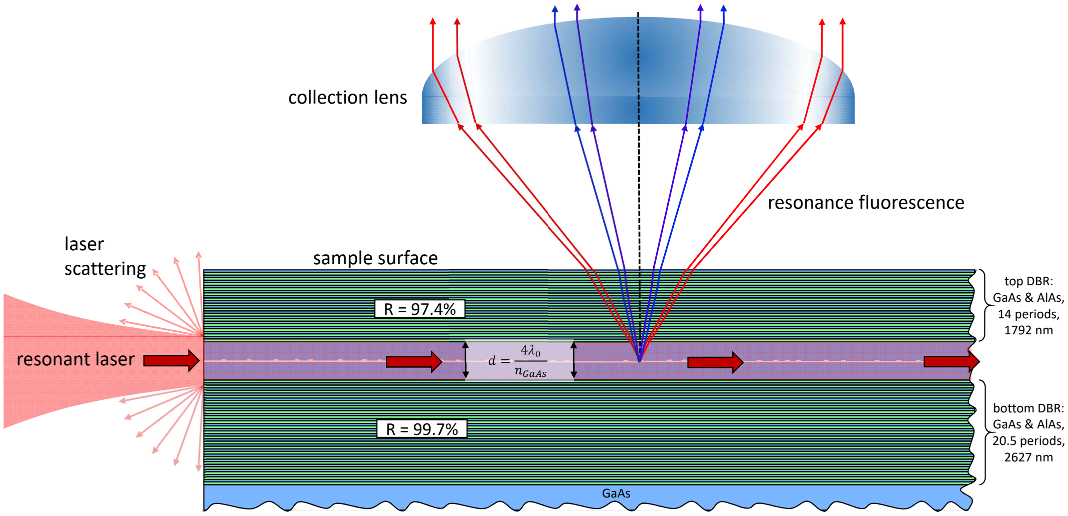

FIGURE 1.3: Diagram showing the resonant side-excitation and fluorescence collection geometry. The resonant laser is focused through the side of a cleaved edge of the sample, into the GaAs planar waveguide. The fluorescence exits the heterostructure from the sample surface parallel to the growth direction. The angular dependence of the resonant Fabry-Perot mode as a function of wavelength induces the fluorescence to exit the sample in a conical shape, which is collected by a large numerical aperture lens. Due to propagation of the resonant laser through the waveguide, and the collection of the QD fluorescence via a high numerical aperture lens, the FOV of the collected fluorescence can be isolated from the sample edge, minimizing collection of laser scattering from the sample edge.

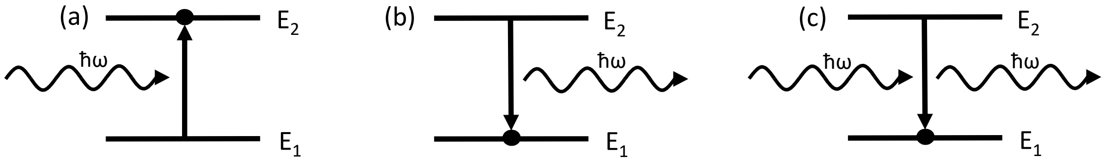

FIGURE 1.4: Optical transitions between two states in an atom: (a) absorption, (b) spontaneous emission, (c) and stimulated emission.

is contained in the growth direction by the DBRs, and thus propagates perpendicular to the growth direction. Any laser light that is not absorbed exits the waveguide on the other side of the sample. Due to the resonant laser propagating through the waveguide, and the use of a large numerical aperture lens to collect the QD fluorescence, the location on the sample that the QD fluorescence is collected and set incident onto the collection path can be almost entirely isolated from any resonant laser scattering from the cleaved sample's edge[6]. Thus, as long as one achieves good coupling of the resonant laser into the waveguide, and chooses a FOV relatively far from the sample edge, very little laser scattering falls onto the optical axis of the fluorescence collection path. This method, as opposed to a con-focal, cross-polarized configuration [46], helps maximize the collection efficiency of QD fluorescence, while minimizing collection of same-wavelength laser scattering from the edge of the sample.

1.3 Light-Matter Interactions

This sections follows the developments presented by Fox [47] and Foot [48]. The reader is referred to them for further details.

1.3.1 Einstein Coefficients

In the quantum theory of radiation, light is absorbed or emitted whenever an atom transitions between two quantum states. Figure 1.4 depicts such a two-level system and its interaction with a photon. Absorption occurs when the atom absorbs a photon and is excited to a higher-energy state, while emission occurs when an atom relaxes from a higher-energy state to a lower-energy state

---

[6] That is, the collection field of view (FOV) can be chosen to be significantly far away from the sample's edge where the resonant laser is focused into the waveguide.

via emission of a photon. Conservation of energy requires the photon involved with either absorption or emission to process to have an energy equal to the difference in energies of the two quantum states:

$$\hbar\omega = E_2 - E_1, \tag{1.2}$$

where E_1 and E_2 are the energies of the lower- and higher-energy states, respectively, ω is the angular frequency of the photon, and $\hbar$ is the Planck constant. We will later use quantum mechanics to calculate emission and absorption rates, but will start with a simple phenomenological analysis based on the Einstein coefficients for the transition.

Figure 1.4(a) depicts the process of absorption. The atom is excited from a lower energy state to a higher energy state via absorbing a photon that carries an energy equal to the difference in energy between the two atomic states. Following Einstein's formulation, we can write the time dependence of the excited state population as:

$$\frac{dN_1}{dt} = -B_{12}^{\omega} N_1 u(\omega). \tag{1.3}$$

where $N_1(t)$ is the time-dependent population of the lower-energy state, B_{12}^{ω} is the Einstein absorption coefficient, and $u(\omega)$ is the spectral energy density of the electromagnetic field at angular frequency ω. The subscript on B_{12}^{ω} signifies the transition is from the lower energy state (1) to the higher energy state (2), and the superscript signifies the absorption coefficient is for a particular angular frequency, i.e. energy. The factor $u(\omega)$ allows us to address that the excited state is only populated by absorption of the part of the incoming electromagnetic distribution with an angular frequency close to ω. Equation 1.3 may be considered as the definition of the Einstein B coefficient.

When an atom is in an excited state, it has a tendency to energetically relax into the ground state, losing its excess energy. During radiative relaxation, the energy of the system is conserved via emission of a photon that carries an energy equal to the energy difference of the excited and ground state, i.e. spontaneous emission (Depicted in Fig. 1.4(b)). The rate of spontaneous emission is defined by the lifetime of the excited state, which is related to the average time the atom stays in the excited state. The Einstein A coefficient is defined as the probability per unit time that the electron will drop from the excited state to the ground state via emission of a photon. The photon emission rate is thus proportional to the population of the excited state and to the A coefficient for the transition. For an ensemble of atoms, the time dependence for the number of atoms in the excited state, N_2, is:

$$\frac{dN_2}{dt} = -A_{21}N_2. \tag{1.4}$$

The subscript on the A coefficient signifies the system starts in the excited state (2) and ends in the ground state (1). The solution to the above differential equation is a simple exponential:

$$N_2(t) = -N_2(0)e^{-A_{21}t} \equiv N_2(0)e^{-t/\tau}, \tag{1.5}$$

where

$$\tau = \frac{1}{A_{21}}. \tag{1.6}$$

τ is the radiative lifetime of the excited state. Equation 1.5 states that the population of the excited state decreases with exponential time dependence with a time constant τ due to spontaneous emission.

Einstein realized there was a third process to complete the analysis of types of optical transitions of a two-level system. Stimulated emission happens when the incoming electromagnetic field induces an electronic transition from the higher energy state to the lower energy state, inducing emission of a photon that carries an energy equal to the difference in energies of the two states (Depicted in Fig. 1.4(c)). The rate of stimulated emission is characterized by a second Einstein B coefficient, B_{21}. We can then write the differential equation for the rate of change of the excited state due to stimulated emission as:

$$\frac{dN_2}{dt} = -B_{21}^{\omega}N_2u(\omega). \tag{1.7}$$

Stimulated emission is a coherent quantum-mechanical effect in which the photons that induce emission and the emitted photons are in phase with each other. Under continuous excitation, the total rate of change of population from the excited state to the ground state is the sum of spontaneous and stimulated emission rates.

The three Einstein coefficients relate to each other in a way such that if one knows the value of one coefficient, one can calculate the other two. We will follow Einstein's analysis to work out these relations. Consider a gas of N atoms in a closed volume with black-body radiation at temperature T. We assume the atoms interact with the black-body radiation, which induces both absorption and stimulated emission, and not with each other. We assume stimulated emission occurs at a rate governed by the Einstein A coefficient. When the atoms are in thermal equilibrium with the surrounding black-body radiation, the transition rate from the lower-energy state to the higher-energy state via absorption is equal to the transition rate from the higher-energy state to the lower-energy state via spontaneous and stimulated emission, i.e. $\frac{dN_1}{dt} = \frac{dN_2}{dt}$. This leads to the following relation:

$$B_{12}^{\omega} N_1 u(\omega) = A_{21} N_2 + B_{21}^{\omega} N_2 u(\omega). \tag{1.8}$$

Due to the laws of thermodynamics, since the atoms are in thermal equilibrium with the surrounding black-body radiation at temperature T, the ratio N_2 to N_1 is governed by Boltzmann's law:

$$\frac{N_2}{N_1} = \frac{g_2}{g_1} e^{-\frac{\hbar\omega}{k_B T}}, \tag{1.9}$$

where g_1 and g_2 are the degeneracies of the energy states 1 and 2, respectively, and k_B is the Boltzmann constant. The spectral energy density $u(\omega)$ of the black-body radiation is given by Planck's law:

$$u(\omega) = \frac{\hbar\omega^3}{\pi^2 c^3} \frac{1}{e^{\frac{\hbar\omega}{k_B T}} - 1}. \tag{1.10}$$

Dividing Eqn. 1.8 by N_2 and inserting Eqns. 1.9 and 1.10 gives the following relations for the Einstein coefficients:

$$A_{21} = \frac{\hbar\omega^3}{\pi^2 c^3} B_{21}^{\omega}, \tag{1.11}$$

and

$$g_1 B_{12}^{\omega} = g_2 B_{21}^{\omega}. \tag{1.12}$$

From these relations we see that the probabilities for absorption and stimulated emission are equal if the degeneracy of the two states are equal. If the degeneracy of the higher-energy state is larger than that of the lower-energy state, then absorption will be preferred over stimulated emission. While if the degeneracy of the lower-energy state is larger, stimulated emission will be preferred. Additionally, we see that as the spontaneous emission rate increases, so does the stimulated emission rate, and vice versa.

1.3.2 Radiative Transition Rates

Quantum dots are often referred to as 'artificial atoms'. Due to their confinement, only a small number of discrete energy states are available for bound electrons and holes. Consequently, relaxation of the bound electrons and holes, or excitons, results in photon emission that is similar to optical transitions observed in atoms. Due to this similarity, we will discuss how quantum mechanics can be used to model radiative transitions in atoms. Time-dependent perturbation theory is used to calculate radiative transition rates from a quantum mechanical approach. The rate of spontaneous emission is calculated using Fermi's golden rule, which describes state transition probabilities:

$$W_{1\rightarrow 2} = \frac{2\pi}{\hbar}|M_{12}|^2 g(\hbar\omega), \tag{1.13}$$

where M_{12} is the matrix element for the transition from state 1 to state 2, and $g(\hbar\omega) = g(E)$ is the density of states of the final state. The number of final states per unit volume that fall within an energy range of E and $E + dE$ is $g(E)dE$. In the case of transitions between discrete electron states within an atom, the density of states of the final state is the density of photon states.

Consider the incoming field induces a perturbation, H', to the Hamiltonian of the system, which causes an electronic transition from state 1 to state 2. The matrix element for this transition is given by:

$$M_{12} = \langle 2| H' |1\rangle = \int \psi_2^* H'(\vec{r})\psi_1 \, d^3\vec{r} \tag{1.14}$$

where H' is the perturbation to the Hamiltonian induced by the incident electromagnetic field, and $\psi_1(r)$ and $\psi_2(r)$ are the spatial wave functions of the initial and final states, respectively. Of course, it's more convenient to write this using standard Dirac notation with bras and kets.

We will use a semi-classical approach, where the light will be treated classically. The incident electromagnetic field interacts with multipoles of the atom, which corresponds to inducing different transitions in the atom. The Einstein

A coefficient is greatest for the transition corresponding to the electromagnetic field coupling with the electric dipole, and is orders of magnitude smaller for every increase in mulitpolarity. Additionally, the magnetic interactions are orders of magnitude weaker than their electric counterpart interactions[7]. Lastly, due to the electrons' small effective mass with respect to the protons', we assume only the electrons respond to the incoming electromagnetic field. Thus, we only consider the response of the electronic states to the perturbation caused by the interaction of the incoming light with the atom's electric dipole. The perturbation takes on the following form:

$$H'(\vec{r}) = -\vec{p} \cdot \vec{E}, \tag{1.15}$$

where $\vec{p}$ is the electric dipole of the atom, and $\vec{E}$ is the electric field of the incoming light. The electric dipole between an electron at position $\vec{r}$ and nucleus at the origin is:

$$\vec{p} = -e\vec{r}. \tag{1.16}$$

In Cartesian coordinates, the perturbation is then:

$$H' = e(xE_x + yE_y + zE_z). \tag{1.17}$$

The wavelength of the incoming light is much larger than the size of the atom, thus we can assume $\vec{E}$ is constant over the spatial span of the atom. Plugging Eqn. 1.17 into 1.14 we get:

$$M_{12} = e \int \psi_2^* (xE_x + yE_y + zE_z) \psi_1 \, d^3\vec{r}, \tag{1.18}$$

which can be written more compactly as:

$$M_{12} = -\vec{\mu}_{12} \cdot \vec{E}, \tag{1.19}$$

where

$$\vec{\mu}_{12} = -e \langle 2| \vec{r} |1\rangle \tag{1.20}$$

is the dipole moment of the atom associated with the transition. The dipole

---

[7] That is, the light field interacts much more strongly with the electric dipole than it does with the magnetic dipole of the atom.

moment is the key physical parameter that determines the transition rates associated with the electric dipole's interaction with the electromagnetic field.

If the initial and final wave functions are known, Eqn. 1.19 can be used to evaluate the matrix elements for particular transitions. The absorption transition rate per atom can be calculated with Fermi's golden rule and equated to the transition probability $B_{12}^{\omega}u(\omega)$ in Eqn. 1.3. The electric field amplitude can be eliminated from the transition rate since the energy density is proportional to $|E|^2$, and the Einstein spontaneous emission and absorption coefficients for unpolarized light of angular frequency ω can be written as:

$$B_{12}^{\omega} = \frac{\pi}{3\epsilon_0\hbar^2}|\vec{\mu}_{12}|^2, \tag{1.21}$$

and

$$A_{21} = \frac{\omega^3}{3\pi\epsilon_0\hbar c^3}|\vec{\mu}_{12}|^2. \tag{1.22}$$

1.3.3 Resonant Light-Atom Interactions

Preliminary Information

As in the previous section, we consider electronic transitions between a lower-energy state and a higher-energy state via emission and absorption of a photon with energy equal to the difference in energies between the two states[8]. We assume excitations induced by part of the light field with frequencies far from the natural frequency (off-resonance) to be negligible compared to the on-resonance coupling.

We must also introduce the concept of coherent superposition states, and how they differ from classical statistical mixtures, to understand the interaction of an incident light field and an atom. Consider a two-level quantum system, such as the two-level higher-energy state and lower-energy state we've discussed so far. In Dirac notation, we can write the wave function of the system as:

$$|\psi\rangle = c_1\,|1\rangle + c_2\,|2\rangle\,, \tag{1.23}$$

where $|1\rangle$ and $|2\rangle$ are the wave functions of state 1 and state 2, respectively. c_1 and c_2 are the wave function amplitude coefficients for states 1 and 2, where upon measurement of the quantum state, the probability to find the system in

---

[8] That is, on-resonance with a natural frequency of the atom.

state $|n\rangle$ is $|c_n|^2$. The wave function amplitudes of any coherent superposition state must be normalized:

$$\sum_n |c_n|^2 = 1. \tag{1.24}$$

Consider a statistical mixture of N identical gas particles with N_1 particles in the lower-energy state and N_2 particles in the higher-energy state. If we set $|c_1|^2 = N_1/N$ and $|c_2|^2 = N_2/N$, we would obtain the same results as if we performed many measurements on the coherent superposition state given by Eqn. 1.23. The main difference between the statistical mixture and the coherent superposition state is that each individual particle of the statistical mixture is thought to be in either state 1 or state 2 upon measurement of the system, while in the coherent superposition state, every particle is in some percentage of both state 1 and state 2 before measurement. It is upon measurement that the wave function collapses into one of the constituent wave functions of the superposition. Additionally, in the coherent superposition state, inference between wave functions somewhat analogous to interference between classical waves is possible, while it is not in the classical statistical mixture.

A convenient mathematical representation of an N-level system utilizes the density matrix, $\vec{\rho}$, of which the elements are defined by:

$$\rho_{ij} = \left\langle c_i c_j^* \right\rangle, \tag{1.25}$$

where c_i is the wave function amplitude for the ith quantum level of the N-level system. The bracket symbol $\langle\rangle$ indicates an average ensemble value for a system that contains many particles. The difference between a coherent superposition state and a classical statistical mixture is manifested in the existence of off-diagonal terms in the density matrix. In regards to a classical statistical mixture, each individual particle will be in a given energy state. This corresponds to each individual atom having the absolute value of one given amplitude coefficient equal to unity, and the rest equal to zero. Thus, the off-diagonal terms of the density matrix are all zero for a statistical mixture. However, in regards to a coherent superposition state, individual particles have wave functions in which all wave function amplitudes of the N-level system can be non-zero, resulting in non-zero off-diagonal elements of the density matrix. We mention the density matrix here for completeness, but will not expand upon it further due to it not being utilized in the investigations discussed in this dissertation.

Time-dependent Schrödinger Equation

We continue to consider a two-level system and its interaction with an incoming electromagnetic field. The time-dependent Schrodinger equation is as follows:

$$\hat{H}\Psi = i\hbar\frac{\partial\Psi}{\partial t}. \tag{1.26}$$

We assume the incoming light is close to resonance with the transition, such that:

$$\omega = \omega_0 + \Delta\omega, \tag{1.27}$$

where

$$\hbar\omega_0 = E_2 - E_1. \tag{1.28}$$

E_n is the energy of state n, and it is assumed $\Delta\omega$ is very small compared to ω_0 (near-resonance).

The Hamiltonian can be broken up into a time-independent term and a time-dependent term:

$$\hat{H} = \hat{H}_0(\vec{r}) + \hat{V}(t), \tag{1.29}$$

where $\hat{H}_0(\vec{r})$ is the unperturbed Hamiltonian and $\hat{V}(t)$ is the perturbation induced by the incoming light field. For a two-level system, the general solution to the Schrödinger equation is:

$$\Psi(\vec{r}, t) = c_1(t)\psi_1(\vec{r})e^{-E_1 t/\hbar} + c_2(t)\psi_2(\vec{r})e^{-E_2 t/\hbar} \tag{1.30}$$

where, as before, $c_n(t)$ is the amplitude coefficient of energy state n and $\psi_n(\vec{r})$ is the spatial wave function corresponding to state n. Upon substituting Eqn. 1.30 into 1.26, application of some steps of algebra that I will omit here, utilizing a trick by multiplying by ψ_1^*, integrating over space, and application of the orthonormality of the eigenfunctions, we obtain a differential equation describing the time-dependence of c_1:

$$\dot{c}_1(t) = -\frac{i}{\hbar}\left(c_1(t)V_{11} + c_2(t)V_{12}e^{-i\omega_0 t}\right), \tag{1.31}$$

where

$$V_{ij}(t) \equiv \langle i|\, \hat{V}(t)\, |j\rangle\,. \tag{1.32}$$

Using the same trick, but multiplying by ψ_2^* instead of ψ_1^*, we obtain the time-dependence of c_2:

$$\dot{c}_2(t) = -\frac{i}{\hbar}\big(c_1(t)V_{21}e^{i\omega_0 t} + c_2(t)V_{22}\big). \tag{1.33}$$

As previously stated, the perturbation is described by the interaction of the incoming electric field and the electric dipole of the atom:

$$\hat{V}(t) = e\vec{r}\cdot\vec{E}(t). \tag{1.34}$$

We can choose the polarization of the incoming light to be polarized along an arbitrary direction, say the x-direction:

$$\vec{E}(t) = E_0\cos(\omega t)\hat{x}. \tag{1.35}$$

The perturbation to the Hamiltonian then becomes:

$$\hat{V}(t) = exE_0\cos\omega t = \frac{exE_0}{2}(e^{i\omega t} + e^{-i\omega t}). \tag{1.36}$$

We now introduce the electric dipole matrix element μ_{ij}:

$$\mu_{ij} \equiv -e\left\langle i\right| x \left|j\right\rangle. \tag{1.37}$$

We can then write the perturbation matrix elements as:

$$V_{ij}(t) = -\frac{E_0}{2}(e^{i\omega t} + e^{-i\omega t})\mu_{ij}. \tag{1.38}$$

The diagonal elements of $\vec{\mu}$ are equal to zero since x is an odd parity operator and the atomic states have either even or odd parity. Additionally, since the matrix elements of the electric dipole represent measurable quantities, $\mu_{21} = \mu_{12}^*$ and consequently $\mu_{21} = \mu_{12}$. Finally, we introduce the Rabi frequency as:

$$\Omega_R = |\mu_{12}E_0/\hbar|. \tag{1.39}$$

In the end, we obtain a set of coupled differential equations describing the time dependence of the wave function amplitude coefficients:

$$\begin{aligned} \dot{c}_1(t) &= \frac{i\Omega_R}{2}(e^{i(\omega-\omega_0)t} + e^{-i(\omega+\omega_0)t})c_2(t), \\ \dot{c}_2(t) &= \frac{i\Omega_R}{2}(e^{-i(\omega-\omega_0)t} + e^{i(\omega+\omega_0)t})c_1(t). \end{aligned} \tag{1.40}$$

There are two regimes for which these differential equations can be solved: the weak-field limit and the strong-field limit.

The weak-field regime applies to low-intensity light sources such as a blackbody lamp. In this regime, we assume the lamp is turned on at time $t = 0$ and the system initially starts out with its entire population in the lower-energy state. The excited state is never significantly populated in the weak-field regime. The probability of finding the atom in the higher-energy state 2 as a function of times is[9]:

$$|c_2(t)|^2 = \frac{\pi}{\epsilon_0 \hbar^2}\mu_{12}^2 u(\omega_0)t. \tag{1.41}$$

Here ϵ_0 is the permittivity of free space and $u(\omega_0)$ is the value of the excitation spectral energy density at the resonant angular frequency. The transition probability rate $W_{1\to 2}$ in Eqn. 1.13 becomes:

$$B_{12}^{\omega} = \frac{\pi}{3\epsilon_0 \hbar^2}\mu_{12}^2. \tag{1.42}$$

In the strong-field regime the higher-energy state is significantly populated. This is the case under resonant excitation using laser light as the excitation source. To start, we make the rotating wave approximation in which we can neglect terms that oscillate at $\pm(\omega + \omega_0)$, since the oscillations are fast compared to those that oscillate at $\pm(\omega - \omega_0)$, and thus average out to zero for long times. If we consider the excitation source to be perfectly on-resonance, such that $\Delta\omega = 0$, Eqn. 1.40 becomes:

$$\begin{aligned} \dot{c}_1(t) &= \frac{i}{2}\Omega_R c_2(t), \\ \dot{c}_2(t) &= \frac{i}{2}\Omega_R c_1(t). \end{aligned}$$

---

[9] The following solution is reached by first considering that in the weak-field limit, $c_1(t) \gg c_2(t)$, such that $c_1(t) \approx 1$, setting $c_2(0) = 0$, solving for $c_2(t)$ in Eqn. 1.40, and implementing the rotating wave approximation.

If we assume the system starts out entirely in the lower-energy state, i.e. $c_1(0) = 1$ and $c_2(0) = 0$, the solutions become sinusoidal oscillations:

$$\begin{aligned} c_1(t) &= \cos(\Omega_R t/2), \\ c_2(t) &= i\sin(\Omega_R t/2). \end{aligned} \tag{1.43}$$

Upon measurement of the system, the time-dependence of the probabilities to find the election in either the lower-energy or higher-energy states become:

$$\begin{aligned} |c_1(t)|^2 &= \cos^2(\Omega_R t/2), \\ |c_2(t)|^2 &= \sin^2(\Omega_R t/2). \end{aligned}$$

One can see the electron oscillates between the lower-energy and higher-energy states with a frequency of $\Omega_R/2\pi$. This oscillatory behavior in response to application of a strong excitation field is called Rabi oscillations.

Under pulsed excitation, such as excitation using a pulsed Ti:Sapph laser source, the electric field amplitude E_0 varies with time, and consequently so does the Rabi frequency. It becomes useful to define a dimensionless parameter, the pulse area Θ:

$$\Theta = \left| \frac{\mu_{12}}{\hbar} \int_{-\infty}^{\infty} E_0(t)\, dt \right| . \tag{1.44}$$

The pulse area is determined by the energy of the full pulse, which is proportional to the integral of the the pulse intensity (or square of the electric field) as a function of frequency. When the pulse area is equal to π, it's called a π-pulse, and completely converts the system from one state to the other. In other words, if the system described is initially entirely in the lower-energy state, a π-pulse will leave the system entirely in the higher-energy state and vice versa.

Damping

At low excitation powers, the Rabi oscillations will have a long period relative the radiative lifetime of the excited state. There are two classifications of damping mechanisms for Rabi oscillations. First, spontaneous emission events destroy the coherence of the electronic wave function, consequently causing a damping of Rabi oscillations. These damping processes are called longitudinal relaxation, and are quantified by the time constant, T_1. The value of T_1 is governed by the lifetime of the excited state, which is dictated by both radiative and non-radiate decay rates that bring the system out of the excited state to lower energy state. If non-radiative processes are insignificant, the ultimate value of T_1 is dictated by radiative transitions to all possible lower-energy states.

There are other types of mechanisms related to dephasing processes. These are called transverse relaxation and are quantified by the time constant, T_2. There exist possible events in which the electron in the excited state will undergo elastic collisions which induce phase changes to the excited-state wave function, but do not change the population of the excited state. These can include collisions with other atoms or the walls of the container for gases, or interactions with impurities/defects or phonons that induce electronic transitions. Inducing a random phase to the wave function destroys effects which rely on phase coherence, such as Rabi oscillations.

1.4 The Bloch Sphere

Although not used directly in my research, and thus not expanded upon in rich detail in this dissertation, I would like to mention the convenience of using the concept of the Bloch sphere to describe a two-level quantum state. The Bloch sphere is depicted in Fig. 1.5. A pure state is represented by a vector starting at the origin with a radius of unity. A Bloch vector pointing towards the south pole of the Bloch sphere represents the system being entirely in the ground state $|\Psi\rangle = |0\rangle$, such as an InAs QD held at 4K before arrival of any excitation light. A vector pointing straight to the north pole signifies the system is entirely in the excited state $|\Psi\rangle = |1\rangle$[10]. Quantum superpositions of the two states $|\Psi\rangle = c_1 |0\rangle + c_2 |1\rangle$ are represented by a vector with a latitude θ between 0 and π, where a vector pointing along the equator ($\theta = \pi/2$) implies $c_1 = c_2 = 1/\sqrt{2}$. Of course, the coefficients c_1 and c_2 are complex numbers, where $c_1^2 + c_2^2 = 1$. We can define c_1 to be a real, positive number and the imaginary components of the coefficients be incorporated into a phase ϕ between the two real parts of the coefficients. The phase angle ϕ is represented by the longitudinal angle on the Bloch sphere, and can have a value between 0 and 2π. Any pure state of the

---

[10] It's arbitrary which pole is defined as $|0\rangle$ and which as $|1\rangle$. I think it more intuitive to define the south pole as the system being entirely in the ground state.

two-level quantum system can be written as[11]:

$$|\Psi\rangle = \cos(\theta/2)\,|0\rangle + e^{i\phi}\sin(\theta/2)\,|1\rangle\,. \tag{1.45}$$

A π-pulse mentioned in the previous section rotates θ by π, hence the name. For any polarization state, the oscillatory term $e^{i\phi}$ will cause the Block vector to precess about the z-axis as a function of time. Lastly, a mixed state is represented by a Bloch vector with length less than unity, and a Bloch vector with length greater than unity has no physical meaning. It is worth noting the potentially useful generalized n-level Bloch vector [49]. Although a geometrical representation cannot be drawn for n-level systems with $n > 2$, the mathematics can still be useful[12]. Often in an n-level system, certain optical transitions between given states aren't allowed. Prohibited transitions are represented mathematically by rotations of the Bloch vector associated with those transitions being prohibited.

1.5 Spectral Line Characteristics

This section follows the development presented by Fox [47]. The spectrum of radiation emitted during electronic transitions from a higher energy state to a lower energy state in a two-level system are not delta functions in frequency/wavelength, due to the finite lifetimes of any given transitions. There are different mechanisms that can contribute to the exact width and shape of the emission spectrum. The spectral lineshape $g_\omega(\omega)$ describes the emission spectrum's shape. The center peak of the spectral lineshape ω_0 is the optical frequency associated with the on-resonance value of the excitation energy, i.e, the energy difference between the higher and lower energy states of the transition:

$$\omega_0 = \frac{(E_2 - E_1)}{\hbar}. \tag{1.46}$$

The spectral lineshape is normalized as such:

$$\int_0^\infty g_\omega(\omega)\,d\omega \;= 1. \tag{1.47}$$

---

[11] Note, the polar angle θ is conventionally measured with respect to the north pole of the Bloch sphere, which is conventionally defined to represent $|0\rangle$. I define the south pole of the Bloch sphere as $|0\rangle$, and θ is measured with respect to the south pole.

[12] For instance, an $n = 3$ system is represented by an 8-dimensional Bloch sphere.

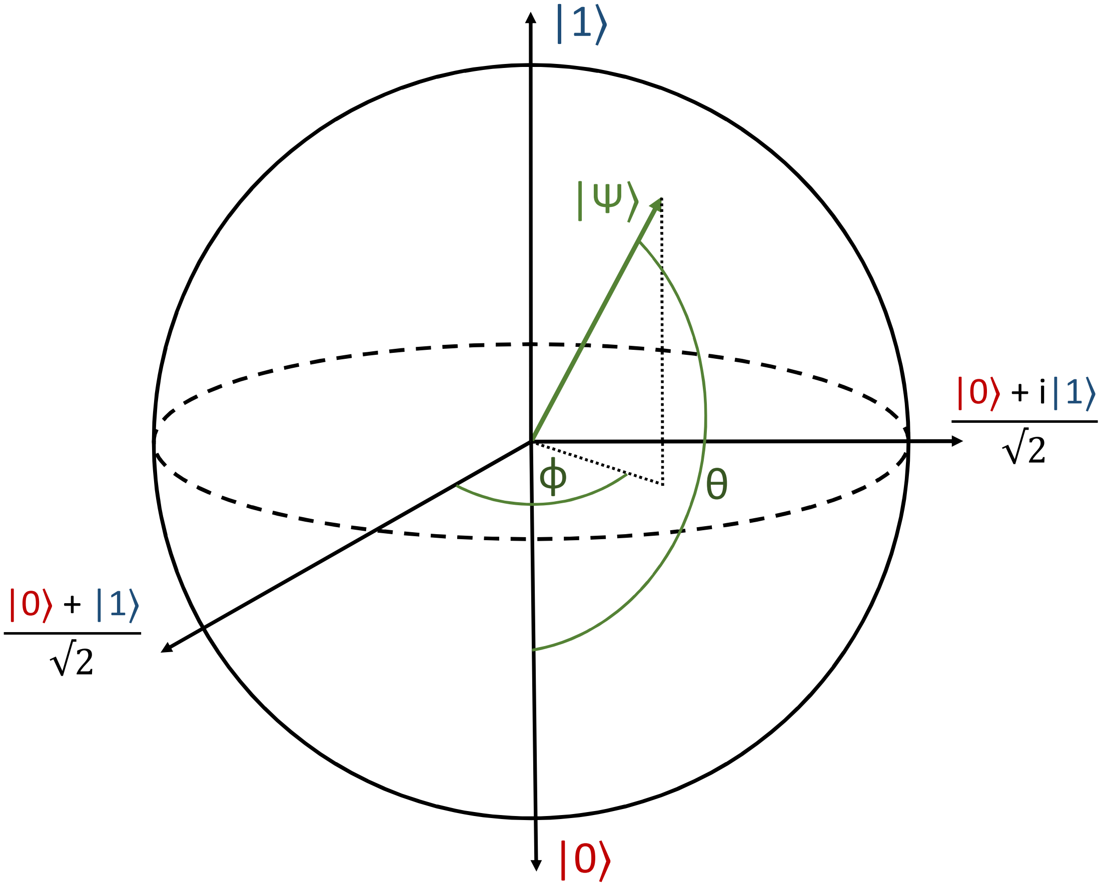

FIGURE 1.5: The Bloch sphere. The two-level quantum system is represented by a vector $|\Psi\rangle$ on a unit sphere. The system being entirely in the ground state $|0\rangle$ is represented by a Bloch vector pointing towards the south pole, while the system being entirely in the excited state $|1\rangle$ is represented by a Bloch vector pointing towards the north pole. Any pure state that is a linear superposition of the ground state and excite state has a length of unity. θ defines the relative magnitudes of the real part of the amplitude coefficients of the linear superposition. ϕ defines the complex phase angle between the coefficients. Due to the two-level atom having an intrinsic angular frequency, and in making the transformation to the Block sphere representation, a Bloch vector will precess about the vertical axis as a function of time. Mixed states are represented by vectors with length less than unity.

An important feature used to describe the lineshape is the full width at half maximum (FWHM) $\Delta\omega$.

The two general classifications of types of spectral broadening are homogeneous and inhomogeneous broadening. Homogeneous broadening is sometimes referred to as 'natural broadening'. Homogeneous broadening affects each emitting species in an environment equally, while inhomogeneous broadening affects each one differently and is usually caused by inhomogeneities in the local environment of the emitter(s), hence the name. A classic example of homogeneous broadening is caused by the finite lifetime of an electronic transition (lifetime broadening), which will be shown below to give the emission spectrum a Lorentzian lineshape. On the other hand, the random fluctuations of the electrical environment, such as the influence of nearby charge traps discussed in Chapter 3, results in small fluctuations of the bound-state energies of the electrons and holes in the QD, and hence fluctuations in center wavelength of the emitted fluorescence. The charge traps are oriented stochastically about the sample and their charge occupancy is time-dependent, resulting in a random jittering of the color of the emitted fluorescence about some center value. This effect is called spectral diffusion. In itself, the random jittering of the center wavelength of the fluorescence about some mean value can in itself induce a Gaussian, Voigt[13], or broadened Lorentzian lineshape. Most homogeneous broadening mechanisms result in Lorentzian lineshapes, whereas inhomogeneous broadening often leads to Gaussian lineshapes. In the real world, often both types of broadening exist. In the InAs QDs studied in this dissertation, a Lorentzian lineshape is induced by the finite lifetime of the electronic transition, while the lineshape induced solely by spectral diffusion is not well known, but often takes on a Voigt profile.

Lifetime (natural) broadening resulting in a Lorentzian lineshape is rather simple to explain. The finite lifetime in a two-level quantum system leads to a broadening of the emission spectrum in accordance with the energy-time uncertainty principle:

$$\Delta E \Delta t \geq \hbar. \tag{1.48}$$

Setting Δt equal to the radiative lifetime τ, the resulting spectral width must then satisfy:

$$\Delta\omega = \frac{\Delta E}{\hbar} \geq \frac{1}{\tau.} \tag{1.49}$$

---

[13] A Voigt profile is given by the convolution of a Lorentzian and a Gaussian profile.

Equation 1.5 shows how the radiative lifetime τ induced by spontaneous emission takes on a decaying exponential form. The spontaneous emission can be considered as a burst of light that decays exponentially with a time constant τ, with maximum intensity at $t = 0$. The intensity as a function of time is simply $I(t) = I(0)e^{-t/\tau}$. The frequency profile of the intensity is naturally equal to the Fourier transform of the temporal profile, which results in the spectral lineshape:

$$g(\omega) = \frac{\Delta\omega}{2\pi}\frac{1}{\left(\omega - \omega_0\right)^2 + \left(\Delta\omega/2\right)^2}, \tag{1.50}$$

where the FWHM is:

$$\Delta\omega = \frac{1}{\tau}. \tag{1.51}$$

Equation 1.50 is called a Lorentzian lineshape. Compared to a Gaussian, it is tighter around the center peak, but its tails extend farther. The Lorentzian lineshape is shown in Fig. 1.6.

We have shown that lifetime/natural broadening caused by spontaneous emission results in a spectral lineshape that takes on a Lorentzian form. This shape can be interpreted as being proportional to the probability distribution in frequency space of measurable fluorescence frequencies for a given electronic transition. In turn, this can be attributed to the energies of any given transition not being completely discrete, but having some finite band of possible frequencies centered about a mean frequency, dictated by the energy-time uncertainty principle. It is then a logical progression that the probability of the excitation laser populating the excited state as a function of excitation frequency takes on the same Lorentzian shape, with a center at the resonant frequency and a FWHM equal to the inverse of the radiative lifetime. Indeed, the excitation spectra of near-resonant excitation of InAs QDs takes on a Lorentzian form. Acquisition of excitation spectra in our lab is expanded on in Chapter 2.

1.6 Planar Fabry-Perot Interferometer

This section mostly follows the development presented by Fox [47]. The Fabry-Perot interferometer (FPI) is important to our research for two major reasons. The two DBRs of our sample discussed previously create an effective Fabry-Perot cavity, promoting transmission of a particular window in frequency that is engineered to be centered around the peak of emission wavelengths of the

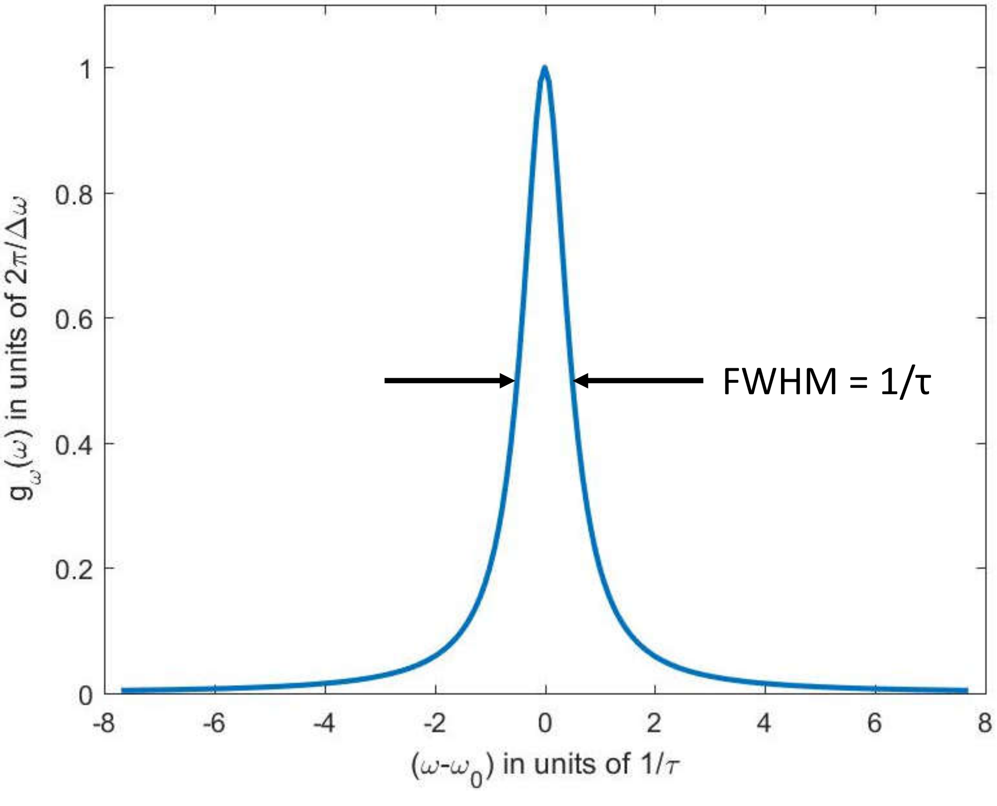

FIGURE 1.6: The Lorentzian lineshape. The function has a center peak at $\omega = \omega_0$ and a FWHM of $1/\tau$. The function is normalized such that the integral over all values of ω is unity.

InAs QD ensemble. Additionally, our lab is working on constructing a fine-tunable FPI that will be used to measure the fine structure of the QDs' emission spectra, making it possible to resolve phenomenon such as the emergence of the Mollow triplet at high excitation powers [50]. Indeed, I constructed a custom built FPI, in which the cavity's optical path length was tuned via stepping the pressure of nitrogen in a chamber in which the FPI was enclosed[14], and hence stepping the index of refraction of the medium inside the cavity, and ultimately the optical path length. The device worked, but the pressure regulator used was not sufficient to step the nitrogen pressure in small enough increments to give a good enough resolution to adequately measure the fine-structure of the emission spectra of our QDs. A new method using an optical cavity attached to a piezo-electric and a shearing interferometer, which provides feedback regarding the precise cavity length, is currently under development by Raju KC. The mirrors used in our FPI to measure QD emission spectra are curved to help prevent loss out of the sides of the cavity. The cavity described below is the simple planar FPI, but the theory discussed still applies.

Consider a planar cavity defined by two mirrors with reflection coefficients R_1 and R_2, and a cavity length L, that is filled with an optical medium with index of refraction n. The mirrors are parallel to each other to allow for many reflections within the cavity. Light of wavelength λ is sent into the cavity from one side and is allowed to reflect back and forth between the mirrors. The finesse of the cavity is defined as:

$$\mathcal{F} = \frac{\pi (R_1 R_2)^{1/4}}{1 - \sqrt{R_1 R_2}}. \tag{1.52}$$

Additionally, the phase shift of the light after one round trip is:

$$\phi = \frac{4\pi n L}{\lambda}. \tag{1.53}$$

The transmission through the cavity in terms of $\mathcal{F}$ and ϕ is:

$$\mathcal{T} = \frac{1}{1 + (4\mathcal{F}^2/\pi^2)\sin^2(\phi/2)}. \tag{1.54}$$

The transmission is equal to 1 (full transmission) whenever $\phi = 2\pi\ell$, where ℓ can take on any integer value. Under these circumstances, the optical path

---

[14] This is further expanded upon in Chapter 8.

length of the cavity is equal to an integer number of half wavelengths of the light reflected within. That is, when:

$$nL = \ell \frac{\lambda}{2}. \tag{1.55}$$

In this situation the cavity is said to be on resonance.

The Fabry-Perot cavity will thus allow maximum transmission when the light is on resonance with the cavity mode, and minimum transmission directly in between resonances. The bandwidth of a transmission peak is dictated by the finesse of the cavity, and characterized by the full width at half maximum (FWHM) of the Fabry-Perot mode. To find the relation of the FWHM to the finesse, we solve Eqn. 1.54 for $\mathcal{T} = 0.5$. In the limit of large $\mathcal{F}$, and referring to Eqn. 1.54, we find that:

$$\phi = 2\pi m \pm \pi/\mathcal{F}. \tag{1.56}$$

The FWHM is thus equal to

$$FWHM = \frac{2\pi}{\mathcal{F}}. \tag{1.57}$$

The higher the finesse, the higher the resolution of the FPI when used for spectroscopic measurements, such as measurement of the fine details of the excitation spectra of InAs QDs.

The resonant modes' angular frequencies can be calculated from Eqn. 1.55:

$$\omega_\ell = \frac{\pi c \ell}{nL}. \tag{1.58}$$

We can use Eqn. 1.57 to calculate the spectral width $\Delta\omega$ of the resonant modes:

$$\frac{\Delta\omega}{\omega_\ell - \omega_{\ell-1}} = \frac{FWHM}{2\pi} = \frac{1}{\mathcal{F}}, \tag{1.59}$$

resulting in:

$$\Delta\omega = \frac{\pi c}{n\mathcal{F}L}. \tag{1.60}$$

We additionally consider the photon lifetime inside the cavity. Consider a symmetric, high-finesse cavity where $R_1 = R_2 = R \approx 1$. Suppose when the light is first introduced into the cavity we start with N photons. After a time equal to the optical path length divided by the speed of light, $\Delta t = nL/c$, the photons reach the far mirror and commence their first reflection. After every reflection, there exist RN photons (Recall, R is the reflection coefficient) in the cavity. On average, in the time it takes the photons to travel from one side of the cavity to the other we lose $\Delta N = (1 - R)N$ photons from the cavity. Thus, the time rate of change of the number of photons can be written as:

$$\frac{dN}{dt} = -\frac{\Delta N}{\Delta t} = -\frac{c(1-R)}{nL}N. \tag{1.61}$$

The solution to this differential equation is a simple decreasing exponential with a characteristic decay time (lifetime) given by:

$$\tau_{cav} = \frac{nL}{c(1-R)}. \tag{1.62}$$

If $R \approx 1$, then the spectral line-width can be approximately written as:

$$\Delta\omega = \frac{1}{\tau_{cav}} \equiv \kappa, \tag{1.63}$$

where κ is defined as the photon decay rate. This shows that the width of the spectral line is directly proportional to the photon decay rate, analogously to how the width of an atomic emission line is proportional to the rate of spontaneous emission.

Lastly, for any type of cavity it is useful to define the cavity's quality factor, Q:

$$Q = \frac{\omega}{\Delta\omega}, \tag{1.64}$$

which is the ratio between the frequency of a resonant mode and its linewidth.

From an experimentalist's standpoint, it is convenient to define the finesse as the ratio of the free spectral range (FSR) to the FWHM, or bandwidth of a transmission peak. The FSR is defined as the distance between transmission peaks in frequency space. The FSR is dictated by the optical path length of the cavity by $FSR = c/(2nL)$, which is the inverse of the average time it takes a photon in the cavity to go through one round-trip[15]. For the two custom FPIs I built and discuss in Chapter 8, this definition of the finesse was utilized during characterization of the FPI cavities.

---

[15] Or the average round-trip rate.

1.7 Optical Transitions in InAs Quantum Dots

1.7.1 Charge Carrier Bound States

InAs QDs are dubbed "artificial atoms" because their quantum confinement of charges leads to discrete optical transition frequencies in the emitted fluorescence, as is observed in atoms. The size of individual QDs varies, leading to varying emission center frequencies. In general, as with the simple particle in a box problem found in any introductory quantum mechanics textbook, the tighter the quantum confinement, the higher the optical frequencies of the emitted fluorescence for a given transition. The smaller band-gap InAs embedded in the larger band-gap GaAs enables three-dimensional confinement of charge carriers in a small volume. The de Broglie wavelength of a free charge carrier in a bulk semiconductor is on the order of $\lambda = 2\pi\hbar/\sqrt{2m^{*}E}$, where the kinetic energy of the particle E is approximated by the thermodynamic relation $E = \frac{3}{2}k_{B}T$ and m^{*} is the effective mass of the charge carrier. For the cryogenic temperatures our samples are held at, the de Broglie wavelength of an electron in the conduction band of GaAs and InAs has a wavelength of approximately 340 nm and 200 nm, respectively. Whereas, for heavy holes the de Broglie wavelength is 80 and 70 nm in GaAs and InAs, respectively. The physical size of InAs QDs, and hence the extent of the confinement potential, is on the order of 20 nm perpendicular to the growth direction (base length) and 5 nm parallel to the growth direction. Thus, both electrons and holes experience strong confinement, resulting in the creation of bound excitons, and the discrete 'atom-like' energy structure emerges.

The depth of the potential well that the QD provides, or in other words the strength of the electric potential, is mostly dictated by the difference in band-gap energies of the embedded QD material and surrounding bulk semiconductor. However, the physical size of the QD dictates the number of possible bound states. As previously mentioned, as the physical size of the QD is reduced, the energies of the bound states are increased. In order for, say, an electron to be bound in the potential well, the energy of the associated bound state must be less than the energy of the bottom of the conduction band of the surrounding bulk material. Thus, as the physical size of the QD is reduced, the bound state energies increase and the energies of the higher-energy bound states become greater than the energy of the bottom of the bulk semiconductor's conduction

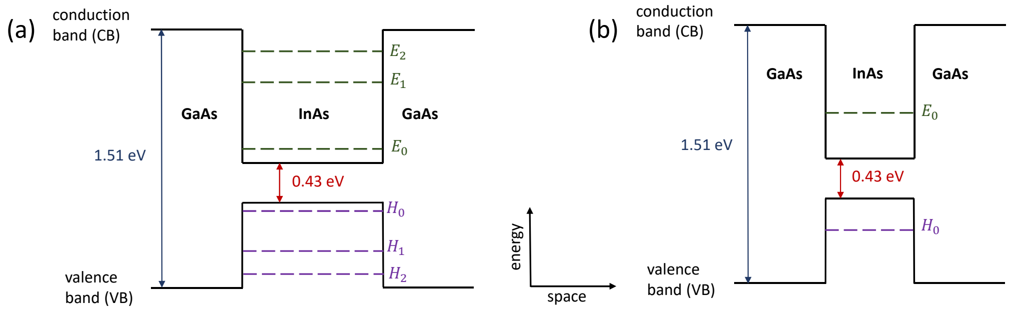

FIGURE 1.7: Representation of energy levels of excited bound states for electrons and holes in InAs QDs. The vertical direction is energy and the horizontal is space. (a) An InAs QD showing three possible excited bound state energies for the charge carriers. E_n represents the energy of the n^{th} excited state for an electron, where the subscript 0 represents the first excited bound state. The hole energies are depicted by H_n. (b) As the size of the QD is decreased, the bound state energies increase until higher energy states have associated energies greater than the bottom of the conduction band of the bulk GaAs host, and thus represent free carrier states, leaving only one possible bound state for electrons and holes.

band, resulting in those bound states no longer being possible (free carriers). Theoretically, if the QD is made small enough, only one bound state is possible. The same dynamics apply to the holes but in the opposite direction in energy space. A bound hole in the QD has an energy greater than the energy of the top of the valence band of the surrounding bulk material, which intuitively makes sense since a hole is a lack of an electron in the valence band of the material in which it resides. Figure 1.7 shows a qualitative depiction of bound state energies in two differently sized QDs.

Additionally, the crystal symmetry is reduced by the strain induced by the lattice mismatch between InAs wetting layer and GaAs substrate, which is utilized to grow the QDs that provide the confinement potential for charge carriers [51, 52]. The valence band states are p-states with angular momentum $\ell = 1$ and spin $s = 1/2$, resulting in a total angular momentum quantum number j that can take on a value of $1/2$ or $3/2$. Spin-orbit coupling lowers the energy of the electron $j = 1/2$ states and raises the energy of the hole $j = 1/2$ states, forming the 'split-off' band. The $j = 3/2$ states can have z-projections $m = -3/2, -1/2, 1/2, 3/2$, which have different effective masses. Light holes (LH) have $|m| = 1/2$ and heavy holes (HH) have $|m| = 3/2$. Their energies are the same in bulk GaAs at the Gamma point (the center of the Brillouin zone of reciprocal space). However, when carriers are confined, the different effective masses change the resulting discrete energy levels. The splitting is a minimum of tens of meV, and can be as large as 0.5 eV [53]. At the cryogenic temperature of 4K, the energy difference is too large to allow thermal excitation, and consequently the possible admixture of HH and LH states is significantly reduced. Thus, the significantly high-energy LH states can be neglected due to little mixing with HH states.

Ultimately, excitons are created by the significant overlap of wave functions of bound electrons and HHs caused by the tight confining potential of the band structure. Just as with atoms, the coupling of the electric dipole of the exciton[16] with the electric field of the excitation light induces electronic transitions to excited states, creating bound excitons. Also as with atoms, the exciton state decays back to the ground state via spontaneous emission. The electron in the conduction band (CB) of the QD falls back into the empty valence band (VB) state, i.e. the electron and hole recombine, and a photon carries an energy equal to the difference in energy of the bound electron and hole. This process of radiative recombination via resonance fluorescence is depicted in Fig. 1.8.

1.7.2 Optical Properties

The optical properties of QDs are almost exclusively dictated by the radiative recombination induced by decay of the electron from the lowest-energy excited bound state. Higher-energy states do not decay efficiently via emission of photons because decay from such states via emission of phonons happens on a much faster time scale. For instance relaxation of higher energy states via phonon emission happens on the order of 1-10 ps [54], as opposed to radiative recombination lifetimes on the order of 1 ns. Thus, almost any charges promoted to the higher-energy bound states quickly decay to the lowest-energy bound state via phonon emission where the exciton can then recombine via radiative recombination.

---

[16] Recall, the electric dipole in an atom exists due to the Coulomb field between the spatially separated excited electron and atomic nucleus.

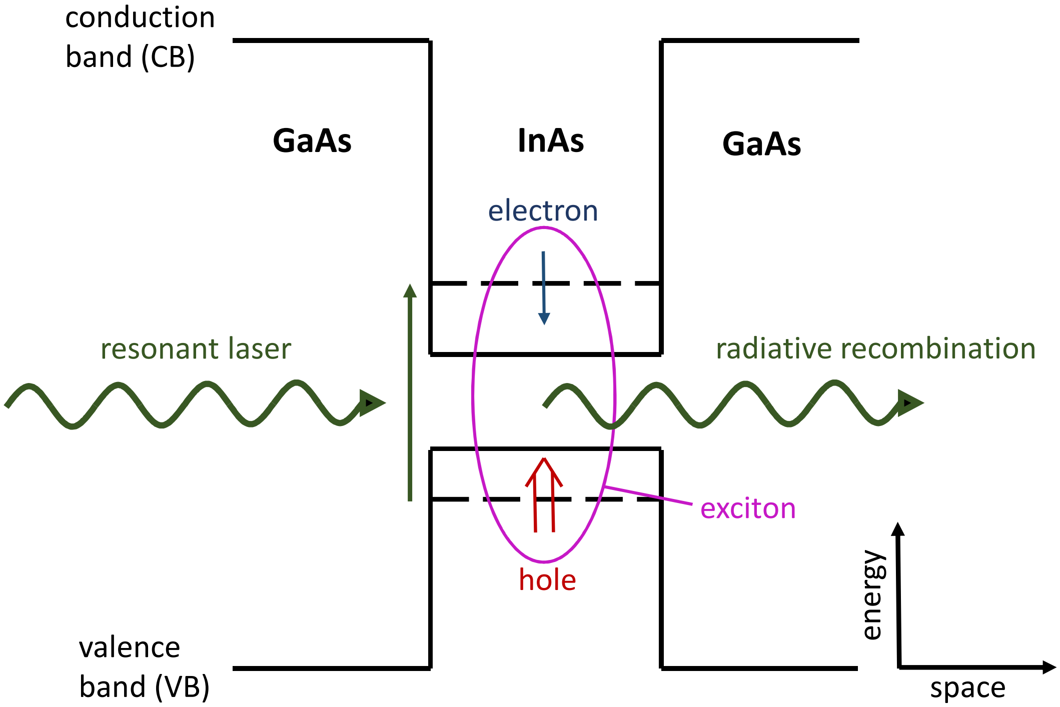

FIGURE 1.8: Diagram showing resonant excitation and radiative recombination in an InAs QD. Shown here is an electronic transition of a neutral exciton, as opposed to that of a charged QD (trion). The resonant laser excites an electron in the InAs from the VB to the CB, leaving behind a hole in the VB. Resonant excitation refers to the photon energy of the laser being equal to the transition energy. Due to quantum confinement of the charge carriers, bound excitons are formed when an electron is excited to the CB of InAs. The electron eventually decays from the excited state via spontaneous emission and falls back to the VB, recombining with the hole. A photon carriers an energy equal to the energy lost by the electron during energetic decay, hence the term radiative recombination.

There are a few major interactions between the electron and hole that contribute to the optical properties of the emitted fluorescence. The center wavelength of the emitted fluorescence is defined by the difference in energy between the lowest-energy bound electron state and highest-energy bound hole state. The physical size of the QD plays the largest role in the energy of the bound exciton. A physically smaller QD induces higher-energy bound states. As previously mentioned, the spectral lineshape of the emitted fluorescence (emission spectrum) often takes on a Voigt lineshape, which is the convolution of a Lorentzian and Gaussian. The Lorentzian component emerges from the finite lifetime of spontaneous emission, the shorter the lifetime the broader the FWHM of the associated Lorentzian. The Gaussian component emerges from spectral diffusion. The larger the fluctuations to the local electric environment, the larger the FWHM of the associated Gaussian. Lastly, spin interactions of the possibly optically active transitions dictate the polarization of the emitted fluorescence.

In Dirac notation, we signify a spin-up electron as $|\uparrow\rangle$ and a spin-up hole as $|\Uparrow\rangle$. For a given bound-state energy in the QD, there are two possible quantum states for both electrons and holes. Due to the Pauli exclusion principle, two particles cannot occupy the same quantum state, which results in like-charge carriers with the same bound-state spatial wave function taking on opposite spins. That is, the z-projection of the spin of a bound electron can take on the value $\pm\hbar/2$ and the hole's spin projection can take on a value of $\pm 3\hbar/2$. Angular momentum of the entire system must be conserved, and photons carry an angular momentum of $\pm\hbar$. For a neutral QD, and without considering the exchange interaction, both the electron and HH are doubly degenerate, resulting in the confined exciton state being 4-fold degenerate. The excitonic states $|\uparrow\Uparrow\rangle$ and $|\downarrow\Downarrow\rangle$ are not optically active, because when the electron recombines with the hole, there will be a total change in angular momentum of $\pm 2\hbar$. Theoretically, the momentum of the system could be conserved via simultaneous emission of two photons, but this happens with a very small probability, and is thus negligible. Hence, these excitons are dubbed dark excitons. The states with the electron and hole having oppositely signed spins $|\uparrow\Downarrow\rangle$ and $|\downarrow\Uparrow\rangle$, however are optically active because when the electron falls into the hole, a change of $\pm\hbar$ in angular momentum is carried by an emitted photon, and the angular momentum of the entire system is conserved. These excitons are hence dubbed bright excitons.

The exchange interaction between the HH spin $J_{h,i}$ and electron spin $S_{e,i}$ lifts the degeneracy between the dark and bright exciton manifolds. The part of the Hamiltonian describing the exchange interaction takes on the form [55–57]:

$$H_{exchange} = -\sum_{i=x,y,z} \left(a_i J_{h,i} S_{e,i} + b_i J_{j,i}^3 S_{e,i} \right) \tag{1.65}$$

where a and b are spin-spin coupling constants, $J_{h,i}$ is the hole's total angular momentum along the Cartesian direction i, and $S_{e,i}$ is the electron's spin along the Cartesian direction i. The exchange interaction induces an energy splitting, without mixing of the two manifolds, equal to $\delta_0 = \frac{3}{2}(a_z + 2.25 b_z)$ [58]. The splitting of the doubly degenerate exciton states is $\delta_1 = \frac{3}{4}(b_x + b_y)$ for the dark excitons and $\delta_2 = \frac{3}{4}(b_x - b_y)$ for the bright excitons. The splittings are accompanied by mixing of the states within each manifold.

For a neutral QD with in-plane[17] rotational symmetry $b_x = b_y$, the splitting is zero, and the eigenstates of Eqn. 1.65 are $|\uparrow\Downarrow\rangle_z$ and $|\downarrow\Uparrow\rangle_z$. These two transitions couple to circularly polarized light, represented by σ^+ and σ^-. Most real QDs are not perfectly circularly symmetric in the x-y plane; asymmetric strain often induces a uniaxial deformation. In this case $b_x \neq b_y$ and even mixing of $|\uparrow\Downarrow\rangle_z$ and $|\downarrow\Uparrow\rangle_z$ ensues, resulting in the new eigenstates $|\downarrow\Uparrow\rangle_x$ and $|\uparrow\Downarrow\rangle_y$[18]. The optical emission from neutral transitions in most real-life QDs thus is linearly polarized in the x-y plane.

For a charged QD, we will consider the negative trion[19]. The expectation value of $H_{exchange}$ is zero for a state with two electrons and one hole[20]. Consequently, a charged QD shows no exchange splitting in the trion transitions. Similar to the neutral transition in a circularly symmetric QD, we find the eigenstates to be $|\uparrow\downarrow\Uparrow\rangle_z$ and $|\downarrow\uparrow\Downarrow\rangle_z$, and the optical transitions to be circularly polarized (σ^+ and σ^-) [58]. The optical transitions for a symmetric neutral QD, an asymmetric neutral QD, and a negative trion are depicted in Fig. 1.9.

There are interesting interactions of InAs QDs with an applied external magnetic field. For instance, the interaction between an external magnetic field and

---

[17] z is in the growth direction. Here, in-plane refers to the perpendicular direction, or the x-y plane.

[18] Note, here the subscripts x and y refer to the polarization of the emitted photons, not the direction that spins point. However, for the kets with the subscript z, the subscript does indicate the direction of the spin.

[19] The same argument applies to the positive trion.

[20] Or for two holes and one electron, i.e. the positive trion.

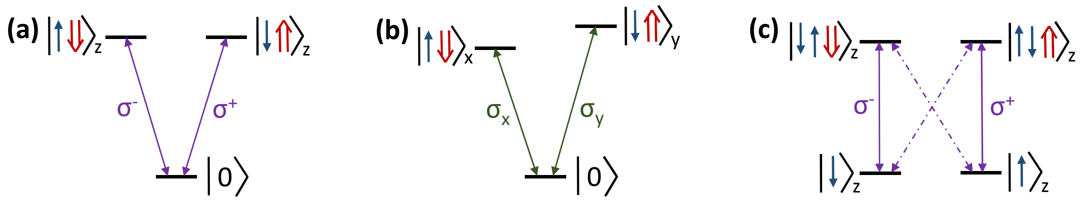

FIGURE 1.9: Depiction of optical transitions for (a) a symmetric neutral QD, (b) an asymmetric neutral QD, and (c) a negative trion. Single blue arrows represent electrons, double red arrows represent holes, and the arrow directions represent spin projections. Optical transitions depicted by purple double-sided arrows represent circularly polarized light, while green double-sided arrows depict linearly polarized light. The dotted double-sided arrows in (c) depict transitions that are prohibited due to conservation of angular momentum of the system, since photons carry angular momentum equal to $\pm\hbar$.

charge carriers that have different spin z-projections lifts degeneracies of the possible excitonic states. As an example, a neutral QD that is circularly symmetric in the direction perpendicular to the growth direction has two possible lowest-energy bound states that are degenerate in energy. However, application of an external magnetic field lifts this degeneracy. Another example involves the interaction of a trion (excited charged state) with an external magnetic field. Without an applied external magnetic field, there are two possible circularly polarized optical transitions. There exist two transitions that are not optically active due to conservation of angular momentum of the system and the fact that a photon carriers an angular momentum of $\pm\hbar$. However, application of a Voigt magnetic field, in which the magnetic field is perpendicular to the growth direction, mixes the ground states and excitonic states, leading to four new linearly polarized optical transitions. However, I did not investigate any charge dynamics nor optical properties of InAs QDs in an external magnetic field, so only some effects are briefly mentioned here. If the reader would like detailed information regarding the interactions of charge carrier spin with an external field, and the induced effects on the optical transitions, they are encouraged to refer to Ref. [58].

One of the optical properties of InAs QDs most relevant to my research involves the difference in resonant energies of neutral and charged transitions.

The excited state of a charged QD is dubbed a trion. A negative trion is composed of two bound electrons and one bound hole, while a positive trion is composed of one bound electron and two bound holes. The lowest energy trion state involves all three charge carriers being in the lowest energy excited bound states, with bound energies E_0 and H_0 depicted in Fig. 1.7. Due to Pauli's Exclusion Principle, the two carriers of the same charge must have opposite spin, while the other carrier can take on either spin projection. The negative trion has a smaller optical transition energy than the neutral exciton (red-shifted), while the positive trion has a larger (blue-shifted) [59]. The difference ultimately boils down to the difference in effective masses for electrons and holes. The negative trion can be visualized as an additional electron added to the neutral exciton. Compared to the neutral exciton, there are two additional Coulomb interactions: attraction felt between the additional electron and hole, and repulsion felt between the two electrons. The same idea describes the positive trion but with an additional electron-hole attraction and additional hole-hole repulsion. Due to the quantum confinement and the larger effective mass of the hole, the wave function of holes are more localized than that of electrons [60]. This leads to a tighter net charge distribution for the positive trion compared to the neutral exciton and a broader charge distribution for the negative trion. The tighter charge distribution is associated with a larger potential energy. Thus, relative to the neutral exciton the positive trion has a negative binding energy and the negative trion a positive binding energy. Figure 1.10 qualitatively depicts resonance fluorescence for different charge states of a given InAs QD.

The fact that a charged QD's electronic/optical transitions have a different energy than a neutral QD's is an important characteristic that is relevant to the investigations discussed in this dissertation. The resonant laser can, with a high probability, change the charge state of the QD, causing a neutral state to become charged and vice versa[21]. If the charge state is changed, the resonance fluorescence intensity is significantly or entirely diminished, since the resonant laser is no longer resonant with the available transition. This is the case because the difference in energies of the trion transitions and neutral transition is much greater

---

[21] When I refer to charge state, I am referring to both the ground state and excited state of that transition. That is, the negative charge state has an electron in the CB of InAs when there is no incident excitation light, and has two electrons in the CB (with opposite spin) and one hole in the VB when the resonant laser induces excitation.

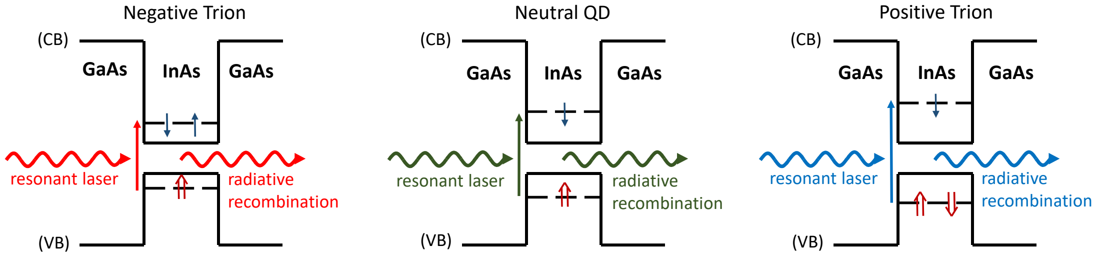

FIGURE 1.10: Depiction of resonance fluorescence for different charge states of a given InAs QD. (a) Depicts the negative trion, (b) the neutral exciton, and (c) the positive trion. Single blue arrows represent electrons, while double red arrows represent holes. For a given QD, the resonant energy of the negative trion is red-shifted with respect to the neutral exciton, while that of the positive trion is blue-shifted.

than the bandwidth of the laser. It has been known for quite some time that application of a low-power above-band laser returns the QD to the initial charge state, allowing the resonant laser to again populate the observed transition, and ultimate reemergence of the fluorescence intensity ensues [42]. However, the exact pathways through which the charge carriers migrate through the sample to return the QD to its initial charge state are not well understood. The pathways/mechanisms by which they do so are investigated in Chapters 4 and 5.

1.8 Photon Statistics

This sections follows the developments presented by Fox [47] and Loudon [61]. The reader is referred to them for further details.

1.8.1 Introduction

In this section we consider the statistics affiliated with the particle nature of light, i.e. that light is composed of individual, discrete quanta, or photons. Let us consider a photon counting experiment in which we use a detector that is capable of detecting single photons. An example is a single-photon avalanche photo-diode, such as the ones we use in our lab, which outputs a measurable voltage pulse upon detection of a photon. We consider a perfectly coherent monochromatic beam of constant intensity that is incident on the detector. The photon flux is the number of photons passing through a given cross-section per unit time. The flux incident on the detector is equal to the power of the beam divided by the energy of an individual photon in the beam:

$$\Phi \equiv \frac{P}{\hbar\omega}. \tag{1.66}$$

No single photon detector is perfect, and even the most efficient ones, such as superconductor based detectors [62], will only detect a certain percentage of incident photons. This effect is characterized by the quantum efficiency (QE) of the detectors, which is defined as the percentage of photon arrival events that generate a voltage output from the detector. Then, the count rate measured is:

$$R = \frac{(QE)P}{\hbar\omega}. \tag{1.67}$$

Although a light beam may have a well-defined flux, an observer (detector) witnesses fluctuations in the photon number, especially at short time scales. For instance, if the window of time is shorter than the average time between adjacent photons, the fluctuations in the photon number are high, since one will often not detect a photon within the sampled time. These fluctuations are described by the photon statistics of light. There are three main categories of light regarding photon statistics: Poissonian, super-Poissonian, and sub-Poissonian.

1.8.2 Poissonian, Super-Poissonian, and Sub-Poissonian Light

Consider of beam of perfectly coherent light with a single angular frequency ω, and a constant intensity along the entire beam. Although the photon flux is constant in time, we would expect to see statistical fluctuations caused by the discrete particle nature of the light. This light is described by Poissonian statistics. The average number of photons $\bar{n}$ within a length segment L of the beam is given by:

$$\bar{n} = \frac{\Phi L}{c}. \tag{1.68}$$

Consider we chop this beam into N small subsegments, such that the probability of finding a photon within a subsegment is small enough that there is a high probability of finding either one or zero photons within a given subsegment. The probability of finding a photon within a given subsegment is simply

$p = \bar{n}/N$. Ultimately, the statistics are characterized by defining the probability of finding n photons within the full length L containing N subsegments. The probability is equivalent to the probability of finding n subsegments containing one photon and $N - n$ containing no photons. We use the binomial distribution to give the probability:

$$\mathcal{P}(n) = \frac{N!}{n!(N-n)!} p^n (1-p)^{N-n}. \tag{1.69}$$

Insertion of $p = \bar{n}/N$ into 1.69 gives:

$$\mathcal{P}(n) = \frac{1}{n!} \left(\frac{N!}{(N-n)! N^n} \right) \bar{n}^n \left(1 - \frac{\bar{n}}{N} \right)^{N-n}. \tag{1.70}$$

Sterling's formula tells us:

$$\lim_{N \to \infty} \ln N! = N \ln N - N. \tag{1.71}$$

Application of Stirling's formula to the first large-parenthesis term in 1.70, and raising e to the resulting equation shows that:

$$\lim_{N \to \infty} \left(\frac{N!}{(N-n)! N^n} \right) = 1. \tag{1.72}$$

Additionally, one can show that the binomial expansion of the second large-parenthesis term in 1.70 in the limit $N \to \infty$ is equal to the series expansion of $\exp(-\bar{n})$:

$$\lim_{N \to \infty} \left(1 - \frac{\bar{n}}{N} \right)^{N-n} = e^{-\bar{n}}. \tag{1.73}$$

Application of these two results to 1.70 gives the Poisson distribution:

$$\mathcal{P}(n) = \frac{\bar{n}^n}{n!} e^{-\bar{n}}, \quad n = 0, 1, 2, \ldots\,. \tag{1.74}$$

Generally, random processes that involve counting integer numbers of particles or events will exhibit Poissonian statistics. The Poissonian distribution tell us the probability of measuring n counts within a given time window. The average value $\bar{n}$ dictates the width of $\mathcal{P}(n)$. The Poissonian distribution peaks at $n = \bar{n}$ and increases in width as $\bar{n}$ increases. The variance of n is equal to the average value $\bar{n}$, and thus the standard deviation of the photon number is given by:

$$\Delta n = \sqrt{\bar{n}}. \tag{1.75}$$

Ultimately, we see that the relative size of the fluctuations, $\Delta n/\bar{n}$ decreases as $\bar{n}^{-1/2}$.

The three types of photon statistics can be classified by their relation of the standard deviation Δn to the average photon number $\bar{n}$ in the distribution as follows:

- sub-Poissonian statistics: $\Delta n < \sqrt{\bar{n}}$,
- Poissonian statistics: $\Delta n = \sqrt{\bar{n}}$,
- super-Poissonian statistics: $\Delta n > \sqrt{\bar{n}}$.

Recall, a perfectly coherent beam with a constant intensity throughout (such as light from a cw laser) is described by Poissonian statistics. Since a perfectly stable intensity is described by Poissonian statistics, any classical light beam that has a time-variant intensity will exhibit super-Poissonian statistics. Two of the quintessential examples are thermal light from a black-body source and chaotic light. In comparison to perfectly coherent light with a constant average intensity, super-Poissonian light has larger fluctuations in the photon number, and hence in the intensity. On the other hand, sub-Poissonian light has smaller fluctuations in the photon number when compared to Poissonian light. We will see in a later section how super-Poissonian light leads to the phenomenon of photon bunching, while sub-Poissonian light leads to anti-bunching.

Super-Poissonian light does not pertain to the work described in this dissertation, but for completeness we will give the results for a given mode of black-body radiation. Consider an enclosed cavity at constant temperature T. Using Planck's Law and Boltzmann's Law, one can work out that the probability that there will be n photons in the mode is given by the Bose-Einstein distribution [47]:

$$\mathcal{P}_\omega(n) = \frac{1}{\bar{n}+1}\left(\frac{\bar{n}}{\bar{n}+1}\right)^n. \tag{1.76}$$

We also find that the standard deviation of the number of photons for the Bose-Einstein distribution is:

$$\Delta n = \sqrt{\bar{n}+\bar{n}^2}. \tag{1.77}$$

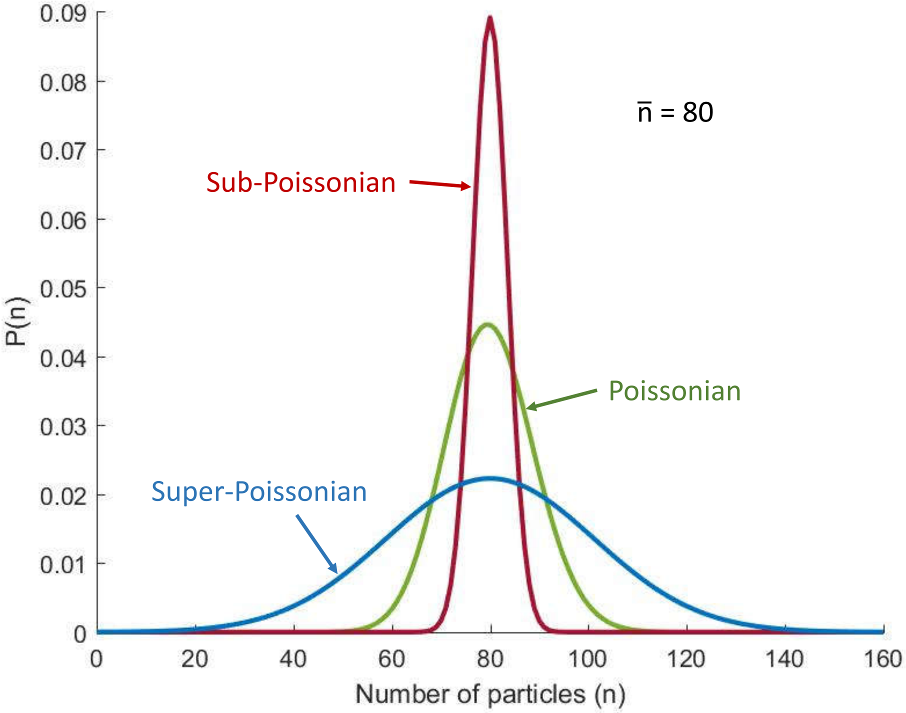

FIGURE 1.11: Comparison of sub-Poissonian, Poissonian, and super-Poissonian photon number distributions for an average photon number $\bar{n} = 80$. Compared to the Poissonian distribution, the sub-Poissonian distribution is narrower in n, while the super-Poissonian is broader.

This shows that the standard deviation is always greater than that of a Poissonian distribution, i.e, exhibits super-Poissonian statistics. If we consider the variance of the number of photons, which is the square of the standard deviation, we can consider the first term to originate from the particle nature of light, and the second to originate from thermal fluctuations of the electromagnetic radiation's energy.

Recall, light is described by sub-Poissonian statistics when:

$$\Delta n < \sqrt{\bar{n}}. \tag{1.78}$$

Since the standard deviation of the number of photons is smaller for sub-Poissonian light as compared to Poissonian light, it is considered more stable than Poissonian light. However, from a classical perspective a perfectly coherent beam of constant intensity is the most stable possibility. Light characterized by sub-Poissonian statistics has no classical counterpart, and is a signature of the quantum nature of light.

The most extreme theoretical case we can conceived of is a stream of single photons all separated by the same distance/time, with no fluctuations in the distance/time between adjacent photons. In this case, the probability of measuring n photons is simply a delta function centered on the average number of photon $\bar{n}$. Photon streams of this type are called photon number states. These are the purest form of sub-Poissonian light. However, one can conceive of a situation in which we have a beam of single photons with spacing that is less regular than described above, but more regular than the random time intervals associated with a beam described by Poissonian statistics. For instance, collected resonance fluorescence of InAs QDs is composed of a stream of single photons separated by distances dictated by the lifetime of the excited state in the QD. However, since the lifetime is an average value, there exists small fluctuations and ultimately small fluctuations in the time distance/time between adjacent photons in the stream.

It is worth mentioning that the detector being used will affect the necessary integration time needed to adequately observe the photon statistics. Recall, previously we mentioned the quantum efficiency of a photo-detector. A detector with a low quantum efficiency will detect a small percentage of photon arrival events. Thus, to study sources that are highly sub-Poissonian, such as resonance fluorescence of InAs QDs, it's advantageous to use detectors with both a short response time and high quantum efficiency, so we miss as little photon arrival events as possible, and can implement reasonable integration times.

1.8.3 Hanbury Brown-Twiss

In the mid-1950s astronomers Hanbury Brown and Twiss (HBT) developed an intensity interferometer to measure the diameters of distant stars. Since the 1920s, the Michelson stellar interferometer had previously been implemented for this purpose. The Michelson stellar interferometer involved sending incoming starlight to two mirrors separated in space and recombined at a telescope objective. The spacing of the interference fringes gave information about the solid angle of the incoming starlight. Although the distance between the initial collection mirrors could be larger than the diameter of the telescope's objective lens, thus improving the angular resolution, efficiency was lost due to the relatively small size of the initial collection mirrors. It thus could only be used for observing bright stars.

The larger the distance d between the mirrors, the better the possible resolution. However, as d is increased the stability of the Michelson interferometer is compromised, and eventually the observation of interference fringes becomes impossible. Hanbury Brown's and Twiss' interferometer involved two focusing mirrors that each focused incoming starlight onto their own separate detectors. Their interferometer did not produce any interference fringes; instead they were able to simply measure the intensity correlations between the two detectors to calculate the solid angle of incoming starlight. This allowed them to effectively increase d greatly, providing an enormous improvement to the resolution of the measured solid angle.

Hanbury Brown and Twiss decided to test the principles of their experiment with a simple laboratory arrangement. They filtered light from a mercury lamp such that only the 435.8 nm emission line was incident on a 50:50 beam-splitter (BS). Two different photomultipliers then detected the reflected and transmitted intensities $I_1(t)$ and $I_2(t)$. One detector was set on a translation stage, such that the two detectors could register light separated by a distance d. The generated photocurrents were sent through AC-coupled amplifiers, which generated signals proportional to the fluctuations in the photocurrents, Δi_1 and Δi_2. One signal was then electronically delayed by a time τ. Lastly, the two signals were connected to a multiplier-integrator unit which calculated the time average of the product of the two signals, $\langle \Delta i_1(t) \Delta i_2(t+\tau) \rangle$, where $\langle \rangle$ signifies a time average. Since the photocurrents generated by the photomultipliers were proportional to the incident intensities, the output was proportional to $\langle \Delta I_1(t) \Delta I_2(t+\tau) \rangle$. This experiment is similar to HBT experiments one would conduct in a quantum optics laboratory setting.

The principle behind the HBT experiments was that a light beam's coherence is related to the intensity fluctuations. If the light incident on the detectors is coherent, then the intensity fluctuations measured by the detectors will be correlated with each other. Using such a setup to measure the correlations of the intensity fluctuations turned out much easier than setting up a classic Michelson interferometry experiment.

Consider the case in which $d = 0$ and the beam splitter (BS) is a perfect 50:50 BS. The intensities measured by either detector are:

$$I_1(t) = I_2(t) \equiv I(t) = \langle I \rangle + \Delta I(t), \tag{1.79}$$

where $\Delta I(t)$ is the fluctuation from the mean intensity $\langle I \rangle$. If we then set the temporal delay between the two optical paths equal to zero ($\tau = 0$), the output of the HBT experiment is proportional to:

$$\langle \Delta I(t) \Delta I(t+\tau) \rangle_{\tau=0} = \left\langle \Delta I(t)^2 \right\rangle. \tag{1.80}$$

Due to the intensity fluctuations in the chaotic light from the mercury lamp (as was used by Hanbury Brown and Twiss), $\langle \Delta I(t)^2 \rangle$ will be non-zero, and hence a non-zero output for a zero time delay. However, if τ is much greater than the correlation time of the light τ_c, the intensity fluctuations will be completely uncorrelated, and consequently $\Delta I(t) \Delta I(t+\tau)$ randomly changes sign in time and averages to zero:

$$\langle \Delta I(t) \Delta I(t+\tau) \rangle_{\tau >> \tau_c} = 0. \tag{1.81}$$

Since the output decreases to zero at times much larger than the coherence time of the light, this regime can be used to calculate the coherence time τ_c.

1.8.4 The Second-Order Correlation Function

In order to quantify the results of the HBT experiment and ultimately quantify the single photon nature of our InAs QDs' fluorescence, we use the second order correlation function. The second order correlation function is defined as:

$$g^{(2)}(\tau) = \frac{\langle \mathcal{E}^*(t)\mathcal{E}^*(t+\tau)\mathcal{E}(t+\tau)\mathcal{E}(t)\rangle}{\langle \mathcal{E}^*(t)\mathcal{E}(t)\rangle \langle \mathcal{E}^*(t+\tau)\mathcal{E}(t+\tau)\rangle} = \frac{\langle I(t)I(t+\tau)\rangle}{\langle I(t)\rangle \langle I(t+\tau)\rangle}, \tag{1.82}$$

where $\mathcal{E}(t)$ and $I(t)$ are the electric field amplitude and intensity of the light beam as a function of time, respectively, and as usual * represents the complex conjugate.

We will first consider the measurement of $g^{(2)}(\tau)$ using a coherent light source with constant average intensity, such that $\langle I(t)\rangle = \langle I(t+\tau)\rangle$. If $\tau \gg \tau_c$, the intensity fluctuations at time t and $t+\tau$ will be completely uncorrelated with each other. Using $I(t) = \langle I\rangle + \Delta I(t)$ and $\langle \Delta I(t)\rangle = 0$, we have:

$$\begin{aligned}\langle I(t)I(t+\tau)\rangle_{\tau>>\tau_c} &= \langle(\langle I\rangle + \Delta I(t))(\langle I\rangle + \Delta I(t+\tau))\rangle \\ &= \langle I\rangle^2 + \langle I\rangle\langle \Delta I(t)\rangle + \langle I\rangle\langle \Delta I(t+\tau)\rangle \\ &+ \langle \Delta I(t)\Delta I(t+\tau)\rangle \\ &= \langle I\rangle^2 .\end{aligned} \tag{1.83}$$

It then follows that:

$$g^{(2)}(\tau)_{\tau>>\tau_c} = \frac{\langle I(t)I(t+\tau)\rangle}{\langle I(t)\rangle^2} = \frac{\langle I(t)\rangle^2}{\langle I(t)\rangle^2} = 1. \tag{1.84}$$

If we consider $\tau = 0$, then there will exist correlations between the fluctuations of the reflected and transmitted beams resulting in:

$$g^{(2)}(0) = \frac{\langle I(t)^2\rangle}{\langle I(t)\rangle^2}. \tag{1.85}$$

For any light source in which the average intensity varies with time, $\langle I(t)^2\rangle > \langle I(t)\rangle^2$[22], since the time average of the square of the intensity will always be greater than the square of the time average of the intensity, and hence $g^{(2)}(0) > 1$. Thus, for chaotic or thermal light, we see a value of $g^{(2)}(\tau)$ greater than unity at $\tau = 0$, which asymptotically falls to unity as τ increases. Due to this relation of the second order correlation function, this type of light is said to be 'bunched' around $\tau = 0$. One the other hand, if we were to have a perfectly

---

[22] There are equal positive and negative fluctuations about the average, and squaring exaggerates the fluctuations above the average value.

coherent light source that has constant intensity throughout the beam, such as light emitted from a cw laser, $\langle I(t)^2 \rangle = \langle I(t) \rangle^2$ and $g^{(2)}(\tau) = 1$ for all values of τ. However, we will see next that for non-classical light, such as a single photon source, $g^{(2)}(0)$ can be less than unity, leading the phenomenon that is antibunching.

Let us now consider the HBT experiment conducted on a stream of photons, as opposed to a classical electromagnetic wave. The stream of photons is incident on a 50:50 BS and the reflected and transmitted beams are incident on two separate single photon detectors, such as the avalanche photodiodes (APDs)[23] used in our lab. The detectors' photo-induced voltage pulses are then sent to an electronic time-correlated single photon counting module (TCSPCM). One input to the TCSPCM starts a clock, while the other stops the clock. The TCSPCM measures the delay time τ between a photon detection event starting the clock and another stopping the clock. The TCSPCM also measures the photon count rates on each detector in real time.

We've discussed $g^{(2)}(\tau)$ classically in terms of intensity correlations. The count rates detected by the APDs are proportional to the incident intensities, and we can write $g^{(2)}(\tau)$ for the stream of photons as:

$$g^{(2)}(\tau) = \frac{\langle n_1(t) n_2(t+\tau) \rangle}{\langle n_1(t) \rangle \langle n_2(t+\tau) \rangle}, \tag{1.86}$$

where n_i is the number of counts registered on detector i. Thus, $g^{(2)}(\tau)$ describes the relative probability of detecting a photon at detector 2 at a time delay of τ after a photon is detected at detector 1, compared with the probability of detecting two photons separated by an infinitely long time.

Consider a situation in which the photon stream consists of single photons all spaced in time larger than the response time of the detectors. When a photon initiates the start clock upon registering at detector 1, there will be a zero percent probability of simultaneously registering a photon at detector 2 and stopping the clock. Thus, we see for this case $g^{(2)}(0) = 0$. When a second photon arrives at

---

[23] Often the acronym SPAD is used, which stands for single-photon avalanche diode, which is a type of APD. I tend to use the shorter APD acronym throughout this dissertation. Note, the APDs used in the experiments discussed in this dissertation are, indeed, SPADs.

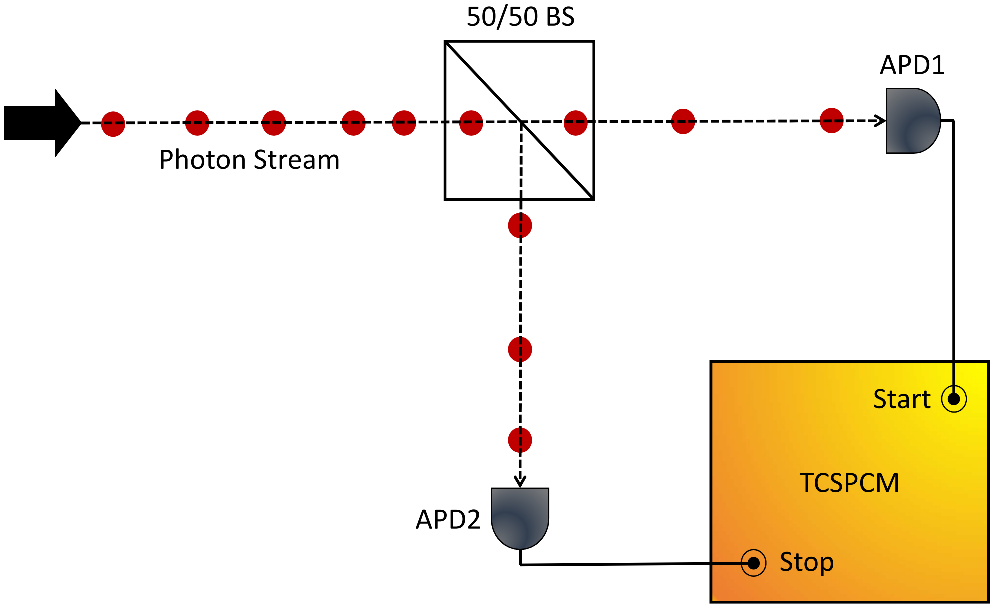

FIGURE 1.12: Schematic of a Hanbury Brown-Twiss setup used to measure photon statistics. The photon stream is incident on a 50:50 BS. The reflected and transmitted streams are incident on two separate single-photon avalanche diodes (APD1 and APD2). The detectors output a voltage pulse upon detection of a photon. The pulses are collected by a time-correlated single photon counting module (TCSPCM). The pulses from APD1 start a clock and the those from APD2 stop the clock. The TCSPCM then builds a histogram of time arrival times τ equal to the time between start and stop events. The TCSPCM also measures the photon count rates on each detector in real time.

the 50:50 BS, it has a 50% chance of going to detector 1, in which nothing happens[24], and a 50% chance of going to detector 2, in which it will stop the clock. After enough photon arrival events at the 50:50 BS, we are bound to register a photon at detector 2 and stop the clock. Thus, as τ approaches infinity, $g^{(2)}(\tau)$ approaches unity. This type of light is known as antibunched light and has no classical counterpart, since its existence is directly tied to the particle-nature of light.

Now, consider a light source in which photons come in dense bunches. When a photon starts the clock at detector 1, there is a very high probability that another photon will simultaneously stop the clock at detector 2, and we will measure a large value for $g^{(2)}(0)$. After a time passes that is much longer than the average temporal width of the bunches, the probability of registering a photon arrival event at detector 2 and stopping the clock becomes constant, but with a smaller probability than stopping the clock at $\tau = 0$. Thus for this case, $g^{(2)}(\tau)$ starts at some value greater than unity and asymptotically decreases to unity as $\tau \to \infty$. This type of light is known as bunched light.

Lastly, a photon source that is neither bunched nor anti-bunched, i.e, a light source consisting of a completely random distribution of photons, has an equal probability of stopping the clock at any delay time, and thus $g^{(2)}(\tau) = 1$. This type of light is known as coherent light. We can then make the connection to sub-Poissonian, Poisson, and super-Poissonian light discussed classically:

- antibunched light, sub-Poissonian: $g^{(2)}(0) < 1$,
- coherent light, Poissonian: $g^{(2)}(0) = 1$,
- bunched light, super-Poissonian: $g^{(2)}(0) > 1$.

The three type of light are depicted in Fig. 1.13. Additionally, Fig. 1.14 depicts example $g^{(2)}(\tau)$ for the three types of light.

1.8.5 Hong-Ou-Mandel Interference and the Mach-Zehnder Interferometer

In 1987 Hong, Ou, and Mandel published a paper that described the relation between the input and output states described by photon number states, or Fock

---

[24] Nothing happens because arrival of a photon at detector 1 starts the clock, while it is arrival of a photon at detector 2 that stops the clock.

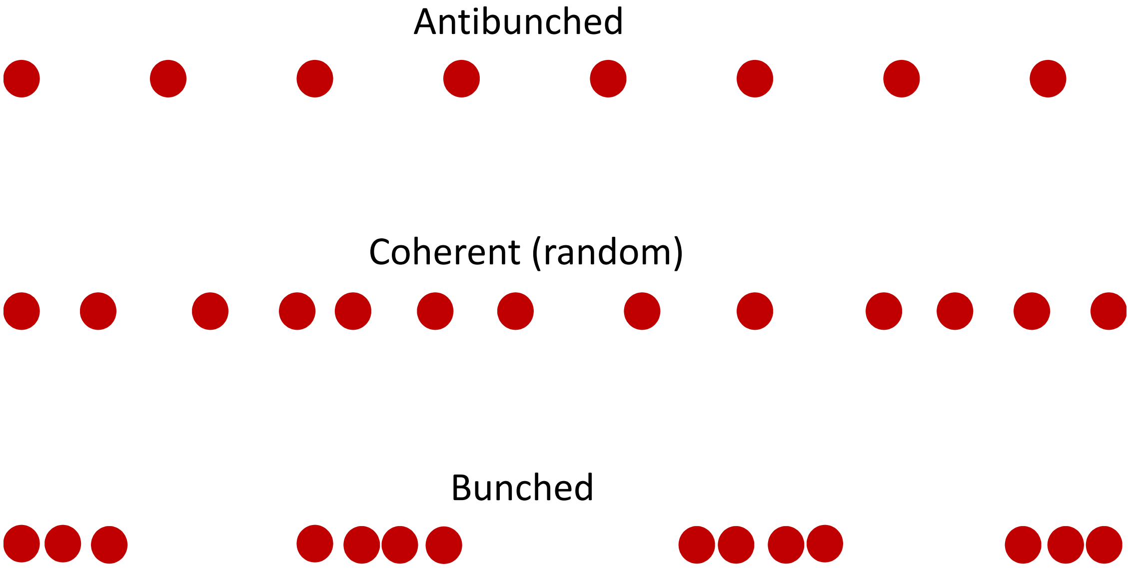

FIGURE 1.13: Representation of the three types of light as depicted with streams of photons.

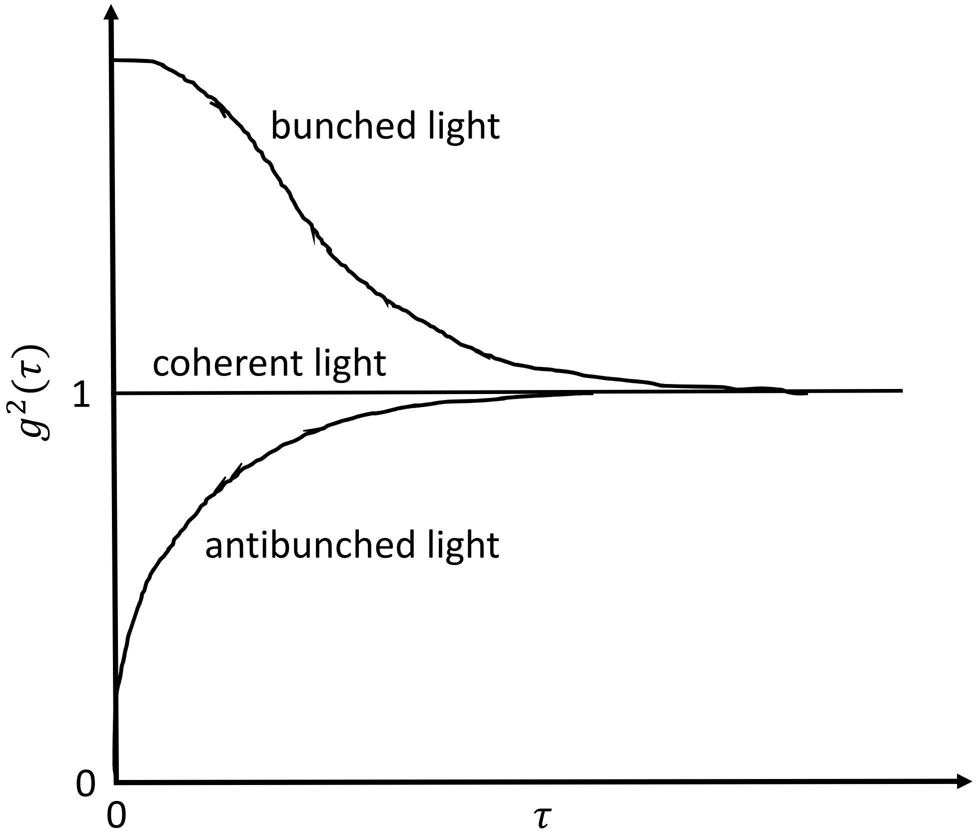

FIGURE 1.14: Examples of $g^{(2)}(\tau)$ for the three types of light.

states, of single photons incident on a beam-splitter (BS) [36]. They showed that two completely indistinguishable photons simultaneously incident on the two different inputs of a 50:50 BS will always leave together in the same output mode. It is equally likely for the photons to exit either port, but they will always exit the same port if they are indistinguishable. Consequently, if one were to conduct a correlation measurement of the two outputs, which utilizes the start and stop clocks previously discussed, then one would measure zero coincidence counts for $\tau = 0$, since when the clock is started, there is a zero percent probability that another photon simultaneously initiates the stop clock. This two-photon interference is a manifestation of the quantum nature of light, and is essential for quantifying a photon source's indistinguishability. Although not studied in this dissertation, this quantum effect is essential to provide the physical mechanisms for logic gates in linear optical quantum computation [63].

Let us describe the Hong-Ou-Mandel (HOM) effect mathematically. Depicted in Fig. 1.15, we consider two single photons simultaneously incident on a 50:50 BS in perpendicular input modes. For a 50:50 BS, the reflection and transmission coefficients are equal, $|r| = |t| = 1/\sqrt{2}$. The probabilities for reflection or transmission are equal to the square of the corresponding coefficient, i.e. 50%. We assign labels a and b to the two input modes and labels c and d to the two output modes. From a classical standpoint, the electric field amplitudes of the output modes can be written as linear superpositions of the electric field amplitudes of the input modes as follows:

$$\begin{aligned} E_c &= \frac{E_a + E_b}{\sqrt{2}} \\ E_d &= \frac{E_a - E_b}{\sqrt{2}} \end{aligned} \tag{1.87}$$

Standard plate beam-splitters have one face coated with a dielectric. The minus sign in the relation of E_d in Eqn. 1.87 arises due to reflection from the dielectric surface from air. Consider a polarized light wave with a polarization parallel to the reflecting dielectric surface. For the side of the BS in which there is the dielectric coating, Fresnel equations [61] dictate that the reflected wave will acquire a phase shift of π, hence introducing the negative sign in the associated reflective term in the appropriate output mode. One can also think about this as reflection from opposite sides of the 50:50 BS induce a relative phase shift of π between the two cases. We shall see this plays a crucial role in the ultimate

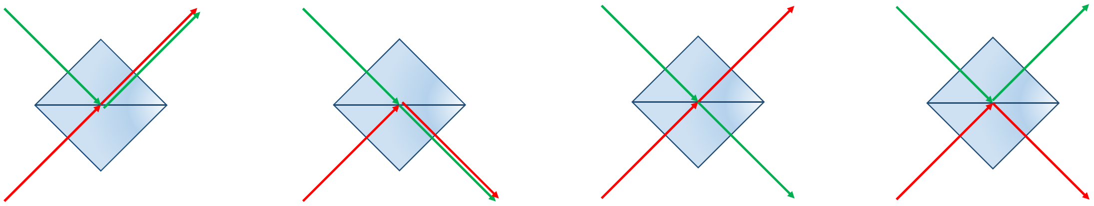

FIGURE 1.15: Depiction of possibilities when two photons are incident on a BS from perpendicular input ports. Green arrows signify the path of the photon incident on the BS from the top and red arrows signify the photon incident from the bottom. Each photon has a 50% chance of either transmission or reflection. When the photons are identical, the probability amplitudes associated with both photons reflecting and both transmitting cancel, and the photons always leave the BS into the same output mode.

outcome of the two-photon interference.

Let us now consider the system from a quantum mechanical point of view. We shall utilize a second-quantized Fock state formalization. We first introduce a set of bosonic annihilation and creation operators, $\hat{a}$ and $\hat{a}^{\dagger}$ respectively, which represent annihilation and creation of a photon. The annihilation and creation operators have the following commutation relation: $[\hat{a}_i, \hat{a}_j^{\dagger}] = \delta_{ij}$, where δ_{ij} is the Kronecker delta, and the indices i and j represent specific photon modes. The creation operator acting n times on the vacuum gives:

$$(\hat{a}_i^{\dagger})^n |0\rangle = \sqrt{n!}\, |n\rangle_i \,, \tag{1.88}$$

where $|n\rangle_i$ represents an n-photon Fock state in mode i and $|0\rangle$ is the vacuum state, i.e. no photons. In conjunction with our previous assignment of mode labelling for the classical standpoint, it's convenient to drop the conventional subscript that signifies specific photon modes, and use $\hat{a}^{\dagger}$, $\hat{b}^{\dagger}$, $\hat{c}^{\dagger}$, and $\hat{d}^{\dagger}$ to represent creation operators in the input modes a and b and output modes c and d [64]. Analogous to the electric field amplitudes of the output modes in terms of the input modes when approached classically, we can write the annihilation/creation operators for the output modes in terms of the input modes, and vice versa. For our mathematical development here, it is convenient to write the input modes' creation operators in terms of the output modes' creation operators:

$$\begin{aligned} \hat{a}^\dagger &= \frac{1}{\sqrt{2}}\left(\hat{c}^\dagger + \hat{d}^\dagger\right) \\ \hat{b}^\dagger &= \frac{1}{\sqrt{2}}(\hat{c}^\dagger - \hat{d}^\dagger) \end{aligned} \tag{1.89}$$

Let us first consider the case in which two perfectly distinguishable photons are simultaneously incident on a 50:50 BS, one in mode *a* the other in mode *b*. They may be able to be distinguished from each other via a number of degrees of freedom: polarization, spatial modes, center frequency, arrival time[25], etc. Let us assume one photon is polarized horizontally relative to some arbitrary coordinate system, while the other is polarized vertically. For instance, the photon in mode *a* is horizontally polarized, while that in mode *b* is vertically polarized. We can write the input state as $\hat{a}_H^\dagger \hat{b}_V^\dagger |0\rangle$. Upon interaction with the BS, this can be written in terms of the output creations operators as follows:

$$\begin{aligned} \hat{a}_H^\dagger \hat{b}_V^\dagger |0\rangle &= \frac{1}{2}\left(\hat{c}_H^\dagger + \hat{d}_H^\dagger\right)\left(\hat{c}_V^\dagger - \hat{d}_V^\dagger\right)|0\rangle \\ &= \frac{1}{2}\left(\hat{c}_H^\dagger \hat{c}_V^\dagger - \hat{c}_H^\dagger \hat{d}_V^\dagger + \hat{d}_H^\dagger \hat{c}_V^\dagger - \hat{d}_H^\dagger \hat{d}_V^\dagger\right)|0\rangle . \end{aligned} \tag{1.90}$$

The two photon interference occurs when the photons are identical, that is identical in polarization, wavelength, etc. There is no longer a need to specify the polarization with subscripts *V* and *H*. Then, the system can be described as follows:

$$\begin{aligned} \hat{a}^\dagger \hat{b}^\dagger |0\rangle &= \frac{1}{2}\left(\hat{c}^\dagger \hat{c}^\dagger - \cancel{\hat{c}^\dagger \hat{d}^\dagger} + \cancel{\hat{d}^\dagger \hat{c}^\dagger} - \hat{d}^\dagger \hat{d}^\dagger\right)|0\rangle \\ &= \frac{1}{2}\left((\hat{c})^2 - (\hat{d})^2\right)|0\rangle \\ &= \frac{1}{\sqrt{2}}\left(\, |2\rangle_c - |2\rangle_d \,\right). \end{aligned} \tag{1.91}$$

What this equation signifies is that when the two simultaneously arriving photons are indistinguishable, there is destructive interference of the components of the two-photon output state that correspond to the photons exiting in different modes, and constructive interference of the components that correspond to the

---

[25] Timing can serve as a metric of distinguishability, but here we are concerned with the situation in which the photons arrive simultaneously.

photons leaving in the same mode. We see that upon measurement, it is equally likely to find the photons in mode c or mode d, but they will always exit the BS into the same mode.

In the experiment described in Chapter 6, I use an unbalanced Mach-Zehnder interferometer (MZI) and the HOM effect to quantify photon indistinguishability via correlation measurements at the two outputs of the MZI. A conventional MZI consists of an input photon source that is incident on a 50:50 BS. The two separate arms are each reflected off of a mirror and recombined at a second BS. Ultimately, correlation measurements can be conducted at the two outputs.

Depicted in Fig. 1.16, we will first consider the classic balanced MZI, which uses simple plate BSs. Reflection from a plate BS from the front[26], in which the incident medium has a lower index of refraction than that behind the reflecting surface, results in a π phase shift. Reflection from the backside does not, since the incident medium's index of refraction (glass) is greater than that on the other side of the reflective surface (air). The first BS has the dielectric coating facing forward. The second BS has the dielectric coating facing forward in the path that transmitted through the first BS. Thus, the path that reflected off of the first BS hits the backside of the second BS. At the input of the second BS, the path that transmitted through the first BS has acquired a phase shift of π[27] and the other 2π. If one observes the output that corresponds to the path that has acquired a phase shift of π reflecting from the front of the second BS, both paths will have acquired a phase shift of 2π, and the beams will constructively interfere. If we observe the path that corresponds to the beam that transmitted through the first BS transmitting through the second BS, then one path will have acquired a phase shift of π and the other 2π, resulting in destructive interfere.

A common classical use of an MZI involves insertion of a medium into one of the arms, and the intensity measured at the two outputs can be used to calculate the phase shift induced by the inserted medium. Additionally, one of the MZI's arms can be varied in length. As the optical path length of one arm is shifted by a half wavelength relative to the other arm, one will observe a shift in which output experiences complete constructive interference, and which experiences complete destructive interference. An optical path length difference

---

[26] I am referring to the front as the side for the BS that has the dielectric coating. The back is referred to the side without the dielectric coating.

[27] Reflection from the regular mirrors in either arm results in an additional phase shift of π.

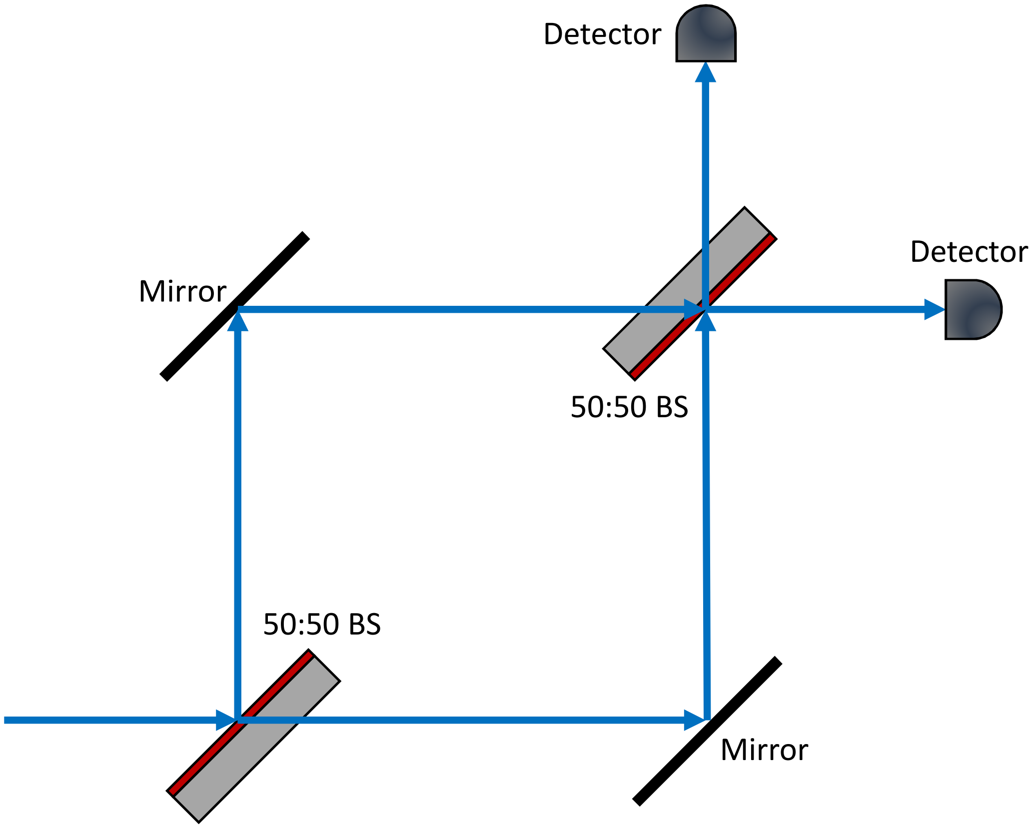

FIGURE 1.16: Schematic of a classic balanced MZI. The blue arrows represent the propagation of a collimated light beam through either arm. The red sides of the 50:50 BSs represent the dielectric surfaces.

of $n\lambda$, where λ is the wavelength of the light, will induce the same state of the interference at the two outputs as to when the two arms are equal in length. As the optical path length difference between the two arms is varied, one observes interference fringes at the outputs. The distances/times between peaks are correlated with the optical path length difference of $n\lambda$. This type of MZI can be used to measure precise distances when the wavelength of a monochromatic source is well-known.

In our lab, we use an unbalanced MZI to measure photon indistinguishability via utilization of the HOM effect. I constructed a custom fiber-based MZI, which is in some ways easier to use than a free-space MZI, to acquire data for the experiment described in Chapter 6. Figure 1.17 depicts our custom fiber-based MZI. The QD fluorescence is first sent through a spectrometer for spectral filtering of light other than that of the fluorescence. The fluorescence is then coupled

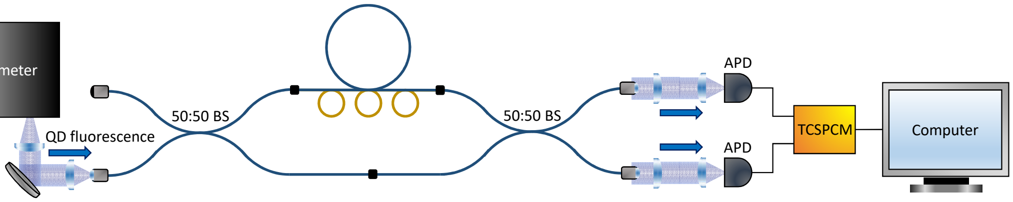

FIGURE 1.17: Schematic of our fiber-based Mach-Zehnder interferometer. The QD fluorescence is first sent through a spectrometer acting as a spectral filter before being sent to the MZI. The fluorescence is coupled into the fiber shown on the bottom left of the figure. The light hits the first 50:50 BS, sending light through two separate arms that have different lengths. Two fibers are interchangeable for the long arm: one that maintains polarization (represented by the blue fiber) and one that rotates the polarization by 90 degrees (represented by the yellow fiber). The photons traveling in the two arms then recombine at the second BS and correlation measurements are conducted at the two outputs. APD stands for avalanche photo-diode and TCSPCM for time-correlated single photon counting module.

into one of the inputs of a fiber BS, while the other input is unused. The fiber BSs are composed of polarization maintaining fibers, so that the polarization is preserved during propagation through the MZI. The QD fluorescence hits the first 50:50 BS and is split into the two arms of the MZI, one short arm and one long arm (unbalanced MZI). The light is recombined at the second BS and correlation measurements can be conducted at the two outputs. The polarization maintaining fibers ensure that the photons will interfere with maximum fidelity when they meet at the second BS.

Two different interchangeable fibers are used in the long arm of the MZI. One fiber is a polarization maintaining fiber. The other fiber is a single-mode fiber that is not polarization maintaining. Depending on the orientation of the fiber that does not maintain polarization, the output polarization will be changed. Indeed, simply lightly shaking the fiber will induce measurable effects. This fiber is mounted in a custom-built polarization controller, surprisingly, adequately constructed using Lego pieces. The Lego chassis consists of three square paddles that one can coil the optical fiber through, and are such that the angles of the paddles can be set and maintained. Figure 1.18 is a schematic of the polarization controller. The first paddle contains one coil of the optical fiber, the second two coils, and the third three coils. The first paddle effectively behaves

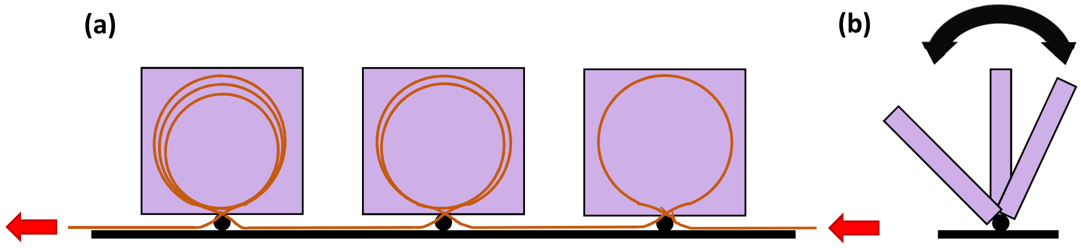

FIGURE 1.18: Schematic of our polarization controller. (a) Side view: The light traveling through the optical fiber is sent into the polarization controller from the right and exits from the left. It first goes through one loop in the first paddle, two in the second, and three in the third. (b) Front/back view: The paddles are able to pivot such that the user can set a maintained angle for each paddle. Since the output polarization is dictated by the spatial configuration of the single-mode fiber coiled within, any input polarization can be converted to any other polarization via carefully setting each paddle's angle. In our measurement of the CTW discussed in Chapter 6, we use the polarization controller to rotate linear-polarized fluorescence by 90 degrees.

similarly to an approximate half-wave plate (HWP), the second an approximate quarter-wave plate (QWP), and the third an approximate three-quarter-wave plate, which is essentially another quarter wave-plate. With a perfect quarter-wave and half-wave plate, one can rotate any polarization to any other polarization[28]. The third paddle helps to compensate for the fact that the first two paddles don't act as a perfect HWP and QWP. The polarization controller lets us rotate the polarization by 90 degrees, making the photons between the two arms completely distinguishable when they combine at the second 50:50 BS. Use of the two interchangeable fibers allows for the comparison of the correlation measurements at the outputs when the photons hitting the second BS are nominally distinguishable or nominally indistinguishable. Ultimately, the coalescence time window (CTW) is calculated to quantify the degree of indistinguishability of a given photon source. This is expanded upon in further detail in Chapter 6.

---

[28] It is convenient to represent a given polarization as a vector within or on the Poincaré sphere, which is illustrated in Appendix B. The polarization state is mathematically represented by the components of the associated Stokes vector. Changes in polarization can be represented as rotations of the Stokes vector and changes in its length. The degree of polarization is represented by the length of the vector, where a length of unity signifies completely polarized light (whether that be linear or elliptical), and a zero vector represents completely un-polarized light.

Chapter 2

Experimental Techniques

2.1 Introduction

The core experimental techniques used during the investigations discussed in this dissertation include time-resolved resonance fluorescence (TRRF) and Hong-Ou-Mandel (HOM) correlation measurements involving a custom-built fiber-based Mach-Zehnder interferometer (MZI).

Resonant excitation of exciton states in InAs QDs is the best method to minimize inhomogeneous broadening of the QDs′ emission spectra, hence producing the optimal source of indistinguishable photons. However, since under resonant excitation the laser wavelength matches that of the emitted fluorescence, techniques must be implemented to minimize incidence of laser scattering onto the optical collection path associated with the QDs′ fluorescence. There exist two major techniques to minimize the collection of laser scattering. One technique involves using a cross-polarization setup. Orthogonally-oriented polarizers in the excitation and collection paths can force the excitation laser polarization to be perpendicular to the collected fluorescence, which enables the laser scattering to be filtered from the collection path. However, via this method, at best only 50 percent of the emitted fluorescence collected by the initial objective lens at the sample can be detected. Under this circumstance, the resonant excitation laser′s polarization is set 45 degrees with respect to the dipole moment of the trapped exciton via the polarizer in the excitation path. The emitted fluorescence has a polarization that matches the dipole moment of the exciton, and thus when filtered by an additional polarizer in the collection path that is oriented perpendicular to the excitation laser′s polarizer, optimally only 50 percent of the fluorescence set incident on the collection path can be collected, excluding any losses due to other optical elements and geometries.

The other major method to filter scattered laser light from the collection path involves a perpendicular geometry. The InAs QDs we study are embedded in bulk GaAs which is contained on two sides by distributed Bragg reflectors composed of alternating layers of AlAs and GaAs, which is depicted in Fig. 1.1(e). This geometry creates a planar waveguide for the excitation laser and also acts as a Fabry-Perot cavity, which induces the QD fluorescence to preferentially exit the sample parallel to the growth direction, normal to the sample surface (upward in the figure shown)[1]. We focus resonant excitation laser light into the waveguide from the side. A low-power above-band laser is incident onto the sample surface parallel to the growth direction (perpendicular to the optical axis of the resonant laser light). The QD fluorescence is collected confocal with the above-band laser by a high numerical aperture lens. The high numerical aperture of the collection lens, along with the resonant laser's propagation through the waveguide, allows for a collection FOV that is far displaced from the sample's edge, where scattering of the focused resonant laser is inevitable. This allows for very little laser scattering to fall onto the fluorescence collection path. The back-reflected above-band laser is filtered from the collection path via a 900 nm long-pass filter. Very little laser scattering from the resonant laser falls incident onto the collection path due to this perpendicular geometry of resonant excitation and fluorescence collection, and the collected fluorescence intensity is not compromised as is filtering via the crossed-polarization technique.

The QD fluorescence can then be collected and analyzed via multiple different methods. The fluorescence can be sent through a Fabry-Perot interferometer to measure the fine structure of the emission spectrum, sent to a CCD camera attached to a spectrometer for coarse measurement of the emission spectrum or direct spatial imaging, sent to an avalanche photodiode (APD) to measure time-resolved resonance fluorescence measured relative to different possible temporal triggers (start clocks), or sent through a Mach-Zehnder interferometer (MZI) with its two outputs set incident on two APDs from which correlation measurements can be made, such as the second order correlation function, and ultimately the photon coalescence time window (CTW).

---

[1] This is expanded upon further in Chapter 1.

2.2 Full Experimental Configuration

The sample is enclosed in a cryostat held at approximately 4.2 K to minimize thermally induced excitations. The resonant excitation laser is first coupled into a fiber. The light emitted from the fiber's output is sent through a beam expander to increase the numerical aperture at the excitation objective lens that focuses the laser into the planar waveguide of the sample. Before being focused into the waveguide via the excitation objective lens, the excitation light is transmitted through a polarizer to force the polarization to be parallel to the waveguide direction (perpendicular to the growth direction), which ensures that the excitation polarization is in the same plane as the QDs' transition dipole moments. An additional, low-power laser with a photon energy greater than the band-gap energy of the bulk GaAs host, hence named the above-band laser, is incident on the sample perpendicular to the sample surface. The above-band laser creates hot, free charge carriers mostly in the top DBR. These carriers move through the environment via two effective mechanisms (expanded upon in Chapters 4 and 5) to make their way into the adjacent vicinity of the QD, where they can be captured by the QD. The resonant laser often changes the charge state of the QD, diminishing the fluorescence intensity from the probed optical transition. The above-band laser's introduction of carriers to the environment allows for ultimate capture of carriers by the QD, returning the QD to the initial charge state being resonantly driven, and hence returning the intensity of the QD's fluorescence from said transition.

The QD fluorescence is captured confocal with the above-band excitation via a 10 millimeter focal length lens. The fluorescence exits through a cryostat window, and is first sent through a 1x magnification telescope with one lens in an x-y mount that can translate perpendicular to the optical axis. Translation of said lens permits one to change the FOV at the sample without changing the position on the ultimate image plane onto which the QD fluorescence is focused. It is then sent through a 3x beam expander, a long-pass filter used to filter backscattered above-band laser light, two liquid crystal variable retarders (LCVRs), and a polarizer, and eventually is focused onto the image plane of the spectrometer (input slit) with a 200 mm lens. The collection lens, 3x beam expander, and lens that focuses the fluorescence onto the image plane of the spectrometer create an overall magnification of 60. The two LCVRs and polarizer are used in conjunction to select the detection polarization. The two LCVRs can rotate any polarization to any other on the Poincaré sphere. Thus, their input voltages can be set to rotate a given polarization of the collected fluorescence onto that of the polarizer preceding the spectrometer, allowing for collection of a specific polarization with minimal loss of intensity. The polarizer preceding the spectrometer is set to force the polarization of light to be perpendicular to the groove direction of the grating inside the spectrometer, optimizing the diffraction efficiency. The QD fluorescence can then be collected via a CCD camera attached to one of the two spectrometer outputs, or can be sent out of the spectrometer via the other output for additional analysis.

The fluorescence transmitted through the spectrometer is coupled into a single-mode, polarization-maintaining fiber that is the input to a fiber-based MZI. A HWP is used before the input of the fiber to rotate the fluorescence's polarization to match that of one of the two propagation modes of the fiber. One of the arms of the MZI can be disconnected so that HBT or TRRF measurements using just the second beam-splitter can be conducted. However, both arms can be left intact, allowing for HOM interference measurements, such as the second-order correlation measurements used to calculate the CTW to characterize photon indistinguishability. Further details regarding TRRF measurements are discussed in Chapters 4 and 5, while further details regarding measurement of the CTW is discussed in Chapter 6.

2.3 Excitation Spectrum

In Chapter1 we made the argument that the excitation spectrum of a resonantly excited QD often takes on a Lorentzian lineshape. I will rewrite the Lorentzian in a slightly different form here, but the mathematical shape remains the same. The intensity of the observed fluorescence of a given transition as a function of resonant laser wavelength ω_L is given by:

$$I(\omega_L) = \frac{A\Gamma}{2\pi\big((\omega_L - \omega_0)^2 + \frac{1}{4}\Gamma^2\big)}, \tag{2.1}$$

where ω_0 is the on-resonance frequency, Γ is the FWHM of the lineshape, and A is the area under the curve[2].

Acquiring an excitation spectrum is quite straight-forward. The intensity of the fluorescence is monitored, in our case by a CCD camera. The excitation laser is then stepped in frequency about the on-resonance frequency ω_0 (laser frequency in which the QD fluorescence is brightest). The intensity is recorded as a function of excitation laser frequency over the full range of frequencies in which a measureable intensity of the probed optical transition exists. The curve is fit with the above Lorentzian function from which on-resonance frequency and FWHM can be extracted.

2.4 Saturation Curve

Investigations of low-power dynamics of course requires minimization of high-power effects, such as observation of Rabi oscillations under high-power resonant excitation. The low-power regime is often defined to be established when an excitation power less than the saturation power of the probed optical transition is used. As the excitation power is increased, the maximum time-averaged population of the excited state saturates, because the absorption rate and stimulated emission rate increase by the same proportion with laser power[3]. This results in a saturation of fluorescence intensity as a function of excitation power with the following form:

$$I = I_{max} \frac{P}{P + P_s}, \tag{2.2}$$

where I_{max} is the maximum fluorescence intensity at high power, P is the excitation power, and P_s is the saturation power, which is defined as the power that results in the fluorescence intensity taking on a value equal to half its maximum value.

---

[2] Recall, without the coefficient A, the integral over the full Lorentzian is unity, thus A is the area under the curve. Multiplication of the Lorentzian by A allows us to fit any general Lorentzian lineshape without normalization.

[3] That is, the two rates become balanced at high power.

2.5 Excited State Lifetime

For lifetime measurements, we excite a QD using a pulsed titanium-sapphire laser. Each pulse is a couple of picoseconds (tens of GHz) in duration and adjacent pulses are separated by 12.5 ns. A typical lifetime for InAs QDs in our sample is on the order of 1 ns or less, resulting in absorption (excitation) and emission bandwidths on the order of a few GHz. The laser power is optimized to maximize the fluorescence of a given transition in a QD, and due to its pulse width, covers the full excitation spectrum for a given transition, regardless of the degree of spectral diffusion. Additionally, the pulsed laser has a narrow enough bandwidth that it does not couple with optical transitions of other charge states of the QD. An incoming pulse populates the excited state, which is allowed to decay entirely before the arrival of the next pulse, due to the time between pulses being roughly an order of magnitude longer than the lifetime of the excited state. The TRRF is then recorded relative to a trigger signal that is synced with the pulse arrival time, and the entire decay of the fluorescence is recorded.

In the optical path of the excitation laser, a sampler is used to pick off a small amount of intensity sent to a fast-photodiode (FPD). The FPD outputs a voltage signal relative to the incident intensity. As long as the FPD's response time is faster than the time between pulses, the FPD creates consequential voltage pulses that are synced temporally with the pulses of the laser. The voltage signal is sent through a passive inverter that creates negative delta-function-like pulses that are used to trigger the TCSPCM and start the clock. The fluorescence from the QD is then sent to an APD and the TCSPCM constructs a histogram of photon arrival times at the APD relative to the start clock that is in sync with the pulse arrival time.

For optical and near-infrared frequencies at 4.2 K, the photon energy is much higher than the energy $k_B T$ associated with black-body radiation, thus stimulated emission and absorption induced from any thermal radiation can be ignored. The decay of the excited-state population is thus dominated by spontaneous emission. The time-evolution of the excited state, and hence the fluorescence intensity, is then given by Eqn. 1.4. Consequently, the fluorescence intensity caused by decay of the excited state population takes on a simple decaying exponential form, as in Eqn. 1.5. We thus fit the decaying TRRF with a simple exponential convolved with the instrument response function (IRF) of the measurement system to extract the lifetime (τ in Eqn. 1.5)[4].

---

[4] Note that although the life time is τ in Eqn. 1.5, T_1 is often used to represent the lifetime.

Chapter 3

Characterization of the Local Charge Environment of a Single Quantum Dot via Resonance Fluorescence

3.1 Introduction

In this chapter we study the photon-statistical behavior of resonance fluorescence from self-assembled InAs quantum dots (QDs) as a function of the density of free charge carriers introduced by an above band-gap laser. Second-order correlation measurements show bunching behavior that changes with above-band laser power and is absent in purely above-band excited emission. Resonant photoluminescence excitation spectra indicate that the QD experiences discrete spectral shifts and continuous drift due to changes in the local charge environment. These spectral changes, combined with tunneling of charges from the environment to the QD, provide an explanation of the bunching observed in the correlations.

Indistinguishable single photons are potentially important in a number of quantum information processing applications, for example linear optical quantum computation [63], entanglement swapping [65–67], and quantum repeaters [68, 69]. Indistinguishable photons are those with identical properties (*e.g.*, wavelength, bandwidth, polarization), which allows them to demonstrate Hong-Ou-Mandel interference [36]. Semiconductor quantum dots (QDs) have been shown to be good sources of single photons [70–72], and photons emitted from the same QD in rapid succession have been shown to have very high indistinguishability when the QD is in an optical cavity [42, 73] or is excited resonantly [74]. Photons spaced more widely in time and those from separate

QDs, however, do not show the same degree of indistinguishability [32, 75, 76] due to the inhomogeneous distribution of photon energies emitted by one QD state at different times. This inhomogeneous distribution is called spectral diffusion, and it is likely caused by fluctuating occupation of charge traps in the environment of the QD [33, 35, 77–80]. In order to produce indistinguishable single photons, the causes of spectral diffusion must be investigated and mitigated. One step in this process is to measure the dynamics and the influence on the QD of fluctuating charge traps in the environment.

The subtle fluctuations of the local electric field environment modify the energy levels of the QD through the quantum-confined Stark effect because of the QD's large DC electric polarizability. Spectroscopically, this effect manifests as a discrete jump, continuous drift or spectral broadening of the QD's absorption (excitation) and emission lines depending on the relative position of the charge traps and characteristic time of the electric fluctuations. A charge trap close to a QD will result in a discrete shift of the peak in the QD absorption spectrum when the trap's occupation state changes. A single trap far from a QD will have an unnoticeable effect on the QD by itself, but a change in mean occupation of a large ensemble of traps will cause a continuous drift or broadening of the QD spectrum. In this study, we show that all of these effects are present in one QD's excitation spectrum when its local environment is perturbed by above band-gap optical excitation.

To resolve the fine change in the QD energy levels, we use resonant photoluminescence excitation (RPLE) spectroscopy, which measures the excitation spectrum by collecting the total resonant fluorescence from the QD using different excitation wavelengths. The resolution of this technique is solely dependent on the linewidth of the excitation laser, which is $\sim$1 MHz in our case. RPLE spectra with additional variable-intensity above-band excitation illustrate discrete spectral jumps in the QD resonance due to Stark shifts caused by nearby occupied charge traps. The number, relative position, and average occupation of the nearby charge traps can be deduced from the data. No electrical contacts are necessary as the measurement is entirely optical. Second-order correlation measurements of the emitted fluorescence show photon bunching that characterizes the time-scale of the charge trap dynamics. We found that the switching rate of the charge traps between occupied and unoccupied configurations increases by five orders of magnitude with increasing above band-gap excitation power even below the threshold where the above-band excitation produces photoluminescence (PL) on its own.

3.2 Sample and Experimental Setup

The sample consists of InAs self-assembled QDs grown in the center of a 4-λ GaAs spacer between two AlAs/GaAs distributed Bragg reflectors (DBRs) with 14 and 20.5 periods on the top and bottom, respectively. The DBRs form a planar microcavity with a transmission mode from 923 $\sim$ 930 nm and a waveguide mode that confines light within the plane of the sample. The thickness of the GaAs spacer that defines the cavity is 1.06 um, leaving the QDs more than 500 nm away from either DBR. As discussed later, this relatively large distance rules out the possibility that the observed discrete Stark shifts in the RPLE data are caused by charging of defects at the hetero-interfaces or the sample surface. The sample is maintained at 5 K in a closed-cycle cryostat. The optical excitation and collection scheme is depicted in Fig. 3.1. Laser light resonant with a QD transition is introduced into the waveguide mode of the sample via free-space coupling from the side; the QD is approximately 100 μm from the cleaved sample edge. When the QD transition is resonant with the cavity mode, the fluorescence is preferentially directed normal to the sample surface where it is collected by a 0.5 NA aspheric lens. The resonant excitation is provided by either a tunable continuous-wave (CW) diode laser or a mode-locked Ti:sapphire laser with a pulse length of 2.1 ps. Simultaneous with the resonant laser, an above band-gap excitation laser with a wavelength of 633 nm can be introduced normal to the surface. The fluorescence is directed through a 0.75 m spectrometer and thence either to a TE-cooled CCD camera or through an exit slit to a time-correlated single-photon counting (TCSPC) system. The second-order correlation function, $g^{(2)}(\tau)$, of the CW-excited fluorescence is calculated from the time-tagged photon detection data.

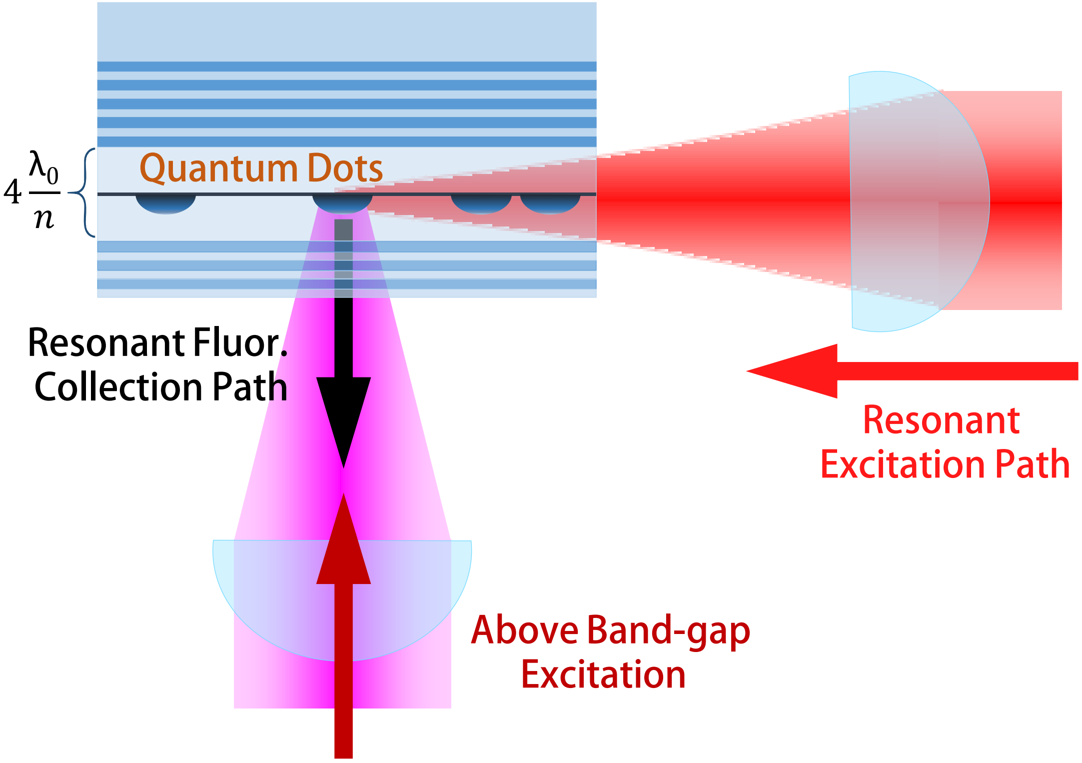

FIGURE 3.1: Quantum dot sample with optical excitation and collection geometry. The resonant laser is focused on the cleaved face of the sample in order to couple into the waveguide mode of the cavity. The fluorescence is collected normal to the sample surface. The above band laser at 633 nm is focused through the collection lens onto the QD location. λ_0 is the cavity resonance wavelength in vacuum (930 nm) and n is the refractive index of GaAs (~ 3.5).

3.3 Experimental Results

3.3.1 Time-Resolved Fluorescence

The QD lifetime T_1 is obtained from time-resolved fluorescence measurements where the QD is resonantly excited by the pulsed laser and the fluorescence is directed to a single-photon counting module (SPCM). The pulse has an energy of 0.17 pJ and a bandwidth of 76 GHz in linear frequency. This is two orders of magnitude wider than the QD's ground state transition linewidth, and well covers the observed spectral shifts due to the charge traps. Figure 3.2 shows an example time-resolved measurement without above-band excitation. The data are fit with an exponential decay convolved with the measured instrument response function of the SPCM. We measured resonantly excited time-resolved fluorescence for different powers of above-band excitation and extracted an average lifetime of $T_1 = (518 \pm 3)$ ps. The extracted lifetimes show no trend with increasing above-band excitation power (inset of Fig. 3.2). Coupled with additional measurements discussed below, this suggests that the lifetime is not affected by the fluctuations of the local charge environment.

3.3.2 Resonant Photoluminescence Excitation Spectroscopy

We use RPLE spectroscopy to quantify the discrete shifts and continuous drifts of the QD energy levels caused by both nearby and distant charge carrier traps. The capture rate of charge carriers at these traps is expected to depend on the local free charge carrier density, which is controlled by adjusting the power of an above band-gap laser through 6 orders of magnitude. For each power, two RPLE spectra with orthogonal detection polarizations (H & V) are collected by scanning the frequency of a tunable 1 MHz bandwidth CW laser through the QD resonance at 10% of the saturation power $\mathrm{P}_0 = 4.7\mu\mathrm{W}$. The two spectra are then summed to give a final spectrum whose amplitude is proportional to the exciton population in the QD. In the summation, the polarization-dependent absorption due to the optics in the collection path is corrected.

Figure 3.3(a)–(c) shows three examples of summed spectra in three different power regimes of the above-band laser, *i.e.* low, medium and high power. Each spectrum is fitted with 8 Voigt profile peaks whose Lorentzian linewidth is

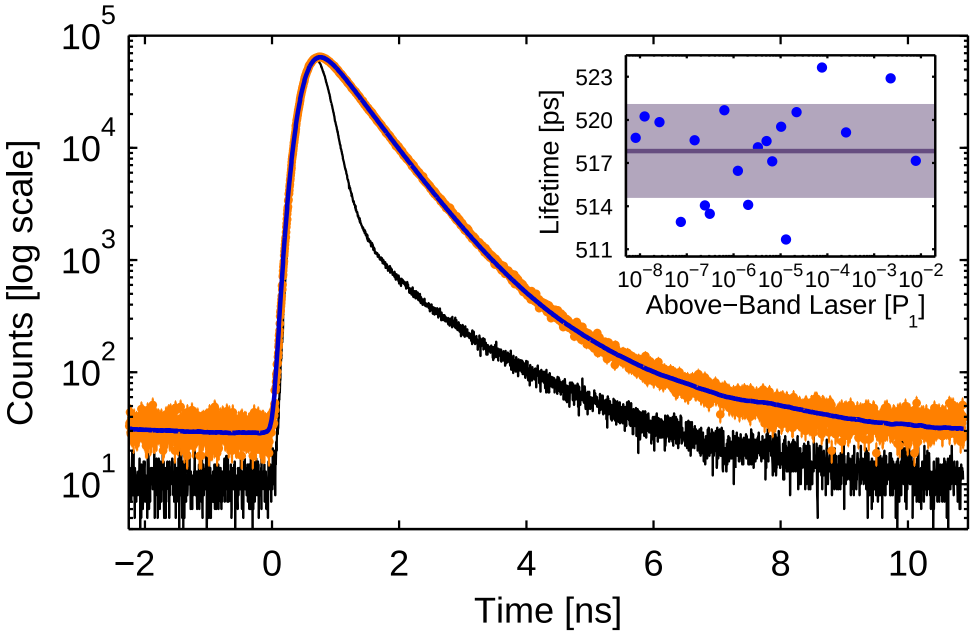

FIGURE 3.2: (Color online) Time-resolved fluorescence from a single QD under pulsed resonant excitation and without above-band excitation. The data (orange dots) are fit by an exponential decay model convolved with the measured instrument response function of the SPCM (black curve). The blue curve is the convolved result. The inset shows the lifetimes extracted from similar time-resolved fluorescence measurements with different levels of above-band laser power represented as a fraction of the saturation power $P_1 = 28.5\mu W$. The lifetime varies little with above-band laser power, with an average value of $T_1 = 518 \pm 3$ ps. The average T_1 is depicted by the dark line in the inset, while the gray area is the standard uncertainty range.

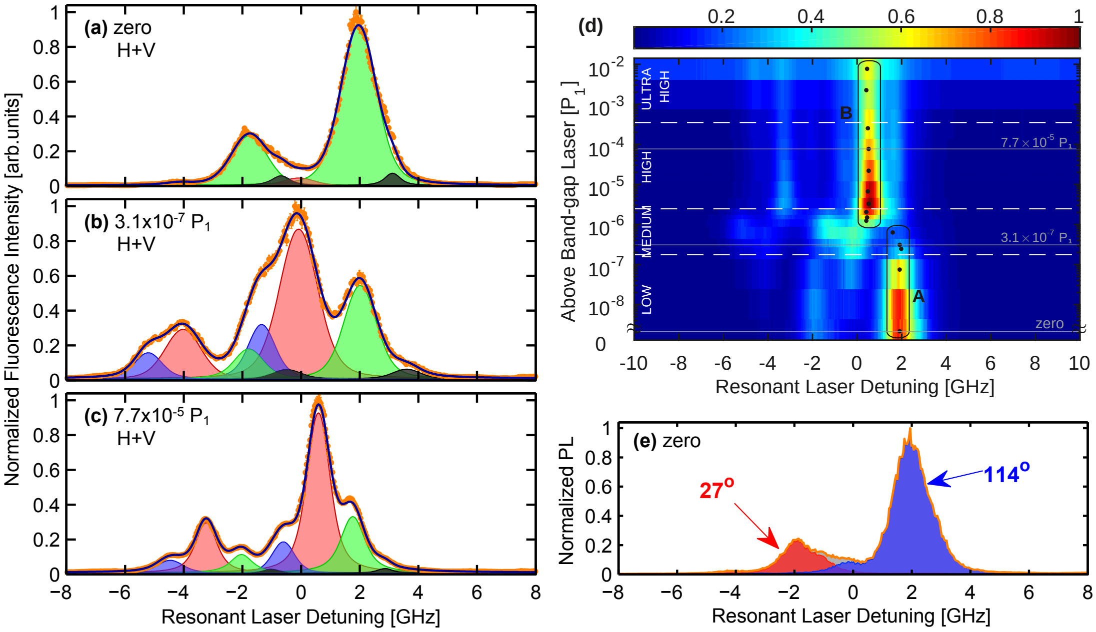

FIGURE 3.3: (Color online) **(a)–(c)** Three examples of normalized resonant photoluminescence excitation spectra (RPLE) at above-band laser powers of zero, 3.1×10^{-7} P$_1$ and 7.7×10^{-5} P$_1$ respectively. The filled curves are the individual Voigt peaks used to do the fitting; the blue curve along the orange data points is the sum of these individual peaks. Zero detuning is defined as the middle point of the two Voigt peaks with largest amplitude (green) in (a), which corresponds to 928.3713 nm. Each curve is normalized to its own maximum. **(d)** 2D plot of 16 RPLE spectra taken at different above-band laser powers plotted in a logarithmic scale on the vertical axis. The color–scaled spectral intensity is normalized to the overall maximum of the measured fluorescence intensity. The grey lines denote the three spectra in (a), (b) and (c). The black dots are the positions where correlation data are collected. Box A denotes the data shown in Fig. 3.5(a) and box B those in Fig. 3.5(b). The white dashed lines indicate the boundaries for the different above-band power regimes. **(e)** An example of polarization-dependent RPLE without above-band laser. Two RPLE spectra were recorded using a linear polarizer oriented at 114° (blue) and 27° (red) from the horizontal. Their sum is displayed as the orange curve with grey filled area. The red and blue peaks are the same shape but displaced and with different amplitudes, which implies that the two peaks are the orthogonally polarized emission from the two fine structure split states of a neutral QD.

restricted to be not less than the lifetime-limited value of 308 MHz in linear frequency according to T_1. Polarization dependent RPLE (Fig. 3.3(e)) suggests that these emission lines are from a neutral QD. Thus, 8 Voigt peaks gives 4 pairs corresponding to four different discrete Stark shifts (including the case where the shift is zero) experienced by the QD during the measurement.

We measured RPLE spectra for a number of QDs, and all those we surveyed showed either 1, 2, or 4 different Stark shifts. These are all powers of 2, which is consistent with an integer number of nearby 2-level charge traps. For example, two charge traps would result in $2^2 = 4$ different configurations. None of the QDs we surveyed showed 3 or 5 Stark shifts. Regarding the QD detailed here, to match the 4 discrete shifts observed in the RPLE data, the only possible trap arrangement is either two 2-level traps or one 4-level trap. Candidates for 2-level traps abound – for example, dopant impurities and other crystal defects – while to the authors' knowledge no 4-level traps have been reported in the literature. Thus we discard the latter possibility and conclude that there are two nearby 2-level charge traps influencing the QD. We denote the first trap as α, the second as β, and the possible trap configurations as $(\alpha\beta)$, where α, β can take a value of 0 or 1 representing the empty (neutral) or occupied (ionized) state of each trap.

In Fig. 3.3(a)–(c), the 8 Voigt peaks are color coded into 4 pairs so that each pair stands for one trap configuration: the green peaks correspond to charge configuration (00), black peaks to configuration (01), blue peaks to configuration (10), and red peaks to configuration (11). Below we discuss the underlying reasoning for the assignment of these labels. There may be additional charge carrier traps far from the QD and randomly distributed, but their influences on the QD energies are limited. Their effect on the RPLE spectra is described by spectral line broadening, which consists of two parts: Gaussian widths of the Voigt profiles for inhomogeneous environmental broadening and additional Lorentzian widths for homogeneous non-radiative broadening. Due to the significant overlapping of multiple peaks in the spectra, the fitting is too ambiguous to distinguish these two sources definitively. But the Voigt line widths of all peaks are broadened by about a factor of 4 compared to the lifetime-limited value. Considering the relatively weak effect on the electric field at the QD from the free charge carriers and distant charge traps, the orientation of the asymmetry axis of the confinement potential of the QD will remain the same for all above-band powers. Therefore the amplitude ratio of the two fine structure peaks in each pair of Voigt profiles is constant for all above-band powers. We perform a global fitting of four spectra from different power regimes simultaneously to determine the ratios. Afterwards, each spectrum is fitted individually with the fixed amplitude ratios.

With no above-band excitation, one pair of peaks dominates the RPLE spectrum (the green peaks in Fig. 3.3(a)) showing that 83% of the time the traps are in the corresponding configuration. Without above-band excitation, the traps are expected to be in thermal equilibrium. If the traps are either shallow donor or acceptor impurities, in bulk GaAs at 5 K the fraction that are ionized is approximately zero. The fraction of ionized dopants near the QD may be increased by the proximity of the wetting layer quasi-continuum states, but it is still expected to be low. Therefore, we assign the neutral trap configuration (00) to the green peaks dominating the spectrum in Fig. 3.3(a).

At high above-band laser power we expect the free charge carrier density to be greater, and the charge traps correspondingly more likely to be charged compared to the case of low above-band power. Therefore, we assign trap configuration (11) to the pair of peaks that dominates the spectrum in Fig. 3.3(c), which is displayed in red. The other two configurations (01) and (10) are arbitrarily assigned to the black peaks which are shifted by about 1 GHz from the green, and to the blue peaks which are shifted by about –3 GHz from the green.

Figure 3.3(d) shows all 16 RPLE spectra at different above-band laser powers which span 6 orders of magnitude. We identify four regimes of above-band power based on the different patterns in the RPLE spectra: low power regime (zero $\sim 1.7\times10^{-7}$ P_1), medium power regime (0.17 $P_1 \sim 2.5\times10^{-6}$ P_1), high power regime (0.025 $P_1 \sim 3.5\times10^{-4}$ P_1) and ultra-high power regime (above 3.5×10^{-4} P_1). Note that even in the high end of the ultra-high power regime the above-band laser is less than 1% of the saturation power.

Figure 3.4(a) shows the best-fit Voigt peak positions of the spectra in Fig. 3.3(d). In the medium power regime, there is a continuous but quick peak shift of about ~1 GHz for trap configurations (11), (01) and (10). This is possibly caused by partial screening of the electric fields of the trapped charges by the free charge carriers introduced by the above-band excitation. Fig. 3.4(b) shows the spectrally integrated RPLE of the QD as a function of above-band laser power. It reaches its maximum value at 1.2×10^{-6} P_1, indicating that the

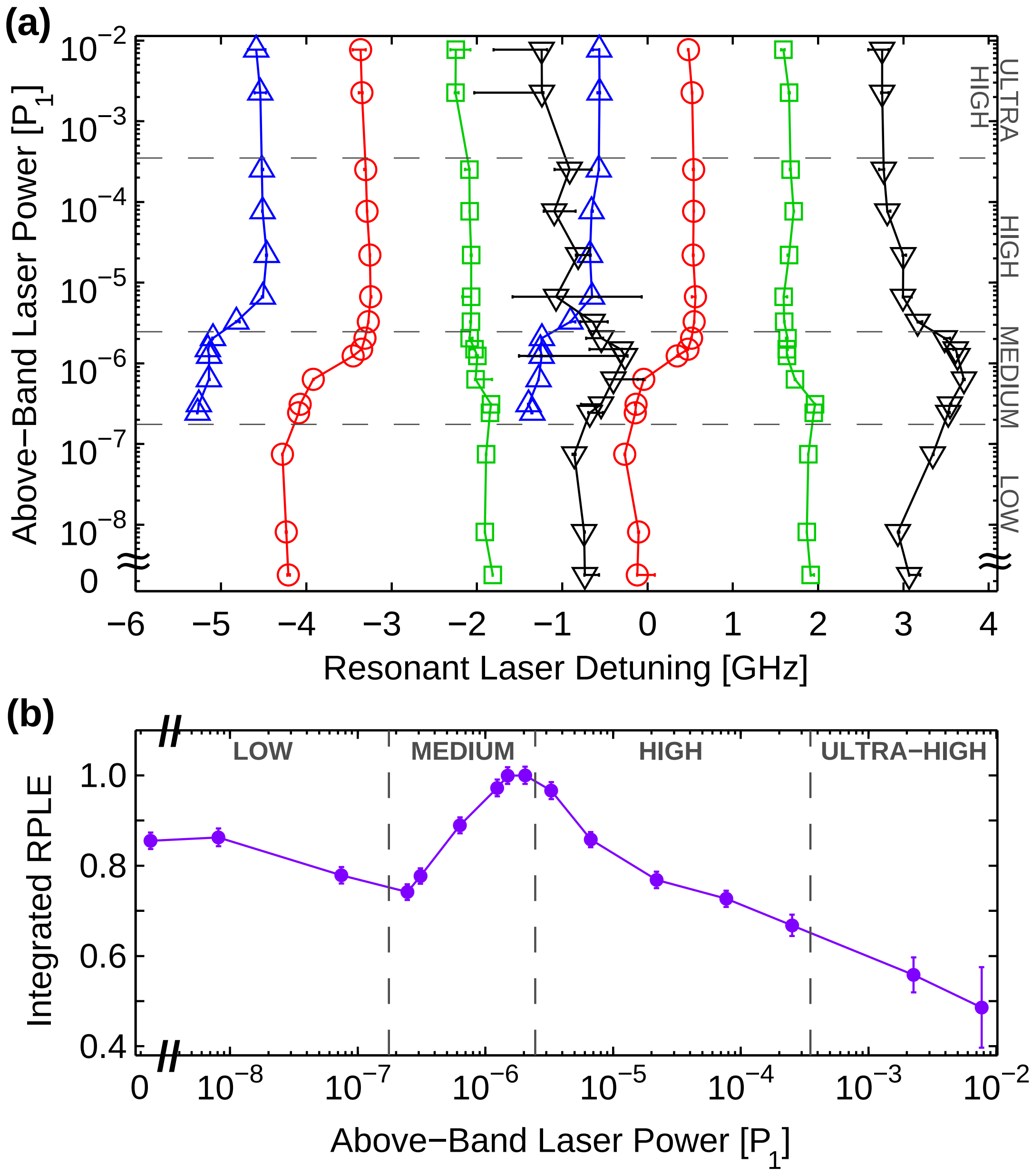

FIGURE 3.4: (Color online) **(a)** Center detunings of resonance peaks. For the RPLE spectra that comprise Fig. 3.3(d), the center detuning of each Voigt profile in the fit is plotted versus the corresponding above-band laser power. The green square curve corresponds to trap configuration (00), the red circle for trap configuration (11), the blue up-triangle for trap configuration (10) and black down-triangle for trap configuration (01). The lines are guides for the eye. The horizontal dashed lines give the boundaries of different above-band power regimes. **(b)** Spectrally integrated intensity of RPLE spectra in Fig. 3.3(d). The baseline offset due to the above-band excitation has been subtracted so that the curve represents the emission solely due to resonant excitation; this effect is only significant in the ultra-high power regime. The error-bars correspond to experimental fluctuation and shot noise. The curve is normalized to its maximum value. The grey vertical dashed lines correspond to the boundaries of different above-band power regimes.

local charge environment around the QD most favors neutral exciton emission (over trion or biexciton emission) at that power. When the above-band laser goes over this threshold, the QD fluorescence starts to decrease, reflecting the fact that more free charge carriers are available for the QD to capture in favor of trion and biexciton emission, which reduces neutral exciton emission. As the data shows, the QD resonant emission is suppressed by a factor of 2 in the ultra-high power regime compared to the maximum emission intensity at medium power.

All the RPLE peaks show a gradual spectral drift from the low power regime to the ultra-high power regime. This is possibly caused by an asymmetric distribution of many distant charge traps that are far from the QD. By investigating the evolution of the green peaks (configuration (00)), we determined the drift to be an approximately 0.6 GHz red-shift. This red-shift happens to follow the same trend of QD energy drift when the local temperature is increased by a small amount, about 0.2 K [81]. However, other dots show a blue-shift of similar amount over the same above-band excitation power range. Therefore, thermal heating by the laser is not sufficient to explain these observations. In addition, a calculation with a simple two-dimensional thermal conductance model with the maximum above-band power used here (thermal conductivity of GaAs at 4 K is 10 W$\cdot$cm$^{-1}\cdot$K^{-1}, and absorption coefficient at 633 nm is 4×10^4 cm^{-1}) shows that the temperature rise would be less than 0.2 mK. This is too small to account for the observed spectral shift.

3.3.3 Correlation Function of Resonance Fluorescence

The RPLE data quantify both the magnitude of the Stark shifts experienced by the QD and the time-averaged occupation probability of the charge traps that cause them. The time-dependent behavior of the charge traps can be characterized by the photon statistics of the resonance fluorescence. When the resonant laser is tuned to one of the peaks in the RPLE spectrum, the QD will emit strong fluorescence. If a nearby charge trap switches from unoccupied to occupied, or vice versa, the QD resonance will shift and the fluorescence intensity will be reduced. This effect manifests as bunching in the second-order correlation function of the fluorescence, $g^{(2)}(\tau)$, on the time scale of the trap switching rate.

Another effect that manifests as bunching in $g^{(2)}(\tau)$ is charging of the QD. In contrast with QDs in a diode structure [82–84], here the charge state of the

QD in the sample is uncontrolled, and the QD may capture a charge from the environment. The resonant laser is tuned to the neutral exciton transition and when the QD is charged that transition is not available. Thus, when the QD is charged there will be no resonance fluorescence. The charged QD may capture another charge of the opposite polarity from the environment, forming an exciton and returning to a neutral condition. Thus the QD may switch between charged and neutral states, emitting resonance fluorescence while neutral and no fluorescence while charged. Therefore, the emitted photons will be bunched on a time-scale similar to the time it takes the QD to capture a charge.

Figure 3.5(a) and Figure 3.5(b) show how $g^{(2)}(\tau)$ is affected by the variations of the environmental free charge carrier density introduced by the above-band laser. All correlation data are normalized to the long time value at 0.2 seconds and plotted on a logarithmic time scale so both the short-time and long-time behavior can be clearly seen. All data show a clear dip near $\tau = 0$ and an exponential decay at longer times down to an asymptotic value. In a linear-log plot, an exponential decay is characterized by a high plateau followed by a sharp decay at the characteristic time of the exponential, finishing with another lower plateau. The dip is a sign of antibunching, and the decay is a sign of bunching, with the height of the plateau at intermediate τ values indicating the degree of bunching. Correlation functions like this indicate that on short time scales the emitted photons are antibunched (*i.e.* two photons are unlikely to be emitted within one lifetime), but that on long time scales the photon stream is separated into bunches. The antibunching is expected of emission from a single QD, and the bunching indicates that there are phenomena that cause the QD to intermittently stop being excited by the resonant laser. Due to the finite response time of the detectors ($\sim$0.8 ns), the bunching plateau is convolved with the anti-bunching dip to result in the measured $g^{(2)}(0) \geq 1$. This observation is further supported by the fact that a higher bunching plateau accompanies a larger $g^{(2)}(0)$ value. All $g^{(2)}(\tau)$ data presented here show not a single exponential decay, but multiple exponential decays with different characteristic times (10^{-7} s $\sim 10^{-2}$ s). These decays probably originate from both the charging of the QD and the fluctuation of the charge configuration of nearby traps, as discussed above.

To obtain the maximum signal-to-noise ratio in $g^{(2)}(\tau)$, we followed the brightest peak position in the RPLE map to collect the correlation data; the

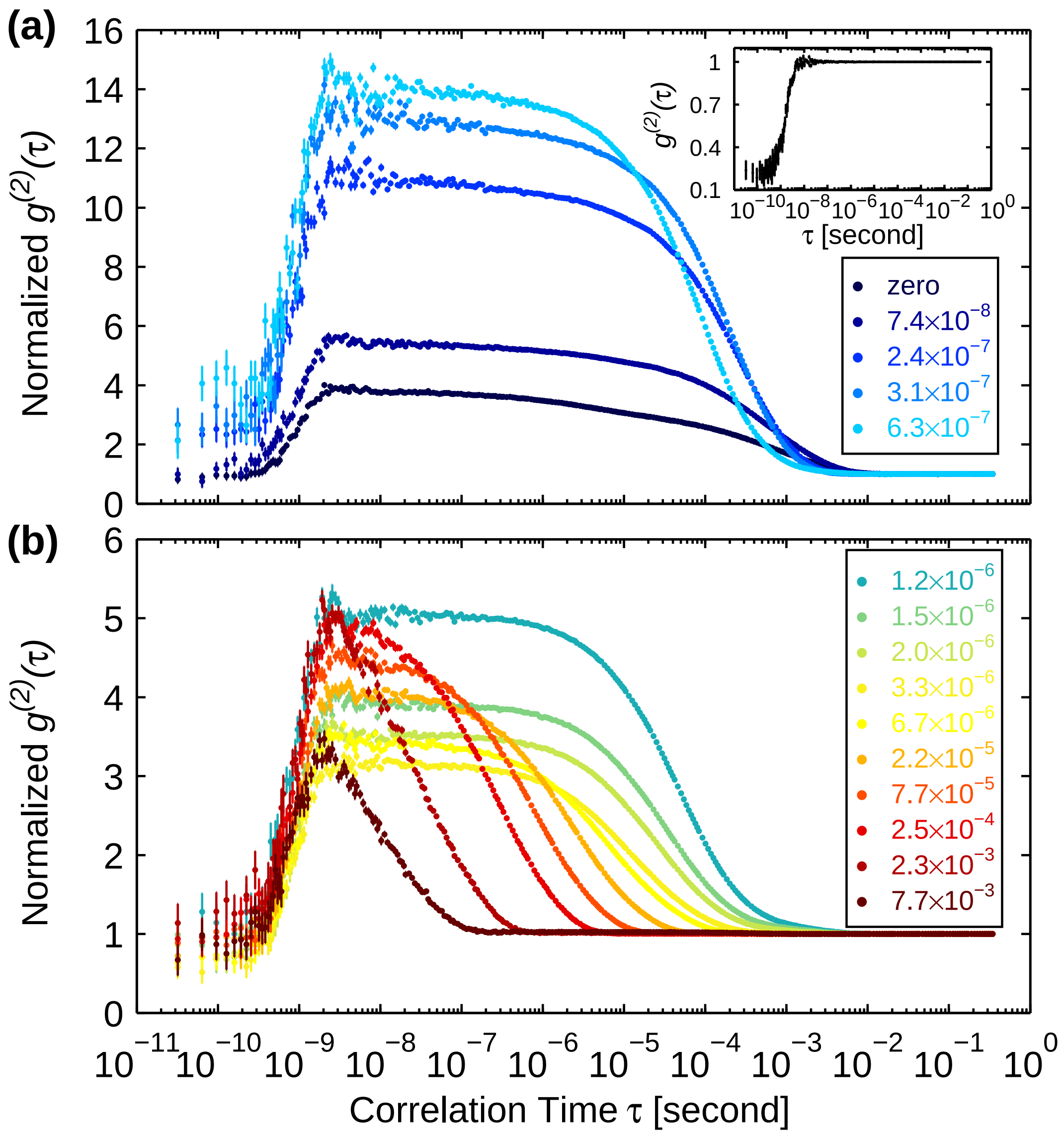

FIGURE 3.5: (Color online) Second-order correlation function of the fluorescence, $g^{(2)}(\tau)$. The legends list the above-band laser power in fractions of the saturation power P_1. **(a)** The $g^{(2)}(\tau)$ measured at the black dots in box A in Fig. 3.3(d). The resonant laser is tuned to $\sim$1.96 GHz detuning with power of 0.1 P_0 and the above-band laser power is varied from zero to 6.32×10^{-7} P_1. A significant increase of bunching amplitude and small shrinking of bunching time can be seen. The inset is the correlation data measured with only above band-gap laser excitation at 0.23 P_1. **(b)** The $g^{(2)}(\tau)$ from box B in Fig. 3.3(d). The resonant laser is at $\sim$0.56 GHz detuning with a power of 0.1 P_0. The power of above-band laser is varied from 1.24×10^{-6} P_1 to 7.69×10^{-3} P_1.

points of collection are marked by black dots in Fig. 3.3(d). Figure 3.5(a) shows the $g^{(2)}(\tau)$ results measured at the points in box A and Fig. 3.5(b) for those from box B. According to the fits to the RPLE data, when recording the correlations in Figs. 3.5(a) and 3.5(b) the resonant laser is mostly exciting the high energy peak of the fine structure doublet for either trap configuration (00) for box A or trap configuration (11) for box B.

As the above-band laser power increases, the bunching amplitude in Fig. 3.5(a) increases monotonically up to 14 due to the decrease of the probability of trap configuration (00) as indicated by the decreasing of fluorescence in Fig. 3.3(d). Bunching means that the overall emission is grouped into clumps of photons, and there is a dearth of photons between the bunches. An increase of the bunching amplitude reflects a reduction in the relative probability of detecting two photons separated by a long time interval. This indicates that the QD is turned into an “off" state or low count-rate state more frequently. If the QD turns “off" more frequently, it reduces the number of photon pairs with a long separation interval compared to those with a short separation interval. This unbalanced change leads to an increase of the relative probability to find a photon pair with a short separation interval, *i.e.* the increase of the $g^{(2)}(\tau)$ bunching amplitude. Pronounced intensity fluctuation (high bunching level) for the medium power regime in both Figs. 3.5(a) and 3.5(b) is associated with accelerated transitions between the different charge trap configurations. This leads to strong intensity fluctuations of the PL that monitors one of the particular configurations, *e.g.*, the (00) state for Fig. 3.5(a) and the (11) state for Fig. 3.5(b). This acceleration is reflected in the shortening of the characteristic decay time of the bunching in $g^{(2)}(\tau)$, from 10 ms to 1 ms for Fig. 3.5(a) and from a few milliseconds to a few microseconds for Fig. 3.5(b) up to the top of the high power regime.

In contrast to the decay time, in this power range (1.2×10^{-6} P_1 $\sim$ 2.5×10^{-4} P_1) the bunching amplitude shows a non-monotonic behavior. First it decreases from 5 to 3 when the above-band power increases up to 3.3×10^{-6} P_1, then it rises back up to 5 at 2.5×10^{-4} P_1, and finally it decreases again. The first decrease is due to the increasing probability for the traps to be in configuration (11), which is the charge configuration with which the laser is in resonance. In fact, an increase in PL at the same above-band power in the RPLE spectra gives a direct support for this argument; see Fig. 3.3(d). The following increase of bunching amplitude is associated with decrease of time-averaged total PL (Fig. 3.4(b)) in the same power range: the QD starts to capture another charge, and the neutral exciton emission becomes less favored while trion or biexciton population get correspondingly increased.

Fluorescence from the trion and biexciton are filtered out by the monochromator, and so do not contribute to the measured correlation. Therefore, one would expect a greater bunching amplitude for a higher above-band power. However, the opposite trend is observed in Fig. 3.5(b) when the above-band power is more than 2.5×10^{-4} P_1. It seems that the anti-bunching dip prevents the bunching amplitude from increasing further at short time scales. Physically this is because there are rarely photon pairs with time interval shorter than the lifetime of the QD. If the lifetime of the QD was shorter, one would expect the bunching amplitude to continue rising. In addition, the high density of free charge carriers in the ultra-high power regime enables both the QD and other sources (*e.g.*, the continuum tail of wetting layer defect states) to emit photons without resonant excitation. These extra photons would fill the gaps between the bunching of the resonant-excited-QD emitted photons, leading to a slight decrease of the anti-bunching dip depth and a decrease of the bunching amplitude.

As a comparison, we did a similar correlation measurement with only above band-gap excitation and found that there is no bunching at all for all the excitation powers used from 7.0×10^{-3} P_1 to 6.3 P_1 and the inset of Fig. 3.5(a) gives one example of those measurements at 0.23 P_1. Although that excitation power is far above the threshold for obtaining emitters aside from the QD, a well-defined anti-bunching dip down to 0.2 is still present. It is possible that the decrease of the dip depth in the resonantly excited correlations in Fig. 3.5(a) is mostly due to the finite response time of the detectors rather than simultaneous photons from multiple sources. Thus the resonantly excited QD even including its environment as a whole would still be a good single photon source at this point.

We note that several essential studies on closely related topics were published in the past few years, such as quantum dot charging [40] and nearby charge trap dynamics [39]. A brief summary of those works and a comparison to our study are provided here. The QD studied by Nguyen *et al.* [40] has an above band excitation saturation power of 30 μW, which is consistent with our value of 28.5 μW. They also note that their QD emits no resonance fluorescence without a particular very small amount of above-band laser power. This is similar in kind if not degree to our observation that the resonance fluorescence is a maximum with a non-zero above-band laser power. Without above-band excitation, Ngugen *et al.* extract a charge trap ionization and neutralization rate on the order of 10^4 s^{-1} while our results show a large range of bunching decay rates from 10^3 s^{-1} to 10^5 s^{-1}. This difference is probably due to the fact that our QD can emit resonance fluorescence without above-band excitation, leading to a $g^{(2)}(\tau)$ measuring both effects of QD ionization and charge trap dynamics. Nevertheless, this rate range is consistent with the study by Arnold *et al.* [39], where the trap loading/unloading rate varies from 4×10^3 s^{-1}to 6×10^4 s^{-1}, although their QD shows much larger discrete Stark shift (∼18 GHz) indicating either a much larger QD dipole moment or a much closer charge trap. Nguyen *et al.* also extracted a QD charging rate of $\sim10^4$ s^{-1} at low above band power (0.01 nW), and of 10^7 s^{-1} at high above-band power (230 nW). Correspondingly at the same above-band power, our transition rate is $\sim10^4$ s^{-1} at 6.3×10^{-7} P_1 and $\sim10^8$ s^{-1} at 7.7×10^{-3} P_1. This is a difference of one order of magnitude at high above band power, which can be understood by noticing that our QD experiences two sources of fluctuation, charging of QD itself and ionization of nearby charge traps, while Nguyen's QD only experiences the former one. Thus, the fluctuation of nearby charge traps increases the bunching decay rate. From Arnold's study, the transition rate of the charge trap is found to be $\sim1.6\times10^6$ s^{-1} for resonant excitation at 230 nW. This value is too low to explain the rate difference between our study and Nguyen's study at high above band power. But it is possible that this number would be significantly higher when using above-band excitation rather than below band gap resonant excitation, and thus bridging the difference. Qualitatively, our $g^{(2)}(\tau)$ bunching decay rate shows a linear relationship with the above-band excitation power, which is consistent with the results of both Nguyen *et al.* and Arnold *et al.*. There the extracted transition rate is proportional to either the above-band power or the square root of the power, but at the powers of interest here the larger linear term dominates if all effects are present in the data. Two other works observing discrete Stark shifts are Houel *et al.* [34] using differential reflection spectroscopy and Hauck *et al.* [85] using differential transmission spectroscopy. Both studied a sample with a Schottky diode structure that is different from ours, but the values of the discrete shifts are close to those presented here. Moreover, their interpretation of the phenomenon involves charges trapped around the QD with a distance of ∼100 nm [34] or ∼30 nm [85], which is close to the result of our calculation shown in the next section.

3.4 Possible Trap Locations

A change in the local electric field such as that produced by a nearby charge trap will shift the resonance frequency of the neutral exciton via the quantum confined Stark effect. Knowing the Stark shifts experienced by the QD allows us to calculate the possible positions of the charge traps. The shift as a function of the change in local electric field, $\Delta \mathbf{F}$, is:

$$\Delta\nu = (-\mathbf{p}\cdot\Delta\mathbf{F} - (\beta\Delta\mathbf{F})\cdot\Delta\mathbf{F})/h \tag{3.1}$$

where $\mathbf{p}$ is the permanent static dipole moment of the exciton in the QD, and β is its polarizability tensor [86]. Here we use typical values for the dipole moment [85] and polarizability [37] of self-assembled InAs QDs: $\mathbf{p} = e \times (0.2\text{nm})\hat{z}$, and $\beta_{xx} = \beta_{yy} = \beta = 4\ \mu\text{eV}/(\text{kV}/\text{cm})^2$. The polarizability is not isotropic because the QD is not spherically symmetric. Given the QD's pancake-like shape it has negligible polarizability in the z-direction, $\beta_{zz} = 0$. From these symmetry considerations, Eqn. 3.1 reduces to

$$\Delta\nu = (-p\Delta F_z - \beta(\Delta F_x^2 + \Delta F_y^2))/h \tag{3.2}$$

The change in electric field produced at the QD location by a single charge at relative position $\mathbf{r}_i$ is:

$$\Delta\mathbf{F}_i = \frac{1}{4\pi\epsilon_0\epsilon_r}\frac{-q_i}{r_i^2}\hat{\mathbf{r}}_i \tag{3.3}$$

where q_i is the charge, and $\epsilon_r = 13.1$ is the dielectric constant of GaAs.

By fitting the data in Fig. 3.3(a) we obtain 4 different values of the Stark shift, which we attribute to the 4 possible charge configurations of 2 nearby charge traps. We assume the charge configuration that is most likely with zero above-band laser power corresponds to the equilibrium configuration, (00), where both charge traps are neutral. We define the corresponding Stark shift to be zero:

$\Delta\nu_0 = 0$ GHz. The other three Stark shifts are:

$$\begin{aligned}\Delta\nu_1 &= -3.3607\,\text{GHz}\,(+0.0201/-0.0064\,\text{GHz})\\ \Delta\nu_2 &= +1.1189\,\text{GHz}\,(+0.1064/-0.0028\,\text{GHz})\\ \Delta\nu_3 &= -2.2145\,\text{GHz}\,(+0.1054/-0.0053\,\text{GHz})\end{aligned} \tag{3.4}$$

where $\Delta\nu_1$ corresponds to configuration (10), $\Delta\nu_2$ corresponds to configuration (01), and $\Delta\nu_3$ corresponds to configuration (11). We make the assignment of $\Delta\nu_3$ to the doubly charged configuration because it corresponds to the predominant fluorescence peak at high above-band laser power. Both traps being charged is the most likely configuration when the above-band laser is producing many free charges that may be captured by the traps.

We can combine Eqns. 3.2 and 3.3 to determine the possible positions $\mathbf{r}_i$ that are consistent with the known values $\Delta\nu_i$ of the resonance shift. For a single charge trap this results in an equation that relates the distance r_i between the QD and the trap to the polar angle θ_i between the $\hat{z}$-axis and the vector $\mathbf{r}_i$:

$$\Delta\nu_i = \frac{pkq_i}{hr_i^2}\cos\theta_i - \frac{\beta k^2 e^2}{hr_i^4}\sin^2\theta_i \tag{3.5}$$

where $k \equiv 1/(4\pi\epsilon_0\epsilon_r)$ and q_i is the charge of the trap when ionized. Since the RPLE data cannot distinguish the polarity of the traps when they are charged, we do not know the sign of q_i. Thus, we consider both the case where the charged trap is positive $(q_i > 0)$ and the case where it is negative $(q_i < 0)$. Using the values and confidence intervals of $\Delta\nu_1$ and $\Delta\nu_2$ and Eqn. 3.5 we can determine the sets of possible values (r_1, θ_1) and (r_2, θ_2). Each set of possible positions defines an azimuthally symmetric volume in the space around the QD. Figure 3.6 shows colored areas which are cross-sections through these volumes for both possible polarities (red = positive; blue = negative) of trap α (solid lines) and trap β (dashed lines); a schematic of a typical 20 nm diameter QD is shown at the origin.

From Fig. 3.6 we can see that to cause the measured Stark shifts, a charge trap must be less than 70 nm away from the QD, which is relatively close: less than four QD diameters. Thus, any charge trap located at the DBR interfaces or surface is too far away to cause these discrete spectral shifts. Two charge traps within a spherical volume of radius 70 nm is consistent with the typical unintentional doping concentration of 10^{15} cm^{-3} for GaAs grown by molecular beam

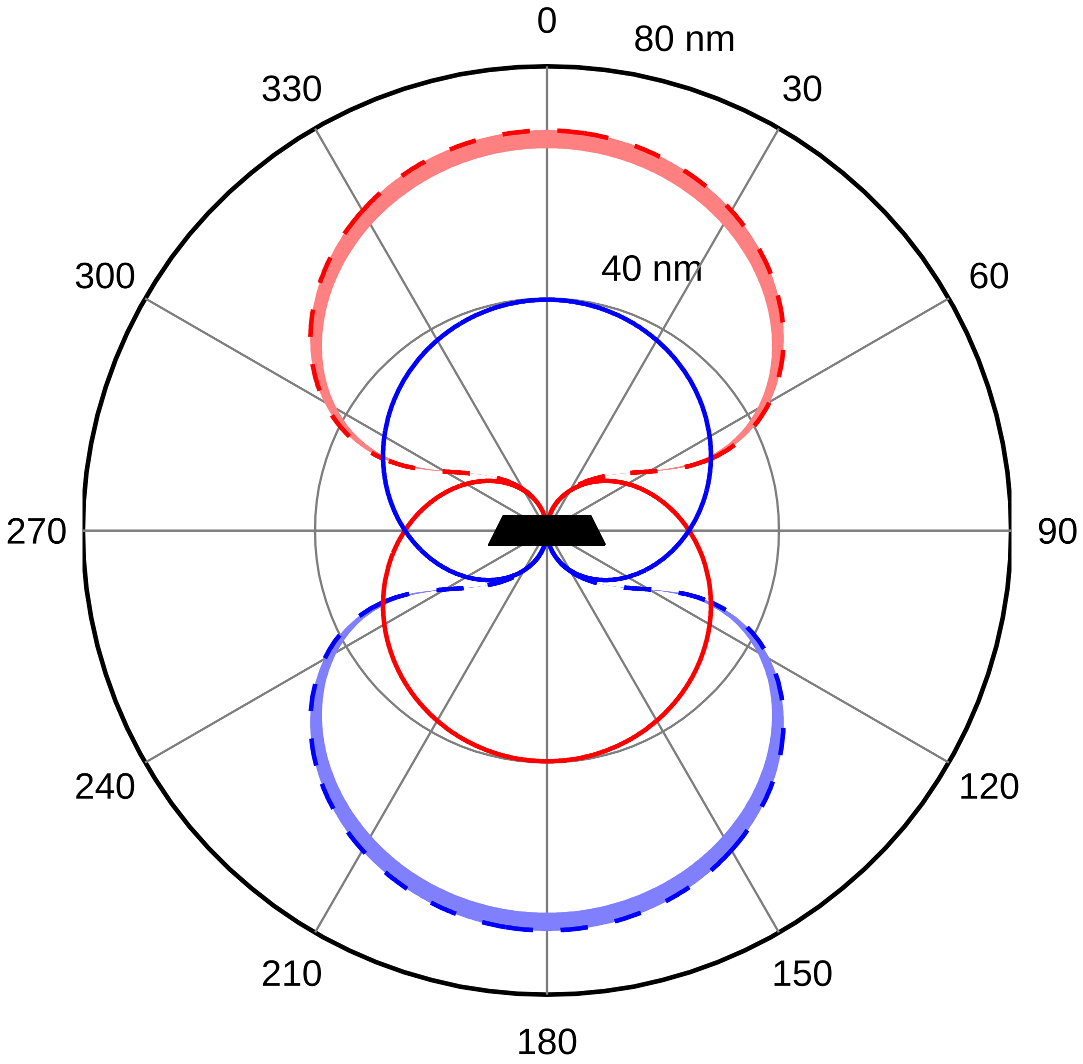

FIGURE 3.6: (Color online) Possible charge trap locations consistent with the measured Stark shifts. Red and blue correspond to positive and negative trap polarity, respectively; the QD is represented schematically at the origin. The solid lines are for trap α; the dashed lines are for trap β. The shaded regions denote locations consistent with the confidence range of $\Delta\nu_2$; the confidence range of $\Delta\nu_1$ is small enough that the corresponding region is hidden by the solid lines.

epitaxy. Notice that trap β must be either above or below the plane of the QD, depending on its polarity, while trap α could be above or below the QD plane regardless of its polarity. The separation between the resonantly excited QD and trap α is 30.6 nm if the trap is in the wetting layer (see Fig. 3.6). For comparison, in a sample with a high-density of self-assembled QDs [87] ($\sim 9.5\times10^9$ cm^{-2}), the average dot-to-dot distance is about 103 nm, which is not much larger than the separation between the QD and trap α if it is in the wetting layer plane. Thus it is possible that trap α is another QD; however, this neighboring QD would be constrained to have only two charge states to be consistent with the RPLE data. Regardless of the identity of trap α, trap β cannot be another QD.

3.5 Conclusion

Resonant excitation spectroscopy successfully characterizes the local electric environment of the QD by providing detailed information about the number of nearby charge traps, their distances from the QD and their time-averaged occupation probability. Combined with weak above band-gap excitation below the level required to produce photoluminescence, the evolution of the local environment with respect to different densities of free charge carriers was studied, and we found that to achieve the maximum of total PL from the QD, a small amount of above-band excitation is required (Fig. 3.4(b)). This is similar to previous work on resonantly excited QDs [39–41, 88, 89], but here the behavior is more complicated. For the QD used in this study, the data indicate that there are two nearby charge traps within 70 nm. Their exact locations depend on the polarity of the trap when ionized, which the current measurement techniques are unable to determine.

Correlation measurements give information about the time-scale of switching from neutral to charged for both the traps and the QD. As the above-band excitation laser increases the density of free charge carriers, the time-scale of the charge trap dynamics speeds up, decreasing the switching time, which is reflected in the decay time-scale of the correlation bunching amplitude of resonantly excited fluorescence. This time-scale spans five orders of magnitude from 10^{-2} s to 10^{-8} s. Given the very long time-scales of bunching with zero or low above-band laser power, it is possible that many previous experiments did not recognize that the resonance fluorescence was bunched. We also note that the fastest bunching decay time of 10^{-8} s is only one order of magnitude longer than the anti-bunching time of about 10^{-9} s. In that case, the equivalent photon stream would be bunches of fewer than 10 photons, and long stretches of time with no emission between the bunches.

The combined techniques of resonant excitation spectroscopy and resonant fluorescence correlation can determine many details of the local charge environment of a single QD. The QD chosen for this work exhibits multiple spectral behaviors: discrete spectral jumps, continuous spectral shift, and spectral diffusion. These behaviors have been observed before by others, but the techniques demonstrated here allow quantitative investigation of the details. A QD that may be a suitable source of indistinguishable photons can be investigated using the same techniques to determine its potential.

Chapter 4

Charge Dynamics of Single InAs Quantum Dots Under Resonant and Above-Band Excitation

4.1 Introduction

In this chapter we investigate the charging dynamics in epitaxially grown InAs quantum dots under resonant excitation with and without additional low-power above-band excitation. Time-resolved resonance fluorescence from a charged exciton (trion) transition is recorded as the above-band excitation is modulated on and off. The fluorescence intensity varies as the QD changes from charged to neutral and back due to the influence of the above-band excitation. We fit the transients of the time-resolved resonance fluorescence with models that represent the charging and neutralization processes. The time dependence of the transients indicate that Auger recombination of resonantly excited trions is largely responsible for neutralization of the charged state when the above-band excitation is off. The addition of above-band excitation revives the resonance fluorescence signal from the trion transition.

We conclude that the above-band laser excites charges that relax into the bound state of the quantum dot via two different charge transport processes. The captured charges return the QD to its initial charge state and allow resonant excitation of the trion transition. The time dependence of one charge transport process is consistent with ballistic transport of charge carriers excited non-local to the QD via above-band excitation. We attribute the second charge transport process to carrier migration through a stochastic collection of weakly-binding sites, resulting in sub-diffusion-like dynamics.

Sources of single, indistinguishable photons are a promising candidate for implementation of quantum information protocols [63, 65–67, 90]. Semiconductor quantum dots (QDs) can act as sources of single photons to be utilized in these protocols, but certain experimental factors can complicate their single photon emission. Spectral diffusion broadens the emission line shape [33], and in samples without independent electrical control of the QD charge, blinking occurs when the QD changes charge state [40, 91–93]. Even with electrical control of the QD charge, Auger recombination from the trion state may neutralize the dot [94]. Resonant excitation of either a neutral or charged QD can cause a transition to the opposite charge state, which greatly diminishes the time-averaged fluorescence and reduces a dot's suitability to act as an efficient photon source [40, 95, 96]. A counter to this effect is the application of a low-power above-band-gap laser that supplies the local charge environment with extra charge carriers [40, 97]. These charge carriers can be captured by either a charged QD, resulting in neutralization and allowing resonant excitation of the exciton state, or by a neutral QD, allowing resonant excitation of the trion state. The exact processes by which the above-band excited carriers arrive in the QD is so far uncertain. Understanding those processes will inform the design of future QD-based sources of single photons.

Here we investigate the charge dynamics of a QD under both resonant and above-band excitation. We measure the rise and fall of the fluorescence of a resonantly excited trion transition as the above-band laser is turned on and off. We characterize the time-dependent dynamics as a function of the two excitation powers using two models that describe the time evolution of the fluorescence after the above-band laser either turns on or turns off. We conclude that Auger recombination is the primary mechanism by which the QD becomes neutralized, by which we mean it changes from a charged state (e.g. the trion or a single bound charge) to a neutral state (e.g. the exciton, biexciton, or the empty QD). After such a neutralization event, the resonance fluorescence is absent and the QD remains neutral until it captures another charge. The time dependence of the fluorescence rise and decay indicate that there are at least two processes that provide charge carriers to be captured by the QD. One is ballistic super-diffusion of hot carriers generated near the surface of the sample by the above-band laser. The other is sub-diffusion of carriers through a stochastic collection of weakly-binding transport sites which are likely an ensemble of shallow states in the semiconductor.

4.2 Experimental Configuration

Our sample consists of epitaxially grown self-assembled InAs QDs embedded in the GaAs spacer of a planar microcavity defined by two distributed Bragg reflectors (DBRs). The resonant excitation laser is focused into the waveguide mode of the microcavity from the side and the fluorescence is collected normal to the sample surface, perpendicular to the resonant excitation direction, which minimizes collection of laser scattering [38, 98, 99]. The above-band excitation is provided by a helium-neon laser with a wavelength of 632 nm that is focused onto the QD normal to the sample surface and confocal with the resonance fluorescence collection path. The above-band excitation power used throughout is too low to cause any detectable fluorescence on its own. Only when the resonant and above-band lasers are both on does the QD emit fluorescence. The above-band excitation is modulated with an acousto-optic modulator (AOM) while the resonant laser intensity remains constant. The above-band light is filtered from the fluorescence via a dichroic mirror, long-pass filters, and a spectrometer. Ultimately, the fluorescence is incident on a silicon-based avalanche photodiode capable of detecting single photons with a time resolution of approximately 500 ps. The photon arrival times are then recorded via a time-correlated single-photon counting module (TCSPC). The voltage signal used to modulate the AOM is also used to create a trigger sent to the TCSPC. The time-resolved fluorescence can then be constructed as a histogram of the photon arrival times relative to the preceding modulation trigger. A diagram of the experimental setup is shown in Fig. 4.1.

4.3 Data Acquisition

We demonstrate that the QD transition probed is that of a trion (a charged exciton) by measuring the resonant excitation spectrum. The resonant laser is scanned over the transition wavelength and the intensity is recorded. The spectrum is shown in the inset of Fig. 4.2(a). The single peak indicates that the state is a trion; a neutral exciton would have a double peak. The QD was chosen because it did not show discrete shifts of its transition energy as the above-band laser

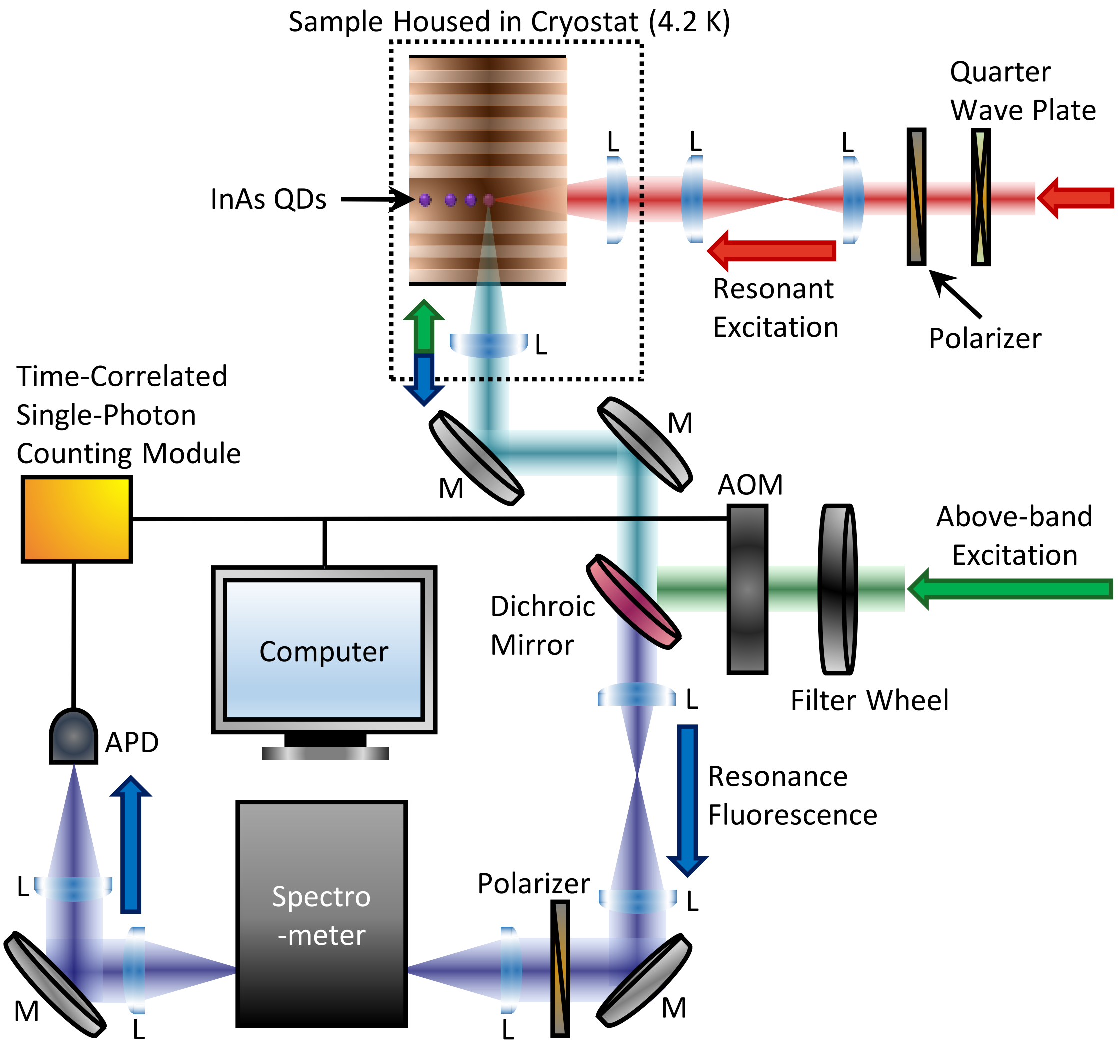

FIGURE 4.1: A schematic of the experimental setup. The sample is housed in a cryostat kept at approximately 4.2 K. The red path depicts resonant excitation, the green above-band excitation, the blue resonance fluorescence, and the cyan where the above-band excitation and resonance fluorescence overlap in the confocal optical path. M-mirror, L-lens, AOM-acousto-optical modulator, APD-avalanche photodiode.

power was varied [34, 91]. This criteria is necessary so that the time-resolved resonance fluorescence intensity measurements are not confounded by spectral shifts, and only probe the charge state of the QD.

Without the above-band excitation, the fluorescence signal is negligibly small despite constant resonant excitation. When the above-band laser is turned on, the fluorescence signal increases asymptotically to a steady state value. When the above-band laser is turned off, the fluorescence signal decreases asymptotically to zero. Figure 4.2(a) shows typical time-resolved resonance fluorescence data for a given power of both above-band and resonant excitation. The time scale for the system to reach steady state is on the order of hundreds of microseconds for the rise transient after the above-band excitation is turned on, and tens to hundreds of microseconds for the fall transient after the above-band excitation is turned off. Time-resolved fluorescence was recorded for multiple different powers of both the resonant and above-band lasers. In all cases the above-band power was too weak to cause fluorescence on its own. The laser powers spanned approximately two orders of magnitude, defining a two-dimensional acquisition space. The rise and fall sections of the example data in Fig. 4.2(a) are shown separately in Figs. 4.2(b-c), respectively, using a log-log scale to illustrate the short-time dynamics. The models discussed below fit the data well at all time scales and particular model curves are shown on top of the data in Figs. 4.2 (a-c).

4.4 Analysis

The models we use involve the shaped exponential function, $e^{-(\alpha t)^{\beta}}$, which fits well a large variety of relaxation phenomena in complex condensed-matter systems [100–105]. When $0 < \beta < 1$, the above mathematical form is referred to as a stretched exponential, whereas when $1 < \beta < 2$ it's referred to as a compressed exponential. The time-resolved fluorescence intensity is fit with either the sum of a normal and a stretched exponential (for the fall), or the numerical solution of a differential equation containing capture rates that saturate with stretched and compressed exponential time dependencies (for the rise). The details of the models are discussed below. We extract the model parameters and discuss their dependencies on laser power. Throughout this letter we will refer to α as a scale parameter and β as a shape parameter.

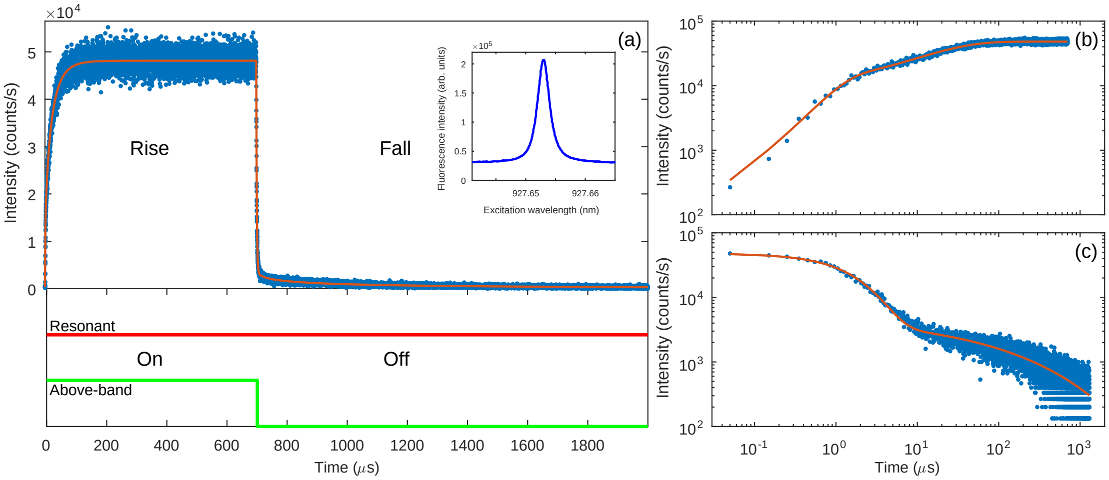

FIGURE 4.2: (a) Typical time-resolved resonance fluorescence. For the displayed data the resonant excitation power is 2.5 μW, while the above-band power is 0.27 μW. The orange line is the fit to the data. Below, the green line indicates when the above-band excitation power is on and off. The red line indicates the resonant excitation power, which is always on. The inset shows the excitation spectrum of the trion transition of the QD. (b) A fit to the rise section on a log-log scale. (c) A fit to the fall section on a log-log scale.

The stretched exponential $(0 < \beta < 1)$ has been sporadically used for over 160 years to explain relaxation phenomenon in condensed matter systems. The first known instance was carried out by the physicist Rudolf Kohlrausch to explain relaxation of residual charge from a glass Leiden jar [106]. The shaped exponential has mostly been used as a phenomenological fit and there has been much difficulty in applying direct physical connections to the scale and shape parameters α and β. Despite the difficulty in making clear physical correlations to the parameters, there has been some headway for the development of a physical model that explains the shaped exponential behavior in the solid state. Klafter *et al.* illustrated three different physical approaches that result in stretched exponential charge transfer in the solid state [103]. The similarity between the models presented by Klafter *et al.* shows that either multiple different pathways into a trap or multiple different pathways out of a trap are required. Random numbers and physical shapes of the pathways for charges to migrate through, due to being part of a stochastic environment, seem paramount for the emergence of stretched exponential relaxation. Migration through such a stochastic environment results in slower than exponential relaxation via this channel.

In 2003, Sturman *et al.* described how stretched exponential relaxation in the solid state can result from charge carriers migrating through an environment of stochastically distributed transport sites before ultimately relaxing into a trap [107]. For clarity we briefly summarize their results here. Consider an environment containing a stochastic distribution of many weakly-binding potential wells called transport sites plus a few strongly-binding potential wells called traps. From an initial transport site, a charge carrier will naturally have a higher probability to hop to closer transport sites as opposed to farther ones, defining random pathways through which charge carriers will likely migrate. Some of these pathways lead to transport sites in the close vicinity of traps, resulting in a significant probability of the charge being captured by the trap. Simulations of such a system show that the process of slow migration through a stochastic environment results in stretched exponential relaxation into the traps; see Ref. [107] for more details. A stretched exponential can be mathematically represented as a linear sum of normal exponentials with a certain weighting function [108]. Due to different relaxation rates associated with different paths through the transport sites, the relaxation is described by a sum of many exponential decays, and more compactly a single stretched exponential term to describe the net process.

The compressed exponential $(1 < \beta < 2)$ has been less widely used to describe charge relaxation in the solid state. However, Ref. [105] gives examples of instances where compressed exponential relaxation in the sold state is observed. The common theme is the presence of an external driving force resulting in faster than exponential relaxation. Morishita describes compressed exponential relaxation dynamics in liquid silicon above 1200 K [109]. He attributes the compressed exponential relaxation to ballistic-like motion of high-energy carriers, similar to the material described by Bouchaud. This type of motion can be described as super-diffusion, due to the associated faster-than-diffusion-like behavior.

In the analysis below we will describe how the shaped exponential growth and decay behavior of the time-resolved fluorescence is consistent with either ballistic transport of carriers or migration through a stochastic distribution of transport sites. We start by discussing the fall section of the fluorescence, depicted in Fig. 2(c), because without the above-band laser the behavior is less complicated.

4.4.1 Fluorescence Fall

At the beginning of the fall section depicted in Fig. 4.2(c) the above-band excitation is turned off and the fluorescence signal decreases asymptotically to zero as the QD becomes neutralized. There is an initial fast decay in the resonance fluorescence followed by a slower decay at long times. The fluorescence intensity data were fit with the sum of a normal exponential and a stretched exponential. The functional form is:

$$I = A_1 e^{-\alpha_1 t} + A_2 e^{-(\alpha_2 t)^{\beta_2}}. \tag{4.1}$$

A_1 and A_2 are amplitudes where $A_1 + A_2$ is the steady-state value of the intensity when the above-band excitation is on, α_1 is a neutralization rate while α_2 is a scale parameter, and the exponent β_2 is a shape parameter.

Figure 4.2(c) shows an example of this model fitting the fall data for a certain pair of laser powers. The fast decay corresponds to the normal exponential term in the fit, while the slower decay corresponds to the stretched exponential term. As described below, the power dependence of the fast decay indicates that it results from Auger recombination of the excited trion state. We attribute the slower decay to recharging of the dot by capture of charge carriers from a reservoir whose own population is decaying with a stretched exponential dependence.

Figure 4.3(a) plots the neutralization rate α_1 versus resonant laser power, and it increases sub-linearly with increasing resonant power. Its power dependence is similar to that of the excited state population of a resonantly excited two-level system, which saturates as the laser power increases. The two-level system in this case is the single-charge/trion system of the charged QD. Since α_1 has a similar saturation behavior, it implies that the rate of the neutralization process represented by the normal exponential is proportional to the trion population in the QD. Such a dependence is consistent with Auger recombination of the trion, which ejects the extra charge carrier and neutralizes the QD. Thus, Auger recombination is responsible for the fast, normal exponential decay. This conclusion is consistent with other experiments that have measured time-dependent charge state dynamics [94, 97]. The values of α_1 in Fig. 4.3(a) are fit with a saturation curve, $\alpha_1 = (\Gamma_A P)/2(P + P_{\text{sat}})$, where Γ_A is the Auger recombination rate for the trion, P is the resonant laser power, and P_{sat} is the saturation power. We

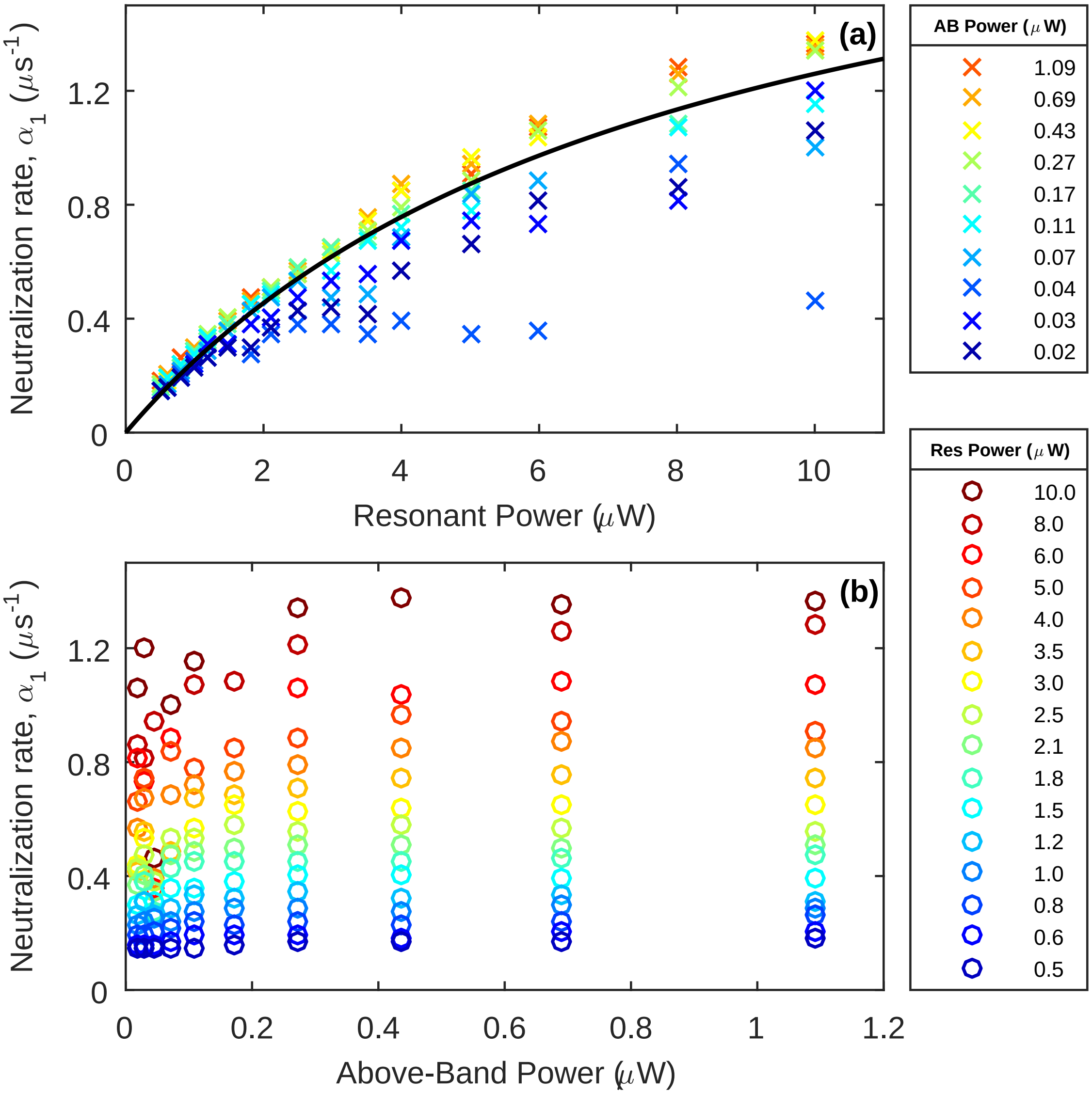

FIGURE 4.3: Fast neutralization rate plotted vs. (a) resonant laser power and (b) above-band laser power. The legends and color specify the power of the excitation laser not represented by the horizontal axis. The saturation curve shown in (a) is the best fit to the entire data set shown. A saturation power of 7.9 ± 1.4 μW and an Auger recombination rate of 2.3 ± 0.2 μs^{-1} was extracted from the fit.

obtained a saturation power of 7.9 ± 1.4 μW and an Auger recombination rate of 2.3 ± 0.2 μs^{-1}, which is in very close agreement to the value of 2.3 μs^{-1} found by Kurzmann *et al.* [94] in InAs QDs. We observe little dependence of the Auger recombination rate as a function of above-band power as seen in Fig. 4.3(b).

If Auger recombination was the only process involved in the fluorescence decay, then only one term would be needed in the model. The presence of the additional slow decay implies an additional *recharging* process that weakly counteracts the Auger neutralization of the QD. The recharging process itself must decay with time or the fluorescence would reach a non-zero steady-state value. The stretched exponential time dependence of the slow decay is consistent with the expected decay of charges migrating through a stochastic distribution of transport sites into the dot [107], as discussed above. In this case, the transport sites are likely shallow impurities, iso-electronic dopants, or other defects in the GaAs host, which can weakly bind charge carriers at the low temperature of the cryostat. The transport sites close to the QD comprise a reservoir that can recharge the QD under investigation as long as they contain charges. While the above-band excitation is on, the reservoir is continually repopulated. When the above-band excitation turns off, the charge population of the reservoir begins to decay. As the population decays, so too will the average value of the QD charge state. Thus the reservoir decay is reflected in the long-time decrease of the measured fluorescence.

The scale parameter α_2 increases with resonant laser power regardless of the above-band laser power, as seen in Fig. 4.4(a). The resonant laser can excite carriers weakly bound to transport sites to higher energy continuum states in the semiconductor host, which increases the rate of reservoir depletion after the above-band excitation is turned off, and hence the value of α_2 increases with resonant laser power. Figure 4.4(b) shows that α_2 decreases as a function of above-band power. Each transport site that is a component of the sub-diffusion-like reservoir can only hold (on average) one charge. When many transport sites are filled with higher above-band power, charges move to adjacent transport sites with an average slower rate due to the system being 'clogged' with charges occupying transports sites on the way to the QD. Thus, when the above-band power is high before it is shut off, we see a slower depletion of the reservoir via the time-resolved resonance fluorescence measured from the QD.

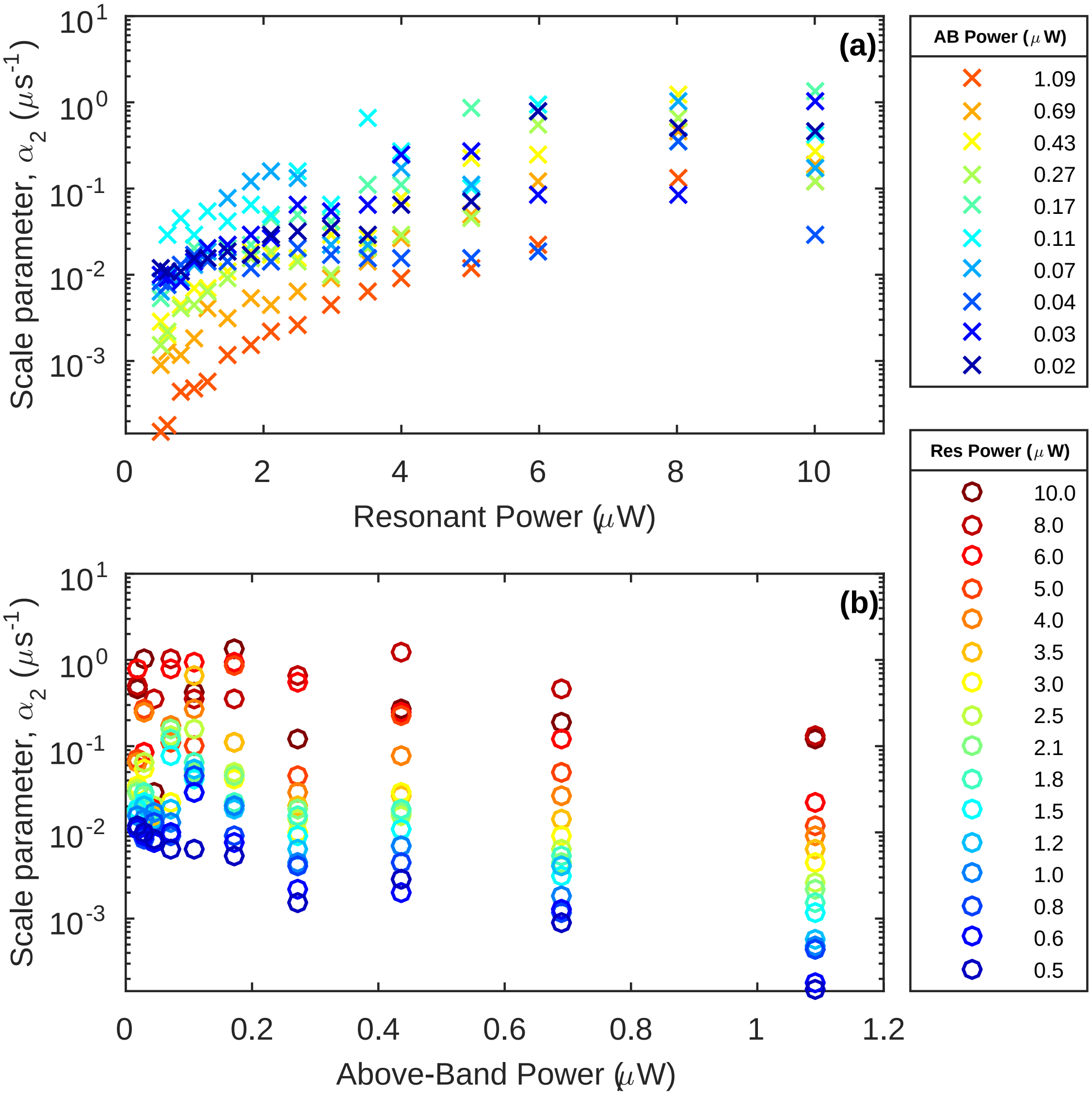

FIGURE 4.4: Scale parameter α_2 vs. (a) resonant laser power and (b) above-band laser power. The legends and color specify the power of the excitation laser not represented by the horizontal axis.

4.4.2 Fluorescence Rise

At the beginning of the rise section depicted in Fig. 4.2(b), the QD starts out neutral and resonant excitation of the trion transition does not cause any fluorescence. When the above-band laser is turned on, charges are excited and begin to relax into the bound state of the QD. The time-averaged charge state of the QD changes from neutral to charged. Towards the end of the rise section, the time-averaged charge occupation in the QD has reached a steady state value and the fluorescence intensity remains at maximum brightness as long as the above-band laser is on. However, the full transient of the rise spans tens to hundreds of microseconds, which implies a situation where the charges excited by the above-band laser do not immediately become bound to the QD. Since excitation of charges occurs within a few ps of the above-band laser turning on, it follows that it is the capture process that is delayed rather than excitation. The reason charge capture is delayed is that the charge carriers are excited non-local to the QD layer.

The above-band laser (632 nm) is focused normal to the sample surface with a beam waist of approximately 4.5 μm. The top DBR is comprised of alternating layers of AlAs and GaAs. The penetration depth, the depth at which the laser intensity decays to $1/e$ of its surface value, is approximately 340 nm for the above-band photons entering the heterostructure [110]. However, the QD layer exists slightly less than 2300 nm below the sample surface. A detailed to-scale schematic illustrating the penetration depth of the above-band laser in the sample can be found in the Supplemental Material. The generated charges can reach the monitored QD via several different transport mechanisms. Depending on the nature of the mechanisms involved, the charges may migrate with sub-diffusion, super-diffusion, or regular diffusion-like dynamics.

As discussed in the previous section, we suggest there exists a stochastic distribution of transport sites through which charge carriers can migrate to relax into the QD . The effective reservoir supplying the QD with charge is the collection of transport sites adjacent to, or in the near vicinity of the QD such that there is a substantial probability for charges occupying those transport sites to become bound to the QD within the time span of the observed transients. These transport sites are part of a larger network of transport sites through which charges migrate with a sub-diffusion-like behavior. Thus, we anticipate the existence of a charging process that has stretched exponential time dependence.

As shown in Refs. [105, 109], the ballistic transport of hot carriers results in super-diffusion which in turn is mathematically represented by compressed exponential time dependence. Almost 90 percent of the above-band induced hot charge carriers are created within 700 nm of the sample surface. The photon energy of the above-band laser translates to an initial excited carrier velocity of 800 nm/ps. The QD layer lies approximately 2300 nm below the sample surface. Hot carriers in bulk GaAs have an average lifetime of approximately 4 or 5 ps [111]. In that time a hot carrier can travel a few thousand nanometers. Thus, it is feasible that hot carriers excited in the first 700 nm from the sample surface can reach the QD layer before relaxing to the gamma point, and ultimately becoming bound to the QD. We hypothesize the existence of a super-diffusion-like pathway into the dot that is supplied by hot carriers created non-local to the QD layer by the focused above-band laser and its associated shallow penetration depth. Some carriers have ballistic trajectories that set them near the QD layer as they cool to the gamma point. This local volume of the bulk semiconductor host thus acts as an additional effective reservoir to supply the dot with charge, and its population saturates with compressed exponential time dependence due to the super-diffusion-like nature by which it is supplied with charge carriers. Thus, we anticipate a charging process that has compressed exponential time dependence.

We numerically model the charging dynamics of the rise section of the data using the solution to a differential equation for the time derivative of the ensemble-averaged QD charge population, p. We include the two charging processes discussed above as terms with stretched and compressed exponential time dependence that are proportional to the unoccupied charge state in the QD, $(1-p)$. Finally, we also include a neutralization term that is proportional to p. The resulting differential equation is:

$$\begin{aligned}\frac{dp}{dt} &= -\Gamma_N p \\ &+ [C_3(1-e^{-(\alpha_3 t)^{\beta_3}}) + C_4(1-e^{-(\alpha_4 t)^{\beta_4}})](1-p). \end{aligned} \tag{4.2}$$

The ensemble-averaged charge population in the dot, p, can take on a value between 0 (neutral) and 1 (charged). Γ_N is the neutralization rate per unit charge in the dot, C_3 and C_4 are long time, or steady state, capture rates per unoccupied charge population $(1-p)$ in the dot for two separate charging pathways, α_3

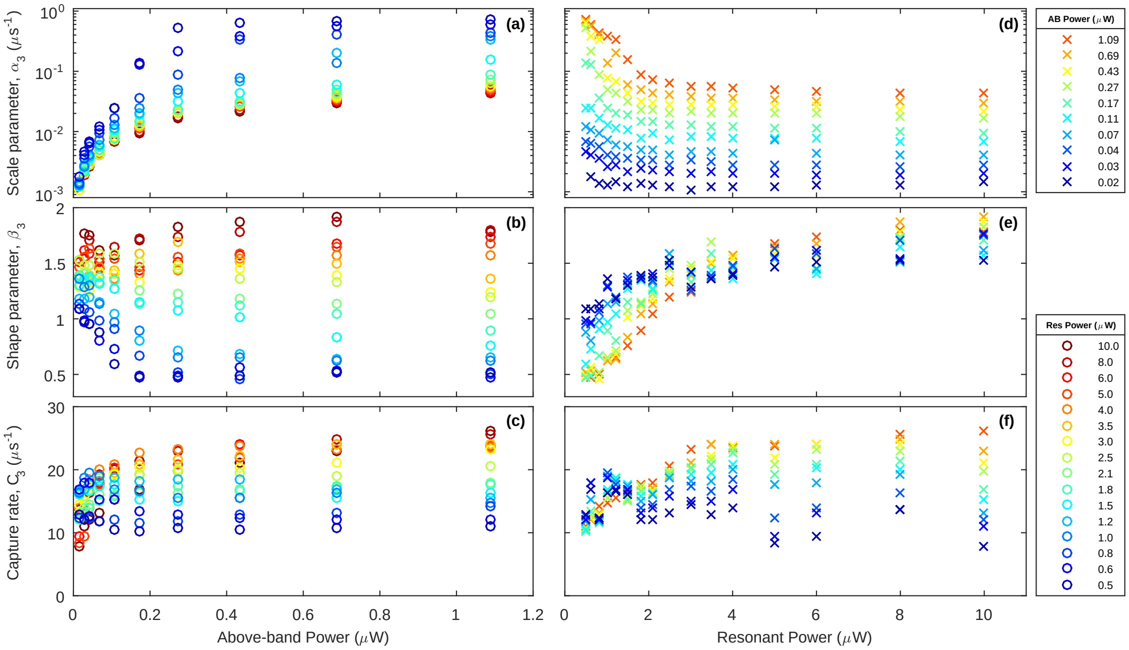

FIGURE 4.5: Model parameters associated with the super-diffusion-like process as a function of (a-c) above-band laser power and (d-f) resonant laser power. The legends and color specify the power of the excitation laser not represented by the horizontal axis.

and α_4 are scale parameters associated with the two separate pathways, and β_3 and β_4 are shape parameters. During development of the model, we assumed a neutralization rate proportional to the ensemble-averaged charge population in the dot and one or two capture rates that were either constant in time or had saturating time dependencies. We ultimately obtained the best fits using two charging terms: one that fills with stretched exponential time dependence and one with compressed exponential time dependence. The rate at which charges enter the dot should be proportional to not only the unoccupied charge in the dot, but also the population of the effective reservoir supplying the associated charging pathway with charges. α_3 and α_4 represent the effective rates of change of charge population in the two reservoirs after the above-band excitation turns on. During the fitting process, β_3 and β_4 always obtained values between 0 and 2. The term with index 3 is associated with the super-diffusion-like process, while the term with the index 4 is associated with the sub-diffusion-like process.

We should expect that as the above-band laser power increases, the model parameters will change to hasten the rise of the fluorescence. The resonant laser causes both fluorescence and Auger recombination. It also suffuses the

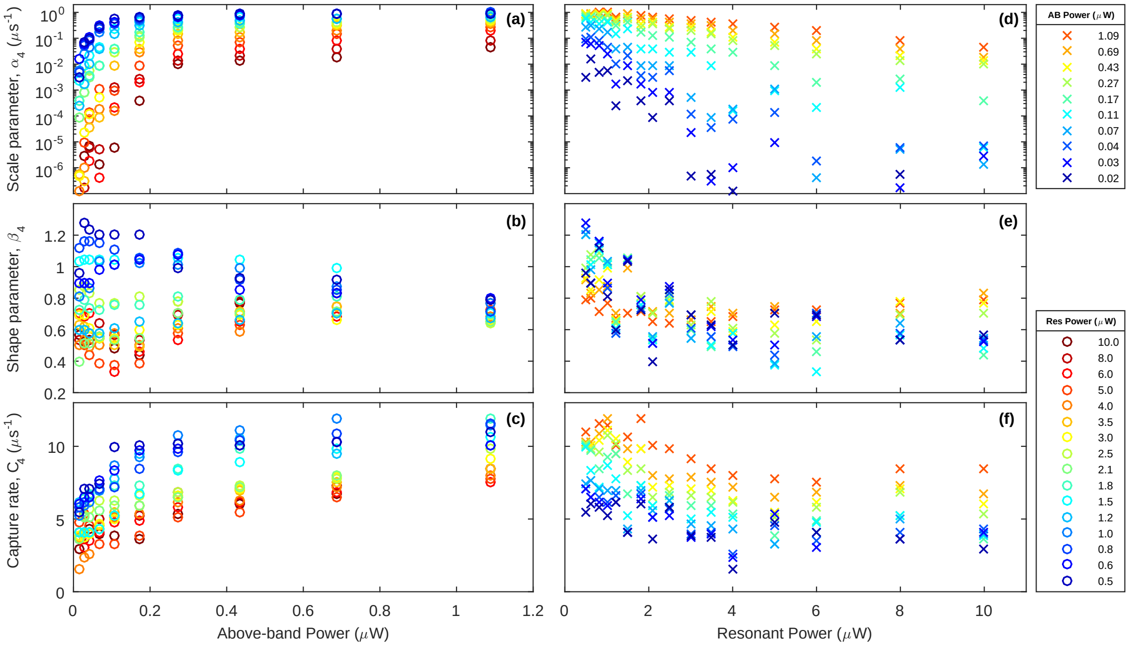

FIGURE 4.6: Model parameters associated with the sub-diffusion-like process as a function of (a-c) above-band laser power and (d-f) resonant laser power. The legends and color specify the power of the excitation laser not represented by the horizontal axis.

entire waveguide region of the sample, not just the QD layer, so it can affect the charge carriers as they migrate to the QD being probed. Intra-band excitation of low-energy charge carriers by the resonant laser would reduce the transport of charge to the QD region. That would affect both normal diffusion of carriers and migration via hopping between transport sites. There will be consequences for the shape parameters of the two transport processes.

Super-Diffusion-Like Process

For the super-diffusion-like process, with increasing above-band power the growth of the capture rate is faster (α_3 increases), the time dependence can become less compressed for lower resonant powers (β_3 decreases), and the steady-state capture rate generally increases (C_3 increases). Figure 4.5(a-c) illustrates how the parameters of the super-diffusion-like process depend on the above-band laser. These dependencies are consistent with the expected behavior of a charge reservoir near the QD that is supplied by a combination of normal diffusion and ballistic transport of charges excited far away. A higher above-band power means more charges are excited per unit time, which will increase the rate

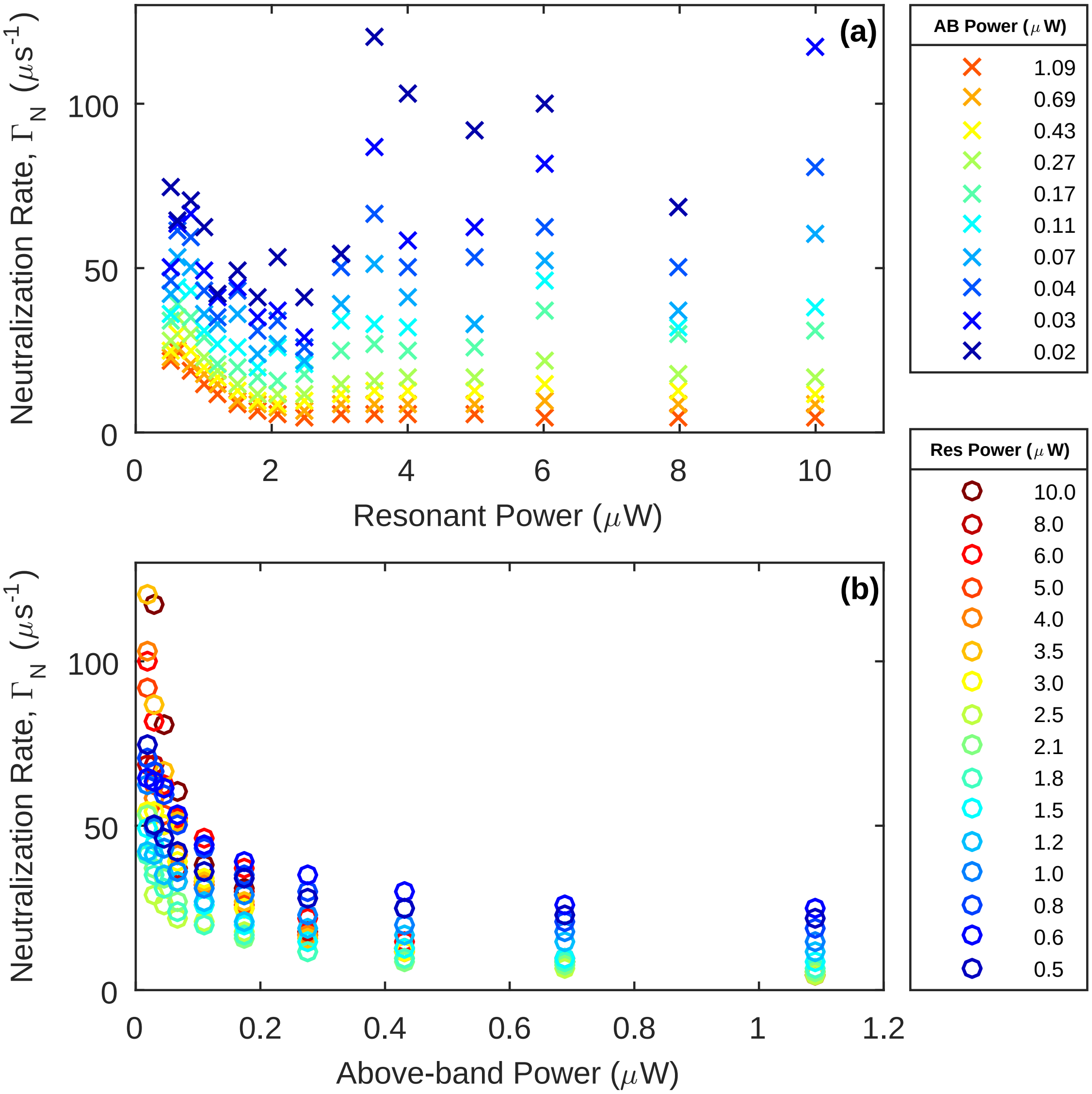

FIGURE 4.7: Neutralization rate per unit charge in the dot while the above-band laser is on as a function of (a) resonant laser power and (b) above-band laser power. The legends and color specify the power of the excitation laser not represented by the horizontal axis.

at which the reservoir near the QD is filled, thus increasing α_3. More charges created means that more charges will travel to the QD layer via normal diffusion as well, which will make the time dependence less compressed, thus decreasing β_3. This only occurs for lower resonant powers because higher resonant powers re-excite the normally diffusing charges, leaving ballistic transport as the dominant process and keeping the time dependence a compressed exponential. A higher excitation rate of charges will generally result in a higher steady-state population of the charge reservoir near the QD, leading to a higher steady-state capture rate, thus increasing C_3.

With increasing resonant power, the super-diffusion-like capture rate increases slower (α_3 decreases), the time dependence becomes more compressed (β_3 increases), and the steady-state capture rate either stays about the same or increases (C_3 increases for high above-band powers). Figure 4.5(d-f) illustrates how the parameters of the super-diffusion-like process depend on the resonant laser. The resonant laser will re-excite charges that are either in the charge reservoir near the QD or traveling there relatively slowly via normal diffusion. That will slow down the rate at which the reservoir is filled, decreasing the value of α_3. Re-excitation will affect normally diffusing charges more strongly than ballistically moving charges because of the difference in transit time to the QD region. This will enhance the dominance of ballistic transport, making the super-diffusion-like nature of the process stronger, and increasing β_3. The steady-state capture rate has an unexpected dependence on the resonant laser power. For low to medium above-band power, the value of C_3 is not strongly affected by the resonant laser power. But for high above-band power, C_3 increases with resonant power. Perhaps for high above-band power, increasing the resonant laser power changes the ratio of electrons and holes that reach the QD region, resulting in a balance that increases the charge capture rate.

Sub-Diffusion-Like Process

For the sub-diffusion-like process, as for the super-diffusion-like process, increasing the above-band laser power will enhance the charge capture effectiveness. With increasing above-band power the capture rate increases faster (α_4 increases), the time dependence converges on a certain stretched character (β_4 converges to ≈ 0.75), and the steady-state capture rate increases (C_4 increases). Figure 4.6(a-c) illustrates how the parameters of the sub-diffusion-like process depend on the above-band power. Similar to the super-diffusion-like process, a higher above-band power excites more charges and increases the rate at which the reservoir near the QD is filled, thus α_4 increases. A higher rate of charge excitation also means a higher steady-state population of the reservoir, leading to a higher capture rate, C_4. The dependence of the shape parameter β_4 is more complicated because it depends on the resonant laser power. For low resonant power and low above-band power, β_4 is actually greater than 1. As the above-band power increases, β_4 decreases to about 0.75. In contrast, for high resonant power and low above-band power, β_4 is significantly less than 1. As the above-band power increases, β_4 increases to about 0.75. At high above-band power, the shape parameter is approximately 0.75 regardless of the resonant laser power.

With increasing resonant power, the growth of the sub-diffusion capture rate is slower (α_4 decreases), the time dependence becomes more stretched (β_4 decreases), and the steady-state capture rate decreases (C_4 decreases). Figure 4.6(d-f) illustrates how the parameters of the sub-diffusion-like process depend on the resonant power. The resonant laser has a similar effect on the sub-diffusion-like process as it does on the super-diffusion-like process. Re-excitation of charges slowly migrating through transport sites to the QD region will decrease the rate at which the reservoir of nearby transport sites are filled, thus reducing α_4. The re-excitation will also effectively slow the hopping transport process, enhancing the stretched exponential character of the time dependence, which translates to decreasing β_4. Finally, higher resonant power means that fewer charges make it to the QD region, which will reduce the equilibrium charge population in that region and thus reduce the steady-state capture rate, C_4.

Neutralization Process

When the above-band laser is off, Auger recombination of the resonantly excited trion is the dominant process by which the QD becomes neutralized. In contrast, when the above-band laser is on—as during the fluorescence rise—Auger recombination is not the dominant neutralization process. The neutralization rate Γ_N does not exhibit the dependence on resonant power that one would expect if it were solely dominated by Auger recombination processes. The dependence of Γ_N on resonant excitation power is depicted in Fig. 4.7. Recall, α_2 in the fall model saturates with resonant power as would the time-averaged trion population. That is evidence that α_2 is associated with neutralization of the QD via

Auger recombination. However, Γ_N *decreases* with resonant excitation power for powers below 2.5 μW. Additionally, Γ_N increases slightly at higher resonant powers for the lowest above-band powers. Thus, when the above-band laser is on, neutralization is not caused solely by Auger recombination. Neutralization may be caused by capture of an oppositely charged carrier. Additionally, carriers populating the transport sites discussed above may be excited to higher-energy continuum states via the resonant laser. The above-band excitation acts against the resonant laser by tending to charge the dot. This may explain why we see an increase in Γ_N at high resonant powers for the lowest above-band powers.

4.5 Conclusion

We studied time-resolved resonance fluorescence from a resonantly excited charged transition in an InAs QD while modulating an additional low-power above-band excitation laser. From the power dependence of the fall transients, we conclude Auger processes dominate the neutralization after the above-band excitation is turned off. After the QD is neutralized by Auger recombination, it gets recharged from a reservoir of carriers in the local environment whose population is itself slowly decaying after the above-band excitation is turned off. Due to the stretched exponential behavior of the associated term, we conclude this reservoir is composed of a stochastic environment of weakly attractive shallow defects acting as transport sites that charges can migrate through to ultimately be captured by the QD.

The time and power dependence of the rise model indicates the presence of two reservoirs that supply the QD with charge: one that fills with super-diffusion-like charge dynamics, and one that fills with sub-diffusion-like charge dynamics. The reservoir that fills with sub-diffusion-like charge dynamics is the same ensemble of shallow defects described in the fall section of the data. The reservoir that fills with super-diffusion-like charge dynamics is supplied by hot carriers created near the sample surface that ballistically travel to the neighborhood of the QD. Both reservoirs are supplied with charge via the above-band laser. The resonant laser populates the trion, causing fluorescence, but also ejects charge from the dot via Auger recombination and retards the establishment of charge in both reservoirs.

It is expected that the two reservoirs posited here would also affect the charging dynamics of the QD when the neutral exciton transition is resonantly excited. The resonance fluorescence signal of a neutral exciton is known to be similarly dependent on low-power above-band excitation [40, 88]. In that case, Auger recombination within the QD would not occur, so other effects will dominate the charging process.

The charging and neutralization processes revealed by our analysis have implications for the design of future single photon sources. If independent electrical control of the QD charge state is impossible (as with certain optical cavities), then an above-band laser can help maintain the charge state. To have a fast time response, the QD should be relatively close to the surface where the above-band excitation is incident. A possible alternative might be to excite in the wetting layer absorption band, which would place the excited charges in the immediate locale of the QD. Though generally thought to introduce complications like spectral diffusion, the presence of defects and impurities is important to the transport of charges over long distances within the GaAs sample. Increasing the defect density by light doping or multiple layers of delta-doping might enhance the transport capability of the semiconductor host.

Chapter 5

Shifting of Resonance Energies in InAs QDs due to Above-Band Excitation Modulation and the Resulting Charge Dynamics

5.1 Introduction

This chapter regards an experiment in which the analysis is currently on-going. The reasons for conducting the experiment, the experimental methods used, and the mathematical approaches to the analysis will be discussed. Some analysis for this chapter has been done, which I will describe. Additional analysis leading to an ultimate publication will be done in the following months.

The experiment described in this chapter involves analysis of time-resolved resonance fluorescence (TRRF) as a low-power above-band laser is turned on and off, as in Chapter 4, however TRRF was recorded for different near-resonance frequencies of the resonant laser. When the low-power above-band laser is turned on, it introduces charge carriers to the local environment. The carriers are mostly created in the top DBR layer due to the shallow penetration depth depicted in Fig. A.2. The charge carriers are initially very hot[1] since the excitation photon energy is significantly greater than the band-gap of the semiconductors making up the heterostructure. This combined with being excited in a small volume due to the above-band laser being focused with a high numerical

---

[1] The energy of the HeNe above-band laser at 633 nm is approximately 1.96 eV per photon. The band-gap energy of GaAs is approximately 1.42 eV. Thus, the carriers excited initially have a high kinetic energy.

aperture lens and its shallow penetration depth into the sample results in initial ballistic-like dynamics of the carriers for the first several ps as they cool. The ensuing super-diffusion-like dynamics results in a compressed-exponential time dependence of the filling of the effective charge reservoir described in Chapter 4 after the above-band laser is turned on. Some of the charge carriers make their way to the GaAs spacer as they cool via emission of phonons.

When their energy becomes close to that at the bottom of the CB of the GaAs matrix, they are able to weakly bind to transport sites that are shallow potentials created by defects and impurities in the GaAs matrix. The transport sites create pathways for the charge carriers to transport through, hence the name. In a sense, the dynamics can be compared to one trying to cross a ford in a creek without wetting their feet via hopping over stepping stones in the ford. If one desires to keep dry, they very likely cannot simply walk in a straight line. The ford will likely have some stochastic distribution of stepping stones and the easiest path(s) to take will likely be the path(s) in which each subsequent stone is closest to the previous. This will result in one or a couple of random, zigzagging, paths to cross the ford. If multiple people are trying to cross, people who stop or hesitate at certain stones will stop those behind them from progressing until they do. Analogously, the charge carriers that weakly bind to shallow potentials will be able to 'skip' to other nearby shallow potentials with a probability that decreases exponentially with distance. Due to the stochastic distribution of shallow potentials acting as transport sites, there will exist random highest-probability pathways through which the carriers migrate. Some pathways will have transport sites that are in close proximity to the QD, allowing migrating charges to be captured by the QD's potential, and ultimately returning the QD to its initial charge state. Similar to multiple people crossing the ford, if a transport site is occupied by a carrier, it will be effectively blocking carriers of the same charge type from traversing through that transport site until it itself 'skips' to another site. The nature of this effective charge reservoir, and subsequent sub-diffusion-like dynamics, was reflected in the stretched-exponential time dependence seen in both the filling and depletion of the effective reservoir discussed in Chapter 4.

In hindsight, it was realized that one potentially significant effect was not considered in the experiment described in Chapter 4. When the above-band laser is turned on, it introduces charge carriers to the local environment as described in the previous paragraph. However, as the effective charge reservoir in the surrounding GaAs matrix fills, charges bound to defects close to the QD under investigation influence the precise electric potential felt by the bound excitons or trions, potentially shifting the resonant energies of the optical transitions. This was not considered in the experiment described in Chapter 4. Thus, we decided to conduct an additional experiment that involved analysis of TRRF while modulating the above-band laser, but not only for different values of the above-band power, but also for different near-resonant values of the resonant laser's frequency. Ultimately, for a given above-band power, the TRRF for different near-resonance values of the resonant laser were stacked side-by-side, resulting in the creation of effective time-dependent excitation spectra.

Since the experiment in Chapter 4 had been conducted, a new sample had been mounted in the cryostat. Thus, the first step was to find a bright QD that exhibited minimal long-time blinking as was observed in Chapter 3. The exact reasons are still unclear, but we were unable to find a bright trion transition in the newly mounted sample. Thus, we decided to perform the experiment on a very bright neutral QD. A simple detection-polarization-dependent measurement can be conducted to determine whether the observed fluorescence is from a typical neutral QD. Very few QDs have perfect circular symmetry in the plane perpendicular to the growth direction. As discussed in Chapter 1, a neutral QD with spatial asymmetry emits light that is linearly polarized. However, fluorescence emitted from a charged QD is circularly polarized. A simple polarization state test is implemented: The fluorescence is sent through first a HWP, then a linear polarizer oriented to a given polarization, say horizontal. The fluorescence intensity is then measured via a detector, say a CCD camera. If the fluorescence is linearly polarized, then as one rotates the HWP through at least a 45 degree rotation, one would observe the fluorescence intensity fluctuate from a maximum value to a value close to zero (nominally zero). While for perfectly circularly polarized light, one would observe no change in the fluorescence intensity. Linearly polarized light is rotated through 90 degrees as the HWP is rotated through 45 degrees. For a given orientation of the HWP, the light before the polarizer will be horizontally polarized, and if the HWP is oriented 45 degrees with respect to that, the light will be vertically polarized. Thus, the intensity after the polarizer will shift between a minimum (nominally zero) and maximum value as the HWP is rotated. Meanwhile, the HWP only changes the handedness of circularly polarized light, that is it will change left circularly polarized to right circularly polarized and vice versa. Since for any orientation of the HWP the light before the polarizer will be circular for a trion transition, no change in the ultimate output intensity will be induced as one rotates the HWP. Using this method we were able to confirm the observed fluorescence was from a neutral transition.

5.2 Experimental Technique

The motivation for the experiment was to not only further investigate the charge dynamics of InAs QDs under both resonant and low-power above-band excitation, but to also investigate the above-band excitation light's effect on the resonant energy of the QD. The excitation optics had been changed such that the resonant laser entered the cryostat from the top, as opposed to the side. This allowed for anticipated incorporation of two magnets on the sides of the cryostat to induce an approximately constant magnetic field at the center of the sample in the Voigt configuration $\vec{B} \perp \hat{z}$ mentioned in Chapter 1. The position of the above-band laser was also changed. However, fundamentally the experimental setup is unchanged from that described in Chapter 4, which was depicted in Fig. 4.1.

The resonant laser is focused into the GaAs planar microcavity, perpendicular to the growth direction. The above-band laser is focused onto the sample surface, parallel to the growth direction. The resonant fluorescence is collected confocal with the above-band excitation laser. The fluorescence is sent through a beam expander, which in conjunction with the collection lens inside the cryostat and the focusing lens before the spectrometer, creates a magnification of 60. The fluorescence is additionally sent through a 900 nm long-pass filter before the spectrometer for further filtering of the resonance fluorescence. After the spectrometer, the fluorescence is coupled into a fiber. The output of the fiber is ultimately focused onto an APD that can detect single photons. A TCSPCM builds a histogram of photon arrival times with respect to a trigger signal that is synced with the turning on of the above-band laser. The above-band laser is modulation with an AOM and the modulation voltage sent to the AOM is split

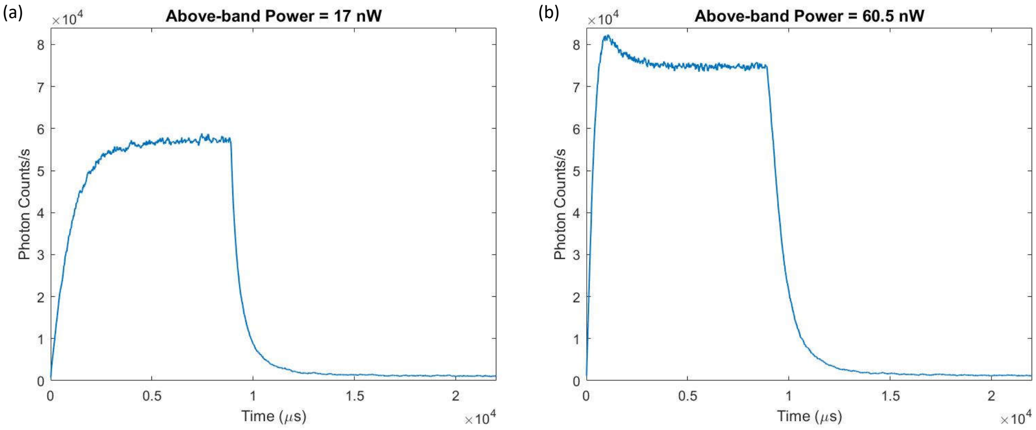

FIGURE 5.1: Example TRRF for two different above-band excitation powers: (a) 17 nW, and (b) 60.5 nW.

and sent through a passive electrical element that creates a trigger signal for the TCSPCM from the edge of the square AOM modulation wave.

The time-dependent fluorescence measured from when the trigger signal starts the clock is the TRRF. Time $t = 0$ corresponds to when the above-band laser is turned on, and at $t = \delta$ the above-band laser is turned off. An example of the TRRF is shown in Fig. 5.1. As in Chapter 4, when the above-band laser is turned on, the fluorescence intensity quickly rises and eventually reaches a steady-state value (rise section). When the above-band laser is turned off, the fluorescence intensity decreases back to zero[2] (fall section). Notice the peculiar bump (bunching) at the beginning of the rise for the higher above-band powers that wasn't present in any of the TRRF in Chapter 4. In this experiment, we introduce a more sophisticated mathematical analysis than was used in Chapter 4. The analysis involves fitting time-dependent areas under effective excitation spectra that are created from the TRRFs with a numerical solution of a model described by a set of differential equations that represent the time-dependence of the neutral and charged populations of the QD. The model fits all of the extracted areas under the effective excitation spectra very well, despite the different shapes of the transients for different above-band powers.

The experiment was conducted using five different above-band powers ranging from approximately 17 to 95 nW. For each above band power, TRRF

---

[2] There is a non-zero background signal detected by the APD that is not subtracted in Fig. 5.1. However, the background signal is a parameter in the fits discussed below.

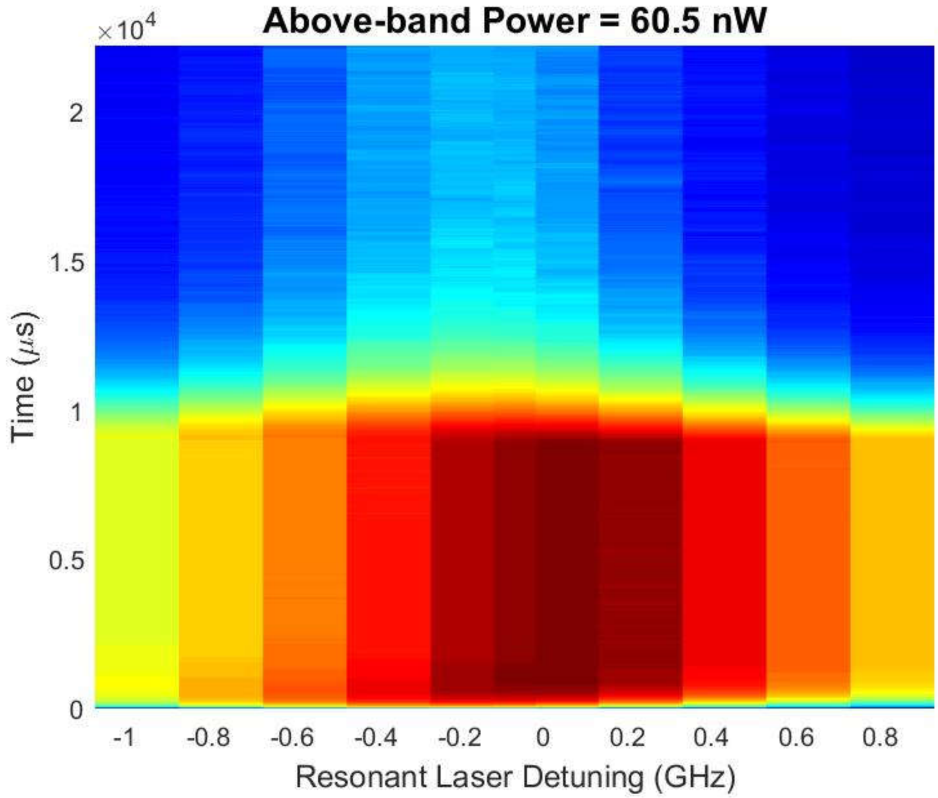

FIGURE 5.2: Example time-dependent excitation spectrum for an above-band power of 60.5 nW. The horizontal axis is resonant laser frequency in units of GHz detuned from the on-resonance frequency. The vertical axis is time in microseconds. Red color signifies a higher fluorescence intensity, while blue signifies a lower intensity.

was recorded for eleven different resonant laser wavelengths, ranging between $\pm 0.9 GHz$ from resonance during the steady state. For a given above-band power, each TTRF was stacked side-by-side such that the horizontal axis of the resulting plot is resonant laser frequency (detuning) and the vertical axis is time. The intensity is represented by the color, where red is high intensity and blue is low intensity. A given horizontal slice of the data at time t, is thus an effective excitation spectrum at the time t. Consequently, the full 2-D plot depicts a time dependent excitation spectrum for a given above-band power. An example effective excitation spectrum is presented in Fig. 5.2.

5.3 Analysis

5.3.1 Resonance Shift and Excitation Linewidth

For each effective excitation spectrum (one for each above-band power) horizontal slices were taken at each temporal data point (roughly 1,100 for each plot). As previously mentioned, a given horizontal slice of Fig. 5.2 depicts the excitation spectrum at the corresponding time. Each excitation spectrum for all times was fit with a Lorentzian lineshape of the form given in Eqn. 2.1. The key parameters to extract as a function of time were the area under the Lorentzian A, the center frequency shift of ω_0, and the FWHM Γ. The area A is proportional to the average population of the neutral state[3] as a function of time, the center frequency shift of ω_0 gives us information regarding the shift in resonance frequency as a function of time, and the FWHM Γ is the excitation linewidth and is related to the degree of spectra diffusion, as well as inversely related to the lifetime associated with spontaneous emission in the QD.

Figure 5.3 displays the time-dependent center frequency shift of ω_0 for each above-band power. The value of the center frequency shift is displayed relative to the on-resonance frequency under the excitation conditions that resulted in the brightest fluorescence in the steady state[4]. During the rise, after the above-band laser is turned on, we observe a blue shift in the resonant frequency for all above-band powers. While during the fall, after the above-band laser is turned off, we observe a red shift back. As expected, the shift is more drastic for the higher above-band powers. As the above-band laser is turned on and off, we observe a shift of approximately 125 MHz for the lowest above-band power and approximately 340 MHz for the highest above-band power. This shift is certainly not insignificant, especially for the higher above-band powers, and likely would affect fine details in the TRRF transients examined in Chapter 4. However, we do not expect this effect to be drastic enough to greatly affect our general conclusions from Chapter 4, since the magnitude of the shift is approximately several times smaller than the absorption linewidth. That is, we expect the observations of the super-diffusion-like and sub-diffusion-like dynamics to still be present, as

---

[3] The neutral state is the state that is being resonantly driven that produces the examined fluorescence.

[4] By steady state, I mean when the above-band laser is not modulated, but kept on at a given power.

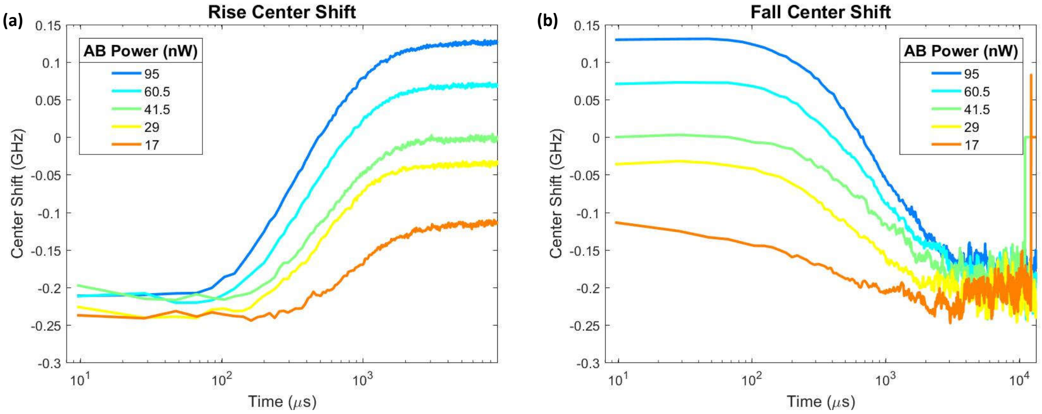

FIGURE 5.3: Semi-log plot of the center frequency shift for each above-band power relative to the resonant frequency under the excitation conditions that resulted in the brightest fluorescence for (a) the rise when the above-band laser is turned on and for (b) the fall when it is turned off. The time on the fall plot has been shifted so that $t = 0$ is aligned with when the above-band laser is turned off.

well as the neutralization of the charged state to be dominated by Auger recombination. However, the exact values of extracted parameters from the fits of the transients would likely change if we had accounted for this effect.

Figure 5.4 shows the FWHM of the effective excitation spectra as a function of time. It is apparent during the fall in Fig. 5.4 that the excitation linewidth (FWHM) increases after the above-band excitation is turned off. Also, the FWHM increases with decreasing above-band power. As the effect of spectral diffusion becomes more prominent, the jittering of the QD's resonance becomes more pronounced, resulting in a widening of the emission spectrum. However, the shifting of this resonance will also affect the width of the excitation spectrum. Thus, a larger FWHM here implies a higher degree of spectral diffusion. The FWHM increasing during the fall (after the AB excitation is turned off), as well as increasing with decreasing AB power, implies that at higher above-band powers the population of carriers occupying the local stochastic distribution of transport sites saturates, resulting in less spectral diffusion. If all, or most, of the transport sites of the effective charge reservoir are occupied, the pathways through which carriers can migrate become 'clogged', and the average rate at which carriers hop to adjacent transport sites decreases. This partial 'freezing' of the local charge reservoir around the QD results in smaller average fluctuations in the local net electric field that the QD feels (less spectral diffusion),

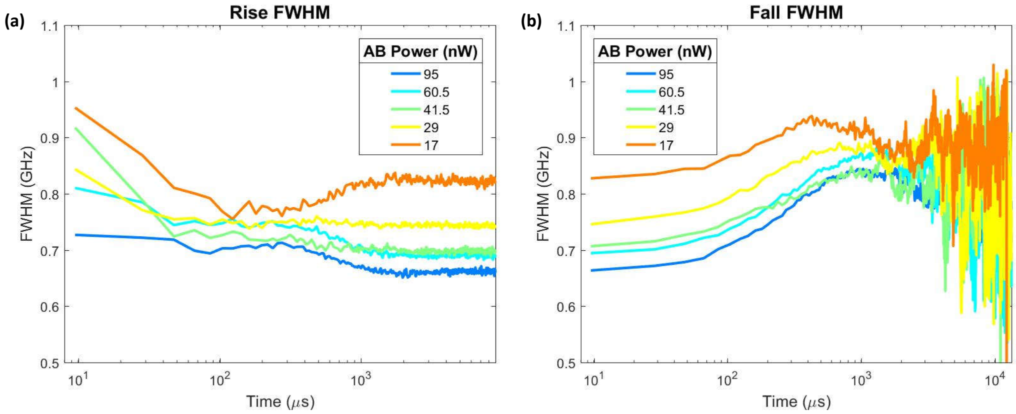

FIGURE 5.4: The excitation linewidth (FWHM) as a function of time for different above-band powers for (a) the rise and (b) the fall.

hence the observed decrease in the excitation spectra's FWHM with increasing above-band power. When the above-band laser is turned off, the charge reservoir begins to deplete. As the depletion ensues, pathways become 'unclogged' and as charges begin to migrate through the pathways at higher rates, the time-dependent local electric field that the QD feels changes at a faster rate, inducing a higher degree of spectral diffusion. Finally, for the lower above-band powers, the pathways only become 'semi-clogged' and the degree of spectral diffusion and corresponding FWHM is larger when compared to the higher above-band powers.

5.3.2 Direct Probe of the Neutral State Population

The most in-depth and interesting analysis is conducted on the extracted areas under the Lorentzian fits of the effective excitation spectra at different times. The extracted areas as a function of time for each above-band power is depicted in Fig. 5.5. Recall from Chapter 1 that generally a Lorentzian is normalized such that the integral from $-\infty$ to $+\infty$ is unity. This makes sense in terms of an excitation spectrum because the integral equalling unity corresponds to adding up all possible excitation frequencies that can excite the transition. Whereas the value of the amplitude of the excitation spectra at any given frequency is correlated to the probability that a delta function at that frequency (such as a cw laser) would

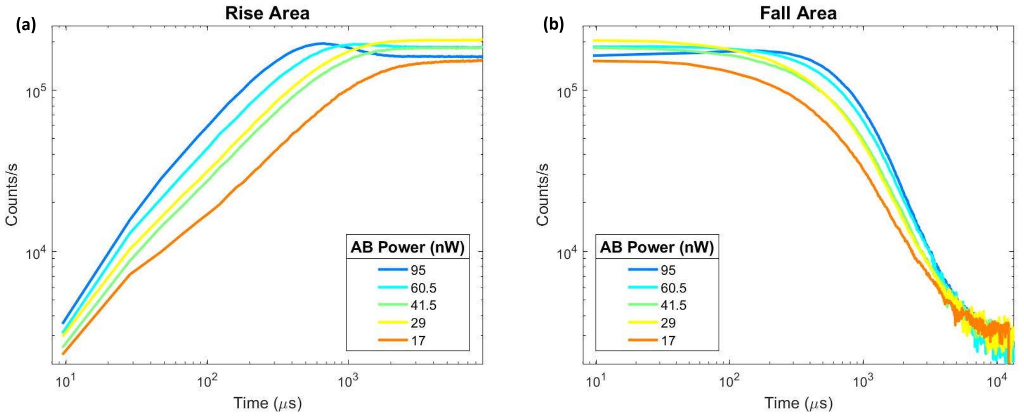

FIGURE 5.5: The time-dependent areas under the Lorentzian fits of the effective excitation spectra as a function of time for (a) the rise and (b) the fall.

excite the QD. We multiply the Lorentzian by the area A so that we can fit it to any general excitation spectrum without normalization[5].

Spectral diffusion will cause random jittering of the resonance frequency about the 'natural' (resonance frequency without spectral diffusion) resonance frequency due to fluctuations in the local charge environment. Spectral diffusion effectively broadens the excitation spectrum, but it does not change the area under the excitation spectrum, because the curve still describes all possible excitation frequencies that will excite the QD. Thus, the integral from $-\infty$ to $+\infty$ remains unity for the normalized Lorentzian, or equal to A for a general, unnormalized Lorentzian. This means that the value of the FWHM of the excitation spectrum is effected by spectral diffusion, but the area under the Lorentzian lineshape is independent of spectral diffusion. On the contrary, the area A is proportional to the time-averaged population of the neutral state. If the charge state of the QD never changed from neutral to charged, then scanning the excitation laser over the neutral transition energy range would result in the largest value of A. However, if the QD was in the charged state, the scanned excitation frequencies over the neutral state would never populate the excited neutral state, and no fluorescence would be observed ($A = 0$). If the QD is switching back and forth between the neutral state and the charged state, then the area under

---

[5] Thus, when the system is in the steady-state, the probability that a given frequency would excite the electronic transition is equal to the amplitude of the Lorentzian at that frequency divided by the integrated area A.

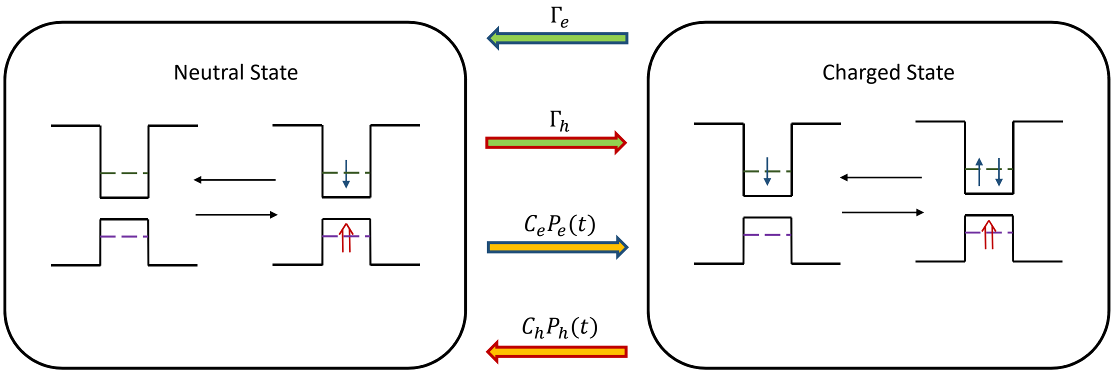

FIGURE 5.6: A two-population charge state model displaying pathways charge carriers can take into and out of the neutral state and a charged state, here arbitrarily chosen is the negative trion. Single blue arrows represent electrons, while double red arrows represent holes. Arrows filled with green depict processes that result in charge ejection from the system, while arrows filled with yellow-orange depict charge capture from the local charge reservoir. Arrows lined in blue represent electron transfer, while arrows lined in red represent hole transfer.

the Lorentzian will be equal to some value between zero and the maximum possible value that corresponds to the QD never leaving the neutral state. Thus, the area under the curve is directly proportional to the time-averaged population of the neutral state.

A schematic depicting the neutral and charged states and possible charge pathways between them is depicted in Fig. 5.6. The model considers two populations, the neutral state n_n and a charged state n_c, where ($0 < n_c, n_n < 1$). The two populations are allowed to go between each other by exchange of holes and electrons via ejection from the system and collection from a local charge reservoir. This reservoir is likely mostly composed of a stochastic distribution of carrier transport sites that are populated with initially ballistic-like carriers created by the above-band laser as they cool, as described in Chapter 4. Each population (n_n and n_c) encompasses both the ground state and excited state of the photo-induced electronic transition. Figure 5.6 depicts the four possible charge pathways that result in a change of the charge state. Due to the symmetry between the system going between the neutral state to the positive trion or the neutral state to the negative trion, just one charged state is considered in order to simplify the model. The model, shown in Eqn. 5.1, considers possible charge transfer rates between the neutral state and the arbitrarily chose negative trion.

Included are rates associated with different pathways for both the electrons and holes. However, since the charge state chosen in the model is arbitrary, and the effective masses, and hence mobilities, of the two carrier types are not incorporated in the model, the rates associated with electrons are realistically only associated with the charge carrier type with the same charge as the charged state of the system, while rates associated with holes are realistically only associated with the other carrier type[6]. Γ_e and Γ_h represent electron and hole ejection rates from the system, respectively. These charges are allowed to leave the system entirely[7] C_e and C_h represent electron and hole capture rates from the reservoir per unit population of the reservoir. The ultimate rates through these capture pathways also depend on the populations of carrier types in the local reservoir, represented by P_e for electrons and P_h for holes. The system can be modelled by the following set of differential equations describing the time-dependence of the two charge states:

$$\begin{aligned} \frac{dn_n}{dt} &= -\Big(\Gamma_h + C_e P_e(t)\Big) n_n + \Big(\Gamma_e + C_h P_h(t)\Big) n_c, \\ \frac{dn_c}{dt} &= -\frac{dn_n}{dt}, \end{aligned} \tag{5.1}$$

where the time-dependent reservoir populations $P_e(t)$ and $P_h(t)$ can take on values between 0 and 1.

At the very beginning of the rise section $(t = 0)$, the reservoir is defined to be deplete of charge carriers. The filling of the reservoir for both electrons and holes were allowed to take on asymptotic shaped exponential time dependence:

$$\begin{aligned} P_e(t) &= 1 - e^{-(\alpha_{re} t)^{\beta_r}}, \\ P_h(t) &= 1 - e^{-(\alpha_{rh} t)^{\beta_r}}, \end{aligned} \tag{5.2}$$

where the subscript r stands for the rise section and the subscripts e and h stand for electrons and holes, respectively. The $\alpha's$ are capture rates into the reservoir for the two carrier types, while β_r is the shape parameter for the rise section, which allows for a regular exponential's shape to be modified, hence the name.

---

[6] The reader must keep this is mind for the rest of the analysis.

[7] If the charge carriers were only able to enter back into the local reservoir upon ejection, a $(1 - P_e(t))$ and $(1 - P_h(t))$ term would need to be present with the Γs, since there would need to exist empty states in the reservoir for charges to enter. This more simple model allows for complete ejection of carriers from the system.

Recall from Chapter 4 and Appendix A, a regular exponential ($\beta = 1$) signifies diffusion-like filling of the charge reservoir, a stretched exponential ($0 < \beta < 1$) signifies sub-diffusion-like filling, and a compressed exponential ($\beta > 1$) signifies super-diffusion-like filling. Due to their difference in effective mass, and consequently in their mobility, the electron and hole filling rates (the $\alpha's$) were allowed to take on different values. The shape parameter β_r is forced to be the same for either charge carrier, because we expect the shape parameter to define the net 'type' of environment through which charge carriers migrate. For example, a reservoir that fills with stretched exponential time dependence is indicative of a reservoir that is composed of (mostly) a stochastic distribution of transport sites that each can occupy one (or very few) charges at a time. As β approaches one, the environment becomes a volume that allows regular-diffusion-like dynamics, that is, the 'stepping-stone-like' dynamics described in Chapter 4 approach a more 'open room' like environment for charges to diffuse.

The populations of the charge reservoirs during the fall section were allowed to take on the following time dependence:

$$\begin{aligned} P_e(t) &= e^{-(\alpha_{fe}(t-\delta))^{\beta_f}}, \\ P_h(t) &= e^{-(\alpha_{fh}(t-\delta))^{\beta_f}}, \end{aligned} \tag{5.3}$$

where the subscript f stands for the fall section and as in the rise section, e and h stand for electrons and holes, respectively. δ is the time corresponding to the beginning of the fall section, defined with respect to the beginning of the rise section (which starts at $t = 0$). In the previous figures depicting the fit parameters of the Lorentzian fits to the time-dependent excitation spectra, I redefined the temporal axis so that the plots of the fit parameters for the fall section would start at $t = 0$. However, in the following analysis, I let the time t range from the beginning of the rise ($t = 0$) to the end of the fall, thus the necessity of the temporal argument $(t - \delta)$ in Eqn. 5.3[8]. β_f is again a shape parameter that allows the regular exponential's shape to deviate.

The above set of differential equations cannot be solved analytically. Thus, we utilize numerical methods to solve for the neutral state $n_n(t)$ to fit the areas

---

[8] This is because the model used was devised for all times. Note, some of the parameters are shared between the rise and fall.

under the Lorentzian fits of the time-dependent excitation spectra[9]. The initial population of the neutral state at $t = 0$ is set to be zero and that of the charged state to be unity[10], and the effective reservoir populations are initially empty. At the beginning of the fall section, the carrier populations of the effective reservoir start with the calculated values at the end of the rise section, and take on the time-dependence described in Eqn. 5.3. The initial charge state populations at $t = \delta$ (beginning of the fall section) are defined to be the calculated values of the numerical solutions of the charge state populations at the end of the rise section. The fit parameters Γ_h, Γ_e, C_h, C_e, α_{re}, α_{rh}, β_r, α_{fe}, α_{fh}, and β_f are extracted for each above-band power. The constants Γ_h, Γ_e, C_h, C_e are considered to be independent of the system being in the rise section or the fall section due to being related to pathway probabilities per population, and are thus common factors between the rise and fall sections. The constants directly associated with the reservoir charge carrier populations $P_e(t)$ and $P_h(t)$ are allowed to differ for the rise and fall sections. During the rise, the reservoirs are filled via creation of mobile carriers induced by the above-band excitation laser. During the fall, the reservoirs deplete and the carriers do not necessarily deplete via the exact mechanisms by which they were filled. Thus, the rates (αs) and the shape parameters (βs) are allowed to vary between the rise and fall sections to account for the different mechanics. Recall, as previously stated, in order to keep the model as simple as possible, we did not allow the shape parameters to vary for electrons and holes, although they were allowed to vary between the rise and fall sections. The justification behind this is that the shape parameters describe the net 'type' of environment through which charges migrate, i.e. whether the environment induces sub-diffusion-like, regular-diffusion-like, or super-diffusion-like dynamics. Of course, the mobility different between electrons and holes will cause the different carriers to migrate through said environment at different rates, which is incorporated in the differing αs. The fits were started on one side of above-band power space and the extracted fit parameters were used as the initial guesses for the fit of the next data set in above-band power space, and so on. Ultimately, the extracted parameters were plotted vs above-band power such that their dependencies on above-band power could be investigated.

---

[9] If the reader is interested in the details of the Matlab code I wrote, they are encouraged to inquire with my advisor or me.

[10] The intensity of the fluorescence when then above-band laser is off is effectively zero, hence the assumption the system is mostly in the charged state at $t = 0$.

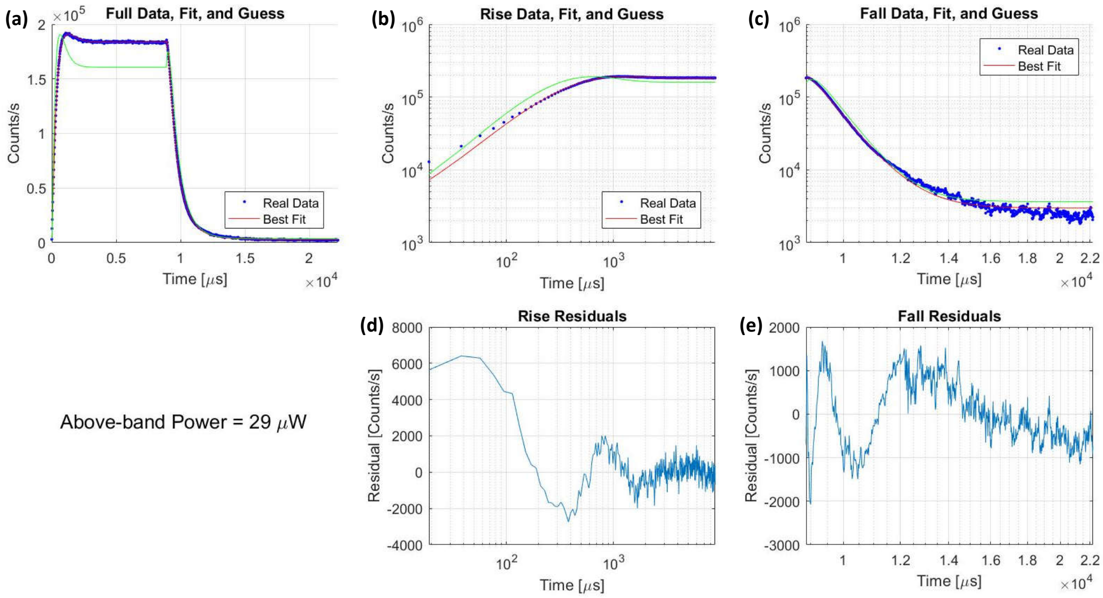

FIGURE 5.7: Example plots of the numerical solution of the model fit to the area under the Lorentzian fit of the time-dependent excitation spectrum for a given above-band power. (a)-(c) shows the fit. The fitting function requires guess values for the numerical model. The real data is depicted by blue dots, the numerical solution using the guess values for the fit parameters is shown in green, and the actual fit is show in in red. (a) shows the entire fit of the rise and fall sections on a linear scale, (b) shows the fit of the rise section on log-log plot, and (c) shows the fit of the fall section on a log-log scale. The residuals of the rise and fall fits are shown in (d) and (e), respectively, which are much smaller than the data values.

The numerical solutions of the areas under the Lorentzian fits of the time-dependent excitation spectra described above are quite good and were able to fit the different shapes of the transients for different above-band powers. An example fit is shown in Fig. 5.7. The analysis of the extracted fit parameters is still in the early stages, and thus cannot yet be discussed in much detail. However, some preliminary analysis can still be addressed here. It needs to be noted that the values of the extracted parameters for the lowest above-band power has very large uncertainties, and thus should be taken with a grain of salt[11]. Because of this, in the following figures, the uncertainties are omitted for a better display of the extracted values, since they are so large for the extracted parameters associated with the lowest above-band power.

---

[11] The following analysis thus partially ignores the values for the lowest above-band power.

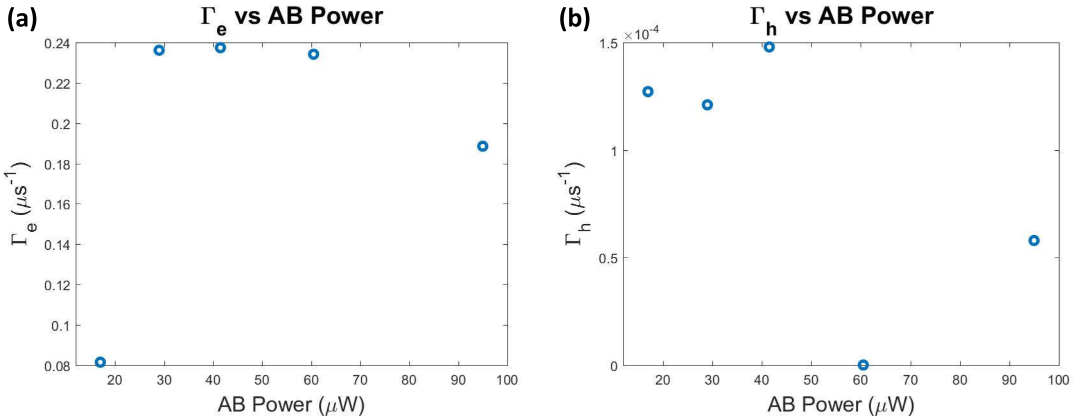

FIGURE 5.8: Extracted carrier ejection rates from the system as a function of above-band power for (a) electrons and (b) holes. The carriers were allowed to leave the system entirely.

Figure5.8 depicts the ejection rates from the system (Γs) as a function of above-band power. There is little dependence of the ejection rates as a function of above-band power for both carrier types. This is consistent with the notion that the ejection rates from the system are likely due to events that are induced by means other than the above-band laser. In regards to relative magnitudes, $\Gamma_e \gg \Gamma_h$. That is, the ejection rate that tends to charge the QD is negligibly small compared to the ejection rate that tends to neutralize the QD.

The capture rates into the QD from the reservoir (Cs) are depicted in Fig. 5.9. The electron capture rate decreases as a function of above-band power, while the hole capture rate has little dependence on above-band power. Recall, the resonantly driven state is the neutral state and the system shifting into the charged state reduces the fluorescence intensity. Capture of an electron from the reservoir when initially in the neutral states causes the system to become charged, while capture of a hole when in the charged state causes the system to become neutral. Carrier capture that induces the system to transfer to the charged state decreases with above-band power, which is consistent with the fluorescence intensity increasing with above-band power. However, the hole capture rate being independent of above-band power is a bit puzzling, because I would expect there to exist an inverse relation to the electron capture rate. Regarding the magnitudes of the capture rates, $C_h \gg c_e$, which means the capture rate of the carrier type that tends to put the system in the neutral state is much greater than that that tends to put the system in the charge state. This imbalance between the

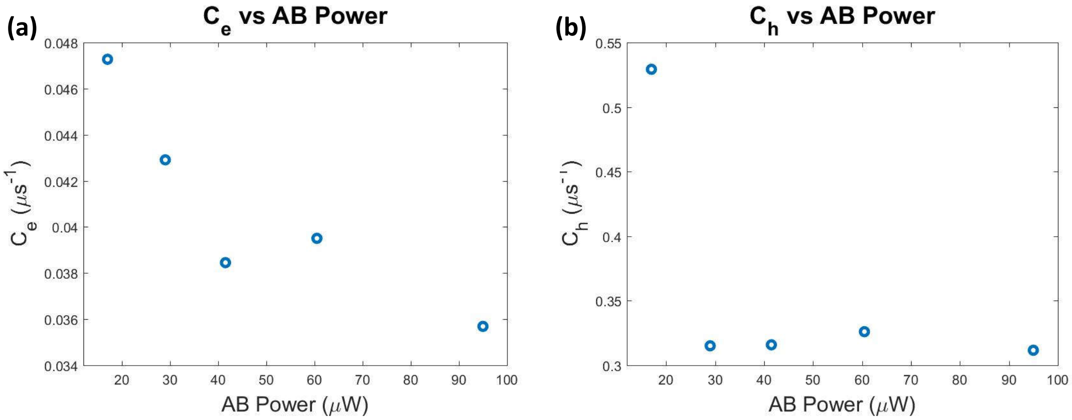

FIGURE 5.9: Extracted carrier capture rates from the reservoir as a function of above-band power for (a) electrons and (b) holes. The capture rates are proportional to the populations of carriers in the reservoir.

capture rates for the two carrier types mimics the imbalance observed between the two ejection rates described above.

We now will discuss the extracted parameters that are directly associated with the reservoir populations $P_e(t)$ and $P_h(t)$. Figure 5.10 depicts the reservoir filling rates during the rise section as a function of above-band power. As a function of above-band power, the electron capture rate into the reservoir increases, while the capture rate for the hole decreases. This is a bit puzzling, because I would expect both rates to increase with above-band power, since the above-band excitation should create both electrons and holes in the surrounding GaAs matrix. The magnitude of the reservoir capture rates are of the same degree, but that for the electron is roughly twice as large.

The reservoir depletion rates vs above-band power during the fall section are depicted in Fig. 5.11 for both carrier types. Both reservoir depletion rates decrease as a function of above-band power. This is consistent with the depletion of the reservoir happening mostly via migration of charge carriers through the stochastic distribution of transport sites described previously in this chapter and Chapter 4. Recall, such an environment results in the sub-diffusion-like charge dynamics analogous to a group of people crossing a ford in a creek via randomly distributed stepping stones. If someone is in front of you, you must wait for them to proceed to the next stone before you can proceed. When the above-band excitation power is higher, more transport sites are occupied during the rise section. Thus, when the above-band laser is turned off in the fall

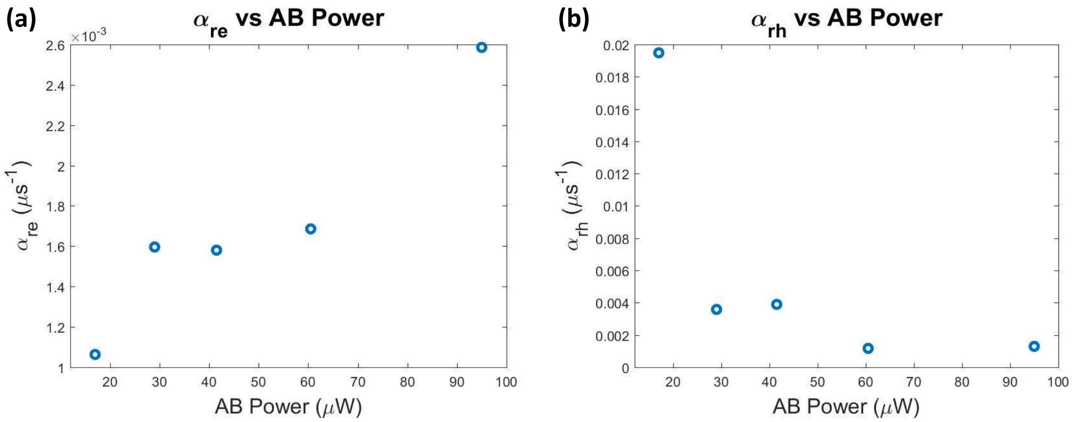

FIGURE 5.10: Reservoir filling rates during the rise section as a function of above-band power for (a) electrons and (b) holes.

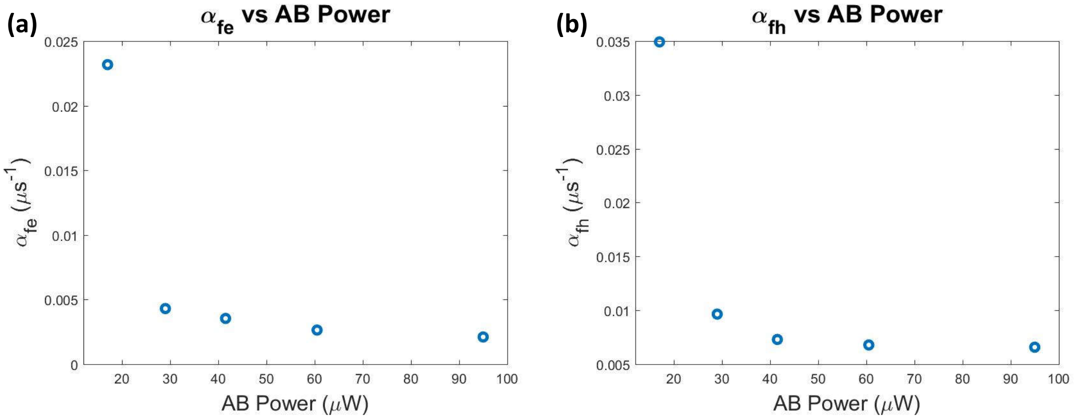

FIGURE 5.11: Reservoir depletion rates during the fall section as a function of above-band power for (a) electrons and (b) holes.

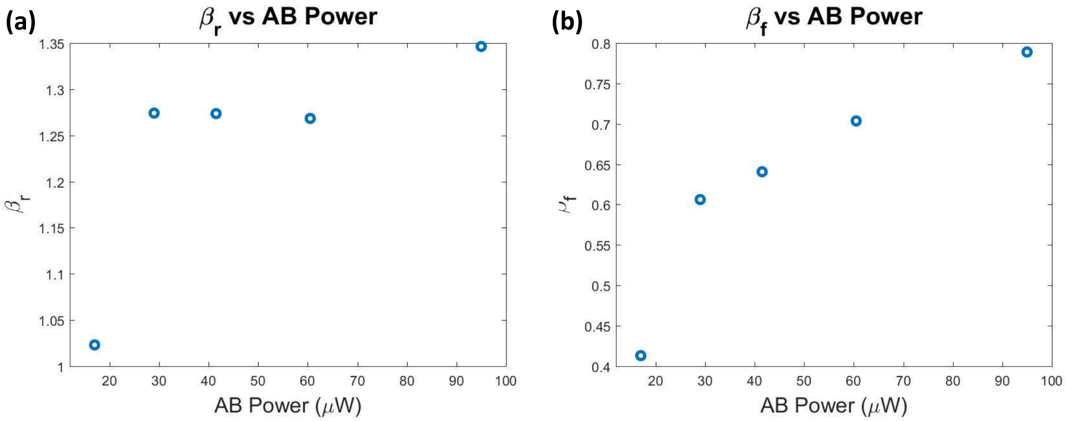

FIGURE 5.12: Exponential shape parameters for the (a) rise and (b) fall.

section for the higher powers, the depletion rates are smaller than compared to lower above-band powers, where a significant population of unoccupied transport sites allows for a higher average rate of carrier migration through the pathways through which the reservoir depletes. Similar to the reservoir filling rates, the magnitudes between the two carrier types are of the same order, but that for the electron is again approximately twice as large.

The unit-less exponential shape parameters are depicted in Fig 5.12. Both shape parameters increase with above-band power, but less so for the rise section as opposed to the fall section. For the rise section, $\beta > 1$, which implies super-diffusion-like charge dynamics into the effective reservoir. Recall, the above-band laser creates hot carriers due to its high photon energy with respect to the band-gap energy of the semiconductors of the heterostructure. Due to their high kinetic energy and being created within a small volume, the carriers initially move ballistically until they cool via phonon emission. As they cool, some of them make their way into the effective charge reservoir in the vicinity of the QD. Thus, it makes sense for the charge reservoir to fill with mostly compressed exponential time dependence after the above-band laser is turned on. It also makes sense that the degree to which the exponential is compressed increases with above-band power, because the higher the above-band power the more hot carriers will be created in a small volume, and the more ballistic-like they will migrate as they cool. For the fall, $\beta_f < 1$, which is consistent with the effective reservoir mostly depleting through the stochastic distribution of transport site of which it is likely composed of. However, I would expect the value of β_f to decrease with above-band power, because as the above-band power is increased, more of the transport sites are occupied with carriers during the rise section. Thus, for higher above-band powers, after the above-band laser is turned off, I would expect the reservoir to deplete with more sub-diffusion-like dynamics, hence be described by an exponential that is more stretched (decreasing β).

5.4 Conclusion

In Chapter 4, the charge dynamics of InAs QDs under both resonant and above-band excitation were investigated via analysis of transients in the TRRF as the above-band laser was turned on and off. However, we neglected to consider that when the above-band laser is turned on and off, the local charge environment in the vicinity of the QD changes, which likely induces shifts of the QD's resonance. In this chapter we similarly measured TRRF relative to the above-band laser turning on and off while exciting a neutral electronic transition[12], but for multiple different near-resonant values of the resonant laser's frequency[13]. For a given above-band power, the TRRF were stacked side-by-side creating effective time-dependent excitation spectra. Temporal slices of the effective excitation spectra were fit with Lorentzian profiles, of which time-dependent center frequencies, FWHMs, and areas under the Lorentzian lineshapes were extracted and analyzed.

The time-dependent center frequency was the directly relevant quantity to our stated concern regarding the analysis in Chapter 4. The above-band laser turning on and off did indeed induce shifts of the QD's resonance ranging from approximately 125 to 340 MHz for the above-band powers investigated. We anticipate this to affect the values of the extracted parameters of the fits of the TRRF in Chapter 4, but not induce a large enough of an effect to make our general conclusions invalid. That is, (1) for a charged QD, the neutralization (change from a charged to a neutral state) is dominated by Auger recombination. (2) There appears to exist a network of two effective charge reservoirs. One reservoir that induces super-diffusion-like dynamics that supplies charges to the second reservoir, and another that induces sub-diffusion-like dynamics of charge that can be

---

[12] Recall, we were unable to find a charged QD in the second sample

[13] Recall, the resonant frequency is defined when the above-band laser is left on and not modulated, i.e, during the steady-state

captured by the QD. The super-diffusion-like process is associated with ballistic-like diffusion of initially hot, densely populated charge carriers excited by the focused above-band laser and its shallow penetration depth into the sample. Some of these carriers make their way into the local environment of the QD as they cool to the bottom of the CB of the bulk GaAs. The sub-diffusion-like dynamics are thought to be induced via migration of charge carriers through a stochastic distribution of weakly-binding transport sites in the local environment after the carriers cool. The transport sites are likely impurities and defects in the GaAs matrix that provide shallow electric potentials for the carriers to weakly bind to. Lastly, (3) that as the QD in Chapter 4 neutralizes after the AB excitation is turned off, there exists a slight recharging of the QD via capture of charges from the local charge reservoir as it depletes.

The FWHM of the Lorentzian fits of the time-dependent excitation spectra were observed to increase after the above-band laser was turned off, as well as to increase with decreasing above-band power. This is consistent with the idea that at the higher above-band powers, the population of charge carriers in the reservoir that consists of pathways of weakly-binding transport sites saturates. As most of the transport sites become occupied by carriers, the pathways through which they can migrate become ′clogged′. This results in a partial ′freezing′ of the local charge environment as the average rate of carrier migration to adjacent transport sites decreases, which consequently results in less spectral diffusion and a smaller FWHM in the measured excitation spectra. When the above-band laser is turned off, the local charge reservoir begins to deplete, and as time progresses, more transport sites become unoccupied. Consequently, the average rate of migration of carriers to adjacent transport sites increases with time after the above-band laser is turned off. The resulting increasing in the temporal derivative of the local net electric field as a function of time induces an increasing degree of spectral diffusion, which is observed in the increasing FWHM.

The integral of the time-dependent excitation spectra (area under the Lorentzian fits) is directly proportional to the time-averaged population, or occupation, of the probed state (here the neutral state). We derived a two-population model of the charge state described by a set of differential equations that quantify the time dependence of time-averaged populations of both the neutral and a charged state. The time-dependent areas of the excitation spectra were fit with a numerical solution of the time-dependant neutral state population in the model for each above-band power. The model's fit parameters were extracted and analyzed[14].

The ejection rates of carriers out of the QD showed little dependence on above-band power. The capture rate of the charge carrier that would put the system in the charged state decreased as above-band power increased, which is consistent with the observed increase in fluorescence intensity from the neutral state with increasing above-band power. The carrier capture rates into the local charge reservoirs (during the rise) showed conflicting dependence on above-band power. The reservoir capture rate of the carrier with the same charge as was arbitrarily chosen for the charged state in the model increased with above-band power, while the capture rate of the opposite carrier type decreased. Since the above-band excitation creates mobile electrons and holes, I would expect both reservoir capture rates to increase with above-band power.

Both reservoir depletion rates (during the fall) decreased with increasing above-band power. This is consistent with the presence of more drastic sub-diffusion-like charge dynamics during depletion of the reservoir when using higher above-band powers. The higher above-band powers induce occupation of a larger number of transport sites that make up the pathways through which the reservoir depletes, resulting in a "clogging" effect of the pathways. Lastly, the shape parameters associated with the time-dependence of the carrier populations in the reservoir took on compressed exponential values for the rise sections, and stretched exponential values for the fall sections. The compressed exponential time-dependence of the filling of the charge reservoir during the rise sections implies it fills significantly via super-diffusion-like dynamics. This is consistent with the reservoir filling with ballistically moving excited carriers. The initial ballistic nature of the carriers is due to them being hot and densely populated upon exciton. This is due to the above-band laser's high photon energy, and them being created in a small volume due to the tight focus and shallow penetration depth of the above-band laser into the sample. The stretched exponential time-dependence of the depletion of the charge reservoir during the fall implies that after the above-band laser is turned off, the carrier populations of the reservoir deplete with sub-diffusion-like dynamics. These dynamics are

---

[14] Recall, at the present, only preliminary analysis has been conducted for this section.

induced by migration of charge through pathways composed of the stochastic distribution of weakly-binding transport sites via which the reservoir depletes.

Chapter 6

Utilization of the Photon Coalescence Time Window to Quantify Photon Indistinguishability as a Function of Above-Band Excitation Power

6.1 Introduction

The analysis for the experiment considered in this chapter has yet to begin, besides a preliminary "first look" analysis; data acquisition has only recently finished. Thus, mostly the experimental methods will be discussed. This experiment involves quantifying photon indistinguishability of the resonance fluorescence from a neutral QD as a function of above-band power. The indistinguishability is quantified by calculation of the coalescence time window (CTW), which will be described below. The preliminary "first look" at the data will be addressed. Further detailed analysis and an ultimate publication will ensue in the following months.

Two major characteristics are required for a photon source to be able to be utilized in the construction of quantum bits for quantum information protocols: it's necessary for the source to produce a stream of single photons, and the photons need to be indistinguishable from each other. The prior characteristic can be quantified via a simple Hanbury Brown-Twiss measurement that was described in Chapter 1. The source is set incident of a 50:50 BS and observation of the photon count rate for each output is measured with single-photon detectors. A detected arrival of a photon at one detector starts a clock, while a detected arrival of a photon at the second detector stops the clock, and the delay time τ between the start clock and stop clock is recorded by a time-correlated single photon counting module (TCSPCM). An integrated measurement over a long time compared to the average time between the clock starting and stopping is conducted, and the TCSPCM builds a histogram of arrival times τ over the duration of the experiment. The resulting measurement is that of the second-order correlation function $g^2(\tau)$. For a single photon source exhibiting sub-Poissonian statistics, $g^2(0) = 0$. This effect is dubbed antibunching and its presence is indicative of a single photon source.

In 1991 Mandel stated that the degree of coherence equals the degree of indistinguishability [112, 113], which heralded the ability to quantify the indistinguishability of a single photon source. Photon indistinguishability is quantified via analysis of correlation measurements on the two outputs of a Mach-Zehnder interferometer (MZI). Until now, our lab had yet performed any such measurements due to lack of an MZI. Thus, I assembled a fiber-based MZI to be used to measure photon indistinguishability. In parallel with my previous experiments in which I investigated the effects of above-band laser power on the charge dynamics in our samples, I used used the MZI to measure photon indistinguishability as a function of above-band power for a neutral electronic transition in an InAs QD.

In a two-photon interference Hong-Ou-Mandel (HOM) experiment [36], as described in Chapter 1, indistinguishable photons from two sources, or from separate arms of an MZI, are combined at the two inputs of a BS (second BS in an MZI) and the coalescence will be detected through a drop of the coincidence rate at the outputs (the HOM dip). In our case, this is achieved by sending quantum dot fluorescence into the fiber based MZI, which is split into two effective sources at the first beam-splitter (BS) and recombined at the second BS of the MZI. If the two effective light sources are indistinguishable, two photons simultaneously arriving at the second BS will be forced to leave the same exit. Ordinarily in an MZI, one arm contains the ability to change its length, which induces different delay times between the two paths. In a fiber-based MZI, the delay time can be changed discretely by insertion of fibers of different lengths into one of the arms, which allows for the coalescence to be measured for multiple different delay times. For a two-level system, the coherence time T_2 and lifetime T_1 are linked to photon indistinguishability. If the radiative limit $T_2 = 2T_1$ is reached, perfect coalescence giving rise to a zero value in the HOM dip is observed. Under continuous wave (cw) excitation, using two ideal ultra-fast detectors, the coincidence rate always vanishes at zero time delay. With real-world detectors that do not have an infinitely short response time, if the temporal resolution T_R (approximately 500 ps for our detectors) is shorter than the coherence time of the photons, the indistinguishability cannot be properly resolved. With a cw source, the value of the coincidence rate at a zero delay time is thus very sensitive to T_R (since T_R T_1, T_2) and does not accurately characterize the intrinsic properties of the source with regard to photon indistinguishability. Thus, a modified approach is necessary to adequately measure photon indistinguishability under cw excitation.

Recent experimental studies focused on the regime of resonant Rayleigh scattering (RRS) under low-power cw excitation, where the incoming photons are elastically scattered. As predicted by theory and shown by homodyne and heterodyne detection experiments [88, 114, 115], the scattered photons inherit the coherence time of the excitation laser T_L, which can be much longer than T_2 and T_R. The resulting QD emission spectrum can be much narrower than the natural linewidth imposed by the radiative limit. Considering that under such conditions the inherited coherence time surpasses T_R, along with Mandel's notion that coherence equals indistinguishability, the RRS regime constitutes the ideal ground for the generation of highly indistinguishable photons.

Proux et al. [116] reported on the coalescence of photons emitted by a single QD resonantly driven by a cw source within the RRS regime. They introduced a new figure of merit, the coalescence time window (CTW), to quantify the delay below which photon coalescence occurs, ultimately estimating the indistinguishability of their photon source as a function of time between photons. Their sample is also InAs/GaAs quantum dots in a planar microcavity and excitation is achieved via a cw tunable external cavity laser diode with variable coherence time. The quantum dot fluorescence was sent through a MZI. In order to prevent fictitious anticoincidences from one-photon interference when performing two-photon interference, the path difference must be larger than the photon coherence time, and thus larger than T_L in the RRS regime. They used optical fibers to create an interferometer delay of up to 43.5 ns. They used a HWP in one of the arms to change the polarization[1] to create either parallel or perpendicular polarizations of the two incident beams at the second BS. If one of the arms is blocked, the setup becomes a Hanbury Brown-Twiss (HBT) setup for measuring the intensity correlation function $g^2(\tau)$. As, previously stated, If an anti-bunching dip is observed at a zero time delay between adjacent photons ($\tau = 0$), then one knows the photon source is a single photon source in the RRS regime. T_1 and T_2 are measured via time-resolved fluorescence using pulsed excitation as described in the lifetime section in Chapter 2.

Proux et al. measures $g^2(\tau)$ under resonant excitation for both parallel and perpendicular polarization setups of the MZI. Theory discussed by Patel et al. [117] predicts the theoretical intensity correlation functions $g_\perp^{(2X)}$ and $g_\parallel^{(2X)}$, convoluted by the instrument response function (IRF) of the HOM setup using single photon detectors with $T_R = 1ns$ [118]. For the perpendicular polarization configuration,

$$\begin{aligned} g_\perp^{(2)}(\tau) = \frac{1}{N}\Big\{&4(T_1^2 + R_1^2)R_2T_2g^{(2)}(\tau) \\ &+ 4R_1T_1\Big[T_2^2g^{(2)}(\tau - \Delta\tau) + R_2^2g^{(2)}(\tau + \Delta\tau)\Big]\Big\}, \end{aligned} \tag{6.1}$$

and for the parallel polarization configuration,

$$\begin{aligned} g_\parallel^{(2)}(\tau) = \frac{1}{N}\Big\{&4(T_1^2 + R_1^2)R_2T_2g^{(2)}(\tau) \\ &+ 4R_1T_1\Big[T_2^2g^{(2)}(\tau - \Delta\tau) + R_2^2g^{(2)}(\tau + \Delta\tau) \\ &- (T_2^2 + R_2^2)V_0|g^{(1)}(\tau)|^2\Big]\Big\}, \end{aligned} \tag{6.2}$$

where $R_{1,2}$ and $T_{1,2}$ are the reflection and transmission coefficients of the first and second BS of the MZI, respectively, $N = 4R_1T_1(R_2^2 + T_2^2) + 4R_2T_2(R_1^2 + R_2^2)$, and $\Delta\tau$ is the delay time between the two arms of the MZI. In Eqn. 6.2 the parameter V_0 is introduced that accounts for all experimental imperfections that destroy the spatial/temporal overlap and/or polarizations of the two beams at the second BS in the MZI. The first-order correlation function $g^{(1)}(\tau)$ is related to the coherence of the two-level system and appears only in the second-order

---

[1] We used the custom polarization controller I constructed and described in Chapter 1.

correlation function for the parallel configuration as part of the two-photon interference term. Note, Proux et al. [116] measured values of the experimental imperfection parameter V_0 of 0.8 for the parallel and 0.15 for perpendicular configurations. If the arms in the MZI created perfect parallel and orthogonal polarizations, V_0 would be 1 and 0 for parallel and perpendicular configurations, respectively.

In the perpendicular polarization configuration in which the photons from each arm of the MZI that are incident on the second BS are nominally completely distinguishable, no interference is expected at the second BS of the MZI, and the measured $g^2(\tau)$ is related to the statistical properties of the single photon source. Compared to an HBT experiment, additional anti-bunching dips shifted by the interferometer path length difference are observed. The measured dip values are resolution limited and determined by the QD intrinsic times T_1 and T_2. At high power, the QD undergoes Rabi oscillations, inducing a narrowing of the antibunching dips [38], and thus a strong reduction of their visibility for a given T_R. Thus, the experiment should be conducted below the saturation power described in Chapter 2 where Rabi oscillations are not observed.

In the parallel polarization configuration in which the photons from each arm of the MZI that are incident on the second BS are nominally completely indistinguishable, in addition to the contribution of the photon statistics, a component due to photon coalescence is observed. At low power, two dynamics can be distinguished: a fast one at $\tau << \tau_R$ characterized by the intrinsic QD time constants T_1 and T_2, and a much slower one characterized by the excitation laser coherence time T_L. The fast dynamics reflects the photon statistics and the coalescence of the inelastically scattered photons, whereas the slower one is directly linked to the coalescence of the elastically scattered photons. At high power, the ratio of the elastically scattered photons drops, inducing the long time component to get notably attenuated [116].

Classically, the photon indistinguishability is characterized by the two-photon inference visibility measured at the outputs of the MZI. The two-photon interference visibility is defined as:

$$V_{HOM}(\tau) = \frac{g^2_{\perp}(\tau) - g^2_{\parallel}(\tau)}{g^2_{\perp}(\tau)}. \tag{6.3}$$

The usual way to assess the indistinguishability of the photon source is to use the value $V_{HOM}(0)$. However, this value is altered by the time resolution of the detectors' T_R. In order to take into account the long coherence time of the elastically scattered photons along with the visibility at $\tau = 0$, one calculates the time integration of the visibility curve, called the coalescence time window (CTW) [116]. This parameter is independent of T_R. Proux et al. measured the CTW for multiple different delay times via implementation of different delay fiber lengths in one arm of the MZI.

6.2 Experimental Methods and Preliminary Analysis

In this report we used the CTW method to characterize the indistinguishability of the resonance fluorescence from a neutral InAS QD as a function of above-band power. The QD was excited resonantly with a cw tunable diode-laser source, and an above-band laser was also focused onto the sample surface to maintain the probed charge state, as in Chapters 4 and 5. In comparison to the experiments discussed in those chapters, the above-band laser was not modulated, but the above-band power was changed between data sets. As in Chapters 4 and 5, the fluorescence was filtered via propagation through a 900 nm longpass filter and a spectrometer. The fluorescence was sent to exit the spectrometer and coupled into a fiber-based MZI composed of polarization-maintaining optical fibers. The experimental setup is depicted in 1.17. After the first BS, the fluorescence is split between the MZI's short and long arms. Two separate fibers were able to be connected and disconnected in the long arm. One fiber was a polarization-maintaining fiber depicted as the single blue coil in 1.17. The other fiber was a single-mode fiber that was not polarization-maintaining and is depicted as the yellow thrice coiled fiber in 1.17. The three coils represent the polarization controller I built through which the fiber is sent, which is depicted in Fig. 1.18.

The polarization controller involves three paddles that are allowed to be angled about a pivot. The fiber is coiled once through the first paddle, twice through the second, and three times through the third. These act roughly as a quarter-wave, half-wave, and three-quarter-wave plate, respectively. Setting a given angle of each paddle is analogous to setting the angle of a corresponding wave plate. With careful positioning of the three paddles, any arbitrary input polarization can be changed to any other polarization at the output. Thus, the polarization controller was used to make the polarization in the long arm perpendicular to that in the short arm.

When the blue fiber is inserted in the MZI's long arm, since both the long and short arms are composed of polarization maintaining fibers, if the fluorescence was made up of indistinguishable photons upon introduction to the input of the MZI, the interference at the second BS of the MZI will be that of indistinguishable photons, and the HOM dip will be observed in the correlation measurements at the output of the MZI. When the yellow fiber is used to make the polarization in the long arm perpendicular to that in the short arm, the light sources recombining at the second BS of the MZI will be nominally completely distinguishable. The second order correlation function ($g^2(\tau)$)[2] is measured at the output of the MZI via two single-photon detectors (labeled as APDs in Fig. 1.17), one at each output of the MZI, and a TCSPCM which constructs a histogram of times between one APD starting the clock and the other stopping it. After $g^2(\tau)$ is measured for both the perpendicular and parallel configurations of the MZI, the visibility can be directly calculated via Eqn. 6.3 and ultimately the CTW, via integration of the visibility.

The spatial/temporal delay between the long and short arms of the MZI were kept constant. In order to be able to sweep through the full interference at the output, the optical path length difference between the arms has to be swept a minimum distance equal to a half wavelength of the propagating light. However, the magnitude of the random fluctuations of the lab's temperature are large enough to induce fluctuations in the index of refraction such that the resulting fluctuations in the optical path length difference between the two arms is greater than a half wavelength of the propagating light. The single-mode fibers used in the experiment consist of an un-doped pure silica core surrounded by a depressed, fluorine-doped cladding. The temperature T dependence of the optical path length S of a transmissive medium is given by,

$$\frac{dS}{dT} = \frac{dn}{dT} + n\alpha, \tag{6.4}$$

where n is the refractive index of the medium, dn/dT is the temperature coefficient of the refractive index (which is wavelength dependent), and α is the coefficient of thermal expansion of the medium material. Koike and Sugimoto [119]

---

[2] See 1 for details regarding measurement of $g^2(\tau)$.

investigated temperature dependencies of optical path length in varies glasses. Since a wavelength of 1550 nm is the most commonly used in optical communications systems due to low absorption at that wavelength, Koike and Sugimoto's experiment used refractive index values for 1550 nm light. However, we still can acquire an idea of the optical path length difference induced in our MZI for the wavelength of the QD fluorescence 925 nm. They show that for pure silica and 1550 nm light $dS/dT = 9.39ppm/^\circ C$. The long arm in our MZI is 5 m longer than the short arm. For a temperature change of $0.1^\circ C$, dS/dT $1ppm$, which corresponds to changes in the optical path lengths of the two arms that differ by approximately 5 microns, which is an order of magnitude greater than a half wavelength of the QD fluorescence propagating through the MZI. Thus, the fiber-based MZI needs to simply sit on the optical table and small natural fluctuations in the ambient temperature will induce large enough fluctuations in the optical path length difference between the two arms to sweep through the full interference observed at the output.

An example of measured $g^2(\tau)$ for both the parallel and perpendicular configurations of the MZI, as well as the calculated visibility and CTW is shown in Fig. 6.1 for a given above-band power. As previously mentioned, the analysis for this project is at ground zero. The following analysis is simply a quick first look; for instance the data shown here is actually the $g^2(\tau)s$ convolved with the IRF of the measurement system. The IRF was indeed measured, and deconvolution will be incorporated in the more sophisticated analysis that will follow in the following months. Note that no fitting is necessary to calculate the CTW, since we measured $g^2(\tau)$ for each polarization configuration directly and the CTW is calculated simply as the integral of the visibility. The reflection and transmission coefficients, as well as the QD lifetime, were measured and will be used to fit the measured $g^2(\tau)s$ with Eqns. 6.1 and 6.2 when the detailed analysis commences.

Consider the possible pathways two adjacent photons can take through the MZI. Both photons can take either the short or the long path, the first can take the long and the second the second the short, or the first the short and the second the long. Every instance results in a measured dip in $g^2(\tau)$ due to the single photon nature of the fluorescence. The dip caused by the first two instances occurs at the same delay time, while the latter two induce dips in $g^2(\tau)$ at their respective delay times. Thus, due simply to the single photon nature of the

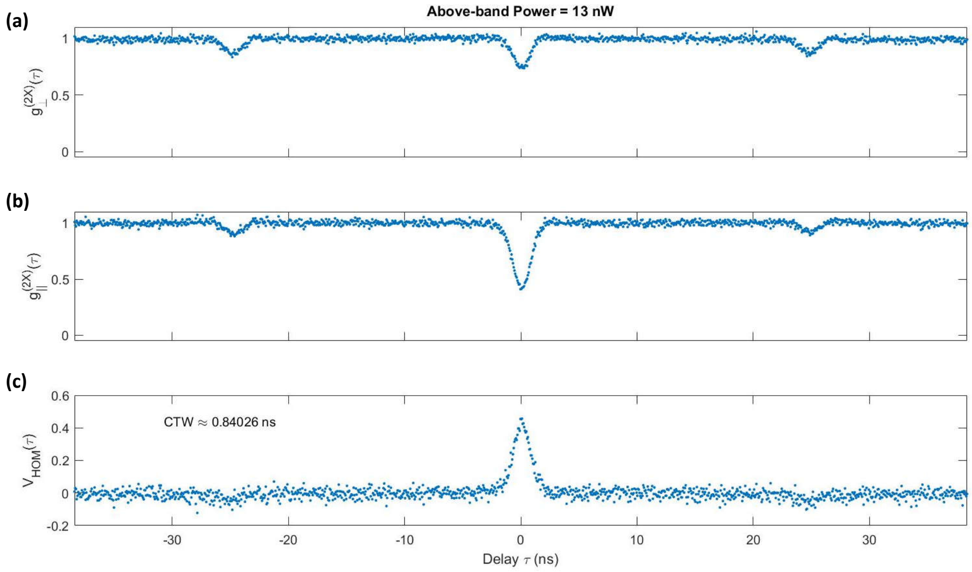

FIGURE 6.1: Example measured (a) $g_{\perp}^{(2X)}(\tau)$ and (b) $g_{\parallel}^{(2X)}(\tau)$, as well as (c) the calculated visibility and CTW for an above-band power = 13 nW.

light source, for the case in which the interference at the second BS of the MZI is between nominally completely distinguishable photons (perpendicular polarization configuration), one observes three dips: one center dip associated with the two photons taking the same path in the MZI, and two side dips for the other two cases, which can be seen in Fig. 6.1(a). Due to twice as many instances creating the center dip as opposed to the side dips, the center dip is deeper. The center dip is set to be at a delay time $\tau = 0$ via an electronic delay set in the TCSPCM's software. The distance of the side dips in time are displaced from the center dip by the time equal to the temporal delay between the two arms of the MZI. However, for the parallel polarization configuration of the MZI, the photons are nominally indistinguishable (or at least possess some degree of indistinguishability), and HOM interference induces a deeper center dip at $\tau = 0$ while the side dips are still only induced by the single photon nature of the light source. Thus, one observes flat features in the calculated visibility at the delay times associated with the side peaks in the $g^2(\tau)s$.

A preliminary look at the CTW vs above-band power without performing deconvolution of the measurement systems IRF with the measured $g^2(\tau)s$ is

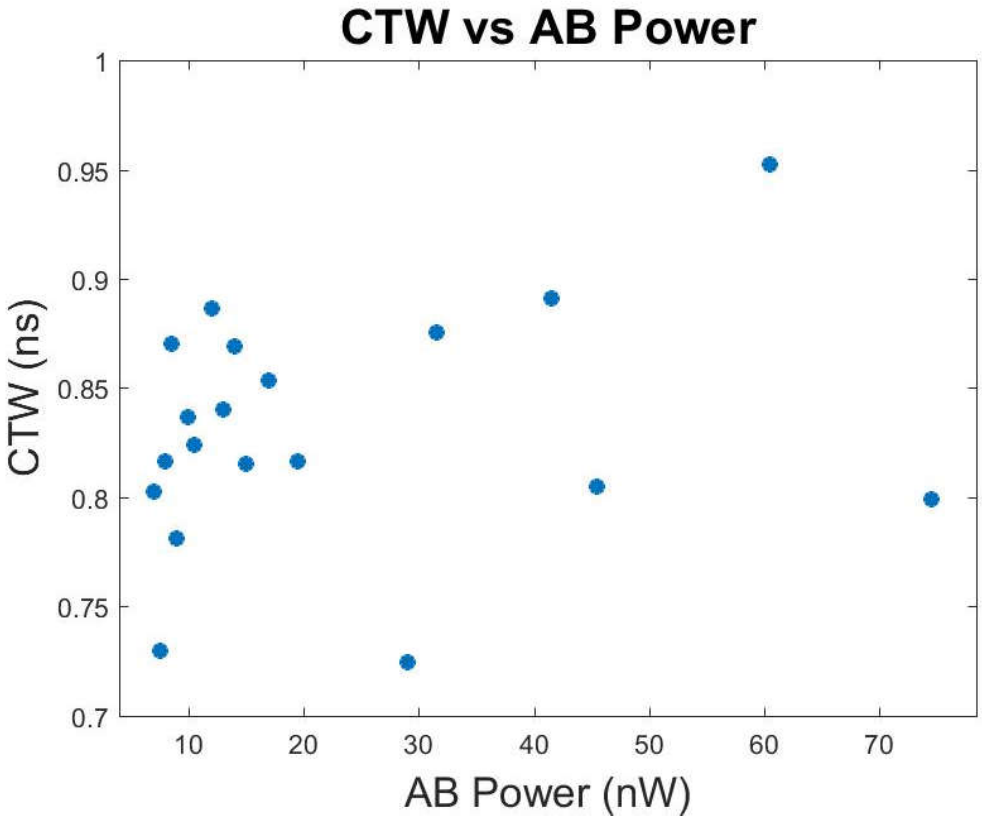

FIGURE 6.2: CTW vs above-band power for the preliminary analysis.

shown in Fig. 6.2. For the 19 above-band powers investigated, there is unfortunately no clear dependence in the calculated CTW vs above-band power. However, the in-depth analysis of the CTW as a function of above-band excitation power, including deconvolution of the IRF from the measured $g^2(\tau)s$, as well as theoretical fits of the $g^2(\tau)s$ will be conducted in the following months. In regards to said future fits, the degree to which the two arms of the MZI contains perpendicular or parallel polarizations is not perfect. This effect is incorporated into the factor V_0 in Eqn. 6.2, and is quantified via measurement of the fluorescence contrast between the two outputs of the MZI. Due to the HOM effect, if the photons in the two arms are completely indistinguishable, the contrast of the measured interference at the outputs of the second BS will be maximum (unity), while if the photons in the two arms are completely distinguishable, a contrast of zero would be measured after the second BS due to complete lack of HOM interference. It is our hope that in the more sophisticated analysis to follow, that we will observe and discuss trends in the CTW as a function of above-band power.

Chapter 7

Conclusion and Outlook

7.1 Conclusion

Sources of single, indistinguishable photons have potential to be used in implementation of quantum information protocols. Resonant excitation of self-assembled, epitaxially-grown InAs QDs is a prime candidate for the production of single, indistinguishable photons. However, resonant excitation often changes the charge state of the QD, resulting in a reduction of the resonance fluorescence intensity from the resonantly-driven optical transition due to differences in excited electronic transition energies for different charge states.

Application of additional low-power above-band excitation can return the initial charge state, allowing the resonant laser to again couple with the resonantly-driven excited transition, ultimately returning the resonance fluorescence intensity. Indeed, for many QDs not incorporated into a diode structure, application of low-power above-band excitation is often necessary to produce any significant fluorescence intensity from resonant excitation [39–41, 89]. Thus, if using low-power above-band excitation, it is important to understand the mechanisms by which free carriers induced by the above-band light make their way into and out of the QDs in the sample, how the above-band excitation affects the excitation (absorption) and emission spectra of QDs, as well as how it affects the photon indistinguishability of the resonance fluorescence.

The low-power above-band excitation supplies the local environment around the QD with free charges that can become bound by the QD's electric potential, returning the QD to its initial charge state. It appears the charge dynamics are mostly described by carrier migration through two subsequent charge reservoirs, one that supplies the QD with close-proximity charge carriers to be captured, and another which supplies that reservoir with free carriers.

Our sample consists of InAs QDs embedded in a bulk GaAs planar microcavity defined by two DBRs, as shown in in Fig. 1.1. Due to the above-band laser's shallow penetration depth into the sample, most of the free carriers excited by the above-band light are created in the top DBR, far from the QD layer. These carriers are initially hot due to the high photon energy of the above-band laser relative to the band-gap energies of the semiconductors of which the heterostructure comprises. The above-band excitation also induces an initial high density of free carriers due to its shallow penetration depth and it being focused onto the sample via a high numerical aperture lens. The initial high kinetic energy and population density of free carriers causes them to move ballistically for the first several ps as they cool. Some of the free carriers make their way into the vicinity of the QD layer as they cool to the bottom of the CB of the surrounding GaAs matrix. After the above-band laser is turned on in Chapters 4 and 5, we observed compressed exponential time dependence of the filling of the charge reservoir in the local vicinity of the QD. This compressed exponential time dependence is indicative of super-diffusion-like charge dynamics that is affiliated with the ballistic-like nature of the initially hot free carriers.

The charge reservoir in the local vicinity of the QD layer that ultimately supplies the QDs with charge is likely mostly composed of a stochastic distribution of transport sites through which carriers migrate. The transport sites are likely weakly-binding shallow potentials created by defects and impurities in the bulk GaAs matrix. Charge carriers weakly bound to transport sites can "hop" to adjacent transport sites with a probability that drops off exponentially with distance to nearby transport sites. Analogous to a group of people trying to traverse a ford in a creek by jumping through a network of randomly positioned stepping stones, the likely pathways through which carriers migrate is a random network, where "high traffic" pathways are defined by pathways consisting of adjacent transport sites that are within close proximity of each other, as depicted if Fig. A.1. Similar to the group of people crossing the ford in a creek, when a transport site is occupied by a bound charge carrier, it must migrate to a close-by adjacent transport site before another carrier of the same type can migrate into that transport site from the previous one in the effective path. Thus, carriers move through the effective reservoir with sub-diffusion-like dynamics that is described mathematically by stretched exponential time dependence of carrier migration [107].

Recall, spectral diffusion, which is observed as an inhomogeneous broadening of the excitation (absorption) and emission spectra, is attributed to the QD's resonance jittering about a center value as the local electric environment changes. As carriers migrate through the local environment, they modify the net electric field that the QD feels, which shifts the QD resonance via the quantum-confined Stark effect. A time-integrated measurement of the excitation or emission spectrum is thus broadened by this effect. Above-band power dependent RPLE data was used in Chapter 3 to study the quantity of charge traps in the local vicinity of the QD, and their effect on the QDs resonance frequency. We observed four discrete Stark shifts in the RPLE for different above-band powers that were attributed to four combinations of charge occupation of two nearby traps. That is, whether no traps, one trap or the other, or both traps were occupied affected the magnitude and direction of the spectral shift. We calculated that the trap locations must have been within 70 nm of the QD and little to no influence from farther occupied traps was observed. In conjunction with the idea that the charge reservoir is composed of a stochastic distribution of transport sites, likely only a couple of transport sites along specific pathways act as the ultimate "doorways" through which carriers can pass into the QD.

In Chapter 4 we studied TRRF from a charged QD as the above-band excitation laser was turned on and off. The TRRF was recorded with a TCSPCM, which constructed a histogram of photon arrival times incident on an APD relative to a trigger signal (start clock) that is synced to the turning on of the above-band laser. The transients in the intensity of the TRRF were fit with analytical solutions involving terms with regular and shaped exponential time dependencies. We observed evidence of the existence of two separate mechanisms which supply the QD with charge. One mechanism involved super-diffusion-like dynamics of charge carrier migration that is associated with the ballistic-like nature of the initially hot free carriers created by the above-band laser. The other mechanism involved sub-diffusion-like dynamics of carrier migration through a stochastic distribution of transport sites in the GaAs matrix surrounding the QD. These two mechanisms were manifested in a compressed exponential time-dependent term and a stretched exponential time-dependent term observed in the rise transients, respectively. We concluded that the decay of the charged state population after the above-band excitation was turned off was dominated by Auger recombination induced by the resonant laser. Additionally, a ’recharging’ effect was observed as the local stochastic distribution of transport sites depleted of charge. These effects were manifested in a regular exponential time-dependence on short timescales, and a stretched exponential time-dependence on long timescales in the transients of the fall section, respectively.

In Chapter 5 we expanded on the experiment addressed in Chapter 4 by studying TRRF as the above-band excitation laser was turned on and off for not only different above-band powers, but also for different near-resonance frequencies of the resonant excitation laser. The TRRF for each frequency detuning of the resonant laser were stacked side-by-side, constructing time-dependent effective excitation spectra for each above-band power. Temporal slices of the resulting time-dependent excitation spectra were fit with Lorentzian profiles from which time-dependent center frequency shifts, FWHMs, and areas under the curves were extracted and analyzed.

We did indeed observe a spectral shift of the resonance towards the blue when the above-band laser was turned on, and back towards the red when it was turned off. The observed spectral shifts were not insignificant, but were still several times smaller than the absorption linewidth. Thus, we expect the general observations in Chapter 4 to still hold: That is, (1) the initially hot free carriers created by the above-band excitation migrate with super-diffusion-like dynamics as they cool, (2) the effective reservoir around the QD likely mostly consists of a stochastic distribution of weakly-binding impurities/defects acting as transport sites, and (3) the neutralization of the charged state is dominated by Auger recombination. However, the exact values of the extracted parameters in the fits of the transients in Chapter 4 would likely change if we had accounted for this effect.

The time-dependent FWHM of the Lorentzian fits in Chapter 5 decreased with above-band power and increased after the above-band laser was turned off. The width of the FWHM is related to the degree of spectral diffusion experienced by the QD. At higher above-band powers, a larger number of transport sites of the surrounding reservoir become occupied during the rise section. When the above-band power is high enough to fill all of the transport sites, migration of charges through the effective reservoir is minimized. This effective "clogging" of the local charge environment results is smaller fluctuations of the local net electric field felt by the QD, hence inducing a smaller degree of spectral diffusion, which is manifested in the smaller FWHM of the absorption spectrum. After the above-band laser is turned off, the reservoir starts to deplete. As it does, a larger number of transport sites become unoccupied, allowing for a larger net charge migration speed. This induces a situation in which the local electric field is changing more drastically with time, which induces a higher degree of spectral diffusion, which is manifested in the increase of the FWHM after the above-band laser is turned off.

In Chapter 5, the time-dependent areas under the Lorentzian fits of the excitation spectra are a direct probe of the time-averaged charge state of the QD. The value of the areas are directly proportional to time-averaged occupation of the QD charge state associated with the resonantly driven transition (in this case the neutral state), and are independent of spectral diffusion. The time-dependent areas were fit with a numerical solution describing the time-evolution of the charge state populations of the system. Two charge state populations were considered in the model, a charged state and a neutral state. A set of coupled differential equations describing the time evolution of the two charge state populations, which involve the possible mechanisms by which carriers can be ejected from the system or captured from the local reservoir, was devised. The time-dependent areas under the Lorentzian lineshapes were fit very well with the calculated time-dependent neutral state populations for all above-band powers used. The parameters of the model were then extracted and analyzed as a function of above-band power.

The coefficients associated with carrier ejection showed little dependence on above-band power, which eludes to ejection processes being dominated by phenomena not associated with the above-band excitation. The ejection rate that would neutralize the dot was greater, which makes sense since we were using the above-band laser to establish population of the neutral state. The capture rate that would charge the dot decreased with above band power, and the capture rate that would neutralize the dot was larger for all values of above-band power. This is consistent with an observed increase in resonance fluorescence intensity with increasing above-band power.

Both rates associated with the depletion of the reservoir after the above-band laser was turned off decreased with increasing above-band power. This is consistent with the average occupation of transport sites increasing with above-band power during the rise section, which results in a "clogging" effect of the pathways through which carriers migrate. As the above-band power is increased and the transport sites are more efficiently occupied during the rise section, it takes longer for the reservoir to deplete through the pathways due to the necessity of empty adjacent transport sites for a given jump from one transport site to the next to be possible. During the rise section, the reservoir filled with compressed exponential time dependence. This implies that super-diffusion-like dynamics dominate the filling of the reservoir, which is consistent with the notion that the reservoir fills via migration of hot free carriers that initially move ballistically due to their high kinetic energy and high population density upon creation. Finally, during the fall section, the reservoir depleted with stretched exponential time-dependence, which inferred sub-diffusion-like dynamics. This implies that the depletion of the local reservoir occurs via migration of carriers through the stochastic distribution of transport sites composed of weakly-binding defects and impurities.

Recall, that one of the most important features a photon source must posses to be utilized in quantum information protocols is photon indistinguishability. Until now, our lab had not conducted any experiments quantifying the indistinguishability for any QD transitions. We thus conducted an experiment to measure photon indistinguishability of a resonantly excited QD as a function of above-band excitation power. In order to measure photon indistinguishability, we utilized calculation of the coalescence time window (CTW). This involved coupling resonance fluorescence from a neutral QD into a fiber-based MZI and measuring the visibility of the second-order correlation functions at the outputs of the MZI for two different polarization configurations.

Two measurements are necessary to compare: one in which the two arms of the MZI before the second BS in which interference occurs have relative parallel polarizations, and one in which they have relative perpendicular polarizations. For each case, three antibunching dips are observed due to the single-photon nature of the fluorescence and the possible paths that adjacent photons can take while traversing the MZI. However, for the parallel configuration only, HOM interference due to photon indistinguishability (observed via coalescence at the outputs) is manifested in a deeper HOM dip at a delay time of $\tau = 0$. The visibility, which is proportional to the difference in the correlation functions of the two cases, is then calculated. Classically, the indistinguishability is calculated from the amplitude of the visibility at a zero delay time (i.e, where the HOM interference occurs). However, this value is modified by the response time of the detectors used to measure the second-order correlation functions. However, the coalescence time window (CTW), which is the integral of the visibility, is independent of the detectors' response times, and thus makes for a better parameter to quantify photon indistinguishability [116].

We measured the coalescence time window for 19 different values of the above-band excitation power. Data acquisition was only recently finished and detailed analysis has yet to commence. Without deconvolution of the data with the measurement system's IRF, we calculated the CTW vs above-band power as a "first look" analysis, and unfortunately found little dependence on indistinguishability as a function of above-band power. However, in the following months, detailed analysis will ensue and hopefully interesting relations will be observed.

7.2 Outlook

7.2.1 Additional Investigations Involving the Charge Dynamics of InAs QDs

The model describing the time evolution of the time-averaged charge state of the QD in Chapter 5 takes into account two different carrier types. However, the difference in carrier mobility is not addressed anywhere in the model. This is likely reflected in the values of the fit parameters associated with ejection from the system, capture from the reservoir, and the filling and depletion rates of the reservoir. However, perhaps a more sophisticated model that incorporates the mobilities of the carriers could be incorporated. We initially devised a three population model that allowed the system to go between the neutral state and either the positive or negative charge states. However, due to the symmetry of that system, we decided to simplify the model by considering only one charged state and a neutral state. We may want to reconsider looking back at the analysis using the three population model to confirm this simplification was indeed justified.

Additionally, only five different above-band powers were used in the experiment described in Chapter 5. From personal experience, I know there is an optimal above-band power that results in a maximum fluorescence intensity for a given optical transition. When the above-band power is increased beyond that, the fluorescence intensity starts to decrease. My hunch is that the maximum fluorescence intensity corresponds to the above-band power that *just* fills the local transport sites, and reoccupies them immediately after transport sites become unoccupied. This will allow for the QD to capture carriers with a high efficiency in order to maintain the largest time-averaged charge state population of which the resonant laser is exciting, and also induce the "clogging" effect described previously. I imagine as the above-band power is increased beyond this point, more free carriers are moving around in the local environment, unable to bind to already occupied transport sites. This would result in an increase in the degree of spectral diffusion and would be manifested in the time-dependent excitation spectrum's FWHM. The power needed to enter this regime may be fairly high, and it would be good to repeat the experiment using many different above-band powers that range from when the fluorescence is barely visible to orders of magnitude greater than the power that results in the maximum fluorescence.

The experiment can also be conducted on a charged QD to see if a similar model can be applied. As opposed to the neutral QD, the model describing the time-averaged charge state for a trion would have to incorporate an additional ejection term associated with Auger recombination. The extracted parameters' values as a function of above-band power could then be compared to the results in Chapter 5.

The entire experiment in Chapter 5 could also be conducted using different resonant powers, so that the rates associated with different types of carrier migration could be studied vs resonant laser power in addition to above-band power. For instance, with a charged QD, I would expect the coefficient associated with Auger recombination to saturate with resonant power, as observed in Chapter 4.

Lastly, these InAs QD samples are often incorporated into a diode structure. In this type of structure, a tunable voltage can be applied across the sample, which bends the entire band structure. Depending on the degree of bending of the band structure and the polarity of the applied electric field, the QDs in the sample can be forced into any charge state (negatively charged, neutral, or positively charged). Of course, there exist intermediate voltages in which occupation of more than one charge state is possible. It would be interesting to conduct an experiment similar to that described in Chapter 5. TRRF could be measured as a function of applied voltage as the electric field is turned on and off in a diode structure. I expect there to still exist sub-diffusion-like dynamics of carrier migration, because the same types of defects and impurities exist in this sample as do in the samples used in my investigations. When the voltage is turned on, I also expect to see super-diffusion-like dynamics of carrier migration, since the electric field will apply a net force, and hence an acceleration, on the carriers, causing them to move ballistically.

7.2.2 Additional CTW Measurements

In addition to studying the indistinguishability of photons emitted from a two-level transition in our sample, we can also use the CTW method to study the indistinguishability of a 3-level system as studied in Ref. [120]. In that work the steady-state coherence between the two neutral exciton states of a given QD was studied via resonant excitation using a cw laser sent through a linear polarizer. The excitation polarization was set to roughly 45 degrees with respect to both dipole moments of the two possible neutral optical transitions (also linearly polarized). Many resonant excitation experiments use crossed polarizers to attenuate the laser scattering and allow detection of the resonance fluorescence [46, 72, 79, 121–123]. The fluorescence detection is necessarily polarization-selective in this experimental setup. In [99], it was shown that when polarization-selective detection is used, orthogonal dipole moments cause an interference effect that results in an unconventionally shaped excitation spectrum. The QD-field interaction will cause both coherent scattering at the laser frequency [88, 124, 125] and incoherent spontaneous emission at the transition dipole frequencies. Interference between the fields coherently scattered from the two orthogonal dipoles results in a noticeable difference between the shapes of the excitation spectra for detection polarizations parallel and orthogonal to the excitation. By measuring polarization-dependent excitation spectra for polarizations aligned to the transition dipole moments and also for polarizations rotated 45-degrees with respect to them, extraction of the real part of the coherence between the two fine structure states was achieved [99].

Multiple resonant photoluminescence excitation (RPLE) spectra were recorded using multiple different detection polarizations and a single excitation polarization. Two liquid crystal variable retarders (LCVRs) in conjunction with a linear polarizer were used in the collection path to be able to rotate any polarization of light onto the measurement axis of a monochromator on which a CCD camera is attached to record the photoluminescence intensity. In this way the detection polarization could be varied and light from other nearby quantum dots could be filtered via the monochromator (our spectrometer).

When the excitation laser couples with both dipole moments associated with a neutral electronic transition, the fields coherently scattered from the two dipoles have a relative phase shift even though the field polarizations are still aligned to each dipole. The detection polarization determines whether these phase-shifted fields combine constructively or destructively [99]. Thus, by measuring with a detection polarization that corresponds to the constructive interference between the fields, one can obtain an enhanced signal.

Ultimately, we can use the CTW method to test the indistinguishability of photons corresponding to the enhanced signal created by the constructive interference of the fields associated with each dipole moment of the V-system that describes neutral transitions in InAs QDs. In order to this, we will have to perform RPLE's with different detection polarizations to find a neutral dot with dipole moments close to 45 degrees with respect to the excitation polarization. The detection polarization will be set by the LCVRs to send the enhanced photoluminescence signal into the MZI, so the CTW method can be implemented to quantify its indistinguishability.

Along with the proposed measurements described above, there are some environmental parameters we can vary to further investigate how the local environment affects the indistinguishability of the resonance fluorescence, and how we may maximize indistinguishability of the photon source. One problem with the ultimate use of photons from an InAs QD source in practical quantum information applications is the need for extremely cold temperatures to produce indistinguishable photons. Our sample is housed in a cryostat and cooled to approximately 4.2 K to minimize any thermal effects. The indistinguishability will worsen as the temperature increases. We can investigate the temperature dependence on photon indistinguishability in our sample and better pinpoint what maximum temperatures can be used to adequately produce a usable photon source.

We can also perform the above-described experiments for multiple neutral quantum dots oriented at different angles with respect to the electric field of the excitation laser. In other words, we can investigate how close to 45 degrees does the excitation polarization have to be to the dipole moments of the neutral electronic transitions to obtain the desired enhanced effect described above.

Lastly, Chen et al. [99] mentions that similar effects to the dipole interference enhancement described above should be present in the "dark-field" resonant excitation of a charged QD in an in-plane magnetic field [46]. We can set the voltage in a diode sample to excite charged transitions while applying an in-plane magnetic field to investigate the optical properties, such as indistinguishability, in such a regime.

Chapter 8

Additional Publications

8.1 Introduction

In this chapter I list additional publications that I was substantially involved with, but the investigated topics do not fall under the subject matter of this dissertation. I will include the publications' abstracts and conclusions, as well as brief descriptions of my contributions to each project.

8.2 Polarization-Dependent Interference of Coherent Scattering from Orthogonal Dipole Moments of a Resonantly Excited Quantum Dot

Abstract

Resonant photoluminescence excitation (RPLE) spectra of a neutral InAs quantum dot show unconventional line-shapes that depend on the detection polarization. We characterize this phenomenon by performing polarization-dependent RPLE measurements and simulating the measured spectra with a 3-level quantum model. The spectra are explained by interference between fields coherently scattered from the two fine structure split exciton states, and the measurements enable extraction of the steady-state coherence between the two exciton states [126].

Conclusion

We demonstrated and modeled an interference effect that occurs during CW resonant excitation of a multi-level quantum system. Including coherent scattering is necessary to explain the strong polarization difference between the excitation and the emission. Such a phenomenon does not occur under incoherent or pulsed excitation. Comparison of spectra with different detection polarizations allows extraction of the steady-state coherence generated between the two excited states. All the spectra and coherences are correctly reproduced by a density matrix model of the QD. Similar effects must be accounted for in any situation where there are two non-degenerate orthogonal transition dipole moments and only a certain polarization is detected. One example is the “dark-field” resonant excitation and detection technique [46] in combination with a charged QD in an in-plane magnetic field.

Contributions

This project was lead by my fellow graduate student, Disheng Chen. I helped him substantially with the experimental setup, data acquisition, and editing during the writing process. I also contributed to regular discussions regarding data analysis and application of appropriate theory with Disheng and Professor Flagg.

8.3 Resonance Fluorescence of an InAs Quantum Dot in a Planar Cavity using Orthogonal Excitation and Detection

Abstract

The ability to perform simultaneous resonant excitation and fluorescence detection is important for quantum optical measurements of quantum dots (QDs). Resonant excitation without fluorescence detection – for example, a differential transmission measurement – can determine some properties of the emitting system, but does not allow applications or measurements based on the emitted photons. For example, the measurement of photon correlations, observation of the Mollow triplet, and realization of single photon sources all require collection of the fluorescence. Incoherent excitation with fluorescence detection – for example, above band-gap excitation – can be used to create single photon sources, but the disturbance of the environment due to the excitation reduces the indistinguishability of the photons. Single photon sources based on QDs will have to be resonantly excited to have high photon indistinguishability, and simultaneous collection of the photons will be necessary to make use of them. We demonstrate a method to resonantly excite a single QD embedded in a planar

cavity by coupling the excitation beam into this cavity from the cleaved face of the sample while collecting the fluorescence along the sample's surface normal direction. By carefully matching the excitation beam to the waveguide mode of the cavity, the excitation light can couple into the cavity and interact with the QD. The scattered photons can couple to the Fabry-Perot mode of the cavity and escape in the surface normal direction. This method allows complete freedom in the detection polarization, but the excitation polarization is restricted by the propagation direction of the excitation beam. The fluorescence from the wetting layer provides a guide to align the collection path with respect to the excitation beam. The orthogonality of the excitation and detection modes enables resonant excitation of a single QD with negligible laser scattering background [99].

Conclusion

Single quantum dots under resonant excitation have been demonstrated to be excellent single photon sources with high brightness, narrow linewidth, and high indistinguishability[74]. This protocol provides a feasible approach to harness these exceptional properties of the self-assembled QD system for various applications, such as quantum information and linear optical quantum computing. Furthermore, photons entangled with either another photon or an electron spin will require collection without regard to polarization, which is a feature of this method.

Contributions

Disheng and I helped build Professor Flagg's lab from the ground up, and thus were both heavily involved with the construction of the optical excitation paths and collection path, as well as most of the optical paths on our optical table. Thus, we were the most qualified to describe and demonstrate the side resonant excitation scheme. I aided Disheng with writing and editing the manuscript, and appeared in the published instructional video.

8.4 Complete Stokes Vector Analysis with a Compact, Portable Rotating Waveplate Polarimeter

Abstract

Accurate calibration of polarization-dependent optical elements is often necessary in optics experiments. A versatile polarimeter device to measure the polarization state of light is a valuable tool in these experiments. Here, we report

a rotating waveplate-based polarimeter capable of complete Stokes vector analysis of collimated light. Calibration of the device allows accurate measurements over a range of wavelengths, with a bandwidth of $> 30nm$ in this implementation. A photo-interrupter trigger system supplies the phase information necessary for full determination of the Stokes vector. An Arduino microcontroller performs rapid analysis and displays the results on a liquid crystal display (LCD). The Arduino can also be interfaced with a computer to store time series of Stokes vectors. The optical measurement apparatus of the polarimeter is compact and can be placed anywhere on an optical table on a single standard post. The components to construct the device are only a fraction of the cost of commercially available devices, while the accuracy and precision of the measurements are of the same order of magnitude [127].

Conclusion

We report a self-contained polarimeter capable of fully characterizing the Stokes vector to within one degree on the Poincaré sphere. Our device provides accuracy comparable to the leading commercial devices for a fraction of the cost with smaller size and greater ease of use compared to previous non-commercial realizations [128–132]. By using a photo-interrupter as a trigger and an Arduino microcontroller to perform the analysis, we provide a compact, user-friendly, and cost effective way to quickly and accurately measure and record the polarization of collimated light.

Contributions

I helped write the sections of the Arduino code regarding timing of the photodiode measurement with rotation of the motor that turns the QWP, as well as averaging of the subsequent calculated Stokes vectors to minimize the error in the displayed values. I designed the device's custom double-sided printed circuit board (PCB), which included all of the internal electrical connections, including power connections, connections to the Arduino chip, and connections to all of the involved mechanisms[1]. The PCB incorporated the use of jumper cables that could be easily plugged in and out of mounted pins. I also drilled the holes for and assembled most of the device's external electrical connections, including placement of the LCD, as well as created custom cables to interface

---

[1] These involved measured photodiode and photo-interrupter voltages, control voltages sent to the motor, LCD connections, a switch to change the display between showing calculated Stokes vectors or angles on the Poincaré sphere, etc.

the box that housed the PCB, LCD, and switch with the measurement instrument. During implementation of the above-mentioned tasks, the ultimate device was engineered to optimize user-friendliness, as well as made to be easily disassembled/assembled to help ease any future modifications and diagnosis of problems.

8.5 A Tunable Fabry-Perot Cavity Stabilized via a Mechanically Connected Shearing Interferometer

Abstract

A tunable Fabry-Perot interferometer (FPI) can be used for high-resolution spectral measurements with precise control of the distance between the two FPI mirrors, which can be accomplished via feedback. We mechanically connect the FPI cavity mirrors to those of a shearing interferometer (SI) that is actively stabilized by a simple and inexpensive optical feedback method comprising a single HeNe laser, photodiode array, and Arduino microprocessor. The FPI transmission frequency can be held constant to within a standard deviation of 0.35 GHz for wavelengths in the near infrared range. Scans of the transmission frequency are repeatable with a standard deviation of 0.11 GHz [133].

Conclusion

The actively stabilized shearing interferometer can stabilize the physically connected Fabry-Perot interferometer. We can control the length of the FPI cavity by choosing the set-point of the SI feedback loop. With a fixed set-point, the transmission frequency of the FPI had a standard deviation of 0.35 GHz. With a scanning set-point, the transmission frequency of corresponding steps in different scans had a standard deviation of 0.11 GHz. These correspond to standard deviations of the FPI cavity length of 8.6 nm and 2.7 nm, respectively. Since the cavity is stable as well as tunable, we can use it as a tunable optical filter for high-resolution spectral measurements.

Contributions

Before Raju KC began work on the above-described FPI, I laid the theoretical and practical groundwork for the necessary external input and output optics during construction of two preceding custom FPIs. The two FPIs that I constructed, as well as the one that Raju constructed, involve an optical cavity defined by two spherical mirrors. This geometry results in a large gain of the TEM_{00} (Gaussian) mode focused at the center of the two mirrors, and minimal loss in the directions perpendicular to the optical axis of the cavity. Investigated light is focused into the cavity through the back of one of the mirrors, and the resonant Fabry-Perot mode that is transmitted out of the other side of the cavity is collected. Each FPI that has been constructed involved measurement of the transmitted intensity while the optical path length of the cavity was finely incremented. The spectral resolution of the ultimately measured transmission spectrum is determined by the precision in the optical path-length increment.

In order to maximize the gain of the TEM_{00} mode and eliminate higher-order resonant modes, one needs to use external launch optics to mode-match the incoming light with that of the TEM_{00} mode focused at the center of the cavity. Recall, the geometry of our sample induces the resonance fluorescence to exit from the sample surface in a conical shape, which after being collimated by the collection objective, results in a ring-shaped propagating mode. The collected fluorescence is sent through two lenses that are used to optimize the coupling efficiency into a single-mode (SM) fiber, which induces a diverging Gaussian mode (TEM_{00}) at its output. The light emitted from the SM fiber is collimated and sent trough two additional mode-matching lenses that are used to create the correct beam waist at the very center of the FPI cavity associated with the resonant TEM_{00} mode. The light transmitted through the FPI is then collimated and its intensity is measured via a CCD camera attached to our spectrometer as the optical path length of the Fabry-Perot cavity is scanned. I referred to Kogelnik and Li [134] to design the above-described optics, which have been used with every version of the FPI.

Although the previous versions of the FPI that I constructed did not lead to a publication, they laid the groundwork to ultimate operation of the third version, and thus I will describe them briefly. The first FPI I constructed involved taking over a project started by another student. The cavity's mirrors were attached to either side of a hollow, cylindrical PZT. One mirror was held fixed while the other could move. The resonant TEM_{00} mode propagated through the hollow axis of the PZT. The distance between the mirrors was changed via voltage-controlled length of the PZT. The longitudinal strain in the PZT changed as the length was changed. If the strain in the PZT could be precisely enough measured, it could be used as active feedback to stabilize the cavity's length via the voltage applied to the PZT. We attempted to measure the changes in strain via changes in impedance of a Wheatstone bridge attached to the PZT. After I constructed and optimized the necessary optics, we were unable to measure changes in the impedance of the Wheatstone bridge as we changed the optical path length precisely enough to adequately measure anticipated emission spectra[2]. I then calculated that the necessary precision in the measured strain was on the order of $\mu\epsilon$, which could not be measured via changes in the impedance of the Wheatstone bridge used. Thus, I proceeded to construction of another prototype.

The second FPI I constructed involved the cavity's mirrors being mounted with a fixed separation and housed in a sealed chamber with windows on opposite sides to allow for optical transmission. The mirrors were attached with a small thermal expansion coefficient adhesive to either side of a hollow, cylindrical Zerodur spacer, which has a near-zero thermal expansion coefficient at room temperature. This method allowed us to minimize changes in the physical distance between the mirrors induced by fluctuations in the ambient temperature. Swagelok connections were established on opposite sides of the chamber, perpendicular to the optical axis, such that nitrogen could flow through the sealed chamber. A throughput hole was drilled into the Zerodur spacer to ease flow of gas through the optical cavity. A pressure regulator was connected at the input, which controlled the flow rate to maintain a set chamber internal pressure controlled by an input voltage. The nitrogen pressure of the chamber was incremented, which incremented the index of refraction inside the chamber, and consequently the optical path length. We had calculated that we would need to increment the nitrogen pressure by amounts close to the pressure regulator's capabilities, but the pressure regulator was inexpensive, so we gave it a try. After fine optimization of the optics and the PID parameters of the pressure regulator, I was indeed able to measure the emission spectrum of a QD, but only about 6-8 data points spanned the full spectrum. The pressure regulator we utilized was used, which may have played a role in its resolution being slightly less than anticipated. However, since we had obtained a spectral resolution that

---

[2] A typical emission spectrum of resonance fluorescence emitted by the InAs QDs studied is on the order of 1 or 2 GHz. We thus need to be able to increment and stabilize the optical path length of the cavity on the order of 100 MHz or less to be able to sufficiently fit typical measured emission spectra.

was roughly half as good as what we desired, we decided this prototype would likely not suffice whether we tried a new pressure regulator or not.

The current FPI utilizes measured changes in the fringe spacing of a diffraction pattern induced by reflection of a cw laser from a shearing interferometer. The intensity of the diffracted light is measured as a function of space with a photo-diode array. The FPI cavity length is changed via the mirrors being mounted to a PZT, as with the first FPI. The optical path length is changed via an applied voltage to the PZT. The Fabry-Perot cavity is made to be rigid with the shearing interferometer, such that the diffraction spacing can be used as active feedback of the measured spacing in the shearing interferometer, and hence the optical path length of the FPI. This active feedback is used to set the real-time voltage applied to the PZT and stabilize the optical path length. Raju led this endeavor, but I helped him immensely to be able to optimize the external mode-matching optics and taught him how to use all of the necessary equipment, such as the oscilloscope, spectrometer, LabVIEW controlled DAQ board, etc.

8.6 High-Throughput Evaluation in Nitrogen Doping of Amorphous Titanium Dioxide

Abstract

We present an ab-initio investigation of the structural, electronic, and optical properties of substitutional nitrogen doping of a-TiO_2. Through observation of multiple N-doped amorphous structures, we find additional localized tail states within the band gap. Some structures show these states nearly 1 eV above the valence band, while most structures show these states very close to the valence band edge. We also observe a general trend of increasing cohesive energy with increasing distance between nitrogen impurities, suggesting the tendency for nitrogen to form localized clusters within the material [135].

Conclusion

We expect that the photoactivity of a-TiO_2 is enhanced by substitutional nitrogen doping, which introduces tail states near the valence band edge. However, in the couple cases when N_2 is formed within the structure, we see the introduction of localized, isolated states near the middle of the band gap that we believe will most likely serve as recombination centers for the charge carriers. We observe a general trend of increasing cohesive energy with increasing N–N separation distance, although the very lowest energy structures had N–N separation distances around 4.5 angstroms, in contrast to the smallest seen N–N separation distances of around 1.5 angstroms. Urbach tails on the valence band and a very highly de-localized state on the conduction band edge were seen and are believed to be a property of amorphous binary materials. We see an increase in the likelihood of N_2 bond formation as the level of N impurities increases. When N_2 bonds are not formed, the introduced tail states will narrow the band gap while not acting as recombination centers for the charge carriers, thus promoting absorption in the visible spectrum and increasing the photocatalytic activity of amorphous TiO_2.

Contributions

I worked extensively on data acquisition and analysis for this project. The code implementing tight-binding molecular dynamics to simulate substitutional nitrogen doping of a-TiO_2 was written mostly by the then postdoc, Barry Haycock, before I joined the group. I used the code to generate large data sets of calculated electronic and optical properties of a-TiO_2 configurations with different locations of the substitutional N impurities. I led the resulting analysis with the guidance of Dr. James Lewis the summer that I worked for him, and wrote most of the ultimately published manuscript.

Appendix A

Chapter 4 Supplemental Material

A.1 Anomalous Diffusion

Throughout our analysis we utilize the shaped exponential function, $e^{-(\alpha t)^{\beta}}$, which fits well a large variety of relaxation phenomena in complex condensed-matter systems [100–105]. When $\beta = 1$, the shaped exponential reduces to the regular exponential. When $0 < \beta < 1$ the shaped exponential is referred to as a stretched exponential, and when $1 < \beta < 2$ it is referred to as a compressed exponential. Charge relaxation described with regular exponential time dependence is attributed to a regular-diffusion-like process. In 2003, Sturman *et al.* described how stretched exponential relaxation in the solid state can result from charge carriers migrating through an environment of stochastically distributed transport sites, resulting in sub-diffusion-like, or slower than regular diffusion, charge relaxation [107]. The compressed exponential has been less widely used to describe charge relaxation in the solid state. Charge relaxation described with compressed exponential time dependence is attributed to a super-diffusion-like, or faster than regular diffusion process. Bouchaud [136] gives examples of instances where compressed exponential relaxation in the sold state is observed. The common theme is the presence of an external driving force resulting in faster than exponential charge dynamics. In the following paragraphs we will discuss why we suggest both stretched and compressed exponential relaxation exists in our sample.

Consider an environment of randomly located deep potential wells in which charges can become electrically bound (traps) as well as a larger number of randomly located shallow wells that weakly bind charge carriers (transport sites). Charges are then introduced to the environment via some external excitation source. Carriers that weakly bind to transport sites have a probability to 'hop' to nearby transport sites that is proportional to the overlap of the wavefunctions corresponding to a bound charge in either trap. Ultimately, a charge may hop to a transport site adjacent to a trap then become strongly bound to the trap. The probability to make a single hop to an adjacent transport site has exponential time dependence. A stretched exponential can mathematically be represented as a sum of normal exponentials with a given weighting function [108]. The time-dependence for a charge to make multiple jumps to adjacent transport sites is a linear sum of the time-dependencies to take individual jumps, and thus the net process for charges to migrate through multiple transport sites to ultimately relax into the dot takes on stretched exponential time dependence. In our sample, migration of charge through a stochastic environment of weakly binding transport sites results in sub-diffusion-like relaxation into the QD [107]. The stochastic environment of our sample is depicted in Fig. A.1.

The timescale for the rise transient of the time-resolved resonance fluorescence indicates the charges excited by the above-band laser are created nonlocal to the QD layer. At the sample surface sits a distributed Bragg reflector consisting of alternating layers of AlAs and GaAs. Propagating through this heterostructure, above-band photons (632 nm) have a penetration depth (depth at which the intensity of the laser drops to $1/e$ of its surface value) of approximately 340 nm [110]. However, the QD layer sits approximately 2300 nm below the sample surface. The carriers created via absorption of above-band photons move with ballistic-like motion due to their high kinetic energies. This results in the carriers spreading throughout the sample with super-diffusion-like characteristics while they are hot and regular-diffusion-like characteristics once they cool [109]. Some carriers have trajectories that set them near the QD layer when they cool to the gamma point of the GaAs host. Afterwards, the carriers can become bound to QDs or the weakly-binding transport sites described above. A to-scale schematic of the sample is shown in Fig. A.2.

A.2 Additional Parameter Dependencies

During the fall section of the data, the above-band excitation is turned off and the fluorescence drops to zero as the dot neutralizes. Note in the following figures the above-band powers specified are those before the above-band excitation is turned off. The time-resolved resonance fluorescence of the fall section was fit

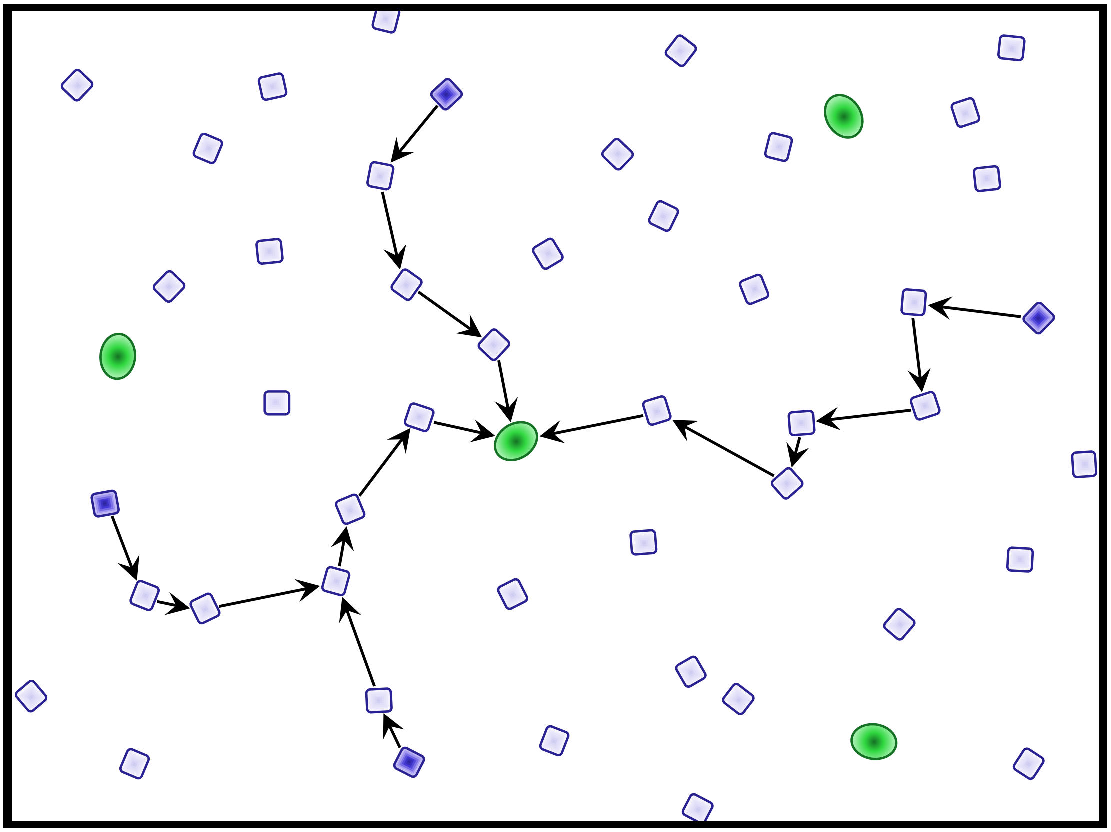

FIGURE A.1: Schematic representation of the stochastic environment of charge transport sites and traps. The white background represents the bulk GaAs host semiconductor surrounding the QDs. Green ovals represent traps, which in our sample are InAs QDs. Blue squares represent transport sites, which are likely impurities and other shallow defects in the bulk GaAs that can weakly bind charge carriers. Dark blue squares indicate the occupation of arbitrary transport sites and the black arrows represent the charges' migration through multiple transport sites to ultimately relax into the QD being studied.

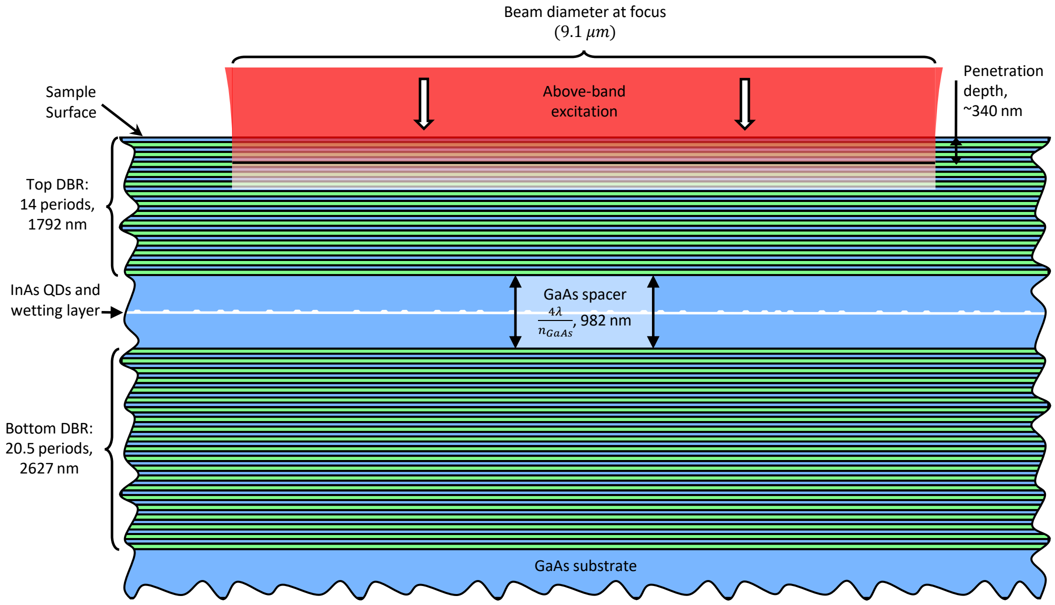

FIGURE A.2: Schematic illustrating the skin depth of above-band photons into the sample. Red signifies the above-band laser, green AlAs, blue GaAs, and white InAs. The penetration depth (depth at which the intensity of the laser drops to $1/e$ its surface value) is depicted by the black line within the focused laser spot. The laser illustration is extended to the skin depth (depth at which the laser intensity drops to $1/e^2$ of it's surface value. All components are to scale except the InAs QDs and wetting layer.

with the following phenomenological function:

$$I = A_1 e^{-\alpha_1 t} + A_2 e^{-(\alpha_2 t)^{\beta_2}}, \tag{A.1}$$

where A_1 and A_2 are amplitudes with $A_1 + A_2$ equal to the steady-state fluorescence intensity before the above-band excitation is turned off, α_1 is a neutralization rate while α_2 is a scale parameter, and β_2 a shape parameter. The first term in the above equation is attributed to ejection of charge from the QD via Auger recombination. β_2 always obtained a value between 0 and 1 during the fitting, indicating sub-diffusion-like depletion of the associated charge reservoir. After the above-band excitation is turned off, the reservoir consisting of the stochastic distribution of transport sites does not deplete instantly and charges from the reservoir can still be captured by the QD while a charge population in the reservoir exists. The second term fits the long-time, slowly-sloping tail in the resonance fluorescence intensity. We attribute the second term in the above equation to *recharging* of the QD from the reservoir before it is depleted of charge. Thus, the second term in the above equation represents the charge population of the reservoir that is comprised of the stochastic distribution of transport sites after the above-band excitation is turned off.

The shape parameter, β_2, is depicted in Fig. A.3. Although $0 < \beta_2 < 1$, two behavioral regimes exist for β_2 as a function of above-band laser power. For powers below 0.07 μW, the shape parameter is about 0.5. As the above-band power increases past that threshold, β_2 rapidly switches to values around 0.3.

Finally, the amplitudes A_1 and A_2 are depicted in Fig. A.4. $A_1 \approx 4A_2$ throughout most of acquisition space, except for the lowest above-band powers. This indicates neutralization of the QD via Auger recombination happens at roughly four times the rate at which charges deplete from the reservoir through the QD after the above-band excitation is turned off.

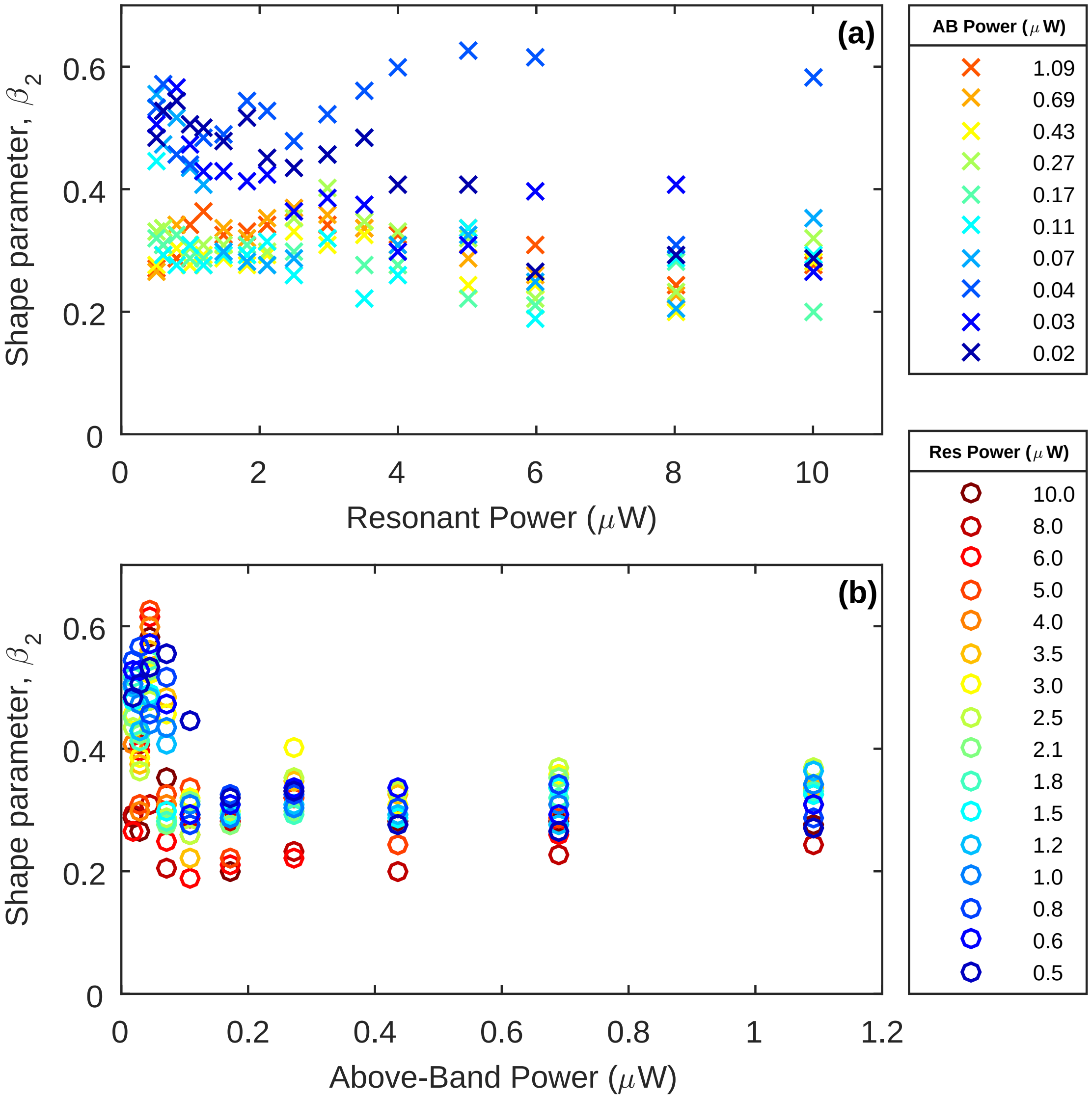

FIGURE A.3: The shape parameter β_2 as a function of (a) resonant and (b) above-band laser power. Note β_2 always relaxed to a value between 0 and 1 indicating association with a sub-diffusion-like process. The legends and color specify the laser power not depicted by the horizontal axis.

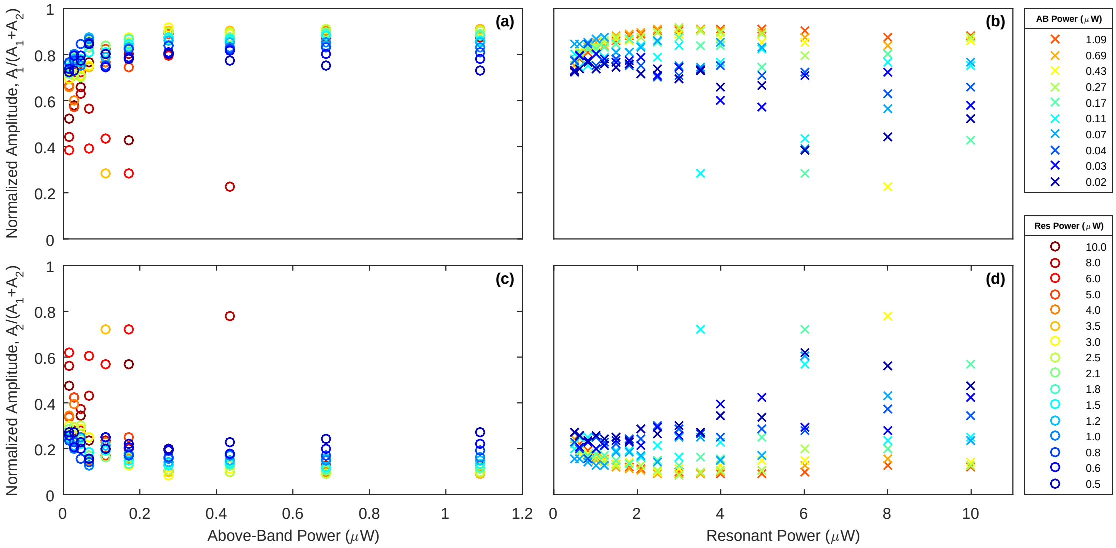

FIGURE A.4: The normalized amplitude associated with Auger recombination, A_1, is depicted as a function of (a) above-band and (b) resonant excitation power. The normalized amplitude associated with the slow depletion of the sub-diffusion reservoir, A_2, depicted as a function of (c) above-band and (d) resonant excitation power. The legends and colors specify the power of the other excitation laser not depicted by the horizontal axis.

Appendix B

The Poincaré Sphere

The Poincaré sphere, depicted in Fig. B.1, is a convenient geometric representation of a light source's polarization state. A light source's polarization state is represented by the the Stokes vector, which has components S_1, S_2, and S_3. S_1 quantifies the horizontal (H) and vertical (V) components of the polarization[1], S_2 the diagonal (D) and anti-diagonal (A) components, which are rotated 45 degrees with respect to H and V in real space, and S_3 the left-circular (L) and right-circular (R) polarized components. The length of the Stokes vector takes on a value between zero and unity, where a length of unity corresponds to completely polarized light, a length of zero corresponds to completely unpolarized light, and a length between zero and unity corresponds to partially polarized light. A Stokes vector on the equator of the Poincaré sphere corresponds to linearly polarized light, while a Stokes vector lying on the vertical axis corresponds to circularly polarized light. Stokes vectors with polar angles in between are elliptically polarized. The two LCVRs mentioned in Chapter 2 each rotate a given polarization through different angles on the Poincaré sphere, allowing for any input polarization to be changed into any output polarization via the applied voltages to the LCVRs.

---

[1] The horizontal and vertical directions in real space are arbitrarily chosen.

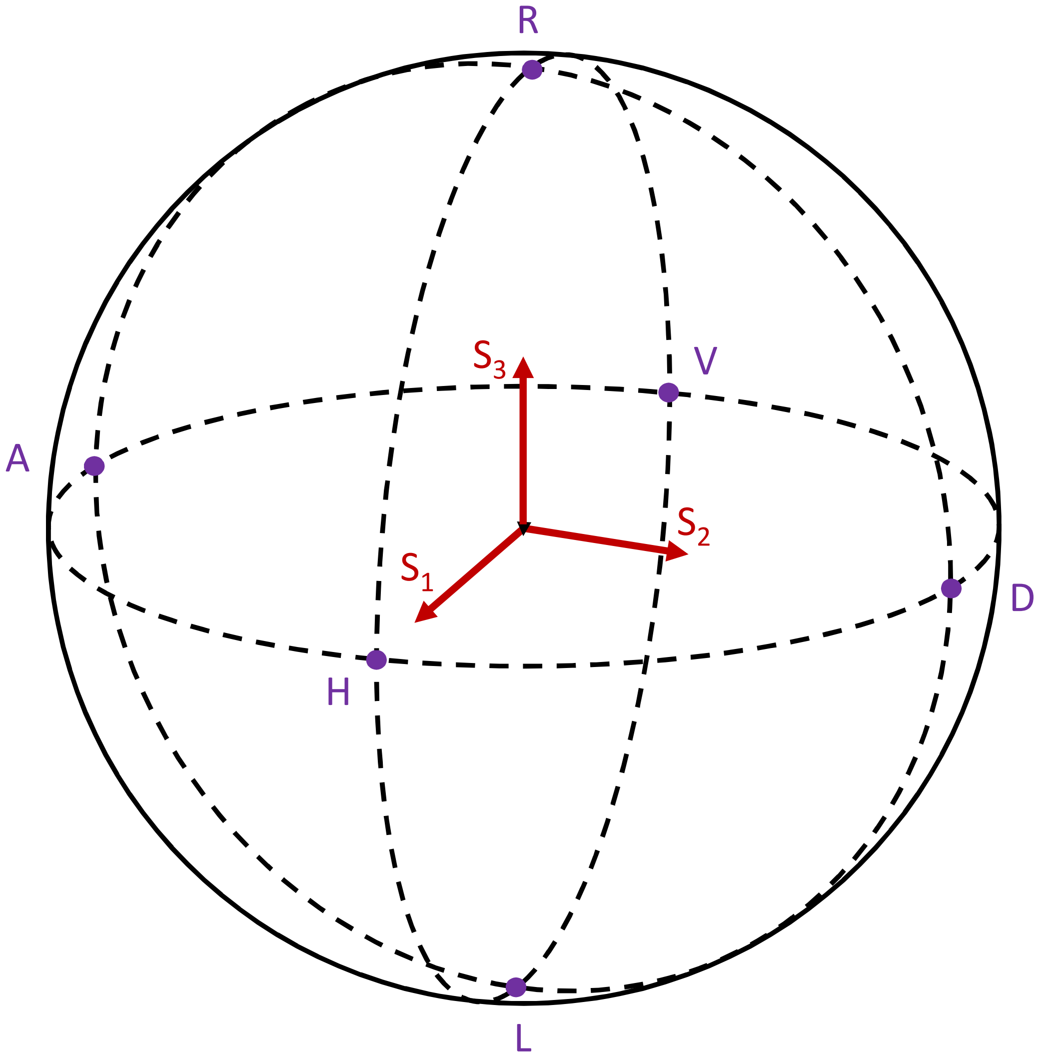

FIGURE B.1: The Poincaré sphere. The red arrows and symbols represent the components of the Stokes vector used to represent a given polarization state. The dark purple circles and symbols represent locations on the Poincaré sphere that correspond to completely horizontal (H), vertical (V), diagonal (D), anti-diagonal (A), left circular (L), and right circular (R) polarized light.

Appendix C

Example Quantum Dot Fluorescence Spatial Images

Figure. C.1 depicts sample spatial images of collected fluorescence from two different QDs. In Chapter 1 it was discussed that the Fabry-Perot cavity in which the QDs are embedded induces the QD fluorescence to exit from the sample surface in a conical shape. The angle of the cone is larger for wavelengths with larger differences from the perpendicular Fabry-Perot mode's wavelength. Light of larger cones will be collimated to a larger diameter by the collection objective, and thus will have a larger numerical aperture when ultimately focused onto the image plane of the CCD camera. This effect is manifested in a tighter Airy disk in the spatial image.

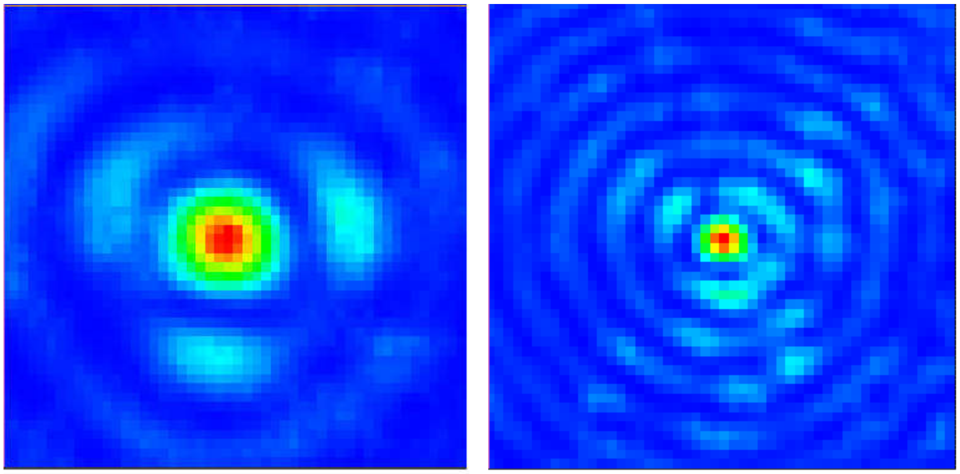

FIGURE C.1: Example spatial images of collected fluorescence from two different QDs taken with a CCD camera. The magnification for either image is 60. Dark blue color signifies lower relative intensity, while dark red signifies higher relative intensity. The image size is dictated by the numerical aperture of the fluorescence when focused onto the image plane of the CCD. A tighter Airy disk surrounded by more observable Airy rings results from a higher numerical aperture. The image on the left is of fluorescence from the QD investigated in Chapter 5, while that on the right is of fluorescence from a QD that I found during my preliminary QD search for the experiment described in Chapter 5.

.

Bibliography

[1] K. Hennessy et al. “Quantum nature of a strongly coupled single quantum dot-cavity system”. In: *Nature* 445.7130 (Feb. 2007), pp. 896–899. ISSN: 0028-0836. DOI: 10.1038/nature05586.

[2] J. P Reithmaier et al. “Strong coupling in a single quantum dot-semiconductor microcavity system”. In: *Nature* 432.7014 (2004), pp. 197–200.

[3] Eric A. Stinaff et al. “Optical Signatures of Coupled Quantum Dots”. en. In: *Science* (Jan. 2006). ISSN: 0036-8075, 1095-9203. DOI: 10.1126/science.1121189.

[4] Danny Kim et al. “Ultrafast optical control of entanglement between two quantum-dot spins”. In: *Nat Phys* 7.3 (Mar. 2011), pp. 223–229. ISSN: 1745-2473. DOI: 10.1038/nphys1863.

[5] Colin M. Chow et al. “Nonlocal Nuclear Spin Quieting in Quantum Dot Molecules: Optically Induced Extended Two-Electron Spin Coherence Time”. In: *Physical Review Letters* 117.7 (Aug. 2016), p. 077403. DOI: 10.1103/PhysRevLett.117.077403.

[6] Alexander Bechtold et al. “Three-stage decoherence dynamics of an electron spin qubit in an optically active quantum dot”. en. In: *Nature Physics* 11.12 (Dec. 2015), pp. 1005–1008. ISSN: 1745-2473. DOI: 10.1038/nphys3470.

[7] Gunter Wüst et al. “Role of the electron spin in determining the coherence of the nuclear spins in a quantum dot”. en. In: *Nature Nanotechnology* advance online publication (July 2016). ISSN: 1748-3387. DOI: 10.1038/nnano.2016.114.

[8] Gary Zaiats et al. “Quantum Dot Light-Emitting Devices: Beyond Alignment of Energy Levels”. In: *ACS Applied Materials & Interfaces* 9.36 (Sept.

2017). Publisher: American Chemical Society, pp. 30741–30745. ISSN: 1944-8244. DOI: 10.1021/acsami.7b07893.

[9] Jongseok Han et al. "Toward high-resolution, inkjet-printed, quantum dot light-emitting diodes for next-generation displays". en. In: *Journal of the Society for Information Display* 24.9 (2016). _eprint: https://sid.onlinelibrary.wiley.com/doi/pdf/10.1002/jsid.467, pp. 545–551. ISSN: 1938-3657. DOI: 10.1002/jsid.467.

[10] J. J. Santaella et al. "Design and fabrication of CuInS$\less$sub$\greater$2$\less$/sub$\greater$/ZnS-based QLED for automotive lighting systems". en. In: *Nanotechnology* 32.10 (Dec. 2020). Publisher: IOP Publishing, p. 105204. ISSN: 0957-4484. DOI: 10.1088/1361-6528/abcced.

[11] Jaemin Kim et al. "Ultrathin Quantum Dot Display Integrated with Wearable Electronics". en. In: *Advanced Materials* 29.38 (2017). _eprint: https://onlinelibrary.wiley.com/doi/pdf/10.1002/adma.201700217, p. 1700217. ISSN: 1521-4095. DOI: 10.1002/adma.201700217.

[12] Hyochul Kim et al. "A quantum logic gate between a solid-state quantum bit and a photon". en. In: *Nature Photonics* 7.5 (May 2013), pp. 373–377. ISSN: 1749-4885. DOI: 10.1038/nphoton.2013.48.

[13] Aymeric Delteil et al. "Generation of heralded entanglement between distant hole spins". en. In: *Nature Physics* 12.3 (Mar. 2016), pp. 218–223. ISSN: 1745-2473. DOI: 10.1038/nphys3605.

[14] David Press et al. "Complete quantum control of a single quantum dot spin using ultrafast optical pulses". en. In: *Nature* 456.7219 (Nov. 2008), pp. 218–221. ISSN: 0028-0836. DOI: 10.1038/nature07530.

[15] Thomas Volz et al. "Ultrafast all-optical switching by single photons". en. In: *Nature Photonics* 6.9 (Sept. 2012), pp. 605–609. ISSN: 1749-4885. DOI: 10.1038/nphoton.2012.181.

[16] C. B. Murray, C. R. Kagan, and M. G. Bawendi. "Synthesis and Characterization of Monodisperse Nanocrystals and Close-Packed Nanocrystal Assemblies". In: *Annual Review of Materials Science* 30.1 (Aug. 2000). Publisher: Annual Reviews Inc., p. 545. ISSN: 00846600. DOI: 10.1146/annurev.matsci.30.1.545.

[17] Jiabin Cui et al. "Colloidal quantum dot molecules manifesting quantum coupling at room temperature". en. In: *Nature Communications* 10.1 (Dec. 2019). Number: 1 Publisher: Nature Publishing Group, p. 5401. ISSN: 2041-1723. DOI: 10.1038/s41467-019-13349-1.

[18] Uwe Kortshagen. "Nonthermal plasma synthesis of semiconductor nanocrystals". en. In: *Journal of Physics D: Applied Physics* 42.11 (May 2009). Publisher: IOP Publishing, p. 113001. ISSN: 0022-3727. DOI: 10.1088/0022-3727/42/11/113001.

[19] X. D. Pi and U. Kortshagen. "Nonthermal plasma synthesized freestanding silicon–germanium alloy nanocrystals". en. In: *Nanotechnology* 20.29 (July 2009). Publisher: IOP Publishing, p. 295602. ISSN: 0957-4484. DOI: 10.1088/0957-4484/20/29/295602.

[20] E. M. Purcell, H. C. Torrey, and R. V. Pound. "Resonance Absorption by Nuclear Magnetic Moments in a Solid". In: *Physical Review* 69.1-2 (Jan. 1946), pp. 37–38. DOI: 10.1103/PhysRev.69.37.

[21] A. Rahmani and G.w. Bryant. "Modification of Spontaneous Emission of Quantum Dots: Purcell Effect in Semiconductor Microcavities". en. In: *physica status solidi (b)* 224.3 (2001). _eprint: https://onlinelibrary.wiley.com/doi/pdf/10.1002/%28SICI%291521-3951%28200104%29224%3A3%3C807%3A%3AAID-PSSB807%3E3.0.CO%3B2-D, pp. 807–810. ISSN: 1521-3951. DOI: 10.1002/(SICI)1521-3951(200104)224:3<807::AID-PSSB807>3.0.CO;2-D.

[22] D. Pinotsi et al. "Charge controlled self-assembled quantum dots coupled to photonic crystal nanocavities". en. In: *Photonics and Nanostructures - Fundamentals and Applications*. PECS IX 10.3 (June 2012), pp. 256–262. ISSN: 1569-4410. DOI: 10.1016/j.photonics.2011.04.008.

[23] Kazuaki Sakoda Kazuaki Sakoda et al. "Purcell effect of GaAs quantum dots by photonic crystal microcavities". en. In: *Chinese Optics Letters* 7.10 (2009), pp. 879–881. ISSN: 1671-7694. DOI: 10.3788/COL20090710.0879.

[24] I. C. Robin et al. "Purcell effect for CdSe/ZnSe quantum dots placed into hybrid micropillars". In: *Applied Physics Letters* 87.23 (Dec. 2005). Publisher: American Institute of Physics, p. 233114. ISSN: 0003-6951. DOI: 10.1063/1.2136433.

[25] Xin Xie et al. “Purcell effect and lasing from quantum dots in a topological photonic crystal nanocavity”. In: *2021 5th IEEE Electron Devices Technology & Manufacturing Conference (EDTM)*. Apr. 2021, pp. 1–3. DOI: 10.1109/EDTM50988.2021.9420936.

[26] D. G. Deppe and H. Huang. “Quantum-dot vertical-cavity surface-emitting laser based on the Purcell effect”. en. In: *Applied Physics Letters* 75.22 (Nov. 1999), pp. 3455–3457. ISSN: 0003-6951, 1077-3118. DOI: 10.1063/1.125294.

[27] D. Leonard, K. Pond, and P. M. Petroff. “Critical layer thickness for self-assembled InAs islands on GaAs”. In: *Physical Review B* 50.16 (Oct. 1994), pp. 11687–11692. DOI: 10.1103/PhysRevB.50.11687.

[28] Richard J. Warburton. “Single spins in self-assembled quantum dots”. en. In: *Nature Materials* 12.6 (June 2013), pp. 483–493. ISSN: 1476-1122. DOI: 10.1038/nmat3585.

[29] C. Latta et al. “Confluence of resonant laser excitation and bidirectional quantum-dot nuclear-spin polarization”. en. In: *Nature Physics* 5.10 (Oct. 2009), pp. 758–763. ISSN: 1745-2473. DOI: 10.1038/nphys1363.

[30] Ivo T. Vink et al. “Locking electron spins into magnetic resonance by electron–nuclear feedback”. en. In: *Nature Physics* 5.10 (Oct. 2009), pp. 764–768. ISSN: 1745-2473. DOI: 10.1038/nphys1366.

[31] Bo Sun et al. “Persistent Narrowing of Nuclear-Spin Fluctuations in InAs Quantum Dots Using Laser Excitation”. In: *Physical Review Letters* 108.18 (May 2012), p. 187401. DOI: 10.1103/PhysRevLett.108.187401.

[32] E. B. Flagg et al. “Dynamics of Nonclassical Light from a Single Solid-State Quantum Emitter”. In: *Physical Review Letters* 109.16 (Oct. 2012), p. 163601. DOI: 10.1103/PhysRevLett.109.163601.

[33] H. D. Robinson and B. B. Goldberg. “Light-induced spectral diffusion in single self-assembled quantum dots”. In: *Physical Review B* 61.8 (Feb. 2000), R5086–R5089. DOI: 10.1103/PhysRevB.61.R5086.

[34] J. Houel et al. “Probing Single-Charge Fluctuations at a GaAs/AlAs Interface Using Laser Spectroscopy on a Nearby InGaAs Quantum Dot”. In: *Physical Review Letters* 108.10 (Mar. 2012), p. 107401. DOI: 10.1103/PhysRevLett.108.107401.

[35] Clemens Matthiesen et al. “Full counting statistics of quantum dot resonance fluorescence”. en. In: *Scientific Reports* 4 (May 2014). DOI: 10.1038/srep04911.

[36] C. K. Hong, Z. Y. Ou, and L. Mandel. “Measurement of subpicosecond time intervals between two photons by interference”. In: *Physical Review Letters* 59.18 (Nov. 1987), pp. 2044–2046. DOI: 10.1103/PhysRevLett.59.2044.

[37] B. D. Gerardot et al. “Manipulating exciton fine structure in quantum dots with a lateral electric field”. In: *Applied Physics Letters* 90.4 (Jan. 2007), p. 041101. ISSN: 0003-6951, 1077-3118. DOI: 10.1063/1.2431758.

[38] E. B. Flagg et al. “Resonantly driven coherent oscillations in a solid-state quantum emitter”. In: *Nature Physics* 5.3 (Mar. 2009), pp. 203–207. ISSN: 1745-2473. DOI: 10.1038/nphys1184.

[39] C. Arnold et al. “Cavity-Enhanced Real-Time Monitoring of Single-Charge Jumps at the Microsecond Time Scale”. In: *Physical Review X* 4.2 (Apr. 2014), p. 021004. DOI: 10.1103/PhysRevX.4.021004.

[40] Hai Son Nguyen et al. “Photoneutralization and slow capture of carriers in quantum dots probed by resonant excitation spectroscopy”. In: *Physical Review B* 87.11 (Mar. 2013), p. 115305. DOI: 10.1103/PhysRevB.87.115305.

[41] H. S. Nguyen et al. “Optically Gated Resonant Emission of Single Quantum Dots”. In: *Physical Review Letters* 108.5 (Jan. 2012), p. 057401. DOI: 10.1103/PhysRevLett.108.057401.

[42] O. Gazzano et al. “Bright solid-state sources of indistinguishable single photons”. en. In: *Nature Communications* 4 (Feb. 2013), p. 1425. ISSN: 2041-1733. DOI: 10.1038/ncomms2434.

[43] T. Walther et al. “Nature of the Stranski-Krastanow Transition during Epitaxy of InGaAs on GaAs”. In: *Physical Review Letters* 86.11 (Mar. 2001), pp. 2381–2384. DOI: 10.1103/PhysRevLett.86.2381.

[44] A.G. Cullis et al. “Stranski-Krastanow transition and epitaxial island growth”. In: *Physical Review B* 66.8 (Aug. 2002), p. 081305. DOI: 10.1103/PhysRevB.66.081305.

[45] A. S. Bhatti et al. "Optical spectroscopy of quasimonolayer InAs at the onset of quantum-dot nucleation". In: *Physical Review B* 60.4 (July 1999), pp. 2592–2598. DOI: `10.1103/PhysRevB.60.2592`.

[46] Andreas V. Kuhlmann et al. "A dark-field microscope for background-free detection of resonance fluorescence from single semiconductor quantum dots operating in a set-and-forget mode". In: *Review of Scientific Instruments* 84.7 (July 2013), p. 073905. ISSN: 0034-6748, 1089-7623. DOI: `10.1063/1.4813879`.

[47] Mark Fox. *Quantum Optics_an introduction*. en. 1st ed. Oxford Master Series in Physics Book 15. Oxford University Press, June 2006. ISBN: 978-0-19-856673-1.

[48] C. J. Foot. *Atomic Physics*. Oxford, UNITED KINGDOM: Oxford University Press, Incorporated, 2005. ISBN: 978-0-19-152314-4.

[49] Gen Kimura. "The Bloch Vector for N -Level Systems". en. In: *Journal of the Physical Society of Japan* 72.Suppl.C (Jan. 2003), pp. 185–188. ISSN: 0031-9015, 1347-4073. DOI: `10.1143/JPSJS.72SC.185`.

[50] S. M. Ulrich et al. "Dephasing of Triplet-Sideband Optical Emission of a Resonantly Driven InAs / GaAs Quantum Dot inside a Microcavity". en. In: *Physical Review Letters* 106.24 (June 2011), p. 247402. ISSN: 0031-9007, 1079-7114. DOI: `10.1103/PhysRevLett.106.247402`.

[51] Hongtao Jiang and Jasprit Singh. "Strain distribution and electronic spectra of InAs/GaAs self-assembled dots: An eight-band study". In: *Physical Review B* 56.8 (Aug. 1997), pp. 4696–4701. DOI: `10.1103/PhysRevB.56.4696`.

[52] Seungwon Lee et al. "Effect of wetting layers on the strain and electronic structure of InAs self-assembled quantum dots". In: *Physical Review B* 70.12 (Sept. 2004), p. 125307. DOI: `10.1103/PhysRevB.70.125307`.

[53] I. Saïdi et al. "Electron and hole energy levels in InAs/GaAs quantum dots: Size and magnetic field effects". In: *Journal of Applied Physics* 109.3 (Feb. 2011), p. 033703. ISSN: 0021-8979, 1089-7550. DOI: `10.1063/1.3524519`.

[54] Gustavo A. Narvaez, Gabriel Bester, and Alex Zunger. "Carrier relaxation mechanisms in self-assembled (In,Ga)As/GaAs quantum dots: Efficient P->S Auger relaxation of electrons". In: *Physical Review B* 74.7 (Aug. 2006), p. 075403. DOI: `10.1103/PhysRevB.74.075403`.

[55] H. W. van Kesteren et al. "Fine structure of excitons in type-II GaAs/AlAs quantum wells". In: *Physical Review B* 41.8 (Mar. 1990), pp. 5283–5292. DOI: `10.1103/PhysRevB.41.5283`.

[56] Lucio Claudio Andreani and Franco Bassani. "Exchange interaction and polariton effects in quantum-well excitons". In: *Physical Review B* 41.11 (Apr. 1990), pp. 7536–7544. DOI: `10.1103/PhysRevB.41.7536`.

[57] E. Blackwood et al. "Exchange interaction of excitons in GaAs heterostructures". In: *Physical Review B* 50.19 (Nov. 1994), pp. 14246–14254. DOI: `10.1103/PhysRevB.50.14246`.

[58] M. Bayer et al. "Fine structure of neutral and charged excitons in self-assembled In(Ga)As/(Al)GaAs quantum dots". In: *Physical Review B* 65.19 (May 2002), p. 195315. DOI: `10.1103/PhysRevB.65.195315`.

[59] S. Rodt et al. "Correlation of structural and few-particle properties of self-organized InAs/GaAs quantum dots". In: *Physical Review B* 71.15 (Apr. 2005), p. 155325. DOI: `10.1103/PhysRevB.71.155325`.

[60] U. W. Pohl et al. "Formation and evolution of multimodal size distributions of InAs/GaAs quantum dots". In: *Physica E: Low-dimensional Systems and Nanostructures*. Proceedings of the 12th International Conference on Modulated Semiconductor StructuresProceedings of the 12th International Conference on Modulated Semiconductor Structures 32.1–2 (May 2006), pp. 9–13. ISSN: 1386-9477. DOI: `10.1016/j.physe.2005.12.145`.

[61] Rodney Loudon. *The Quantum Theory of Light*. Third. Oxford U. Press, 2000.

[62] Paul Seifert et al. "A high-T $_c$ van der Waals superconductor based photodetector with ultra-high responsivity and nanosecond relaxation time". en. In: *2D Materials* 8.3 (July 2021), p. 035053. ISSN: 2053-1583. DOI: `10.1088/2053-1583/ac072f`.

[63] E. Knill, R. Laflamme, and G. J Milburn. "A scheme for efficient quantum computation with linear optics". In: *Nature* 409.6816 (2001), pp. 46–52.

[64] Frédéric Bouchard et al. "Two-photon interference: the Hong–Ou–Mandel effect". en. In: *Reports on Progress in Physics* 84.1 (Dec. 2020). Publisher: IOP Publishing, p. 012402. ISSN: 0034-4885. DOI: `10.1088/1361-6633/abcd7a`.

[65] Anton Zeilinger et al. "Three-Particle Entanglements from Two Entangled Pairs". In: *Physical Review Letters* 78.16 (Apr. 1997), pp. 3031–3034. DOI: `10.1103/PhysRevLett.78.3031`.

[66] Jian-Wei Pan et al. "Experimental Entanglement Swapping: Entangling Photons That Never Interacted". In: *Physical Review Letters* 80.18 (May 1998), pp. 3891–3894. DOI: `10.1103/PhysRevLett.80.3891`.

[67] D. L. Moehring et al. "Entanglement of single-atom quantum bits at a distance". en. In: *Nature* 449.7158 (Sept. 2007), pp. 68–71. ISSN: 0028-0836. DOI: `10.1038/nature06118`.

[68] H.-J. Briegel et al. "Quantum Repeaters: The Role of Imperfect Local Operations in Quantum Communication". In: *Physical Review Letters* 81.26 (Dec. 1998), pp. 5932–5935. DOI: `10.1103/PhysRevLett.81.5932`.

[69] Zhi Zhao et al. "Experimental Realization of Entanglement Concentration and a Quantum Repeater". In: *Physical Review Letters* 90.20 (May 2003), p. 207901. DOI: `10.1103/PhysRevLett.90.207901`.

[70] P. Michler et al. "A Quantum Dot Single-Photon Turnstile Device". en. In: *Science* 290.5500 (Dec. 2000), pp. 2282–2285. ISSN: 0036-8075, 1095-9203. DOI: `10.1126/science.290.5500.2282`.

[71] Charles Santori et al. "Triggered Single Photons from a Quantum Dot". In: *Physical Review Letters* 86.8 (Feb. 2001), p. 1502. DOI: `10.1103/PhysRevLett.86.1502`.

[72] Andreas V. Kuhlmann et al. "Transform-limited single photons from a single quantum dot". en. In: *Nature Communications* 6 (Sept. 2015), p. 8204. DOI: `10.1038/ncomms9204`.

[73] Charles Santori et al. "Indistinguishable photons from a single-photon device". In: *Nature* 419.6907 (2002), pp. 594–597. DOI: `10.1038/nature01086`.

[74] Yu-Ming He et al. "On-demand semiconductor single-photon source with near-unity indistinguishability". en. In: *Nature Nanotechnology* 8.3 (Mar. 2013), pp. 213–217. ISSN: 1748-3387. DOI: `10.1038/nnano.2012.262`.

[75] E. B. Flagg et al. "Interference of Single Photons from Two Separate Semiconductor Quantum Dots". In: *Physical Review Letters* 104.13 (Apr. 2010), p. 137401. DOI: `10.1103/PhysRevLett.104.137401`.

[76] P. Gold et al. "Two-photon interference from remote quantum dots with inhomogeneously broadened linewidths". In: *Physical Review B* 89.3 (Jan. 2014), p. 035313. DOI: `10.1103/PhysRevB.89.035313`.

[77] M. Abbarchi et al. "Spectral diffusion and line broadening in single self-assembled GaAs/AlGaAs quantum dot photoluminescence". In: *Applied Physics Letters* 93.16 (2008), p. 162101. ISSN: 00036951. DOI: `10.1063/1.3003578`.

[78] Marco Abbarchi et al. "Bunched photon statistics of the spectrally diffusive photoluminescence of single self-assembled GaAs quantum dots". In: *Physical Review B* 86.11 (Sept. 2012), p. 115330. DOI: `10.1103/PhysRevB.86.115330`.

[79] Andreas V. Kuhlmann et al. "Charge noise and spin noise in a semiconductor quantum device". en. In: *Nature Physics* 9.9 (Sept. 2013), pp. 570–575. ISSN: 1745-2473. DOI: `10.1038/nphys2688`.

[80] Andrew P. Beyler et al. "Direct Observation of Rapid Discrete Spectral Dynamics in Single Colloidal CdSe-CdS Core-Shell Quantum Dots". In: *Physical Review Letters* 111.17 (Oct. 2013), p. 177401. DOI: `10.1103/PhysRevLett.111.177401`.

[81] Sebastian Unsleber et al. "Two-photon interference from a quantum dot microcavity: Persistent pure dephasing and suppression of time jitter". In: *Physical Review B* 91.7 (Feb. 2015), p. 075413. DOI: `10.1103/PhysRevB.91.075413`.

[82] R. J. Warburton et al. "Optical emission from a charge-tunable quantum ring". en. In: *Nature* 405.6789 (June 2000), pp. 926–929. ISSN: 0028-0836. DOI: `10.1038/35016030`.

[83] M. Baier et al. "Optical spectroscopy of charged excitons in single quantum dot photodiodes". In: *Physical Review B* 64.19 (Oct. 2001), p. 195326. DOI: `10.1103/PhysRevB.64.195326`.

[84] J. J. Finley et al. "Observation of multicharged excitons and biexcitons in a single InGaAs quantum dot". In: *Physical Review B* 63.16 (Apr. 2001), p. 161305. DOI: `10.1103/PhysRevB.63.161305`.

[85] M. Hauck et al. "Locating environmental charge impurities with confluent laser spectroscopy of multiple quantum dots". In: *Physical Review B* 90.23 (Dec. 2014), p. 235306. DOI: `10.1103/PhysRevB.90.235306`.

[86] R. J. Warburton et al. "Giant permanent dipole moments of excitons in semiconductor nanostructures". In: *Physical Review B* 65.11 (Feb. 2002), p. 113303. DOI: `10.1103/PhysRevB.65.113303`.

[87] A. Zolotaryov et al. "InAs-coverage dependence of self-assembled quantum dot size, composition, and density". In: *Applied Physics Letters* 91.8 (Aug. 2007), p. 083107. ISSN: 0003-6951, 1077-3118. DOI: `10.1063/1.2772758`.

[88] Michael Metcalfe, Glenn S. Solomon, and John Lawall. "Heterodyne measurement of resonant elastic scattering from epitaxial quantum dots". In: *Applied Physics Letters* 102.23 (June 2013), p. 231114. ISSN: 0003-6951, 1077-3118. DOI: `10.1063/1.4809594`.

[89] H. Nakajima et al. "Carrier-transfer dynamics between neutral and charged excitonic states in a single quantum dot probed with second-order photon correlation measurements". In: *Physical Review B* 88.4 (July 2013), p. 045324. DOI: `10.1103/PhysRevB.88.045324`.

[90] David Fattal et al. "Entanglement Formation and Violation of Bell's Inequality with a Semiconductor Single Photon Source". In: *Physical Review Letters* 92 (Jan. 2004), p. 037903. ISSN: 0031-9007, 1079-7114. DOI: `10.1103/PhysRevLett.92.037903`.

[91] Disheng Chen et al. "Characterization of the local charge environment of a single quantum dot via resonance fluorescence". In: *Physical Review B* 93.11 (Mar. 2016), p. 115307. DOI: `10.1103/PhysRevB.93.115307`.

[92] Marcelo Davanço et al. "Multiple time scale blinking in InAs quantum dot single-photon sources". In: *Physical Review B* 89.16 (Apr. 2014), p. 161303. DOI: `10.1103/PhysRevB.89.161303`.

[93] Fengrui Hu et al. "Defect-Induced Photoluminescence Blinking of Single Epitaxial InGaAs Quantum Dots". en. In: *Scientific Reports* 5 (Mar. 2015). DOI: `10.1038/srep08898`.

[94] Annika Kurzmann et al. "Auger Recombination in Self-Assembled Quantum Dots: Quenching and Broadening of the Charged Exciton Transition". In: *Nano Letters* 16.5 (May 2016), pp. 3367–3372. ISSN: 1530-6984. DOI: `10.1021/acs.nanolett.6b01082`.

[95] M. Metcalfe et al. "Resolved Sideband Emission of InAs/GaAs Quantum Dots Strained by Surface Acoustic Waves". In: *Physical Review Letters* 105.3 (July 2010), p. 037401. DOI: `10.1103/PhysRevLett.105.037401`.

[96] Klaus D. Jöns et al. "Two-photon interference from two blinking quantum emitters". In: *Physical Review B* 96.7 (Aug. 2017), p. 075430. DOI: `10.1103/PhysRevB.96.075430`.

[97] O. Gazzano et al. "Effects of resonant-laser excitation on the emission properties in a single quantum dot". EN. In: *Optica* 5.4 (Apr. 2018), pp. 354–359. ISSN: 2334-2536. DOI: `10.1364/OPTICA.5.000354`.

[98] A. Muller et al. "Resonance Fluorescence from a Coherently Driven Semiconductor Quantum Dot in a Cavity". In: *Physical Review Letters* 99 (2007), p. 187402.

[99] Disheng Chen, Gary R. Lander, and Edward B. Flagg. "Resonance Fluorescence of an InGaAs Quantum Dot in a Planar Cavity Using Orthogonal Excitation and Detection". In: *JoVE (Journal of Visualized Experiments)* 128 (Oct. 2017), e56435–e56435. ISSN: 1940-087X. DOI: `10.3791/56435`.

[100] Graham Williams and David C. Watts. "Non-symmetrical dielectric relaxation behaviour arising from a simple empirical decay function". In: *Trans. Faraday Soc.* 66.0 (1970), pp. 80–85. DOI: `10.1039/TF9706600080`.

[101] R. Böhmer et al. "Nonexponential relaxations in strong and fragile glass formers". en. In: *The Journal of Chemical Physics* 99.5 (Sept. 1993), pp. 4201–4209. ISSN: 0021-9606, 1089-7690. DOI: `10.1063/1.466117`.

[102] J.C. Phillips. “Stretched exponential relaxation in molecular and electronic glasses”. In: *Reports on Progress in Physics* 59 (1996), pp. 1122–1207.

[103] Joseph Klafter and Michael F. Shlesinger. “On the relationship among three theories of relaxation in disordered systems”. en. In: *Proceedings of the National Academy of Sciences* 83.4 (Feb. 1986), pp. 848–851. ISSN: 0027-8424, 1091-6490.

[104] R. S. Anderssen, Saiful A. Husain, and R. J. Loy. “The Kohlrausch function: properties and applications”. en-US. In: *ANZIAM Journal* 45.0 (Aug. 2004), pp. 800–816. ISSN: 1445-8810. DOI: `10.21914/anziamj.v45i0.924`.

[105] E. N. Bodunov, Yu. A. Antonov, and A. L. Simões Gamboa. “On the origin of stretched exponential (Kohlrausch) relaxation kinetics in the room temperature luminescence decay of colloidal quantum dots”. In: *The Journal of Chemical Physics* 146.11 (Mar. 2017), p. 114102. ISSN: 0021-9606. DOI: `10.1063/1.4978396`.

[106] Kohlrausch R. “Theorie des elektrischen Rückstandes in der Leidener Flasche”. In: *Annalen der Physik* 167.2 (1854), pp. 179–214. ISSN: 0003-3804. DOI: `10.1002/andp.18541670203`.

[107] B. Sturman, E. Podivilov, and M. Gorkunov. “Origin of Stretched Exponential Relaxation for Hopping-Transport Models”. In: *Physical Review Letters* 91.17 (Oct. 2003), p. 176602. DOI: `10.1103/PhysRevLett.91.176602`.

[108] D. C. Johnston. “Stretched exponential relaxation arising from a continuous sum of exponential decays”. In: *Physical Review B* 74.18 (Nov. 2006), p. 184430. DOI: `10.1103/PhysRevB.74.184430`.

[109] Tetsuya Morishita. “Compressed exponential relaxation in liquid silicon: Universal feature of the crossover from ballistic to diffusive behavior in single-particle dynamics”. In: *The Journal of Chemical Physics* 137.2 (July 2012), p. 024510. ISSN: 0021-9606. DOI: `10.1063/1.4730613`.

[110] Aleksandar D. Rakić and Marian L. Majewski. “Modeling the optical dielectric function of GaAs and AlAs: Extension of Adachi’s model”. In: *Journal of Applied Physics* 80.10 (Nov. 1996), pp. 5909–5914. ISSN: 0021-8979. DOI: `10.1063/1.363586`.

[111] Z. Y. Xu and C. L. Tang. “Picosecond relaxation of hot carriers in highly photoexcited bulk GaAs and GaAs-AlGaAs multiple quantum wells”. en. In: *Applied Physics Letters* 44.7 (Apr. 1984), pp. 692–694. ISSN: 0003-6951, 1077-3118. DOI: 10.1063/1.94880.

[112] L. Mandel. “COHERENCE AND INDISTINGUISHABILITY”. In: *Optics Letters* 16.23 (Dec. 1991), pp. 1882–1883.

[113] L. Mandel. “Quantum effects in one-photon and two-photon interference”. In: *Reviews of Modern Physics* 71.2 (1999), pp. 274–282.

[114] K. Konthasinghe et al. “Coherent versus incoherent light scattering from a quantum dot”. In: *Physical Review B* 85.23 (June 2012), p. 235315. DOI: 10.1103/PhysRevB.85.235315.

[115] Clemens Matthiesen et al. “Phase-locked indistinguishable photons with synthesized waveforms from a solid-state source”. en. In: *Nature Communications* 4 (Mar. 2013), p. 1600. ISSN: 2041-1733. DOI: 10.1038/ncomms2601.

[116] Raphaël Proux et al. “Measuring the Photon Coalescence Time Window in the Continuous-Wave Regime for Resonantly Driven Semiconductor Quantum Dots”. In: *Physical Review Letters* 114.6 (Feb. 2015), p. 067401. DOI: 10.1103/PhysRevLett.114.067401.

[117] R. B. Patel et al. “Postselective Two-Photon Interference from a Continuous Nonclassical Stream of Photons Emitted by a Quantum Dot”. en. In: *Physical Review Letters* 100.20 (May 2008), p. 207405. ISSN: 0031-9007, 1079-7114. DOI: 10.1103/PhysRevLett.100.207405.

[118] M. O Scully and M. S Zubairy. *Quantum Optics*. University Press, Cambridge, U. K., 1997.

[119] Akio Koike and Naoki Sugimoto. “Temperature dependences of optical path length in fluorine-doped silica glass and bismuthate glass”. In: ed. by Michel J. Digonnet and Shibin Jiang. San Jose, CA, Feb. 2006, 61160Y. DOI: 10.1117/12.646630.

[120] Disheng Chen. “Resonant Excitation Spectroscopy and Photon Statistics of Self-assembled Semiconductor Quantum Dots”. PhD Thesis. West Virginia University, May 2017.

[121] M. J. Stanley et al. “Dynamics of a mesoscopic nuclear spin ensemble interacting with an optically driven electron spin”. In: *Physical Review B* 90.19 (Nov. 2014), p. 195305. DOI: 10.1103/PhysRevB.90.195305.

[122] A. N Vamivakas et al. “Spin-resolved quantum-dot resonance fluorescence”. In: *Nature Physics* (2009).

[123] Y. He et al. “Dynamically Controlled Resonance Fluorescence Spectra from a Doubly Dressed Single InGaAs Quantum Dot”. In: *Physical Review Letters* 114.9 (Mar. 2015), p. 097402. DOI: 10.1103/PhysRevLett.114.097402.

[124] B. R Mollow. “Power spectrum of light scattered by two-level systems”. In: *Phys. Rev.* 188 (1969), pp. 1969–1975.

[125] F. Y Wu, R. E Grove, and S. Ezekiel. “Investigation of the Spectrum of Resonance Fluorescence Induced by a Monochromatic Field”. In: *Physical Review Letters* 35.21 (1975), p. 1426.

[126] Disheng Chen et al. “Polarization-Dependent Interference of Coherent Scattering from Orthogonal Dipole Moments of a Resonantly Excited Quantum Dot”. In: *Physical Review Letters* 118.3 (Jan. 2017), p. 037401. DOI: 10.1103/PhysRevLett.118.037401.

[127] T. A. Wilkinson et al. “Complete Stokes vector analysis with a compact, portable rotating waveplate polarimeter”. In: *Review of Scientific Instruments* 92.9 (Sept. 2021). Publisher: American Institute of Physics, p. 093101. ISSN: 0034-6748. DOI: 10.1063/5.0052835.

[128] Paul A. Williams. “Rotating-wave-plate Stokes polarimeter for differential group delay measurements of polarization-mode dispersion”. EN. In: *Applied Optics* 38.31 (Nov. 1999), pp. 6508–6515. ISSN: 1539-4522. DOI: 10.1364/AO.38.006508.

[129] Søren Bobach et al. “Note: A portable rotating waveplate polarimeter”. In: *Review of Scientific Instruments* 88.3 (Mar. 2017), p. 036101. ISSN: 0034-6748. DOI: 10.1063/1.4977220.

[130] Matthew J. Romerein et al. “Calibration method using a single retarder to simultaneously measure polarization and fully characterize a polarimeter over a broad range of wavelengths”. EN. In: *Applied Optics* 50.28 (Oct. 2011), pp. 5382–5389. ISSN: 1539-4522. DOI: 10.1364/AO.50.005382.

[131] Toshiki Kihara. "Measurement method of Stokes parameters using a quarter-wave plate with phase difference errors". EN. In: *Applied Optics* 50.17 (June 2011), pp. 2582–2587. ISSN: 1539-4522. DOI: `10.1364/AO.50.002582`.

[132] C. Flueraru et al. "Error Analysis of a Rotating Quarter-Wave Plate Stokes' Polarimeter". In: *IEEE Transactions on Instrumentation and Measurement* 57.4 (Apr. 2008), pp. 731–735. ISSN: 0018-9456. DOI: `10.1109/TIM.2007.913752`.

[133] Raju Bhai KC et al. "A tunable Fabry-Perot cavity stabilized via a mechanically connected shearing interferometer". In: *Photonic and Phononic Properties of Engineered Nanostructures XII*. Vol. 12010. SPIE, Mar. 2022, pp. 49–54. DOI: `10.1117/12.2609815`.

[134] H. Kogelnik and T. Li. "Laser Beams and Resonators". In: *Applied Optics* 5.10 (Oct. 1966), pp. 1550–1567. DOI: `10.1364/AO.5.001550`.

[135] Barry J. Haycock et al. "High-throughput evaluation in nitrogen doping of amorphous titanium dioxide". en. In: *physica status solidi (b)* 251.6 (2014). _eprint: https://onlinelibrary.wiley.com/doi/pdf/10.1002/pssb.201451010, pp. 1225–1230. ISSN: 1521-3951. DOI: `10.1002/pssb.201451010`.

[136] Jean-Philippe Bouchaud. "Anomalous Relaxation in Complex Systems: From Stretched to Compressed Exponentials". In: *Anomalous Transport*. Section: 11. John Wiley & Sons, Ltd, 2008, pp. 327–345. ISBN: 978-3-527-62297-9. DOI: `10.1002/9783527622979.ch11`.